Behavior, Design, and Analysis of Unbonded Post-Tensioned Precast Concrete Coupling Beams

Brad D. Weldon

Publication Date

26-04-2010

BEHAVIOR, DESIGN, AND ANALYSIS OF UNBONDED POST-TENSIONED PRECAST CONCRETE COUPLING BEAMS

VOLUME IV

A Dissertation

Submitted to the Graduate School

of the University of Notre Dame

in Partial Fulfillment of the Requirements

for the Degree of

Doctor of Philosophy

by

Brad D. Weldon

____
Yahya C. Kurama, Director

Graduate Program in Civil Engineering and Geological Sciences

Notre Dame, Indiana

April 2010

CONTENTS

VOLUME IV

CHAPTER 9:

FIGURES

VOLUME IV

CHAPTER 8:

CHAPTER 9:

CHAPTER 10:

TABLES

VOLUME IV

CHAPTER 8:

CHAPTER 9:

CHAPTER 8

SUMMARY AND OVERVIEW OF RESULTS FROM COUPLED WALL SUBASSEMBLY EXPERIMENTS

Chapters 6 and 7 presented the results for the virgin and post-virgin beam tests, respectively, from the coupled wall subassembly experimental program. This chapter is intended to summarize the observed trends and present an overview of the results from these tests as follows: (1) beam shear force versus chord rotation behavior and progression of damage; (2) beam post-tensioning tendon force versus chord rotation behavior; (3) effect of beam post-tensioning tendon area and initial concrete stress; (4) effect of top and seat angles and angle strength; (5) effect of beam depth; (6) longitudinal mild steel strains; (7) transverse mild steel strains at beam ends; (8) transverse mild steel strains at beam midspan; (9) angle connections; (10) beam-to-wall connection and grout behavior; (11) compliance with ACI ITG-5.1 (ACI 2008); and (12) comparisons with monolithic cast-in-place concrete beams.

The graphs in each group of plots in this chapter are made to the same scale so as to facilitate comparisons between the different test specimens. No distinction is made between the beam chord rotations calculated from the beam displacements and the rotations calculated from the load block displacements. Recall from Chapters 6 and 7 that the chord rotations determined using these two different displacement measurements are negligibly small.

8.1 Beam Shear Force versus Chord Rotation Behavior and Progression of Damage

The coupling beam shear force versus chord rotation (V_b-θ_b) plots from the eight subassembly tests are depicted in Figure 8.1. Photographs showing the progression of damage at the south and north ends of the beam specimens are given in Figures 8.2 and 8.3, respectively.

Test 1 – The structure in Test 1 [Figure 8.1(a)] sustained 3 cycles at θ_b = 6.4% with approximately 11.5% loss in V_b. Prior to testing, the concrete at the south end of the beam was patched due to poor consolidation during casting. As shown in Figure 8.2, up through θ_b = 3.0%, concrete cracking and spalling in the beam were small. Beyond θ_b = 3.0%, the patched end of the beam suffered significant damage. The concrete at the unpatched end (see Figure 8.3) performed well throughout the test, with only negligible cover crushing at the corners. The initiation of low cycle fatigue fracture in the angles was observed at θ_b = 5.0%, and the beam ultimately failed during the 2nd cycle to θ_b = 8.0% due to the full (i.e., through thickness) fracture of the horizontal leg of the seat angle at the unpatched end. Angle yielding at the patched end was small since the gap opening at this end was small due to extensive cracking of the patched concrete. The wall test region of the reaction block was not damaged during the test.

Test 2 – The primary differences of Test 2 from Test 1 are increased beam post-tensioning steel area, decreased initial beam post-tensioning steel stress, and increased initial beam concrete nominal axial stress (see Table 3.2). By comparing Tests 1 and 2 in Figures 8.1(a) and 8.1(b), respectively, it can be seen that an increase in the coupling beam post-tensioning tendon area results in an increase in the lateral strength and self-centering capability of the structure. The structure in Test 2 sustained 3 cycles at θ_b = 6.4% with approximately 9.8% loss in V_b, which occurred, primarily, due to the loss of concrete at the beam ends. The test was stopped without going to the next displacement increment at θ_b = 8.0%. Spalling of the cover concrete at the beam ends initiated at θ_b = 1.5%, which is earlier than Test 1 due to the larger compressive stresses. Beyond θ_b = 3.33%, both beam ends suffered significant damage. The initiation of angle fracture was observed at θ_b = 5.0%, but full fracture of the angle legs did not occur during the test. Most of the angle yielding occurred at the north end of the beam since the gap opening at the south end was smaller due to more extensive cracking in the beam concrete. The wall test region of the reaction block experienced a small, negligible amount of cover concrete spalling along the beam centerline at a distance of 1.1875 in. (30 mm) from the beam-to-wall joint.

Test 3 – The primary differences of Test 3 from Test 2 are decreased beam post-tensioning steel area, decreased initial beam concrete nominal axial stress, and decreased angle strength [by using two short 2.5 in. (64 mm) angle strips instead of a single 7.5 in. (191 mm) angle at each top and seat connection]. As compared with Test 2, a drop in the lateral strength of the specimen in Test 3 can be seen in Figure 8.1(c). The structure sustained 3 cycles at θ_b = 5.0% with approximately 12.5% loss in V_b. The loss in V_b was due to damage to the wall test region of the reaction block. The post-tensioned angle-to-wall connections in the two short 2.5 in. (64 mm) angle strips resulted in vertical splitting of the wall test region due to the smaller area over which the connection post-tensioning forces were applied. The test was stopped after the 3rd cycle at θ_b = 5.0% to prevent further damage to the wall test region. Some spalling of the cover concrete at the beam corners was observed at θ_b = 5.0%; however, the damage in the beam was generally small throughout the test.

Test 3A – The primary difference of Test 3A from Test 3 is the use of full-length 7.5 in. (191 mm) top and seat angles with two layers of circular holes drilled in the vertical legs to control the angle yield mechanism and limit the angle strength. The coupling beam and the wall test region of the reaction block did not receive any additional damage during the test. As shown in Figure 8.1(d), the structure sustained 3 cycles at θ_b = 3.33% with approximately 4.9% loss in V_b. The loss in V_b was due to the initiation of low cycle fatigue fracture through the layer of holes near the angle heel in all four top and seat angles. The ultimate failure of the specimen occurred due to the full fracture of the top south angle during the 1st cycle to θ_b = 5.0%.

Test 3B – The primary difference of Test 3B from Test 3 is the use of 0.5 in. (13 mm) thick, 7.5 in. (191 mm wide) (same as the beam width) steel plates behind the vertical legs of the 2.5 in. (64 mm) angle strips. As shown in Figure 8.1(e), the structure sustained 3 cycles at θ_b = 8.0% with approximately 18% loss in V_b. Up through θ_b = 3.33%, there was only a small amount of additional cover concrete spalling at the beam corners. Beyond θ_b = 3.33%, the damage at the beam ends increased and initiation of angle fracture was observed. As described in Chapter 7, the ultimate failure of the specimen occurred due to the full fracture of the top and seat angles. Unlike Test 3, the wall test region did not receive additional damage during Test 3B because of the angle-to-wall connection plates behind the angle strips, which helped better distribute the connection post-tensioning forces to the wall concrete. However, significant deterioration to the grout pad was observed during the rotation cycles to 8.0%.

Test 4 – The primary differences of Test 4 from Test 3 are increased beam depth, decreased initial beam concrete nominal axial stress, and the use of angle-to-wall connection plates (similar to Test 3B). An increase in the lateral strength of the system can be observed in Figure 8.1(f) as compared to the shallower beams. The structure sustained 3 cycles at θ_b = 3.33% with no loss in V_b. The test was stopped at θ_b = 3.33% so that the beam could be retested with additional variations. There was no significant damage to the coupling beam and no additional damage to the wall test region throughout the test.

Test 4A – The primary difference of Test 4A from Test 4 is that no top and seat angles are used at the beam-to-wall connections, resulting in a V_b-θ_b relationship [Figure 8.1(g)] that is close to a bi-linear elastic relationship. The structure sustained 3 cycles at θ_b = 3.33% with no loss in V_b. The test was stopped at this point so that the beam could be reused in Test 4B. There was no significant additional damage to the structure during the entire test.

Test 4B – The primary differences of Test 4B from Test 4 are increased beam post-tensioning steel area, increased initial beam concrete nominal axial stress, and increased angle strength [by using full length 7.5 in. (191 mm) angles], resulting in an increase in the lateral strength of the system. As shown in Figure 8.1(h), the structure sustained 3 cycles at θ_b = 5.0% with a 9.3% loss in V_b. Beyond θ_b = 2.25% and 3.33%, respectively, significant additional damage was observed in the wall test region of the reaction block and at the ends of the coupling beam. This increased damage was expected because of the increased beam post-tensioning force and increased angle forces. During the 2nd cycle to θ_b = 6.4%, a large portion of the grout pad at the north end of the beam fell in between the load block and the vertical leg of the seat angle (when the gap was open), preventing the test to be continued. Note that the structure (and thus the grout pad) was being tested for the 3rd subsequent time, which caused the grout to disintegrate; otherwise, the grout performed well during all of the virgin beam tests. Initiation of angle fracture occurred at θ_b = 5.0%, but there was no full angle leg fracture during the test.

The effects of the various structural design parameters on the behavior of the specimens are discussed in more detail in the following sections.

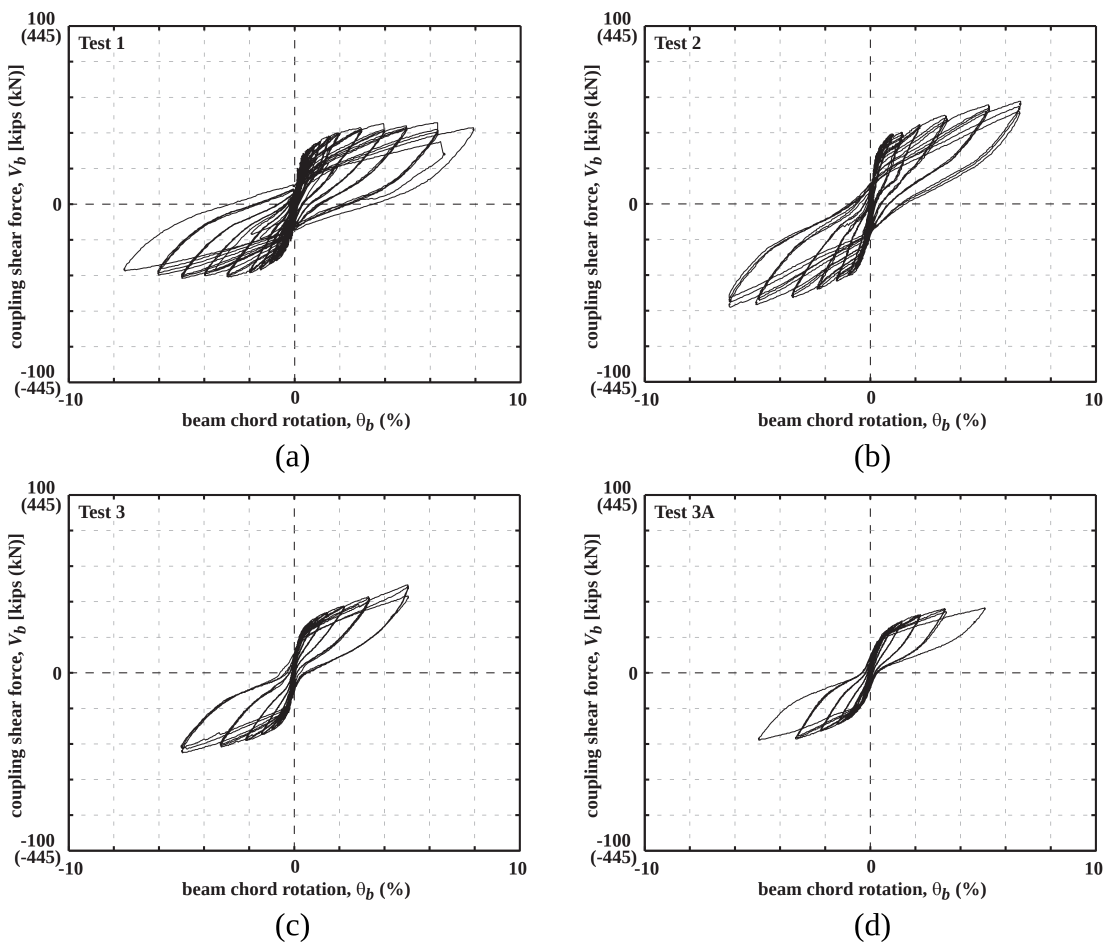

Figure 8.1: Beam shear force versus chord rotation – (a) Test 1; (b) Test 2; (c) Test 3; (d) Test 3A; (e) Test 3B; (f) Test 4; (g) Test 4A; (h) Test 4B.

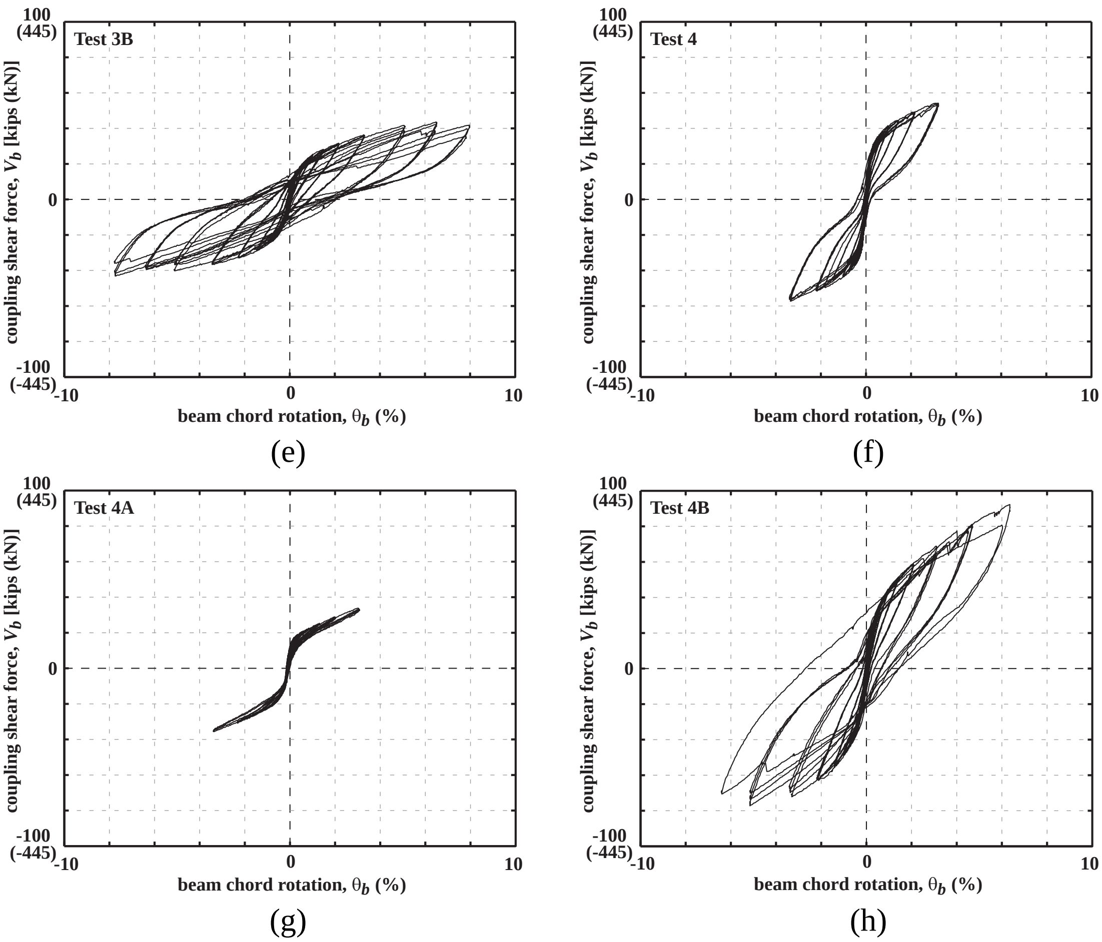

Figure 8.1 continued.

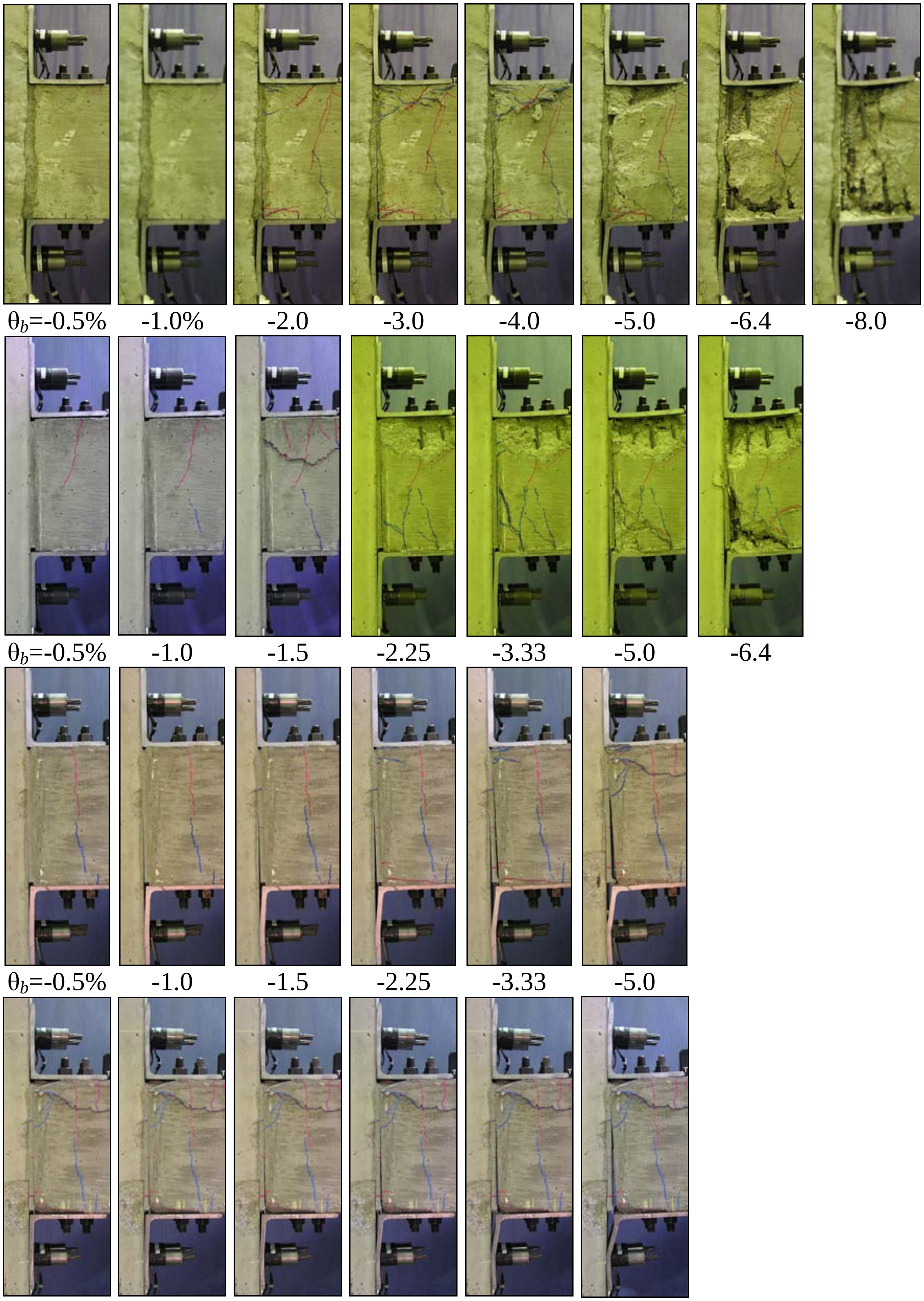

(a)

θ_b=-0.5% -1.0% -2.0 -3.0 -4.0 -5.0 -6.4 -8.0

(b)

θ_b=-0.5% -1.0 -1.5 -2.25 -3.33 -5.0 -6.4

(c)

θ_b=-0.5% -1.0 -1.5 -2.25 -3.33 -5.0

(d)

θ_b=-0.5% -1.0 -1.5 -2.25 -3.33 -5.0

Figure 8.2: Beam south end damage propagation – (a) Test 1; (b) Test 2; (c) Test 3; (d) Test 3A; (e) Test 3B; (f) Test 4; (g) Test 4A; (h) Test 4B.

(e)

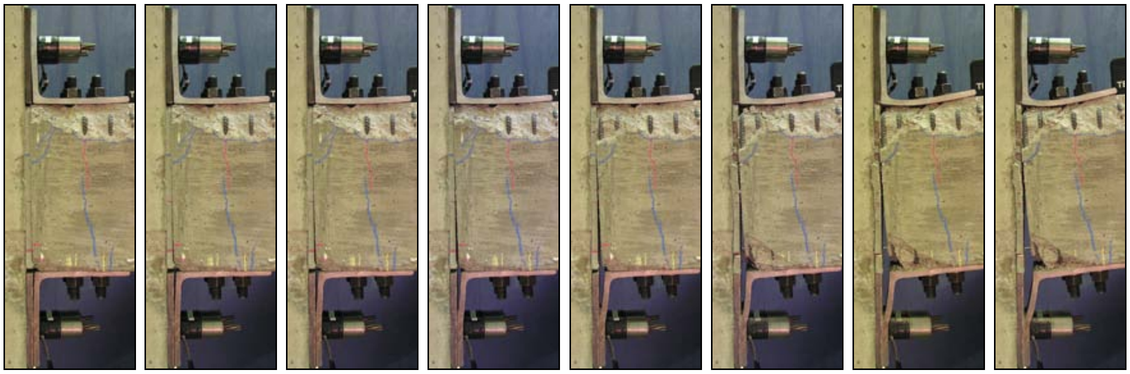

θ_b=-0.5% -1.0 -1.5 -2.25 -3.33 -5.0 -6.4 -8.0

(f)

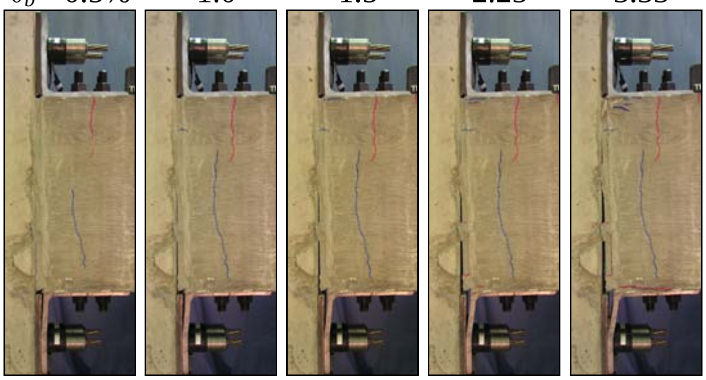

θ_b=-0.5% -1.0 -1.5 -2.25 -3.33

(g)

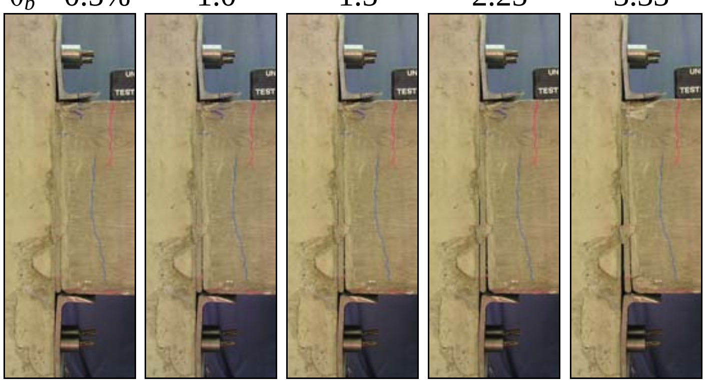

θ_b=-0.5% -1.0 -1.5 -2.25 -3.33

(h)

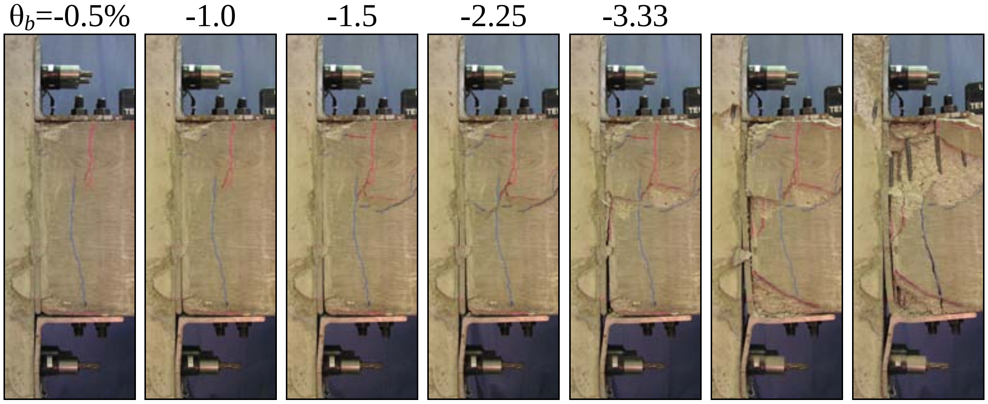

θ_b=-0.5% -1.0 -1.5 -2.25 -3.33 -5.0 -6.4

Figure 8.2 continued.

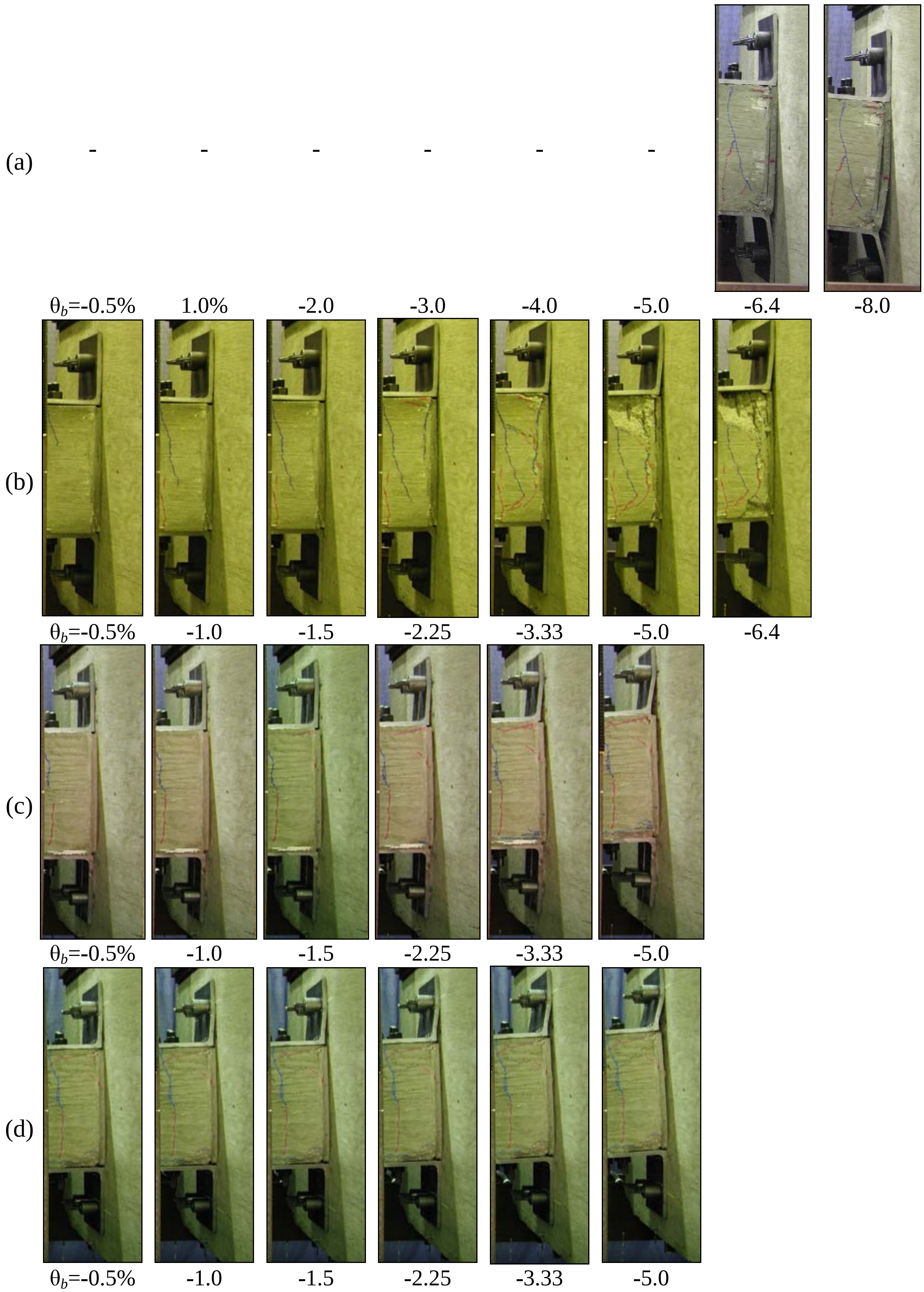

Figure 8.3: Beam north end damage propagation – (a) Test 1; (b) Test 2; (c) Test 3; (d) Test 3A; (e) Test 3B; (f) Test 4; (g) Test 4A; (h) Test 4B.

(e)

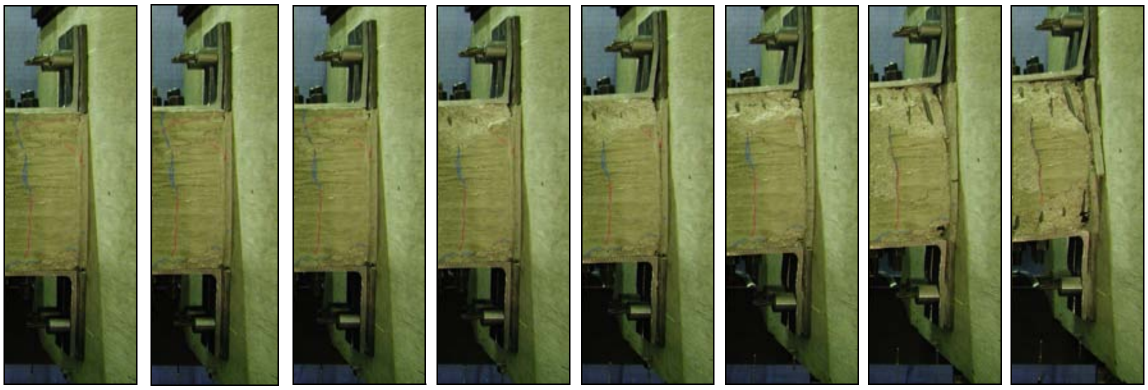

θ_b=-0.5% -1.0 -1.5 -2.25 -3.33 -5.0 -6.4 -8.0

(f)

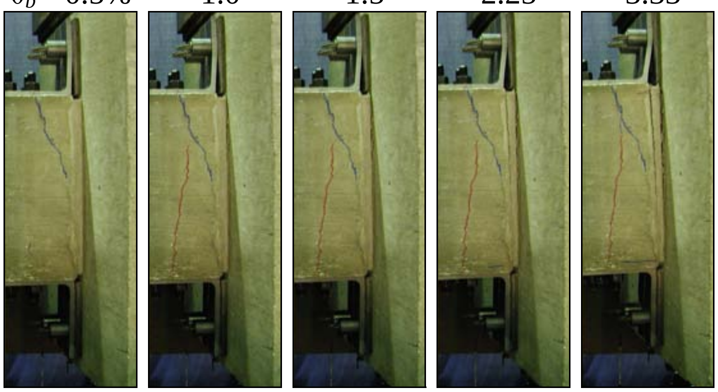

θ_b=-0.5% -1.0 -1.5 -2.25 -3.33

(g)

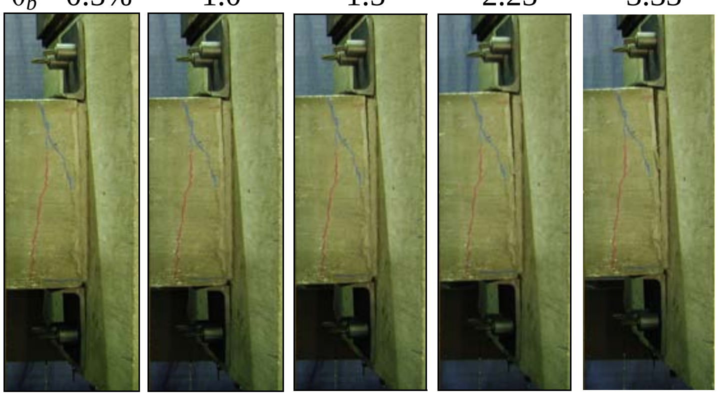

θ_b=-0.5% -1.0 -1.5 -2.25 -3.33

(h)

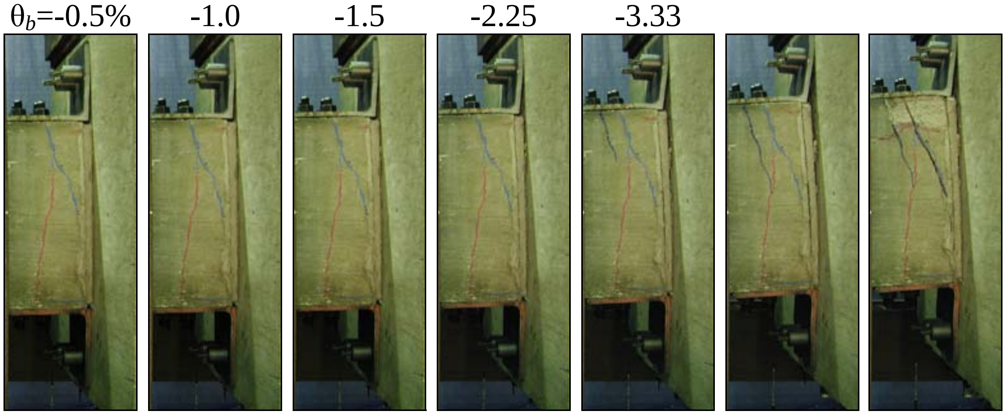

θ_b=-0.5% -1.0 -1.5 -2.25 -3.33 -5.0 -6.4

Figure 8.3 continued.

8.2 Beam Post-Tensioning Tendon Force versus Chord Rotation Behavior

Figure 8.4 shows the total coupling beam post-tensioning tendon force, P_{bp} (sum of the strand forces) versus chord rotation plots from the eight subassembly experiments. The post-tensioning tendon force is normalized with respect to the total design ultimate strength of the tendon, $P_{bpu} = \Sigma a_{bp} f_{bpu}$, where a_{bp} is the area of a single post-tensioning strand and f_{bpu} = 270 ksi (1862 MPa) is the design maximum strength of the post-tensioning steel. All eight specimens show the following general expected characteristics. Before significant gap opening, the total post-tensioning tendon force, P_{bp} is similar to the initial post-tensioning force, P_{bi}. As the subassembly is displaced, the strand forces increase, resisting gap opening. Prestress losses are observed upon unloading from increased displacements; however, these losses are small because the tendon is left unbonded over its entire length preventing significant yielding of the strands.

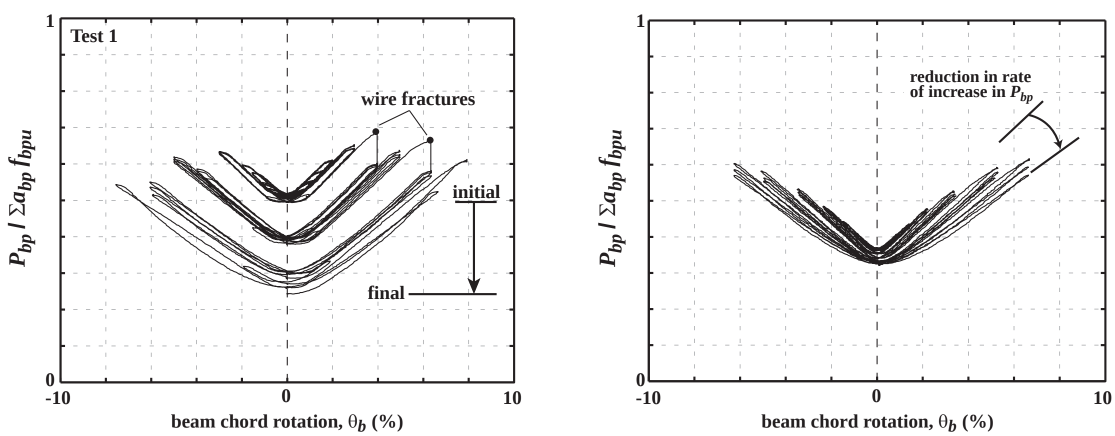

(a) (b)

Figure 8.4: Beam post-tensioning tendon force versus chord rotation – (a) Test 1; (b) Test 2; (c) Test 3; (d) Test 3A; (e) Test 3B; (f) Test 4; (g) Test 4A; (h) Test 4B.

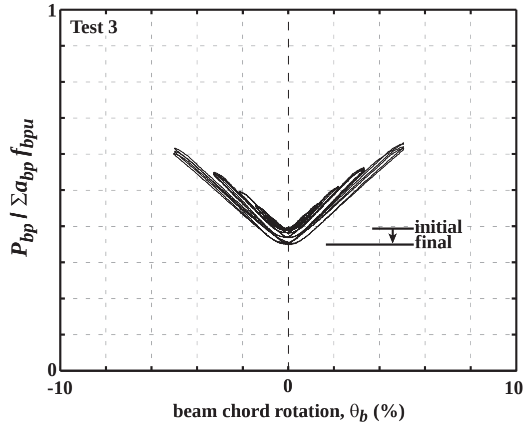

(c)

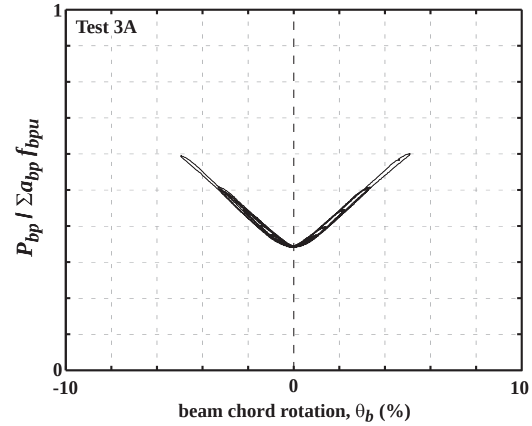

(d)

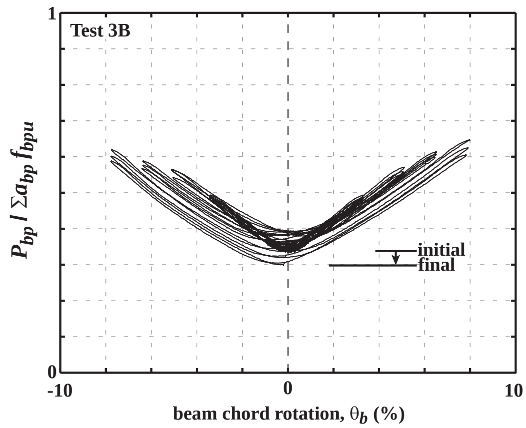

(e)

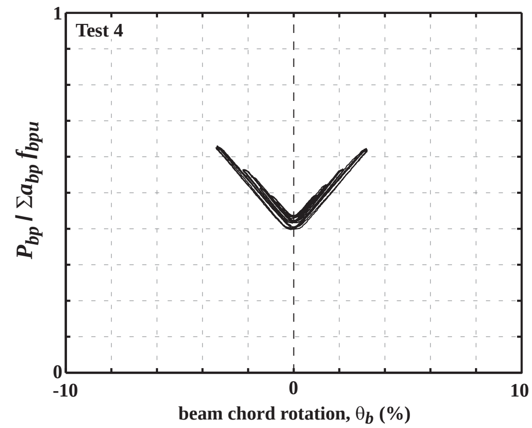

(f)

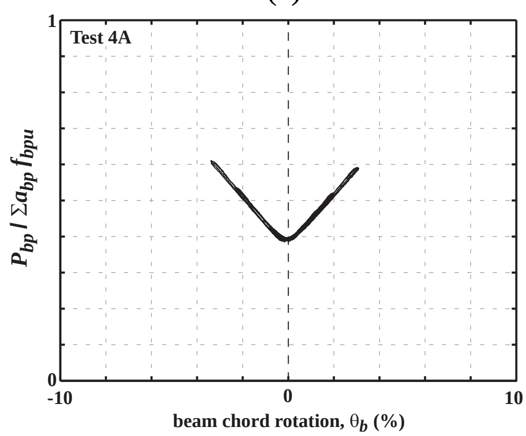

(g)

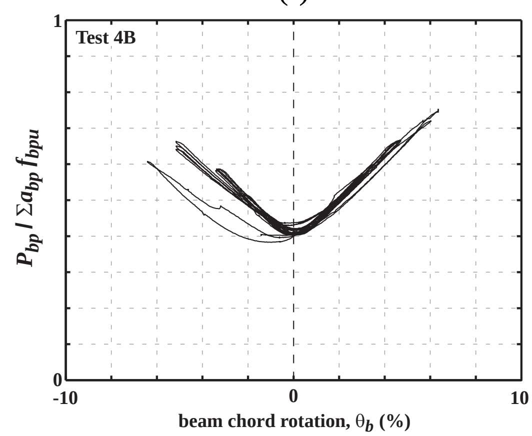

(h)

Figure 8.4 continued.

The expected behavior described above is observed in all eight tests; however, there are differences and deviations between the subassemblies. As described in Chapter 6, premature wire fractures inside the anchors of two post-tensioning strands (similar to the wire fracture in Figure 4.7) in Test 1 resulted in significant and sudden losses in the post-tensioning force as shown in Figure 8.4(a). The losses in P_{bp} resulted in a reduction in the self-centering capability of the structure upon unloading as well as reductions in the lateral stiffness and strength during the subsequent loading cycles. A comprehensive investigation on strand wire fractures in unbonded post-tensioning strand/anchor systems can be found in Walsh and Kurama (2009).

The effects of post-tensioning anchor wedge seating and nonlinear behavior in the beam and/or wall test region can also be observed in the P_{bp}-θ_b plots. For example, in Test 2, significant crushing of the concrete at the beam corners resulted in a gradual reduction in the rate of increase in P_{bp} as θ_b increased. This is expected since the crushing of the concrete at the beam corners results in a smaller amount of tendon elongation as the beam is rotated. Similarly, several tests show gradual losses in P_{bp} as the structure is returned to θ_b = 0% (note that these losses are small since the tendon is left unbonded). The largest strand stresses were reached in Test 4B when the deeper beam was displaced to θ_b = 6.4%. Comparing Test 4 with Tests 1, 2, and 3, it can be seen that the larger beam depth in Test 4 resulted in larger increases in the tendon stresses as the structure was displaced. This is expected since the deeper beam results in larger tendon elongations as the structure is rotated. The effects of the structure design properties (e.g., beam depth, initial strand stress) on the elongations and stresses in the post-tensioning tendon are quantified in Chapter 10. Note that the largest strand stress from the tests was $0.77f_{bpu}$;

and thus, based on the strand material tests in Chapter 4, it can be stated that the nonlinear behavior of the post-tensioning steel was negligible during the entire experimental program.

The losses in P_{bp} due to the strand wire fractures in Test 1 are much larger than the gradual losses due to other effects (e.g., anchor seating, nonlinear behavior of the concrete). To prevent wire fractures in the subsequent tests, a second anchor barrel (with no wedges, see Chapter 6) was used to reduce strand "kinking" at each anchor. In addition, the average initial strand stress was reduced from $f_{bpi} = 0.50f_{bpu}$ in Test 1 to 0.35 – $0.45f_{bpu}$ in Tests 2 – 4B. As shown in Figure 8.4, no strand wire fracture occurred in any of the subsequent tests, thus allowing most of the post-tensioning force to be maintained in each test. Note that since wire fracture did not occur in Test 4B (which had the largest strand stresses), reduced kinking at the anchors may have led to the better strand/anchor performance. Note also that the relatively low initial strand stresses used in this experimental program were precautionary. These stresses may not be representative of typical applications in practice, where the initial strand stresses can be as high as $0.70f_{bpu}$. Thus, it is concluded that strand/anchor systems need to be developed and validated for use in unbonded post-tensioned structural applications for seismic regions.

8.3 Effect of Beam Post-Tensioning Tendon Area and Initial Concrete Stress

The beam post-tensioning forces were sufficient to yield the tension angles back in compression and close the gaps at the beam ends, resulting in a self-centered behavior. Comparing Tests 1 and 2 (Figure 8.1), an increase in the beam post-tensioning tendon area results in an increase in the lateral strength [$v_{\max} = 5.0\sqrt{f'_c}$ ($0.42\sqrt{f'_c}$) versus $6.5\sqrt{f'_c}$ ($0.54\sqrt{f'_c}$) in psi (MPa) for Tests 1 and 2, respectively, see Table 3.2], stiffness, and self-centering of the structure. The beam post-tensioning tendon area, A_{bp} in Tests 1 and 2 were equal to 0.434 in.^{2} (280 mm^2) and 0.868 in.^{2} (560 mm^2), respectively, with an average initial post-tensioning strand stress, f_{bpi} of $0.50f_{bpu}$ and $0.36f_{bpu}$, respectively. The corresponding initial beam concrete nominal axial stress, f_{bci} (based on the actual beam cross-sectional area with the post-tensioning duct area removed) was equal to 0.58 ksi (4.0 MPa) and 0.82 ksi (5.7 MPa) in the two tests, respectively. As described previously, the smaller initial strand stresses in Test 2 were in order to prevent the premature strand wire fractures that were observed in Test 1. It can be seen that the increase in $v_{b,\max}$ is not proportional to the increase in the post-tensioning tendon area or in the total initial post-tensioning force since the post-tensioning steel provides only a part of V_b (with a significant portion of V_b provided by the angles) and since the neutral axis depth (i.e., depth of the compression zone in the concrete) increases as the post-tensioning force increases, reducing the moment arm. The effects of the post-tensioning and angle forces on the lateral behavior of the structure are quantified in Chapter 10.

Due to the increased concrete compressive stresses (resulting from the larger post-tensioning tendon area), Beam 2 had a larger amount of concrete damage than Beam 1. Different from Test 1 where the damage was localized in the patched region at the south end of the beam, the damage in Test 2 occurred at both ends of the beam (see Figure 8.5). Furthermore, the ultimate failure of the specimen in Test 2 was due to the damage in the beam; whereas low cycle fatigue fracture of the angles caused the ultimate failure of the structure in Test 1 (see Chapter 6).

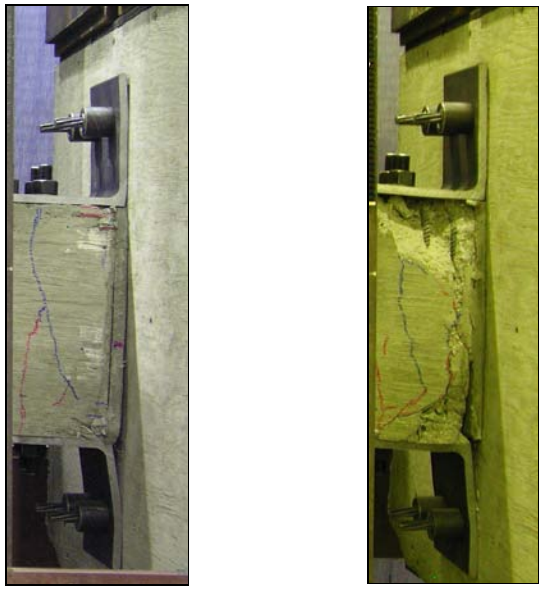

(a) (b)

Figure 8.5: Damage at north beam end at θ_b = 6.4% –
(a) Test 1; (b) Test 2.

8.4 Effect of Top and Seat Angles and Angle Strength

Following Test 4, the top and seat angles were removed and the subassembly was retested with no angles in Test 4A. Figure 8.1(g) shows that the behavior of the subassembly without angles was essentially bilinear-elastic, governed mainly by gap opening at the beam ends, with almost no energy dissipation. Looking at the behavior from Test 4 in Figure 8.1(f), it is concluded that most of the energy dissipation in the structure was provided by the yielding of the top and seat angles.

The effect of the angle strength on the system behavior can also be investigated using Tests 4 and 4B. As shown in Table 3.2, both of these subassemblies used L8x8x1/2 angles; however, the angles in Test 4 had a reduced length of 5.0 in. (127 mm), comprised of two 2.5 in. (64 mm) long angle strips, as compared with the 7.5 in. (191 mm) long angles in Test 4B. As an additional difference, the total post-tensioning tendon area in Test 4B was A_{bp} = 0.868 in.^{2} (560 mm^2), increased from A_{bp} = 0.651 in.^{2} (420 mm^2) in Test 4. Comparing the behavior of the two subassemblies in Figures 8.1(f) and 8.1(h) during the θ_b = ±3.33% cycle, prior to any significant damage in the structures, it can be seen that the increased angle strength and post-tensioning steel area in Test 4B resulted in a stronger structure (note that a similar trend can be observed between Test 2 and Tests 3 – 3B). The self-centering capability of the structure in Test 4B was maintained since the post-tensioning steel area was increased as the angle strength was increased.

The damage at the south end of the beam from Tests 4 and 4B at θ_b = -3.33% can be compared in Figures 8.6(a) and 8.6(b). The damage in Test 4B includes the damage from the prior two tests; nevertheless, it can be stated that the increased angle and post-tensioning forces in Test 4B resulted in larger damage. This can also be observed by comparing the beams from Tests 2 and 3 in Figures 8.6(c) and 8.6(d), respectively. Similar to Tests 4 and 4B, the primary differences of Test 2 from Tests 3 – 3B are increased post-tensioning steel area and angle forces. The effect of the larger angle forces in Test 2 can be seen through increased tension damage (i.e., concrete cracking) at the south bottom corner of the beam in Figure 8.6(c). In comparison, as described previously, increased post-tensioning forces primarily result in increased compression damage (i.e., crushing) in the concrete.

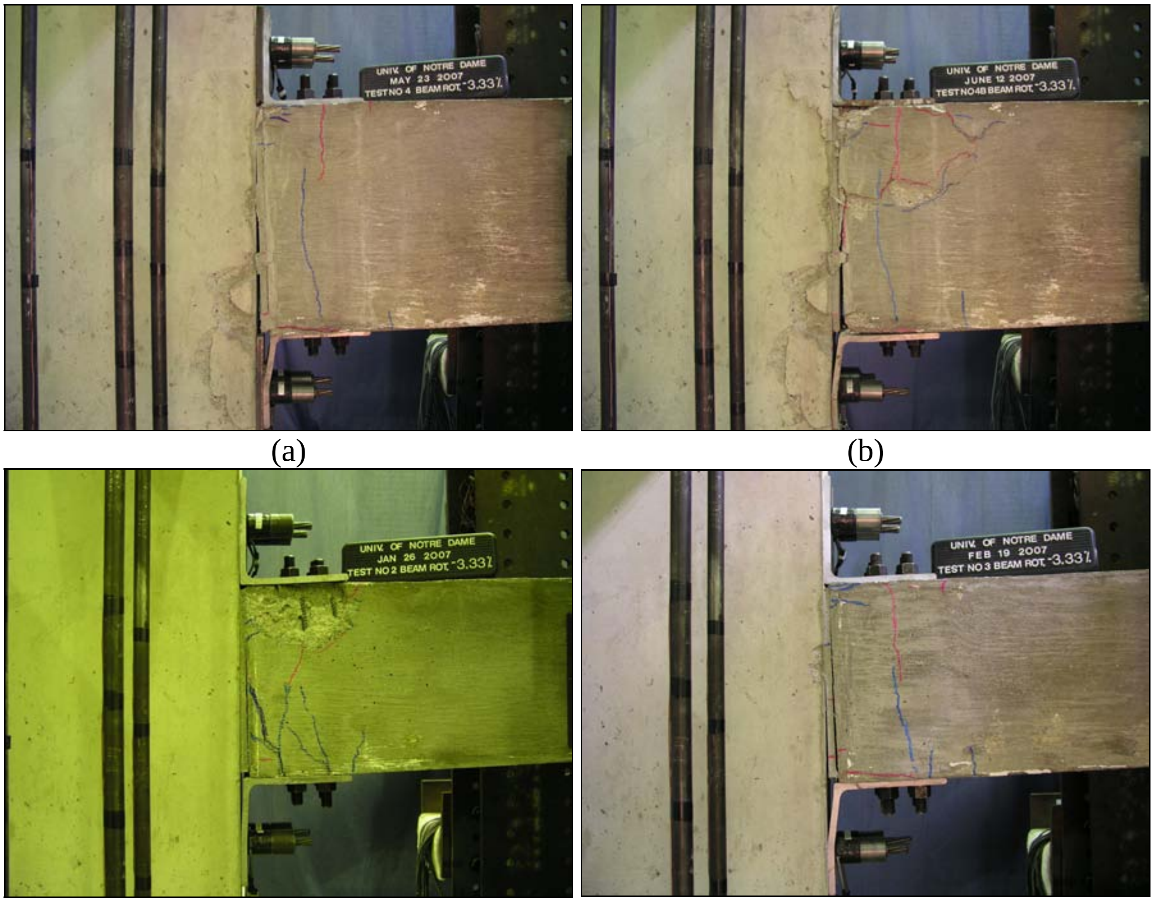

(a) (b)

(c) (d)

Figure 8.6: Damage at south beam end at θ_b = -3.33% –
(a) Test 4; (b) Test 4B; (c) Test 2; (d) Test 3.

8.5 Effect of Beam Depth

Looking at Figures 8.1(f) and Figures 8.1(c)-(e), increased lateral strength, stiffness, and energy dissipation can be observed for the 18 in. (457 mm) deep coupling beam from Test 4 as compared with the 14 in. (356 mm) deep beam from Tests 3-3B. The largest measured beam shear strength from the experimental program is equal to v_{max} = $7.6\sqrt{f'_c}$ ($0.63\sqrt{f'_c}$) in psi (MPa) for Test 4B (see Table 3.2). At a given rotation, the larger beam depth creates larger gap opening at the beam ends, and thus, larger deformations and earlier yielding in the tension angles, as well as larger increases in the post-tensioning strand stresses (see Figure 8.4). Consequently, the displacement and force demands on the angle and post-tensioning tendon components and connections increase with increased beam depth, as quantified in Chapter 10.

As shown in Figure 8.7, the damage in both Tests 3 and 4 was minimal up to a chord rotation of 3.33%, and the amount of mild steel reinforcement in the beam was adequate for both beam depths. Note that even though neither test was loaded to failure, a smaller ultimate sustained rotation would be expected in Test 4 through earlier angle fracture due to the increased gap opening.

(a) (b)

Figure 8.7: Damage at south beam end at θ_b = -3.33% – (a) Test 3; (b) Test 4.

8.6 Longitudinal Mild Steel Strains

As described in Chapter 3, two No. 6 looping reinforcing bars were used to transfer the angle forces into each beam. The same reinforcement design was used in all beams, including the tests conducted with an increased beam depth. Figure 8.8(a) shows the maximum tensile strains measured in the horizontal legs of these bars, which occurred in one of the strain gauges [6(1)T-E, 6(1)T-W, 6(1)B-E, or 6(1)B-W] at the critical section where the angles were connected to the beam. The θ_b values plotted on the horizontal axis correspond to the measured rotation at which the maximum strain during each displacement increment was observed. The vertical dashed line at θ_b = 3.33% represents the ASCE/SEI 41-06 (ASCE 2007) collapse prevention level for monolithic cast-in-place coupling beams with diagonal reinforcement and the horizontal dashed line shows the measured yield strain of the looping reinforcement (ε_{ly} = 0.00283, see Chapter 4).

Looking at the θ_b = 3.33% rotation level, the bar strains remained well below yield. As also shown in Figure 8.8(b), Test 2 resulted in the largest strains due to the large angle forces, with only slightly lower strains in Tests 3B and 4B. Note that for Test 1, the maximum strain in Figure 8.8(b) was measured at a beam chord rotation of θ_b = 3.0%, whereas the strains shown for the other tests were measured at θ_b = 3.33%. The following additional observations can be made regarding the results in Figures 8.8(a) and 8.8(b).

(1) Although Test 1 used the same size angles as those in Tests 2 and 4B, due to the damage in the patched end of the beam (where the bar strain gages were located), gap opening did not occur in Test 1 as much as it did in Tests 2 and 4B, and thus, the angles were not pulled as much in tension. This resulted in smaller longitudinal mild steel strains in Test 1 as compared with Tests 2 and 4B.

(2) Even though smaller angles were used in Test 3B, the longitudinal bars experienced similar tensile strains as in Tests 2 and 4B because the beam had been tested twice before and taken to a chord rotation of 5.0% in both of the previous tests. Based on the results, it can be stated that the longitudinal bar strains increased during each subsequent re-testing of a beam (see Tests 3, 3A, and 3B).

(3) As expected, Test 4A resulted in the smallest tensile strains in the longitudinal bars since no angle forces were transferred into the beam.

As the test specimens continued to be loaded, the strains continued to increase. Looking at the ultimate sustained rotation levels (defined as the largest rotation that a beam is able to sustain with no more than 20% drop in lateral resistance during three fully reversed cycles, see Section 8.12) for Tests 1, 2, 3B, and 4B [see also Figure 8.8(c)], the largest bar strains occurred in Test 1 (a maximum strain of 0.003, slightly above the steel yield strain, was measured at θ_b = 6.4%) due to the significant amount of damage that occurred in the patched region of the beam. The maximum strains in Test 4B were also large and measured 0.0028 (right at the yield strain of the steel) at θ_b = 6.0% due to the large angle size and large gap opening resulting from the increased beam depth. In general, the design of the longitudinal reinforcement was adequate for all of the variables tested (e.g., beam depth) since the steel strains did not reach yield until very large rotation cycles. The following additional observations can be made regarding the results in Figures 8.8(a) and 8.8(c).

(1) At large rotations, the bar strains from Test 1 increased faster than the strains from the other tests (except for Test 4B), possibly due to the disintegration of the patched concrete.

(2) Despite a larger ultimate sustained rotation, the maximum longitudinal bar strains in Test 3B were smaller than the strains in Tests 1, 2, and 4B. This is because of the smaller angle size used in Test 3B.

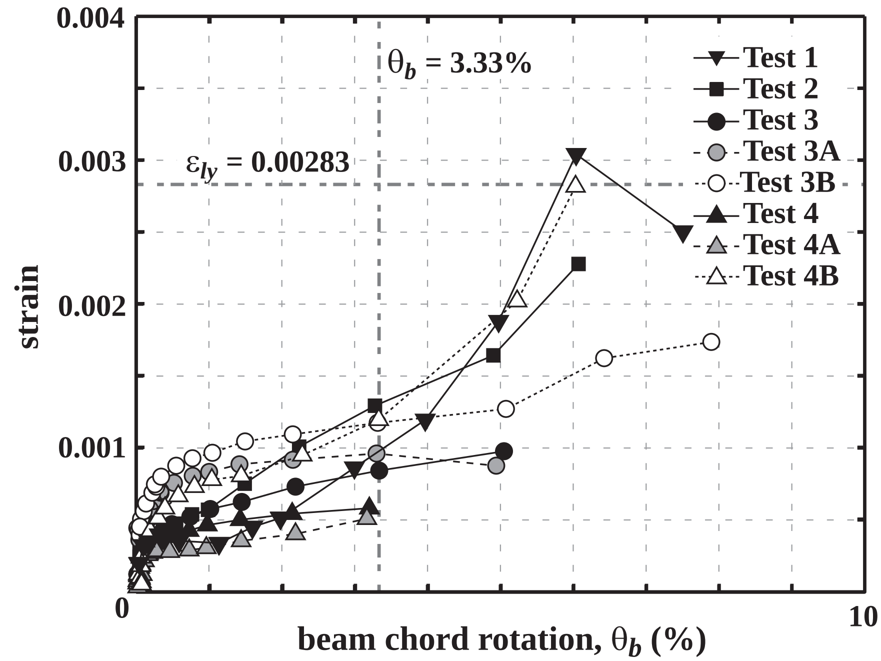

(a)

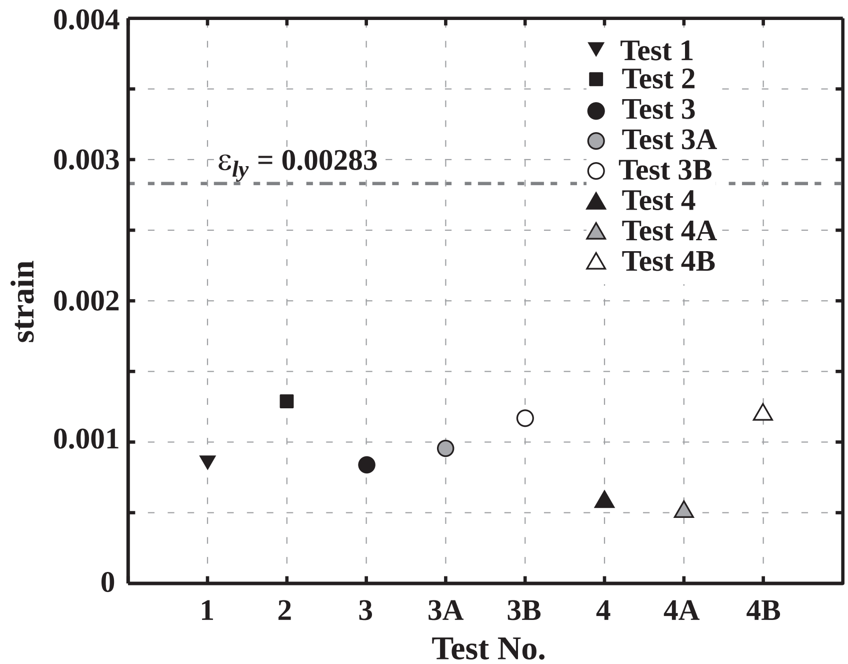

(b)

Figure 8.8: Maximum longitudinal reinforcement strains –
(a) versus θ_b; (b) at θ_b = 3.33%; (c) at ultimate sustained rotation.

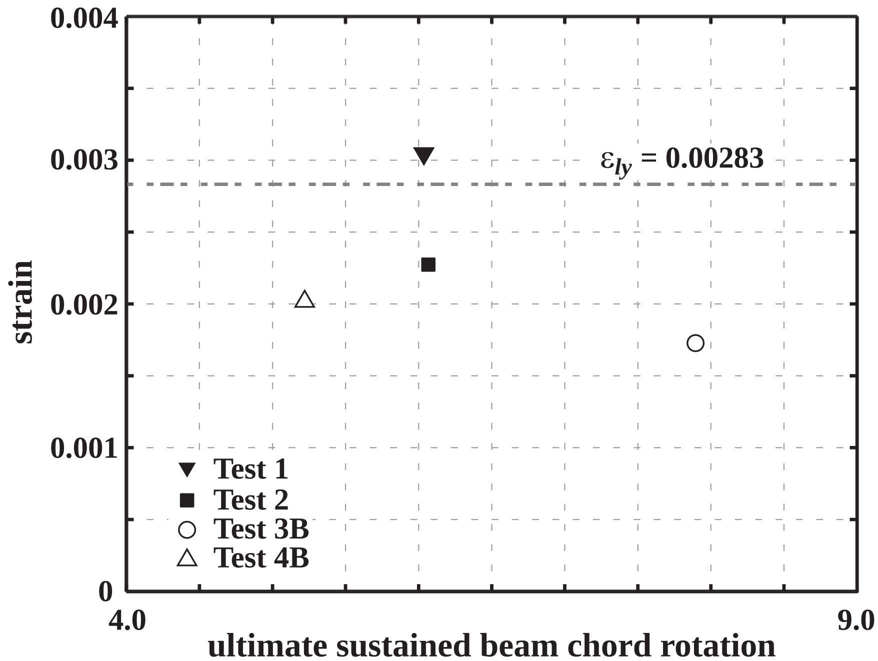

(c)

Figure 8.8 continued.

8.7 Transverse Mild Steel Strains at Beam Ends

Figure 8.9 shows the maximum tensile strains in the transverse (i.e., vertical) legs of the No. 6 bars at the beam ends in a similar format to the maximum longitudinal leg strains in Figure 8.8. The θ_b values in Figure 8.9 correspond to the measured rotation at which the maximum transverse leg strain during each displacement increment was observed, and thus, these rotations may be slightly different than those corresponding to the maximum longitudinal leg strains plotted in Figure 8.8. It can be seen that the bar strains, measured at the mid-length of the vertical leg, remained well below the yield strain throughout each test. Similar to the longitudinal leg strains, the vertical leg strains increased during each subsequent re-resting of a beam (see Tests 3, 3A, and 3B). Consequently, Test 3B had the largest bar strains due to the accumulation of strains from the previous Tests 3 and 3A. Note that the strain gauges in Test 3B were lost prior to the ultimate sustained rotation of 8.0%; therefore, the results are shown for up to θ_b = 6.4%. As expected, Test 4A resulted in the smallest strains since the beam shear force was the smallest in this test.

Tests 1 – 3 had similar transverse reinforcement strains during the smaller displacement cycles. At larger cycles, the transverse strains increased more in Tests 1 and 2 than in Test 3 due the larger amount of damage in the concrete. Beyond θ_b = 3.0%, the transverse bar strains for Test 1 decreased, which may have been due to the loss of bond between the steel and the deteriorating patched concrete. It is concluded that the design of the transverse reinforcement at the beam ends was adequate. Note that the angle-to-beam connection bolts might have taken a portion of the transverse tensile stresses at the beam ends (resulting in, for example, the close-to-zero transverse steel strains for Test 4A in Figure 8.9); however, these bolts were not instrumented and therefore their contribution to the behavior of the test specimens cannot be quantified.

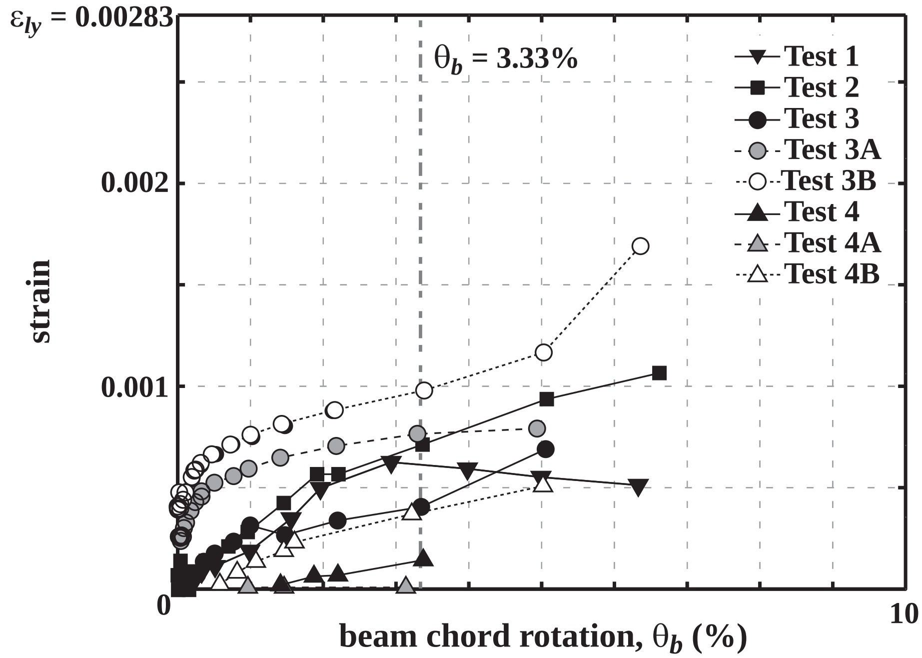

(a)

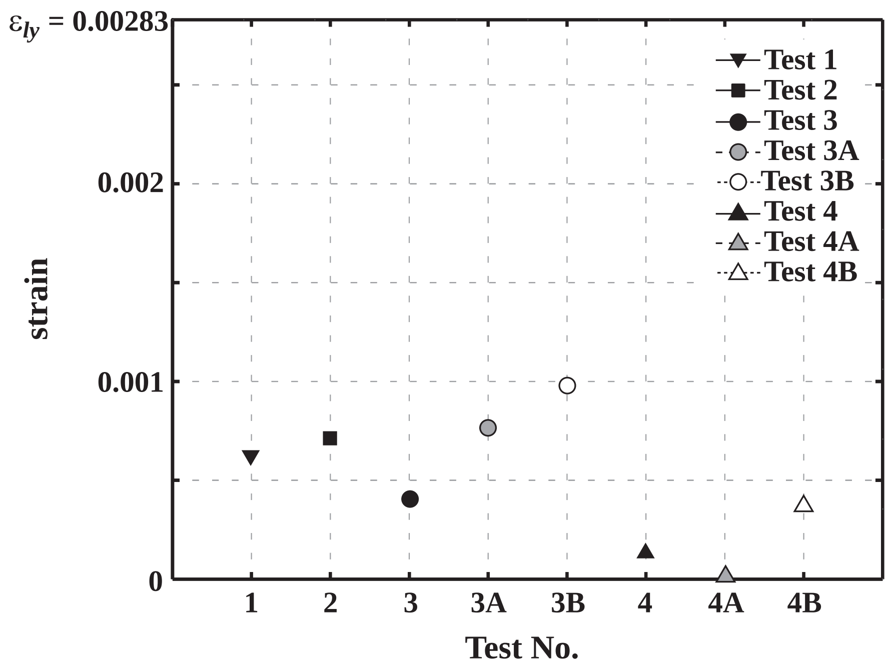

(b)

Figure 8.9: Maximum beam end transverse reinforcement strains – (a) versus θ_b; (b) at $\theta_b = 3.33\%$; (c) at ultimate sustained rotation.

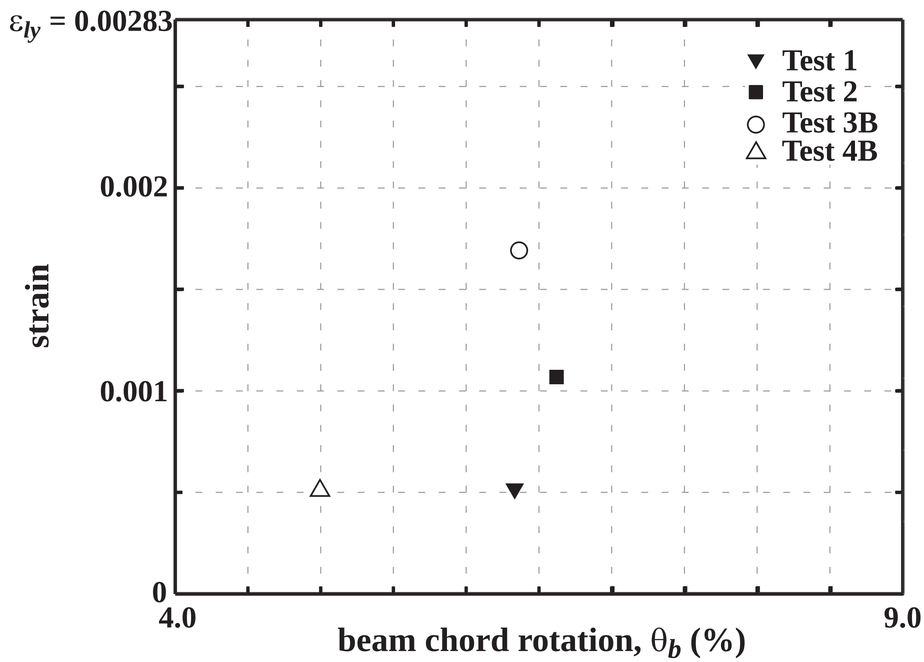

(c)

Figure 8.9 continued.

8.8 Transverse Mild Steel Strains at Beam Midspan

Figure 8.10 shows the maximum tensile strains in the vertical legs of the No. 3 beam midspan transverse hoops in a similar format to the maximum steel strains in Figure 8.9. No data was collected from the midspan hoop strain gauges during the Test 3 series. It can be seen that the strains in the midspan hoop steel, measured at the mid-length of the vertical leg, remained well below the yield strain of the reinforcement and below the cracking strain of the concrete throughout the loading history. Note that the midspan hoop strains in Test 2 exceeded the concrete cracking strain even though no concrete cracking was observed in the midspan regions of the beam. It is not clear why significantly higher steel strains were measured in this test as compared to the other tests.

Nevertheless, it can be stated that the use of nominally spaced minimum transverse reinforcement in the midspan regions of the beams is adequate.

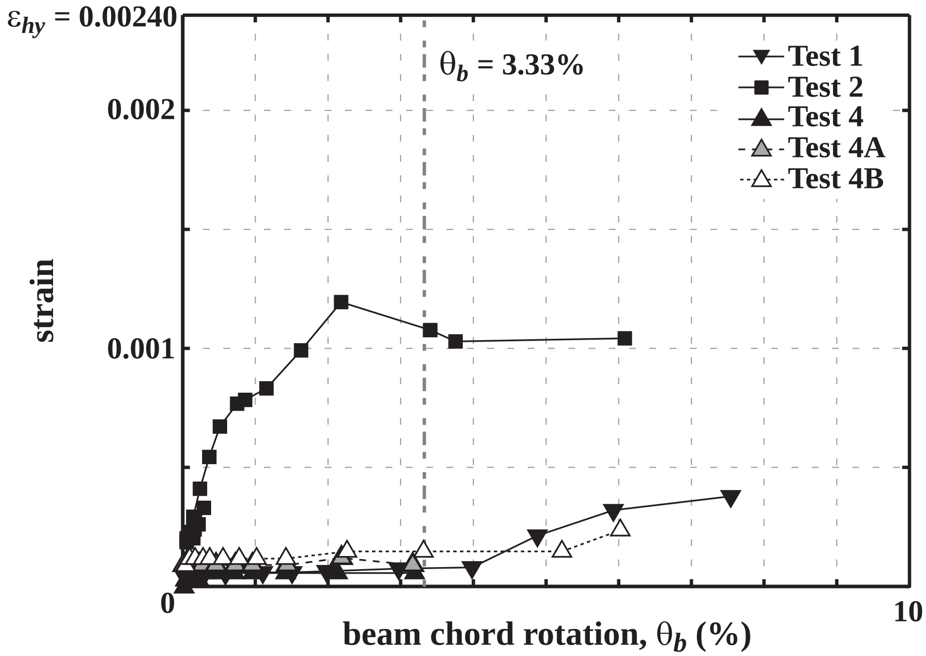

(a)

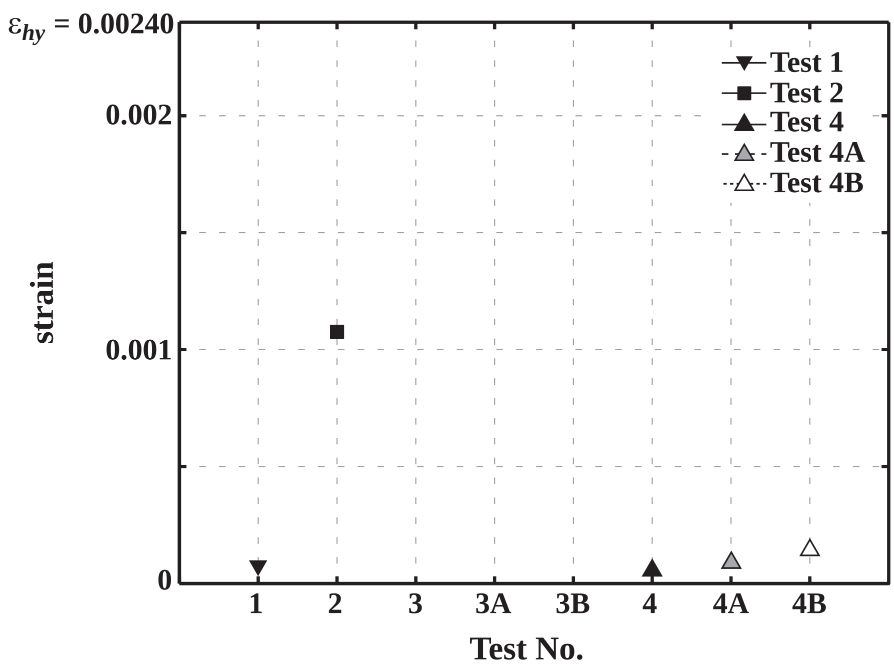

(b)

Figure 8.10: Maximum beam midspan transverse reinforcement strains – (a) versus θ_b; (b) at θ_b = 3.33%; (c) at ultimate sustained rotation.

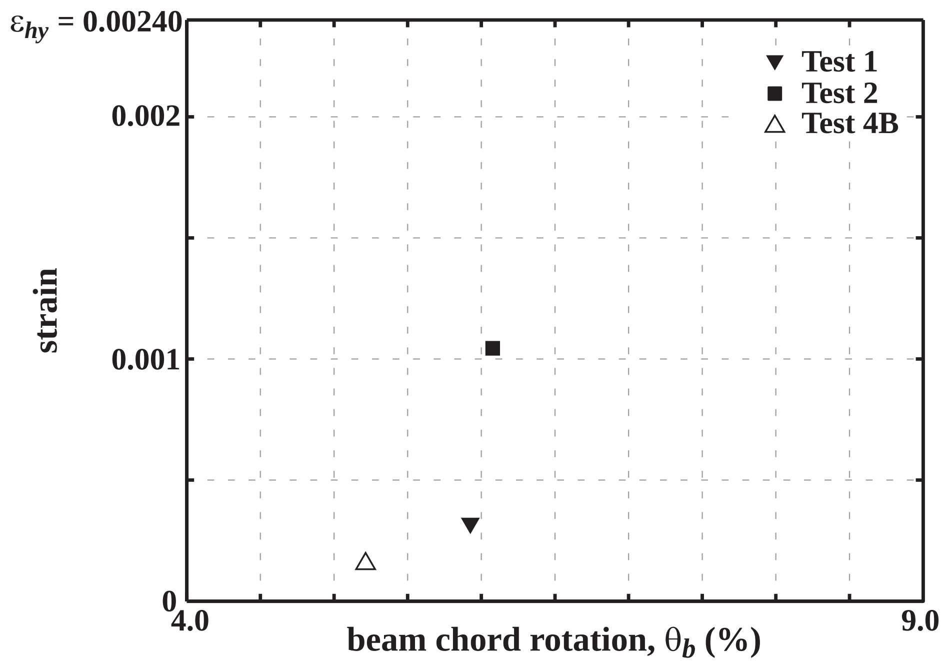

(c)

Figure 8.10 continued.

8.9 Angle Connections

The slip critical angle-to-beam connections worked well during the experimental program. No slip of the horizontal legs of the angles was observed during the tests through θ_b = 3.33%; however, as damage accumulated at the beam ends, the connection bolt forces were reduced and a small amount of slip was observed (e.g., the jumps in the hysteresis curves of Test 4B during the θ_b = 5.0% and 6.4% cycles occurred due to the slipping of the angle-to-beam connections). This typically occurred at beam chord rotations greater than 5.0%.

The unbonded post-tensioned angle-to-wall connections also worked well; however, the use of narrow angle strips in Test 3 caused the concrete in the wall test region to locally crush and split. The use of angle-to-wall connection plates in Tests 3B and 4 enabled these shorter length angles to be used without affecting the behavior of the angles. Thus, the high compressive forces applied to the wall concrete from the angle-to-wall connection strands need to be properly distributed into the wall regions. The connection strands performed well with no yielding, resulting in the connection post-tensioning forces to be maintained throughout each test.

8.10 Beam-to-Wall Connection and Grout Behavior

No slip was observed at the beam-to-wall interfaces of the test specimens, demonstrating that the beam post-tensioning force and the top and seat angles provided adequate vertical support to the beam at the ends. The high-strength fiber-reinforced grout at the interfaces performed well; however, during large rotations of the beam in Test 1, the heels of the angles came into contact with the grout column, causing it to buckle away from the beam ends. This behavior was prevented in the subsequent tests by leaving a small gap [approximately 0.25 in. (6 mm)] at the top and bottom of the grout column. No significant crushing/deterioration of the fiber-reinforced grout was observed in any of the tests, except for the 3rd subsequent testing of the structure in Tests 3B and 4B as described previously. Up to about θ_b=3.33%, gap opening occurred between the grout pad and the faces of the load and reaction blocks due to the use of a bond breaker at the block surfaces. While gap opening was observed at both faces of the grout at large rotations, this did not affect the behavior of the test structure.

8.11 Compliance with ACI ITG-5.1

ACI ITG-5.1 (ACI 2008) defines minimum seismic acceptance criteria for unbonded post-tensioned precast concrete structural walls, including coupled walls, based on experimental evidence and analysis. This section evaluates the test specimens for compliance with the relevant requirements of ACI ITG-5.1. Some of the parameters related to these acceptance criteria are described in Chapter 2.

8.11.1 Probable Lateral Strength

ACI ITG-5.1 requires that the peak measured lateral strength, E_{max} of each specimen fall between $0.9E_{pr}$ and $1.2E_{pr}$, where E_{pr} is the probable strength of the specimen at peak load, calculated using a pre-test design procedure and the measured geometric properties of the structure, measured stress-strain properties of the reinforcement and concrete, a strain and/or deformation compatibility analysis, and a strength reduction factor φ of 1.0. An approximate idealized tri-linear beam end moment (or shear) versus chord rotation relationship for the design of unbonded post-tensioned precast coupling beams is described in Chapter 10. Table 8.1 compares the estimated probable strength, E_{pr} from this procedure (using the measured geometric and material properties of the structure) with the measured strength of the test specimens, E_{max} from Chapters 6 and 7. The E_{pr} values were taken as the estimated coupling beam end shear force corresponding to the beam chord rotation when E_{max} was reached from the experiments.

It can be seen that for all tests, the E_{pr}/E_{max} ratio is very good and the ACI ITG-5.1 requirement (i.e., $0.9E_{pr} < E_{max} < 1.2E_{pr}$) is satisfied. Thus, the results from the experimental program and the proposed design/analysis procedure are validated. More comparisons between the proposed design/analysis procedure and the test results can be found in Chapter 10. Note that no prediction is provided for Test 3A, since there is currently no strength model for the angles used in this test (with two lines of holes drilled in the angle vertical legs).

TABLE 8.1

PROBABLE LATERAL STRENGTH

Test No.	[1] E_{pr} [kips (kN)]	$0.9E_{pr}$ [kips (kN)]	<	[2] E_{max} [kips (kN)]	<	$1.2E_{pr}$ [kips (kN)]	E_{pr}/E_{max}
1	42.3 (188)	38.1 (169)	<	45.7 (203)	<	50.8 (226)	0.93
2	55.2 (245)	49.7 (221)	<	58.2 (259)	<	66.2 (294)	0.95
3	44.6 (198)	40.1 (179)	<	49.5 (220)	<	53.5 (238)	0.90
3A	-						
3B	42.5 (189)	38.2 (170)	<	43.6 (194)	<	51.0 (227)	0.97
4	52.2 (232)	47.0 (209)	<	57.3 (255)	<	62.7 (279)	0.91
4A	33.0 (147)	29.7 (132)	<	35.6 (159)	<	39.6 (176)	0.93
4B	73.4 (327)	66.1 (294)	<	81.2 (361)	<	88.1 (392)	0.90

[1] E_{pr} = probable lateral strength from the tri-linear estimation described in Chapter 10;
[2] $E_{max}=V_{b,\max}$ (maximum measured beam shear force).

8.11.2 Relative Energy Dissipation Ratio

Based on ACI ITG-5.1, the "relative energy dissipation ratio, β_b," is defined for a lateral force (or moment) versus displacement (or rotation) cycle as the ratio of the area A_h enclosed by the hysteresis loop for that cycle to the area of the circumscribing parallelograms. This circumscribing area (see Figure 8.11 for the θ_b = 3.33% cycle from Test 4) is defined by the initial stiffnesses, *K* and *K'*, from the positive and negative directions, respectively, and the peak positive and negative lateral resistances, E_1 and E_2, respectively, during the cycle for which the relative energy dissipation ratio is calculated (ACI 2008). The initial stiffness K is defined as the slope of the line joining the origin to the measured envelope lateral load versus displacement behavior of the structure at $0.75E_{nt}$, where E_{nt} is the nominal lateral resistance calculated using a pre-test design procedure and the measured geometric properties of the structure, measured yield strengths of the reinforcement, measured compressive strengths of the concrete, measured strengths of the coupling elements (top and seat angles), and a strength reduction factor, φ of 1.0. The nominal lateral resistance of the test specimens was calculated as $E_{nt} = 2M_{ay}/l_b$, where M_{ay} is the moment at the tension angle yield state as described in detail in Chapter 10. The initial stiffness K' is defined similar to the stiffness K, but is calculated using the envelope load versus displacement response of the structure in the negative direction.

According to ACI ITG-5.1, the relative energy dissipation ratio, β_b should be greater than or equal to 0.125 during the third cycle of the displacement level for which experimental validation is sought. Table 8.2 shows the β_b values calculated from the third measured complete loading cycle at each beam target chord rotation level from the subassembly experiments. Similarly, Figure 8.12 shows the β_b-θ_b relationship measured from each test, where the θ_b values correspond to the target rotation values for each loading increment. The experimental β_b values that meet the ACI ITG-5.1 minimum requirement (horizontal line in Figure 8.12) are shaded in Table 8.2. The results show that, for rotations equal to or greater than 1.5%, the $\beta_b \geq 0.125$ limit is satisfied for all of the tests with the exception of Test 4A, which used no top and seat angles. Thus, it is concluded that the ACI ITG-5.1 energy dissipation requirement can be satisfied by using yielding steel top and seat angles at the beam-to-wall joints of unbonded post-tensioned coupling beams. For some of the tests, a reduction in β_b can be seen as θ_b is increased. In the case of Test 3B, the reduction in β_b beyond θ_b = 5.0% is expected to have occurred due to the progression of low cycle fatigue fracture in the angles. Note that various other factors may also have played a role in the reduction of β_b with increased θ_b (e.g., reduced tension angle deformations due to the slipping of the angle-to-beam connection bolts).

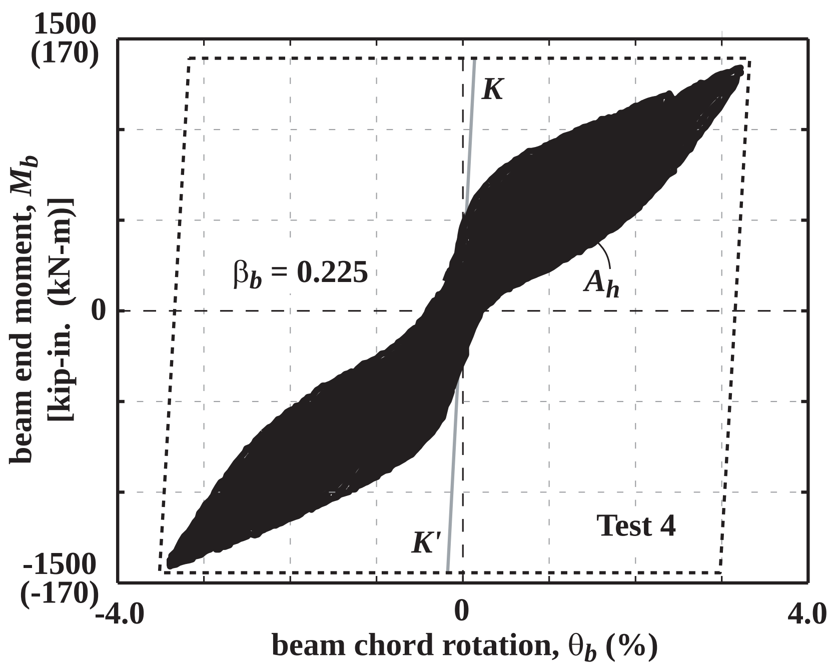

Figure 8.11: Test 4 relative energy dissipation ratio calculations.

TABLE 8.2

RELATIVE ENERGY DISSIPATION RATIO

Test No.	Relative Energy Dissipation Ratio, β_b, for each Rotation Cycle, θ_b										
	0.25%	0.35%	0.50%	0.75%	1.0%	1.5%	2.0%	3.0%	4.0%	5.0%	6.4%	8.0%
1	0.127	0.165	0.274	0.387	0.187	0.166	0.177	0.205	0.205	0.229	0.264	-

Test No.	Relative Energy Dissipation Ratio, β_b, for each Rotation Cycle, θ_b										
	0.25%	0.35%	0.50%	0.75%	1.0%	1.5%	2.25%	3.33%	5.0%	6.4%	8.0%
2	0.212	0.237	0.095	0.097	0.122	0.208	0.176	0.173	0.201	0.187	-
3	0.297	0.117	0.094	0.069	0.083	0.131	0.159	0.203	0.214	-	-
3A	0.334	0.116	0.068	0.105	0.126	0.198	0.199	0.212	-	-	-
3B	0.998	0.274	0.160	0.179	0.170	0.214	0.253	0.285	0.285	0.246	0.191
4	0.179	0.068	0.059	0.076	0.096	0.131	0.174	0.225	-	-	-
4A	0.154	0.033	0.052	0.056	0.041	0.042	0.031	0.045	-	-	-
4B	0.151	0.166	0.139	0.100	0.121	0.150	0.185	0.209	0.216	-	-

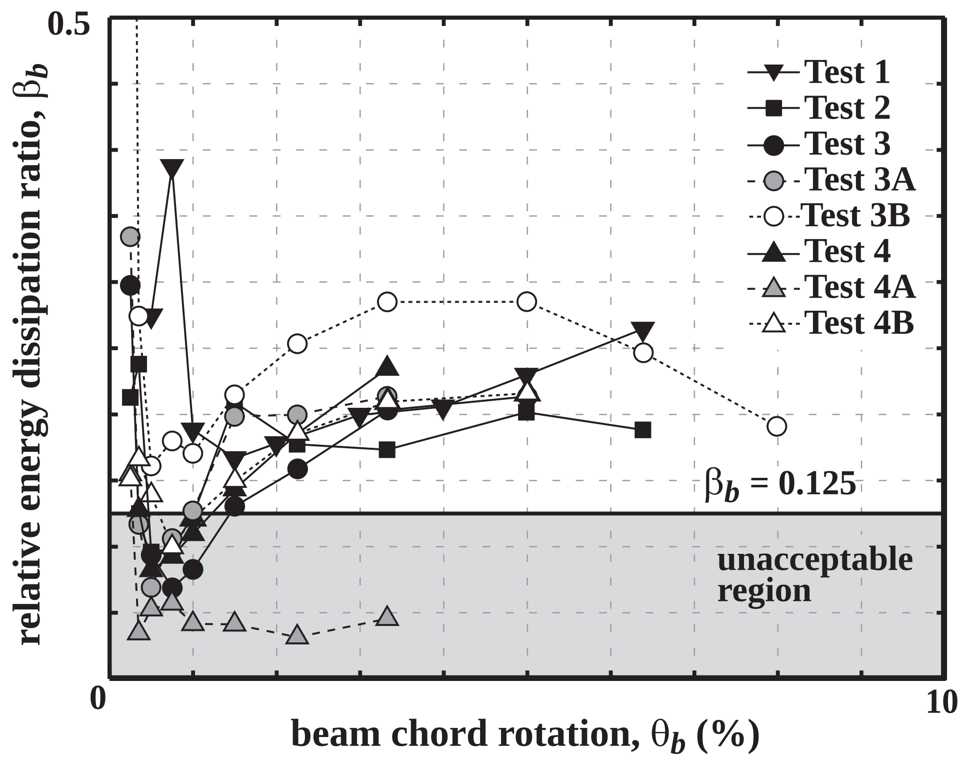

Figure 8.12: Relative energy dissipation ratio versus beam chord rotation.

8.11.3 Stiffness Requirements

According to ACI ITG-5.1, the secant stiffness of the measured lateral load versus displacement hysteresis cycle (e.g., see Figure 8.13 for the θ_b = 3.33% cycle from Test 4) between drift angles of -1/10 and +1/10 of the "limiting drift" should not be less than 0.1 times the initial stiffnesses, *K* and *K'*, defined in Section 8.11.2 above. The limiting drift angle in ACI ITG-5.1 is given as:

$$0.90 \leq 0.8\left[\frac{h_w}{l_w}\right] + 0.50 \leq 3.0 \qquad (8.1)$$

where, h_w and l_w are the wall height and length respectively.

Table 8.3 compares the measured secant stiffnesses of the test specimens with 0.1 times the initial stiffnesses (larger of *K* and *K'* is used for the validation of each test). It can be observed that all specimens satisfy the ACI ITG-5.1 stiffness requirement, thus validating the measured response of the structures. For all tests with the exception of Test 1, the ACI stiffness requirement is satisfied at the ultimate sustained rotation (see Section 8.12) or the largest rotation applied during the test. The stiffness degradation that occurred due to the crushing of the patched concrete in Test 1 resulted in the stiffness requirement to be satisfied at 4.0%, which is smaller than the ultimate sustained rotation from the test but still larger than the upper limit of 3.0% from Equation (8.1).

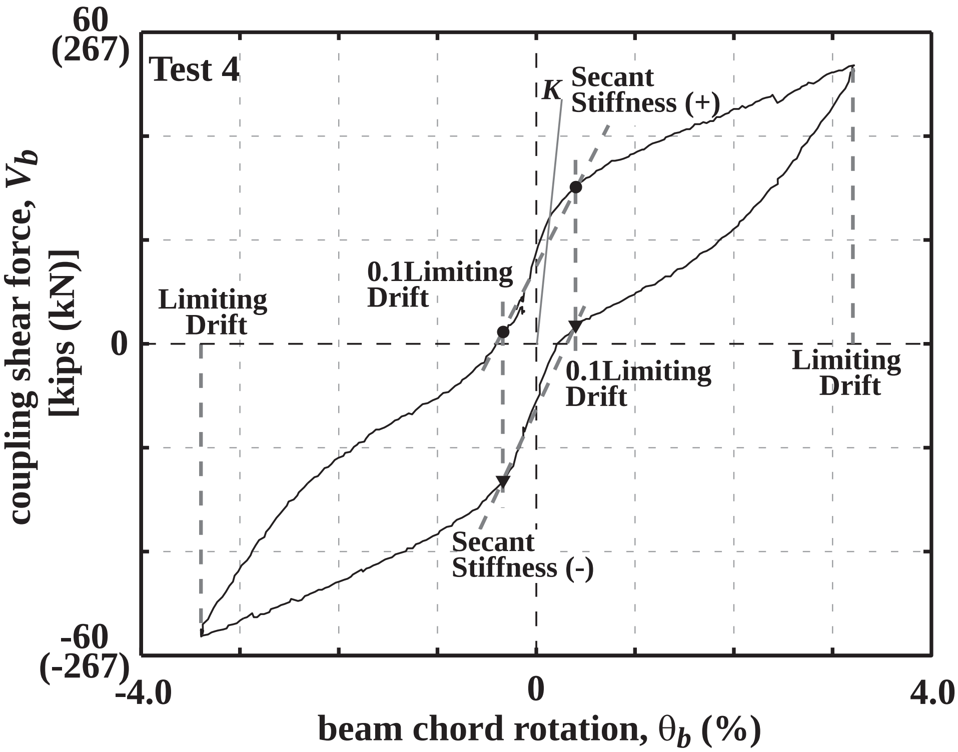

Figure 8.13: Test 4 secant stiffness calculations.

TABLE 8.3

SECANT STIFFNESS

Test No.	Larger of K and K' [kip/θ_b (kN/θ_b)]	θ_b (%)	Secant Stiffness (positive, +) [kip/θ_b (kN/θ_b)]	>	0.1(K or K') [kip/θ_b (kN/θ_b)]	<	Secant Stiffness (negative, -) [kip/θ_b (kN/θ_b)]
1	134 (596)	4.0	17.6 (78.1)	>	13.4 (59.6)	<	15.6 (69.5)
2	80.8 (359)	6.4	10.4 (46.2)	>	8.08 (35.9)	<	8.38 (37.3)
3	89.4 (398)	5.0	17.4 (77.4)	>	8.94 (39.8)	<	19.6 (87.1)
3A[1]	105 (467)	3.33	24.0 (107)	>	10.5 (46.7)	<	25.1 (112)
3B	39.7 (176)	8.0	6.20 (27.5)	>	3.97 (17.6)	<	6.39 (28.4)
4	116 (518)	3.33	38.1 (170)	>	11.6 (51.8)	<	44.0 (196)
4A	41.2 (183)	3.33	28.8 (128)	>	4.12 (18.3)	<	30.9 (137)
4B	49.3 (219)	5.0	19.4 (86.2)	>	4.93 (21.9)	<	13.9 (61.8)

[1]Since no estimate for E_{nt} was available for Test 3A, the initial stiffness was determined visually from the measured V_b-θ_b curve.

8.12 Comparisons with Monolithic Cast-in-Place Concrete Beams

Figure 8.14 compares the ultimate coupling beam “sustained” rotations from this experimental program with the sustained rotations from previous tests of monolithic cast-in-place reinforced concrete coupling beams found in the literature (Barney *et al.* 1978; Bristowe 2000; Canbolat *et al.* 2005; Galano and Vignoli 2000; Tassios *et al.* 1996). Based on ACI ITG-5.1 (ACI 2008), the ultimate sustained rotation is defined as the largest rotation that a beam is able to sustain with no more than 20% drop in lateral resistance during three fully reversed cycles. It is observed that the unbonded post-tensioned precast coupling beams tested as part of this research outperform all of the monolithic beams (including those with diagonal reinforcement) in this database. Note that based on the ACI ITG-5.1 definition, previous coupling beam tests under monotonic loading or cyclic loading with fewer than three repeated cycles at each displacement increment are not included in Figure 8.14, even though the ultimate sustained rotations from many of these tests were also found to be smaller.

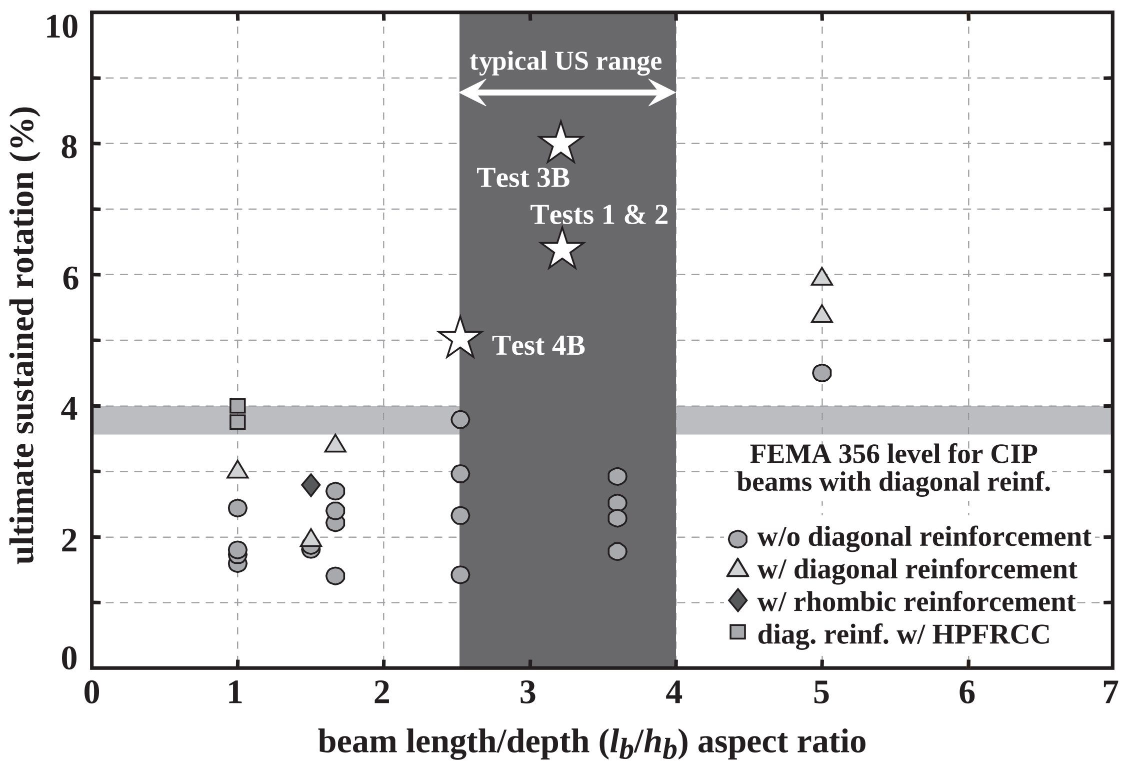

Figure 8.14: Sustained coupling beam rotations.

Furthermore, as compared with conventional monolithic cast-in-place reinforced concrete coupling beams, unbonded post-tensioned precast coupling beams offer the following fundamental similarities and differences:

(1) Before gap opening, the post-tensioning force in the new system creates an initial lateral stiffness that is similar to the uncracked linear-elastic stiffness of a monolithic beam with the same dimensions.

(2) Upon removal of the lateral loads, the post-tensioning tendon in the precast system provides a restoring force that tends to close the gaps and pull the structure back toward its original undisplaced position, reducing the residual deformations and resulting in a self-centered behavior. Thus, the permanent lateral displacements of the new system

after a severe earthquake are expected to be smaller than the permanent displacements of a monolithic system.

(3) Since the post-tensioning force introduces axial compression into the beam, the magnitude of the diagonal compression strut that develops in the new system is significantly greater than the compression strut in a monolithic beam. As a result of this large diagonal compression strut, the amount of shear reinforcement needed in a post-tensioned precast concrete coupling beam is less than the shear reinforcement needed in a monolithic concrete coupling beam.

(4) The only reinforcement crossing the beam-to-wall joints in the new system is the unbonded post-tensioning tendon located at the center of the beam. This leads to simplified details as compared with monolithic systems, which often require heavy reinforcement (e.g., diagonal reinforcement) across the beam ends. In post-tensioned floor slabs, the post-tensioning steel in the coupling beams can be an integral part of the floor post-tensioning steel. If more advantageous for construction, the beams can be cast in place, but with a grout separation joint at each end to result in non-monolithic behavior.

(5) The steel top and seat angles in the new system require adequate connections to the coupling beam and the wall piers, which can be achieved using bolted or welded connections. Bonded mild steel (e.g., Grade 60) reinforcement is needed inside the beam ends to resist the tensile forces transferred to the beam from the angles. The mild steel bars are not continuous across the beam-to-wall joints, and thus, they do not contribute to the coupling between the wall piers.

(6) To resist the large compression stresses due to post-tensioning, significant concrete confinement is needed in the contact regions near the beam-to-wall interfaces of the new system.

(7) Unbonded post-tensioned coupling beams dissipate less energy than monolithic cast-in-place coupling beams. Most of the energy dissipation is provided by the yielding of the top and seat angles at the beam-to-wall joints, which can be inspected and replaced after a significant loading event (unlike the mild steel bars in a monolithic beam).

8.13 Chapter Summary

This chapter provides an overview, summary, and comparisons from the experimental program conducted as part of this dissertation. The effects of various structural design parameters on the lateral load behavior of unbonded post-tensioned precast concrete coupling beams are evaluated. Furthermore, compliance of the measured responses of the test specimens to the acceptance criteria provided by ACI ITG-5.1 (ACI 2008) is demonstrated, validating the use of these structures in seismic regions. The results indicate that unbonded post-tensioned precast beams can be designed to have adequate lateral strength, stiffness, ductility, and energy dissipation under large reversed cyclic loading, and provide an effective and feasible means to couple concrete walls. It is also demonstrated that, as compared to conventional monolithic cast-in-place reinforced concrete coupling systems, unbonded post-tensioned coupling beams are able to sustain (based on ACI ITG-5.1) larger rotations.

CHAPTER 9

ANALYTICAL MODELING OF PRECAST COUPLED WALL SUBASSEMBLIES

This chapter describes the analytical modeling of precast coupled wall subassemblies based on the experiments discussed in Chapters 3 – 8. The chapter is organized into the following sections: (1) analytical modeling assumptions; (2) fiber-element subassembly model; (3) verification of test specimen models; (4) finite-element subassembly model; and (5) comparison of fiber-element and finite-element models.

9.1 Analytical Modeling Assumptions

The following assumptions are made for the subassembly analytical modeling of the precast concrete coupled wall structures in this dissertation:

(1) The objective of this research is to investigate the behavior of isolated coupled wall structures under earthquake induced lateral loads. The interaction between the coupled walls and other structural members (e.g., slabs supported by the coupling beams and the walls) is not within the scope of the analytical model; and thus, is ignored. Note that the floor and roof slabs may affect the expected and desired behavior of a coupled wall structure; however, this is not investigated in this dissertation.

(2) The coupled wall system undergoes in-plane deformations only. Torsion and out-of-plane deformations are not modeled.

(3) Local and/or global instability of the coupling beams and the wall piers are prevented by proper design and detailing.

(4) The transverse reinforcement in the coupling beams and the wall piers is adequately designed and detailed to prevent shear failure.

(5) Shear slip of the coupling beams at the beam-to-wall interfaces is prevented by proper design and detailing.

(6) The behavior of the coupling beams and the wall piers is governed by axial-flexural effects. Nonlinear shear deformations of the structure are small; and thus, are ignored.

(7) The top and seat angles form a ductile failure mechanism.

(8) The angle-to-beam and angle-to-wall connections are properly designed and detailed for the maximum angle forces and deformations.

(9) The longitudinal mild steel reinforcement in the coupling beams is adequately designed and detailed to transfer the angle forces to the beam without yielding or slipping.

(10) The anchorages for the coupling beam post-tensioning tendons are properly designed and detailed for the maximum post-tensioning forces.

9.2 Fiber-Element Subassembly Model

This section describes a fiber-element based analytical model (Figure 9.1) for unbonded post-tensioned precast concrete coupling beam subassemblies as follows: (1)

general modeling of concrete members; (2) modeling of coupling beam; (3) modeling of wall regions; (4) modeling of gap opening; (5) modeling of beam post-tensioning tendons and anchorages; and (6) modeling of top and seat angles. The DRAIN-2DX structural analysis program (Prakash *et al.* 1993) is used as the analytical platform.

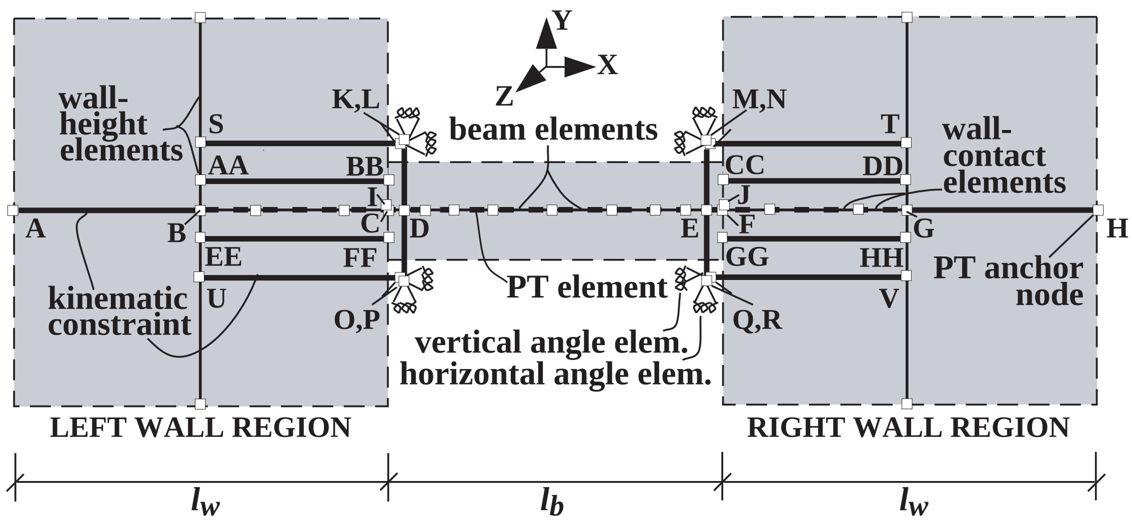

Figure 9.1: DRAIN-2DX fiber-element subassembly model.

9.2.1 General Modeling of Concrete Members

The concrete members of the subassembly (i.e., beam and wall piers) are modeled using the fiber beam-column element in DRAIN-2DX. As shown in Figure 9.2, each fiber element is divided into a number of "segments." The cross-section properties within each segment remain constant, but can vary from one segment to another. Within a segment, parallel fibers in the direction of the element model the cross-section (or "slice") at the mid-length of the segment. Each fiber is characterized by its cross-section area, distance from the longitudinal reference axis of the element, and a uniaxial multi-linear material stress-strain relationship. The force-deformation behavior of the slice is determined by the numerical integration of the stress-strain behaviors of the fibers over the cross-section. The theoretical formulation for the development of the fiber element in DRAIN-2DX is described by Prakash *et al.* (1993); and thus, is not discussed here in further detail.

The discretization of the fiber elements/segments along the length of a concrete member is somewhat flexible, except for the length of the first segment at each beam end and the placement of the nodes that are needed for the model (e.g., top and seat angle connection nodes) as described later. Typically, smaller (i.e., finer) fiber elements/segments and fibers are used where nonlinear behavior is expected to concentrate. For the subassembly model described in this chapter, these regions are located at the beam ends and in the contact regions of the wall piers.

The fiber cross-section properties of the concrete members at the slice locations (i.e., mid-lengths of the fiber segments) are determined from the geometry and material properties of the member cross-sections. The coupling beam and the wall contact regions are modeled without any steel fibers (i.e., only concrete fibers are used in these elements) since: (1) the post-tensioning tendons are unbonded from the concrete, and thus, are modeled separately using truss elements as described later; and (2) the bonded longitudinal mild steel reinforcement in the beam is not continuous through the beam-to-wall interfaces, and thus, does not directly contribute to the lateral resistance of the structure. The mild steel confinement reinforcement hoops in the beam and the wall piers are represented implicitly as part of the confined concrete compressive stress-strain model. Once the different material properties within a cross-section are identified, the corresponding slice is discretized into a number of concrete fibers as shown in Figure 9.2. The concrete area lost due to the post-tensioning ducts (which are not grouted) can be accounted for by reducing the areas of the fibers at the same distance from the reference axis as the ducts; however, this can typically be ignored if the ducts are small or if they are located in regions where nonlinear behavior of the concrete is not expected (e.g., near the mid-depth of the beam).

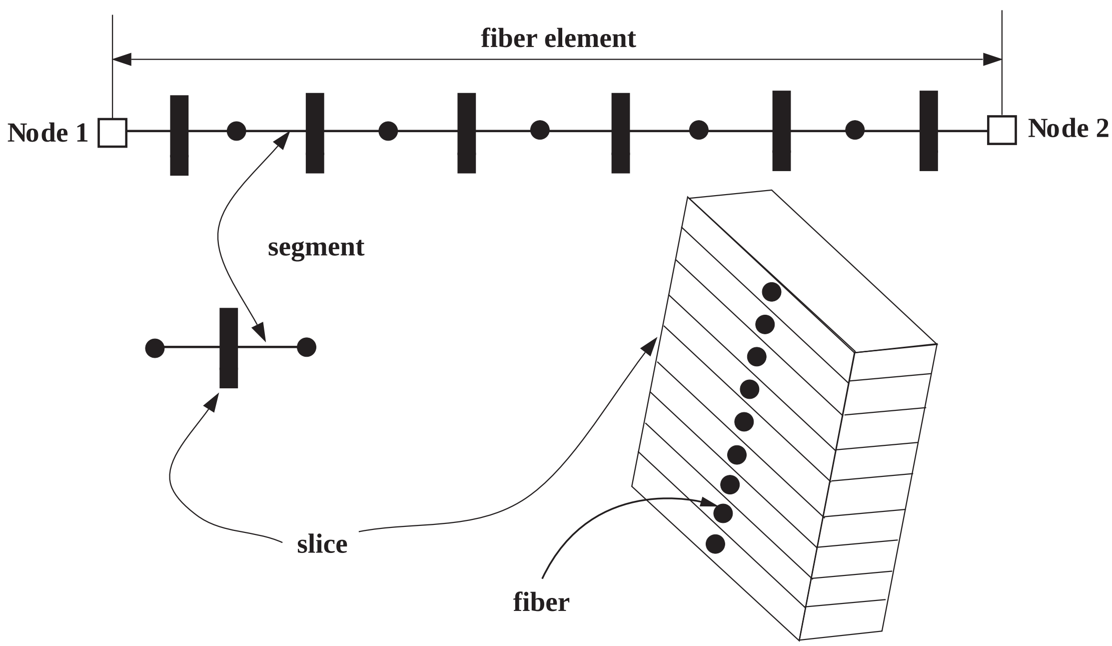

Figure 9.2: Fiber element, segments, and fibers.

Four different types of concrete are used in the modeling of the concrete members in a coupling beam subassembly: (1) compression-only (i.e., zero-tension) unconfined concrete (denoted as C1); (2) compression-only confined concrete (denoted as C2); (3) linear-elastic tension unconfined concrete (denoted as C3); and (4) linear-elastic tension confined concrete (denoted as C4). Each concrete type has an idealized multi-linear uniaxial stress-strain relationship determined from a smooth stress-strain relationship based on Mander *et al.* (1988a). The confined concrete compressive stress-strain parameters (shown in Figure 9.3), which include the maximum strength, f'_{cc}, strain at maximum strength, ε'_{cc}, and ultimate strain, ε_{ccu}, depend on the properties of the confining reinforcement hoops, the longitudinal mild steel reinforcement placed within the hoops, and the unconfined concrete properties. The diameter of the hoop bars, φ_h, the geometry of the hoops (i.e., width, b_h, and depth, d_h), the hoop spacing, s_h, the yield strength of the hoop steel, f_{hy}, the strain, ε_{hm}, at the maximum strength of the hoop steel, and the maximum compressive strength of the unconfined concrete, f'_c (assumed to be reached at a strain of ε'_c = 0.002), are specified to determine the confined concrete model. According to Mander *et al*. (1988a), the ultimate confined concrete strain, ε_{ccu}, is reached when the fracture of the confining hoops occurs, resulting in a loss of confinement and crushing of the confined concrete.

In general, the smooth concrete stress-strain relationships are idealized into multi-linear relationships in a manner that satisfies the following: (1) the slope of the first segment of the idealized stress-strain relationship should be equal to the linear-elastic stiffness of concrete, E_c; (2) the maximum compressive strength of the idealized stress-strain relationship should be the same as the strength, f'_{cc} of the smooth relationship and reached at the same strain, ε'_{cc}; and (3) the ultimate (i.e., crushing) strain of the idealized stress-strain relationship should be the same as the ultimate strain, ε_{ccu} of the smooth relationship.

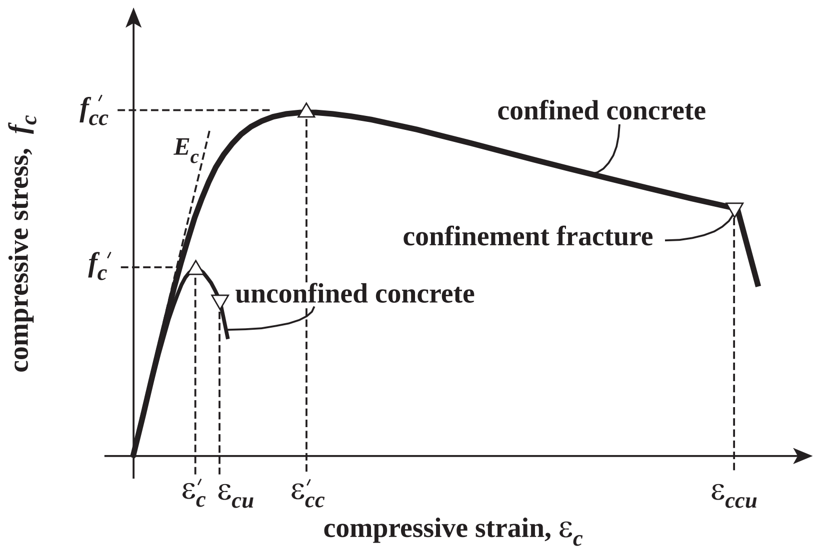

Figure 9.3: Compressive stress-strain relationships of unconfined and confined concrete (Mander *et al.* 1988a).

9.2.2 Modeling of Coupling Beam

As shown in Figure 9.1, fiber beam-column elements are used to model the axial-flexural and shear behavior of the coupling beam. Due to the development of a large diagonal compression strut along the beam span, the diagonal tension stresses in the beam remain small. Thus, the shear deformations in the analytical model are limited to linear-elastic shear deformations only. It is also assumed that the beam-to-wall connections are designed to prevent shear slip at the beam ends. Second order effects (often referred to as P-Δ effects) in the coupling beam (due to the rotation of the beam with respect to the left and right wall piers) are included in the fiber elements.

Figure 9.4 depicts the fiber discretization of the coupling beam cross-sections at the ends. As described previously, the beam cross-section is modeled using unconfined and confined concrete fibers only, without any fibers representing the bonded longitudinal mild steel reinforcement in the beam. This approach is valid because the mild steel reinforcement inside the beam does not cross the beam-to-wall interfaces, and thus, does not directly contribute to the lateral resistance of the structure. Away from the beam ends, concrete with linear-elastic stress-strain behavior in tension is used assuming that the amount of bonded mild steel reinforcement in the beam is such that significant tensile deformations only occur through the opening of gaps at the beam-to-wall interfaces (e.g., it is assumed that steel reinforcement is provided to resist the tensile forces transferred to the beam from the angles and that this reinforcement remains linear elastic under the maximum angle forces). To model the gap opening behavior, the concrete at the beam ends is assumed to have no strength in tension (see Shen *et al.* 2006) as described in more detail later.

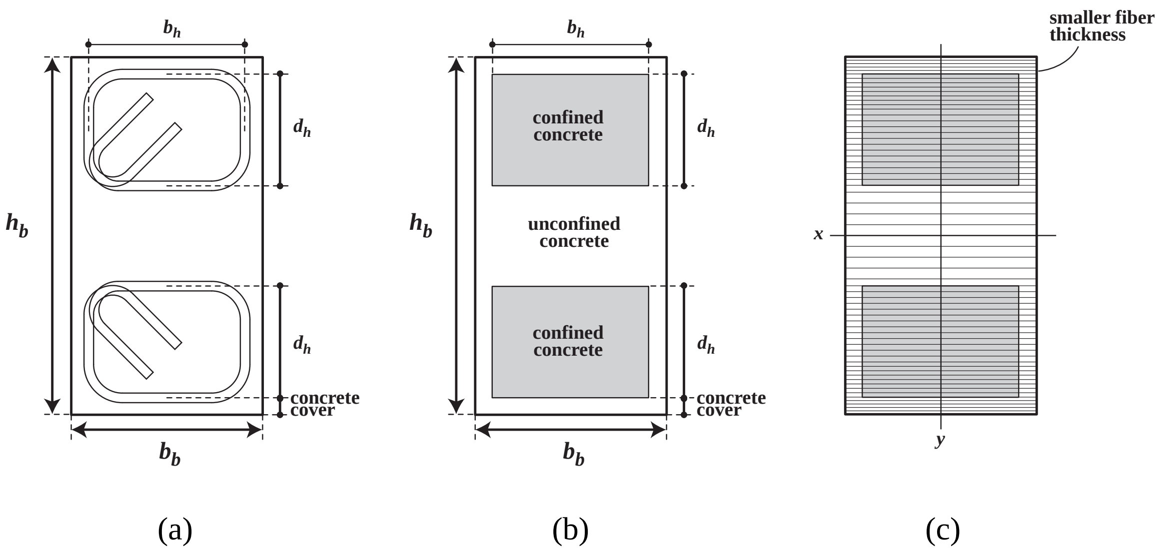

Figure 9.4: Modeling of beam cross-sections near the ends –
(a) cross-section; (b) concrete types; (c) fiber discretization

Figure 9.5 and Table 9.1 show the fiber discretizations used in the modeling of the coupling beams from the experimental program described in Chapters 6 – 8. Note that although the number of fibers along the beam span could have been reduced away from the beam ends, it was kept constant. Typically, smaller (i.e., finer) fiber elements/segments/fibers are needed near the ends of the coupling beam where the nonlinear behavior is expected to concentrate as compared with the midspan region. The angle-to-beam connection ducts are ignored; however, the central post-tensioning tendon duct area is subtracted from the area of the fibers at that location.

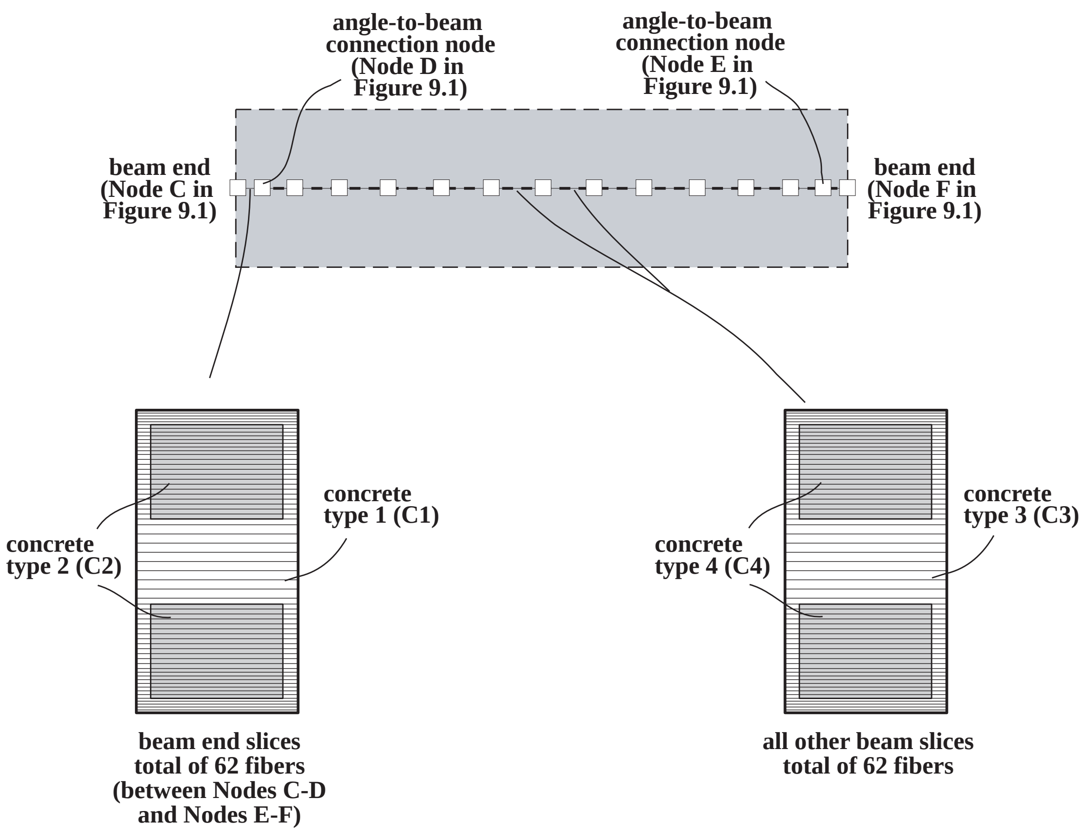

Figure 9.5: Modeling of beam specimens.

TABLE 9.1

TYPICAL FIBER DISCRETIZATION ALONG

BEAM LENGTH

	Total Number of Fibers	Concrete Types	Fiber Thickness[1] [in. (mm)]	
			No.	Thickness
beam ends (between Nodes C-D and Nodes E-F)	62	C1 – compression-only unconfined concrete	1	0.1625 (4.1)
			6	0.25 (6.4)
			1	0.3375 (8.6)
			4	0.50 (12.7)
			3	1.0 (25.4)
		C2 – compression-only confined concrete	5	0.1 (2.5)
			5	0.2 (5.1)
			1	0.375 (9.6)
			2	0.45 (11.4)
			1	0.50 (12.7)
			2	0.55 (14.0)
away from beam ends	62	C3 – linear-elastic tension unconfined concrete	1	0.1625 (4.1)
			6	0.25 (6.4)
			1	0.3375 (8.6)
			4	0.50 (12.7)
			3	1.0 (25.4)
		C4 – linear-elastic tension confined concrete	5	0.1 (2.5)
			5	0.2 (5.1)
			1	0.375 (9.6)
			2	0.45 (11.4)
			1	0.50 (12.7)
			2	0.55 (14.0)

[1]Fiber thicknesses are given from edge of cross-section to centerline, about which they are mirrored.

Each fiber element along the length of a coupling beam was modeled using a single fiber segment (i.e., single slice). The length of the first fiber segment (which was equal to the element length in the models constructed in this dissertation) at each beam end is important in modeling the nonlinear compression deformations that occur adjacent to the beam-to-wall interfaces. The effect of the length of this segment, l_{cr} (see Figure 9.6(a) was investigated by using several trial lengths and observing their effect on the behavior of the subassembly model. For example, Figure 9.6(b) shows the influence of l_{cr} on the coupling shear force versus beam chord rotation behavior of Beam 2 from the experimental program (excluding the top and seat angles). It can be seen that the effect of l_{cr} is greatest during the large non-linear rotations of the beam. In the modeling of the test specimens, l_{cr} was taken as 5.25 in. (133 mm), which is equal to the length from the beam end to the centroid of the angle-to-beam connections. The middle portion of the beam was modeled with significantly longer (i.e., coarser) fiber elements. Note that it is recommended to place a node at the beam midspan so that this location, where the bending moment is zero, does not correspond to a fiber slice.

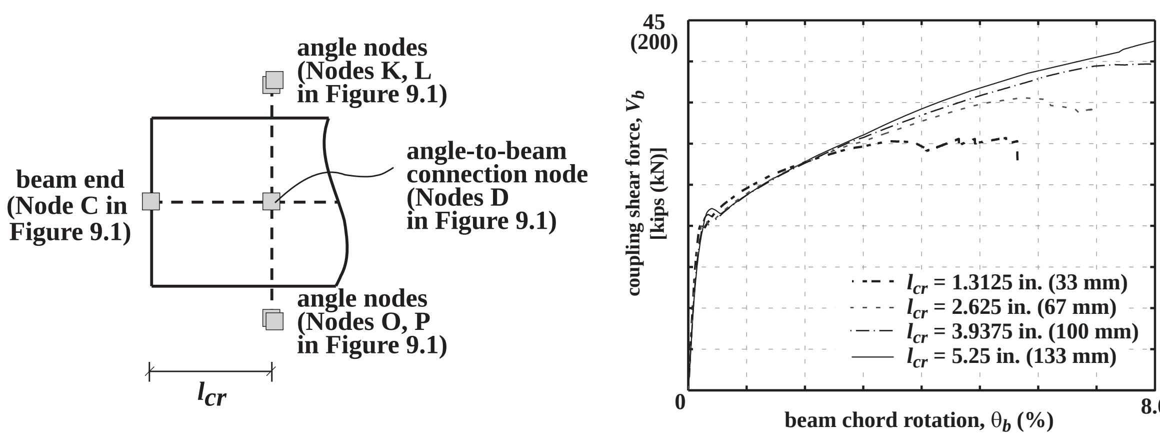

(a) (b)

Figure 9.6: Length of first beam fiber segment, l_{cr} –
(a) model schematic; (b) influence on V_b-θ_b behavior.

Figure 9.7 shows the compressive stress-strain relationships used to model the unconfined and confined concrete in the virgin beam specimens. Since concrete was assumed to be linear-elastic in tension away from the beam ends, the redistribution of beam stresses due to concrete cracking cannot be modeled. However, as validated through the experimental program, the cracks in the midspan regions of a properly-designed beam remain small, and thus, are not expected to significantly affect the behavior. The use of linear-elastic tension concrete is possible due to the unique behavioral characteristics (i.e., gap opening at the ends and development of a large diagonal compression strut along the length) of unbonded post-tensioned precast concrete coupling beams and results in a relatively simple analytical model as compared with conventional monolithic concrete coupling systems, which are often dominated by interactions between the mild steel reinforcement and the concrete.

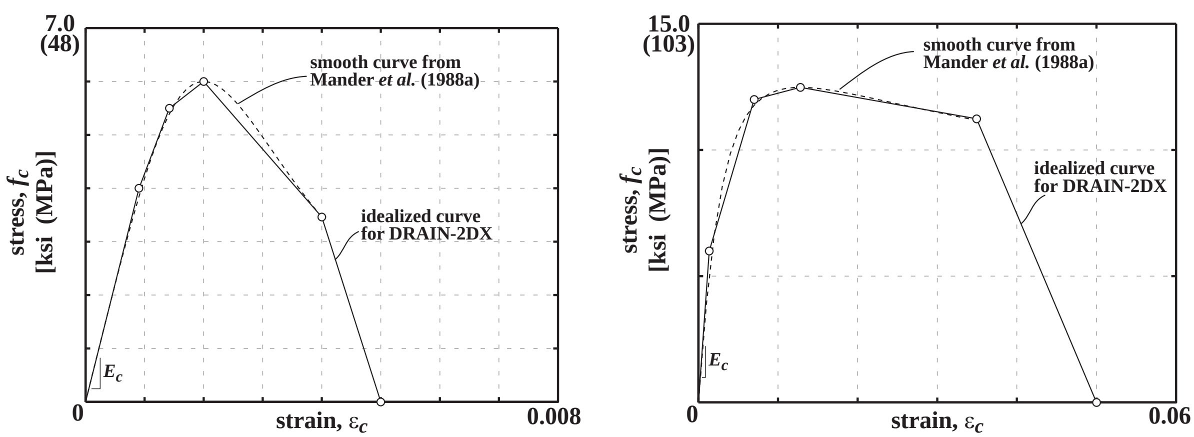

(a) (b)

Figure 9.7: Concrete compressive stress-strain relationships for virgin beam specimens – (a) unconfined concrete; (b) confined concrete.

9.2.3 Modeling of Wall Regions

As shown in Figure 9.1, each wall region in a coupling beam subassembly is modeled using two sets of fiber beam-column elements. The first set consists of elements that are in the vertical direction to model the axial-flexural and shear behavior of the wall region along its height. These elements, referred to as the "wall-height" elements, are used to model the cross-section of each wall pier in the horizontal X-Z plane.

The second set of fiber elements models the local deformations of the concrete in the wall contact regions under the large compressive stresses that develop upon gap opening. These elements, referred to as the "wall-contact" elements, are placed in the horizontal direction to the left and right of the coupling beam. The fiber cross-section properties of the wall-contact elements were determined from "effective" wall cross-sections in the vertical Y-Z plane by comparing the results from the DRAIN-2DX model with a finite-element model described later. The thickness of the effective wall cross-section is equal to the wall thickness, t_w. The depth of the effective wall section is equal to the beam depth, h_b at the beam-to-wall interface and is assumed to increase away from the interface with a slope of 1:3. The compressive stresses in each wall pier decrease away from the interface due to an increase in the depth of the compression region inside the wall. The increase in the depth of the effective wall cross-section represents this increase in the depth of the compression region away from the interface.

Three wall-contact elements (with one fiber segment each) are used between the center of the left wall region (Node B) and the beam-to-wall interface (Node C) as shown in Figure 9.1. The Y-translational degree-of-freedom of Node C is kinematically constrained to Node B. The rotational and X-translational degrees-of-freedom of Node C are not constrained. The length of the first wall-contact element adjacent to Node C is equal to $0.5h_b$ and the length of the second element is equal to h_b. The total length of the wall-contact elements between Nodes B and C is equal to one half of the wall length, l_w. The modeling of the right wall region is similar to the left wall region.

Figure 9.8 and Table 9.2 show the fiber discretizations used in the three wall-contact elements in each wall pier of the subassembly test specimens. A smaller (i.e., finer) fiber distribution is used in the wall-contact elements near the beam ends (i.e., contact regions) where the nonlinear behavior is expected to concentrate. Note that the angle-to-wall connection ducts are ignored; however, the central post-tensioning tendon duct area is subtracted from the area of the fibers at that location. Linear-elastic tension confined concrete (C4) properties are used for all of the fibers, both in the confined concrete regions and the unconfined concrete regions of the wall contact regions. This approach is valid since: (1) the unconfined concrete regions of the wall piers are expected remain mostly in the linear elastic range in compression; and (2) the tensile stresses in the wall contact regions remain small as a result of gap opening at the beam ends.

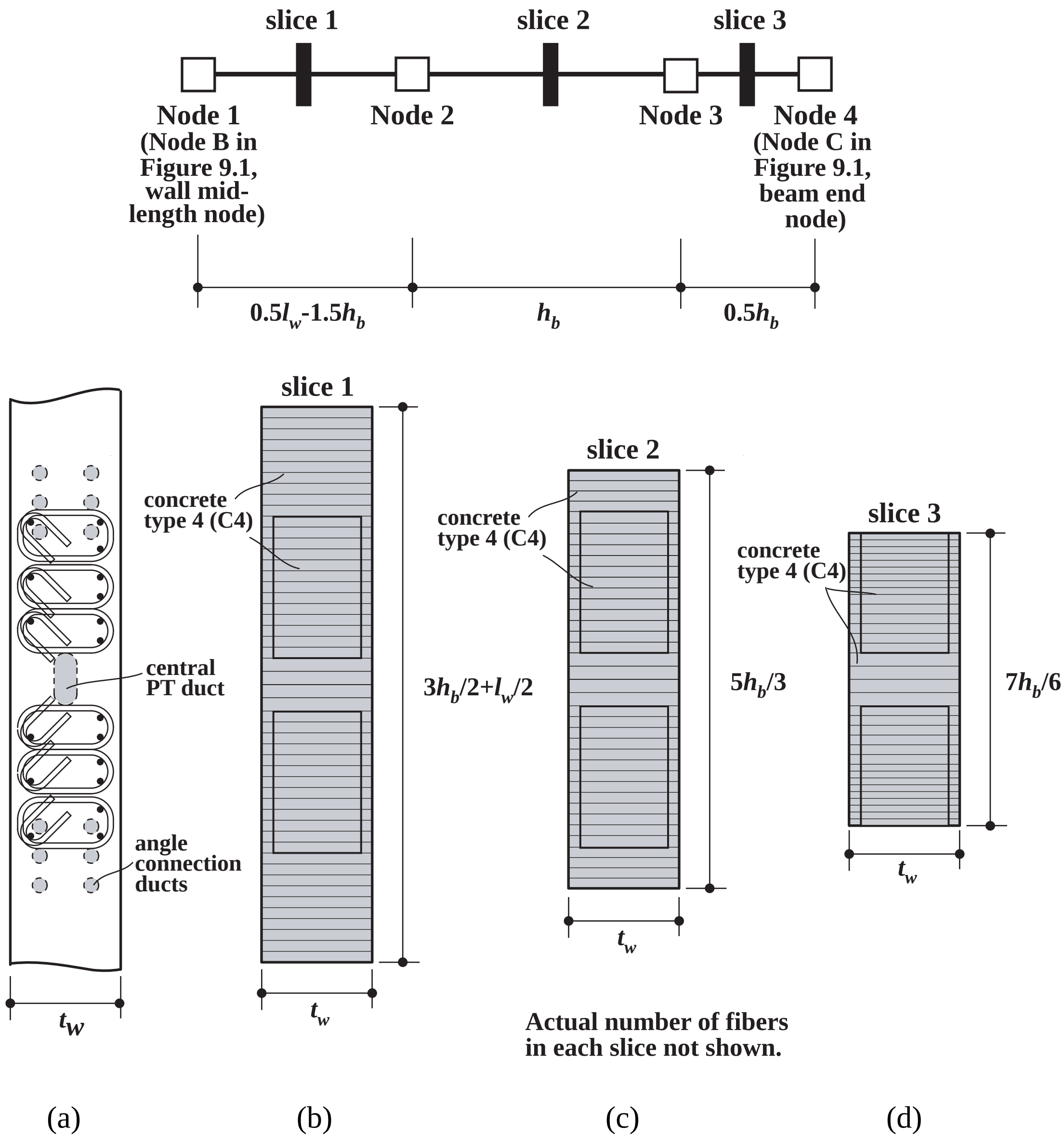

Figure 9.8: Modeling of wall contact regions –
(a) wall cross-section in vertical plane; (b) slice 1; (c) slice 2; (d) slice 3.

TABLE 9.2

TYPICAL FIBER DISCRETIZATION OF

WALL CONTACT REGIONS

	Total Number of Fibers	Concrete Type	Fiber Thickness [in. (mm)]	
			No.	thickness
slice 1	26	C4 – linear-elastic tension confined concrete	1 9 6 9 1	0.25 (6.4) 1.0 (25.4) 2.0 (50.8) 1.0 (25.4) 0.25 (6.4)
slice 2	26	C4 – linear-elastic tension confined concrete	1 2 20 2 1	0.40 (10.2) 0.50 (12.7) 1.0 (25.4) 0.50 (12.7) 0.40 (10.2)
slice 3 (in contact with beam)	48	C4 – linear-elastic tension confined concrete	7 8 18 8 7	0.20 (5.1) 0.25 (6.4) 0.50 (12.7) 0.25 (6.4) 0.20 (5.1)

9.2.4 Modeling of Gap Opening

Gap opening and closing at the beam-to-wall interfaces is one of the most important characteristics governing the behavior of unbonded post-tensioned precast concrete coupling beams. As a result of the opening of gaps and due to the post-tensioning force, large compressive stresses develop near the regions of the beam in contact with the wall piers, while the tensile stresses in a significant portion of the beam (and the wall contact regions) remain close to zero. The compressive behavior of the beam and the wall contact regions is modeled using the uniaxial compressive stress-strain relationships of the concrete fibers in the fiber beam-column elements (e.g., see Figure 9.7). To model the gap opening behavior, the tensile strength and stiffness of the concrete fibers in the first element spanning from the beam end (Node C in Figure 9.1) to the angle-to-beam connection node (Node D) are set to zero. Away from these end regions, the concrete fibers in the beam are assumed to be linear-elastic in tension (i.e., Types C3 and C4) as described previously. The cyclic stress-strain behavior of the compression-only concrete (i.e., Types C1 and C2) fibers at the beam ends is shown in Figure 9.9. The hysteresis rules that govern the concrete fiber cyclic behavior can be found in Kurama *et al.* (1996) and are not discussed herein.

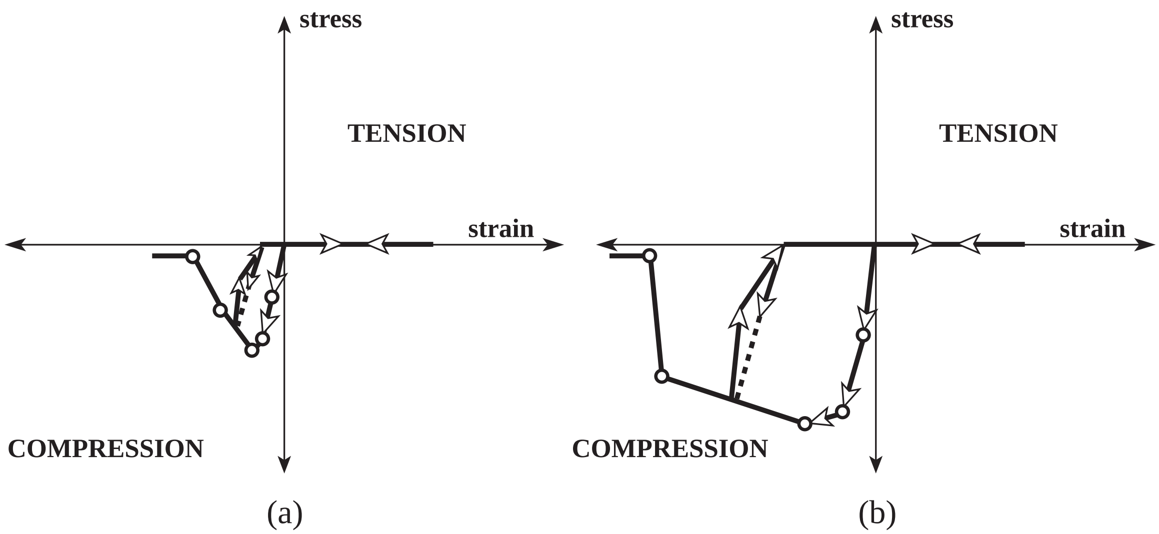

Figure 9.9: Compression-only concrete fiber (i.e., Types C1 and C2) stress-strain behavior – (a) unconfined concrete; (b) confined concrete.

Through this model, the gap opening displacements that occur at the beam-to-wall interfaces are represented as distributed tensile deformations in the adjacent concrete fibers as illustrated in Figure 9.10. The reduction in the lateral stiffness of a coupling beam subassembly as a result of gap opening is modeled by the zero stiffness of the concrete fibers that go into tension when the pre-compression stresses due to the post-tensioning force are overcome by the flexural stresses that develop at the tension corners of the beam due to the lateral loads.

The process of gap opening/closing under the action of lateral loading/unloading causes softening/re-stiffening at the beam-to-wall interface regions. This process is captured in the fiber beam elements by having an increasing number of fibers subjected to tension during loading, and then by having the fibers subjected to tension going back into compression during unloading. As described previously, compression-only concrete fibers are also used in the wall contact regions since, due to gap opening, the tensile stresses in these regions remain small as well.

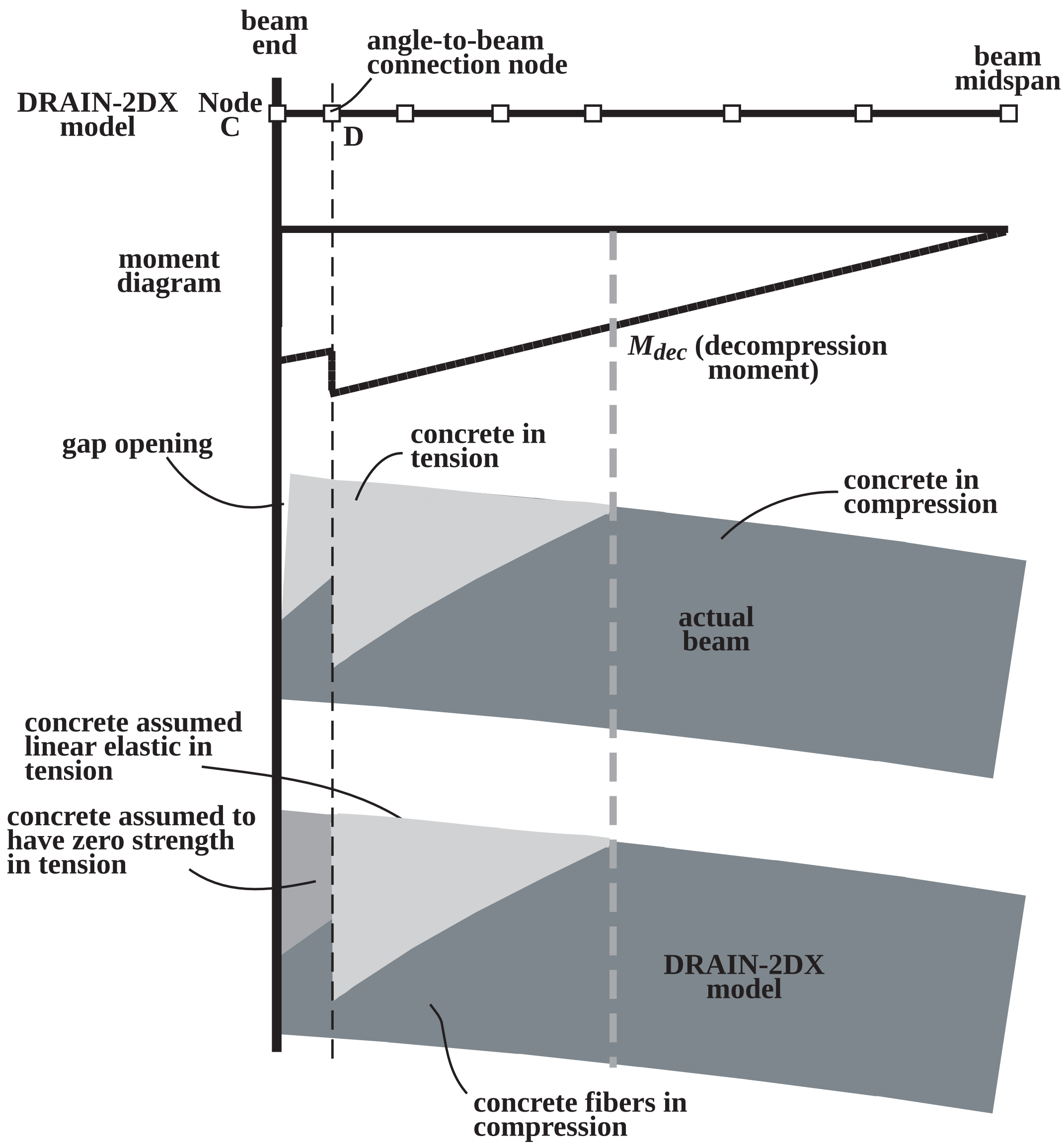

Figure 9.10: Modeling of gap opening.

9.2.5 Modeling of Beam Post-Tensioning Tendons and Anchorages

Three truss elements connected at the beam-to-wall interfaces (between Nodes A-I-J-H in Figure 9.1) model the beam post-tensioning tendon. The post-tensioning of the structure is simulated by initial tensile forces in the truss elements, which are equilibrated by compressive forces in the fiber elements modeling the wall contact regions and the beam. Note that the compression forces that develop in the beam and the wall contact elements result in an elastic shortening and subsequent loss in the forces of the truss elements modeling the post-tensioning tendon. Thus, slightly larger tensile forces are applied to the truss elements such that the desired amount of initial force (i.e., desired force just before the application of lateral loads) is achieved after elastic shortening takes place.

The beam post-tensioning tendon is modeled using three truss elements between Nodes A, I, J, and H at the post-tensioning anchor locations and the beam-to-wall interfaces. The anchor Nodes A and H are kinematically constrained to Nodes B and G (at the center of each wall pier), respectively, assuming that the anchors are properly designed for the maximum post-tensioning forces. Nodes I and J at the beam-to-wall interfaces are free to move in the horizontal direction (since the post-tensioning tendon is unbonded), with gap/contact elements to account for the transverse movement of the tendon inside the oversized ducts used in the test specimens.

Each post-tensioning gap/contact element is placed between a beam post-tensioning node (e.g., Node I at the left end of the beam) and a second node (e.g., Node BB above Node I) that is kinematically constrained to a corresponding wall pier element node at the same elevation (e.g., Node AA). The exact elevation of Node BB is not significant; it can be placed a few inches about Node I. Before the application of lateral loads, the tendon is not in contact with the inside of the ducts (i.e., there is space around the tendon since the oversized ducts are not grouted; this space is referred to as the initial "slack/gap"). As the subassembly is displaced (Figure 9.11), the tendon comes into contact with the inside of the ducts at the beam-to-wall interfaces and the transverse displacements of the tendon at these locations are constrained. The gap/contact elements model this behavior by applying a large transverse force on the tendon nodes at the beam-to-wall interfaces once the tendon comes into contact with the ducts. This is necessary to correctly simulate the displaced shape of the tendon, and thus, to capture the second order forces that develop in the tendon as the beam rotates with respect to the wall piers. Note that the gap/contact elements would not be necessary if the post-tensioning ducts are not oversized and no relative transverse movement of the tendon can occur inside the concrete, which can be modeled directly by kinematically constraining Nodes I and J to Nodes B and G, respectively, in the vertical direction.

The initial slack/gap values used in the modeling of the test specimens were (determined based on the duct inside dimensions as well as the number and size of the post-tensioning strands): 0.8 in. (15 mm) on each side of tendon for Tests 3, 3B, 4 and 4A, and 0.5 in. (7.6 mm) for Tests 2 and 4B. Note that these slack/gap values are slightly larger than the calculated values to account for the "grouping" of the post-tensioning strands (see Figure 9.11).

The stress-strain relationship of the truss elements is a bi-linear idealization of the stress-strain relationship of the beam post-tensioning steel as shown in Figure 9.12. The yield strength is assumed to be equal to the measured yield strength (i.e., the limit of proportionality, see Chapter 4) of f_{bpy} = 166 ksi (1146 MPa). The post-yield stiffness is determined from the nonlinear portion of the steel stress-strain relationship between the yield strain and the largest strain expected in the tendon. Because the post-tensioning tendon is left unbonded, these strains are expected to remain small.

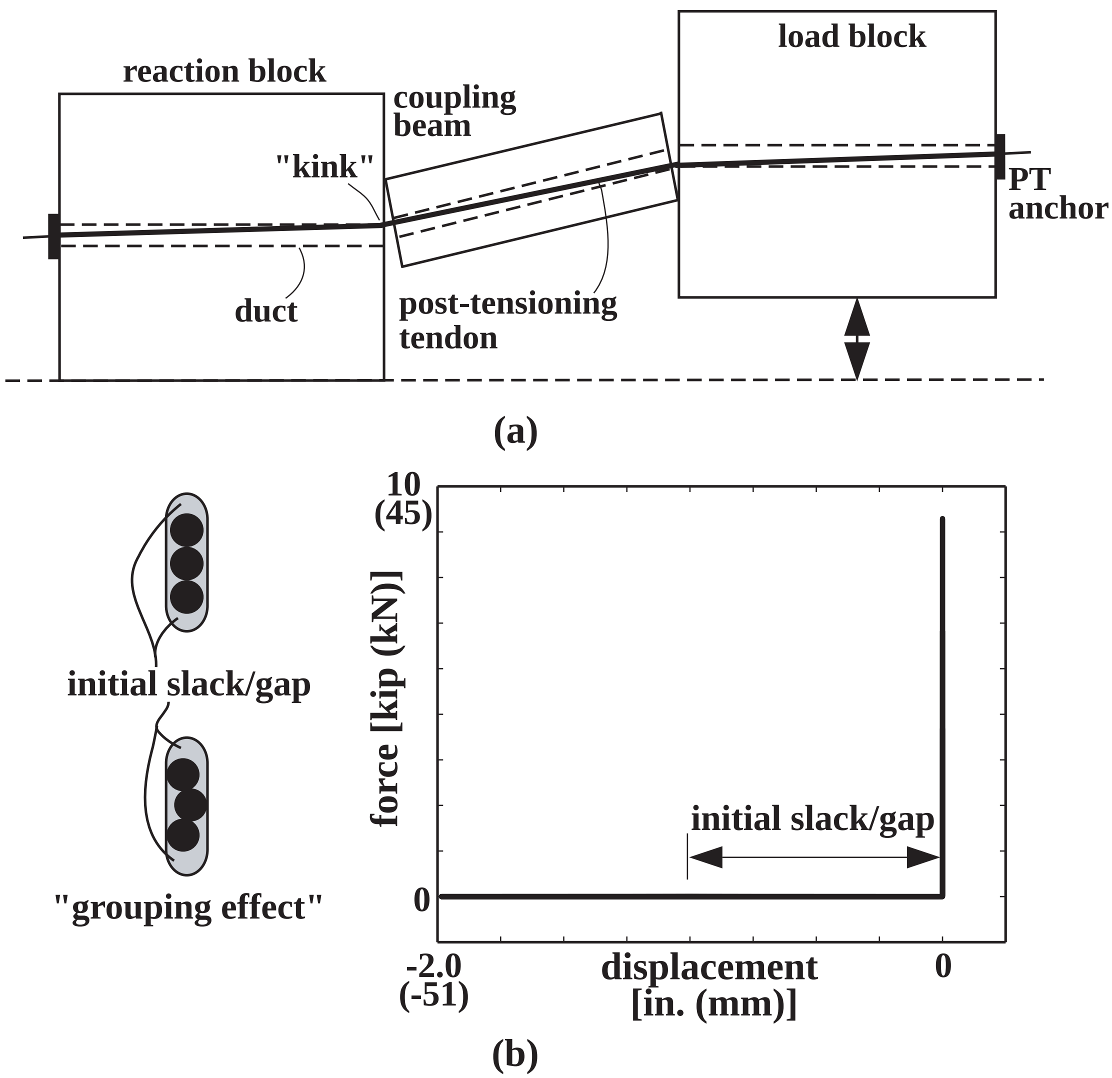

Figure 9.11: Gap/contact “post-tensioning kink” elements – (a) idealized exaggerated displaced shape of tendon inside ducts; (b) gap/contact kink element.

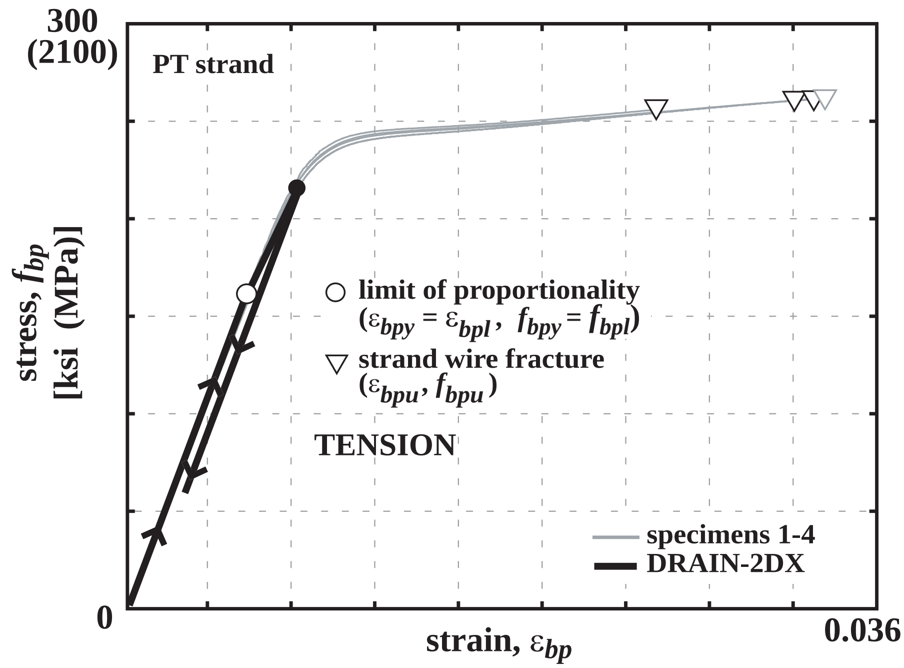

Figure 9.12: Post-tensioning tendon stress-strain behavior.

9.2.6 Modeling of Top and Seat Angles

As shown in Figure 9.1, each top and seat angle at the ends of the coupling beam is represented using two zero-length translational spring elements. The first spring element, referred to as the "horizontal angle element," models the axial (i.e., *x*-direction) force in the horizontal leg of the angle using a tri-linear force versus deformation relationship in tension and a bi-linear relationship in compression [see Figure 9.13(a)]. The second spring element, referred to as the "vertical angle element," models the shear (i.e., *y*-direction) force in the horizontal leg of the angle using a bi-linear force-deformation model shown in Figure 9.13(b). Since the shear force in the angle horizontal leg is significantly smaller than the axial force in the horizontal leg, the contribution of the vertical angle element to the overall behavior of the structure is small, and can be ignored.

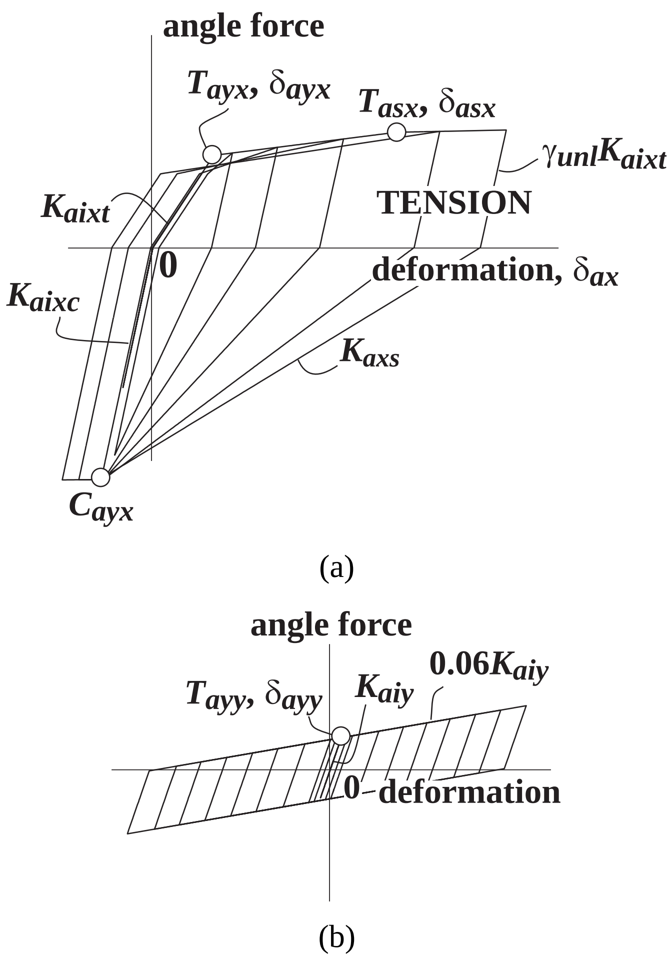

Figure 9.13: Assumed force versus deformation behaviors of the angle elements (adapted from Shen *et al.* 2006) – (a) horizontal angle element; (b) vertical angle element.

Both angle elements are connected to the same pair of nodes (e.g., Nodes K and L for the top left angle) with identical coordinates at the centroid of the bolt group connecting the angle horizontal leg to the beam and at the same elevation as the middle of the horizontal leg thickness. It is assumed that the angle-to-wall and angle-to-beam connections are properly designed for the maximum angle forces (including the forces that develop in the angle-to-wall connectors due to the prying action of the angle vertical leg). Based on this assumption, one of the angle nodes is kinematically constrained to a wall-height element node at the same elevation (e.g., Node S) and the other angle node is kinematically constrained to a corresponding beam node (e.g., Node D).

The behavior of an angle as it is loaded by the beam is governed by many factors including the angle leg thickness, and number, size, layout, and gage length of the angle connectors. Figure 9.14 shows the assumed idealized deformed shape of a seat angle as it is pulled and rotated by the coupling beam. It is assumed that the failure of the angle occurs through the formation of two plastic hinges in the vertical leg. As described in Sims (2000), other angle failure modes (e.g., an additional plastic hinge in the horizontal leg) are possible. The formation and fracture of a plastic hinge adjacent to the fillet in the horizontal legs of the top and seat angles was observed in Tests 1, 3, and 3B conducted as part of this dissertation. Full scale subassembly experiments are needed to investigate the behavior of the angles more thoroughly.

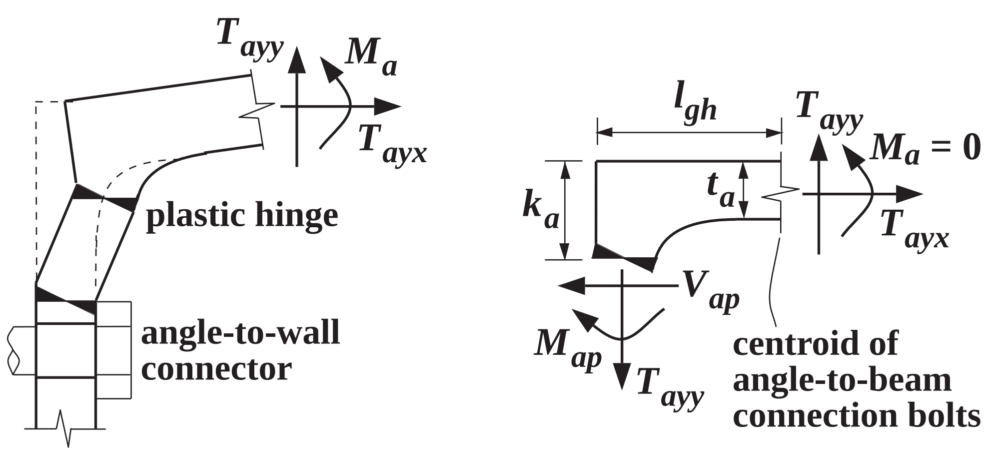

Figure 9.14: Modeling of top and seat angles (from Shen *et al.* 2006).

From the free body diagram of the angle between the plastic hinge adjacent to the fillet on the vertical leg and the centroid of the angle-to-beam connection bolts, it can be shown that:

$$T_{ayx} = V_{ap} \tag{9.1}$$

$$T_{ayy} = \frac{M_{ap} + V_{ap}\left(k_a - \frac{t_a}{2}\right)}{l_{gh} - \frac{t_a}{2}} \tag{9.2}$$

where, T_{ayx} = axial force in the angle horizontal leg; T_{ayy} = shear force in the horizontal leg; M_{ap} = plastic hinge moment and V_{ap} = plastic shear force in the vertical leg including shear-flexure interaction; k_a = distance from heel to toe of fillet of the angle; l_{gh} = gage length of the angle-to-beam connectors (measured from heel of the angle to the centroid of the angle-to-beam connection bolts); and t_a = angle leg thickness. The angle moment, M_a at the centroid of the angle-to-beam connection bolts is small and is ignored.

9.2.6.1 Horizontal Angle Element Force-Deformation Model

The assumed cyclic force-deformation relationship of the horizontal angle element is shown in Figure 9.13(a), where the hysteretic characteristics were determined based on the subassembly experiments described in Chapters 6, 7, and 8. A zero-length spring element developed in DRAIN-2DX by Shen *et al.* (2006) was adapted and modified to model this behavior. Under tensile loading, the yield strength $T_{ayx} = V_{ap}$ and initial stiffness K_{aixt} were determined using a method developed by Kishi and Chen (1990) and Lorenz *et al.* (1993). In this model, the vertical leg is assumed to be fixed along the innermost edge of the line of angle-to-wall connectors and is pulled horizontally by the beam (see Chapter 2). The rotation of the horizontal leg of the angle with respect to the vertical leg, which occurs as a result of the rotation of the beam with respect to the walls as shown in Figure 9.14, is ignored. The yield strength, T_{ayx} is reached when the two plastic hinges in Figure 9.14 develop, considering the interaction between the bending moment and shear force in the vertical leg.

Based on the subassembly experiments, it is assumed that the maximum strength of the horizontal angle element in tension, T_{asx} is equal to 1.25 times the yield strength, T_{ayx}, and is reached at an angle deformation, δ_{asx} of 4 times the yield deformation, $\delta_{ayx} = T_{ayx}/K_{aixt}$. Note that these values are different from the model in Shen *et al.* (2006), which uses $2.0T_{ayx}$ and $5\delta_{ayx}$, respectively.

Under compression, the initial stiffness of an angle as it is pushed back horizontally toward the wall by the coupling beam is assumed to be equal to:

$$K_{aixc} = \frac{1}{40}\frac{E_a A_a}{l_{gh}} \geq K_{aixt} \tag{9.3}$$

where, E_a = Young's modulus for the angle steel; and A_a = gross cross-section area of the angle horizontal leg.

The angle unloading stiffness from a tensile force is assumed to be a factor, γ_{unl} of the initial angle stiffness in tension, K_{aixt}. Based on the experimental results described in Chapters 6 – 8, the unloading stiffness factor, γ_{unl} was found to be 3. Note that in Shen *et al.* (2006), the unloading stiffness is assumed to be equal to the initial stiffness (i.e., γ_{unl} = 1) for the modeling of steel unbonded post-tensioned coupling beams. Thus, more research is needed on the behavior and modeling of top and seat angles in unbonded post-tensioned coupling beam connections.

Upon crossing the zero-force axis, the angle force-deformation behavior shoots towards the angle yield strength in compression, C_{ayx} which is assumed to be equal to 0.75 times the initial slip critical force, C_{asi} of the angle-to-beam connection bolts. The 0.75 factor accounts for the losses that occur in the clamping forces of the angle-to-beam connection bolts and the resulting losses in the slip critical force as the structure undergoes large lateral displacements. The development of the full bearing capacity of the angle horizontal leg cross-section is not expected, and, is not modeled since the analyses and experiments show that extremely small compression deformations occur in the compression angle once the beam corner comes into contact with the wall.

Note that slip of the angle-to-beam connection bolts can also occur when the angle is pulled away from the wall (i.e., tension loading direction in Figure 9.13); however, this is not a desirable type of behavior. It is assumed that the slip critical capacity of the angle-to-beam connection bolts, $C_{as} = 0.75C_{asi}$ is larger than the angle capacity in tension, $1.25T_{ayx}$, and thus, slip does not occur in tension. The angle-to-beam connections should be designed to ensure this behavior.

9.2.6.2 Vertical Angle Element Force-Deformation Model

The vertical angle element models the shear force in the angle horizontal leg using an elasto-plastic force-deformation behavior as shown in Figure 9.13(b). The yield force, T_{ayy} is determined from Equation (9.2), with M_{ap} and V_{ap} calculated as recommended by Kishi and Chen (1990) ignoring the rotation of the horizontal leg with respect to the vertical leg and ignoring the axial force in the vertical leg (note that, as shown in Figure 9.14, this axial force is equal to T_{ayy}). Assuming that T_{ayx} and T_{ayy} are reached at the same coupling beam chord rotation and that the rotation of the beam occurs about the compression corner, the initial stiffness, K_{aiy} of the vertical angle element can be determined as:

$$K_{aiy} = K_{aixt} \frac{T_{ayy}}{T_{ayx}} \frac{h_b}{l_{gh}} \tag{9.4}$$

where, h_b = depth of the coupling beam. The post-yield stiffness of the vertical angle element is assumed to be equal to 6.0% of the initial stiffness, K_{aiy}.

Note that the modeling of the angles as described above assumes that the contributions of the vertical and horizontal angle elements can be superposed, even though this assumption is in general not valid in the nonlinear range. As stated previously, the contribution of the vertical angle element to the subassembly behavior is generally small as compared with the horizontal angle element (it is about 5.0% of the horizontal angle element contribution), and thus can be ignored.

9.3 Verification of Test Specimen Models

This section compares the measured behavior of the test specimens from Chapters 6 – 8 with analytical predictions from the fiber element model as follows: (1) beam shear force versus chord rotation behavior; (2) beam post-tensioning force; (3) contact depth at beam-to-reaction-block interface; (4) gap opening at beam-to-reaction-block interface; (5) concrete compressive strains at beam end; (6) longitudinal mild steel strains at beam end; (7) longitudinal mild steel strains at beam midspan; and (8) angle behavior. The virgin beam specimens from Tests 2, 3, and 4, and the non-virgin beam specimens from Tests 3B, 4A, and 4B are used in the comparisons. Note that the virgin specimen from Test 1 is not used in the analytical model verification due to the large concrete patch at the south end of the beam, which led to unsymmetrical behavior at the two ends of the structure during the experiment. The non-virgin Test 3A is also not used in the analytical model verification due to the lack of parameters to accurately model the behavior of the top and seat angles with holes drilled in the vertical leg.

The analyses replicate what was done in each of the tests. Referring to Figure 9.1, the left wall region (representing the reaction block) of the model is fixed at Node B (ignoring the deformations in the wall-height elements, which are small), and the right wall region (representing the load block) at Node G is allowed to translate in the horizontal and vertical directions, but not allowed to rotate. A vertical force *V* is applied at Node G in displacement control.

Note that similar to the experiments that were conducted, these subassembly analyses do not include the wall pier shear forces that develop in a multi-story structure, and thus, do not capture the axial forces introduced into the coupling beams from the wall shear forces as the structure is displaced laterally. As discussed in Kurama and Shen (2004), these additional axial forces may be large in the lower floor beams [2nd and 3rd floor beams, see Figure 1.1] in a multi-story structure; however, they are negligible for the coupling beams in the upper floor and roof levels. Thus, the results described below are more representative of the behavior of upper level beams in a multi-story structure.

As described in Chapters 6 and 7, the wall test region of the reaction block was patched using a high strength fiber-reinforced grout mix after the damage to the wall test region in Test 3B. Consequently, a reduced concrete initial stiffness (approximately one half of the Young's modulus for virgin concrete) was used to model the compressive behavior of the patched region in Tests 4, 4A, and 4B. The reduced concrete stiffness, which was determined by averaging the Young's moduli for virgin concrete and the patch grout, is shown in Figure 9.15.

In Test 4A, no top and seat angles were used at the beam-to-wall connections. The compressive stress-strain model of the beam end concrete in Tests 3B, 4A, and 4B (during the retesting of the beam) was also modified such that the stress-strain behavior during first loading in each of these repeat tests continued from the last loading cycle of the preceding test to account for any non-linear behavior that the concrete might have experienced during the prior loading (see Figures 9.16 and 9.17, which illustrate the compressive concrete stress-strain relationships used for Test 3B and Tests 4A and 4B, respectively). Note that this was done for the concrete behavior at the beam ends only, where non-linear behavior would be expected. At the beam ends, compression-only concrete is used; and thus, no adjustments were needed for the concrete behavior in tension.

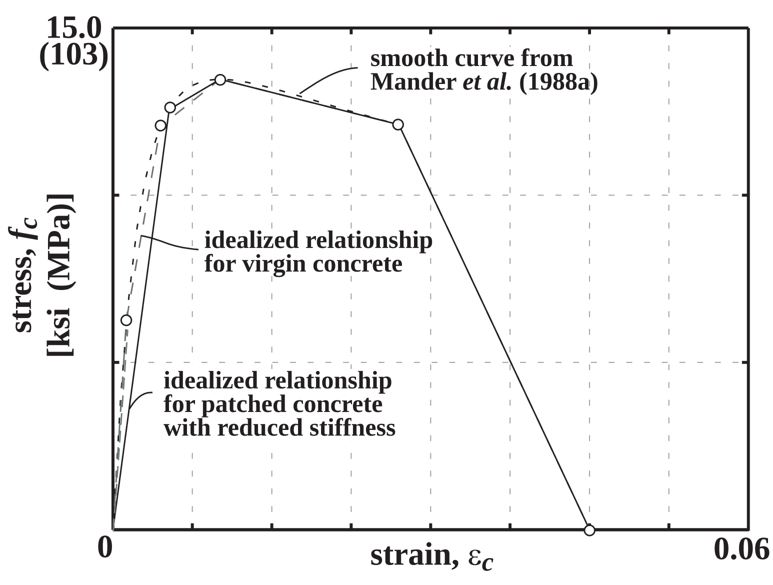

Figure 9.15: Assumed concrete compressive stress-strain

relationship for the patched region of the reaction block.

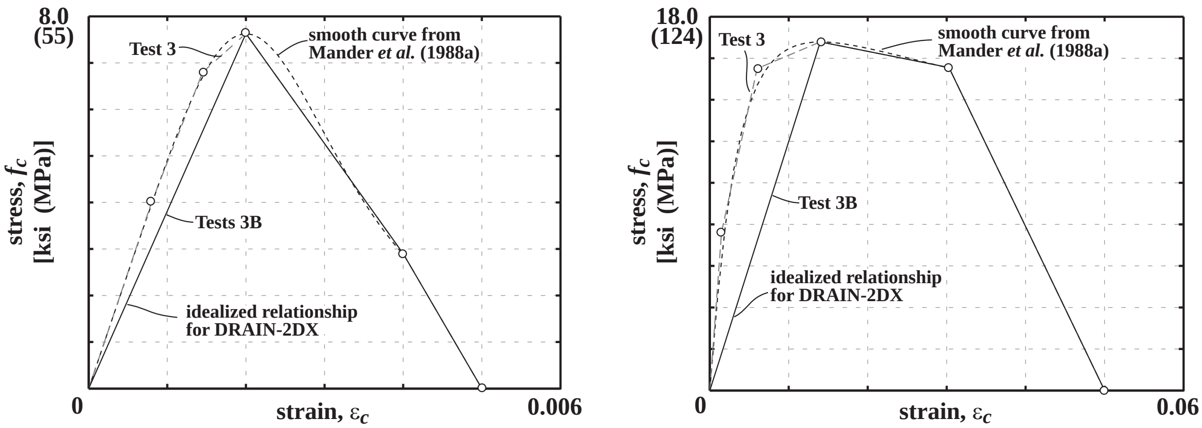

(a) (b)

Figure 9.16: Assumed concrete compressive stress-strain relationships for Test 3B – (a) unconfined concrete; (b) confined concrete.

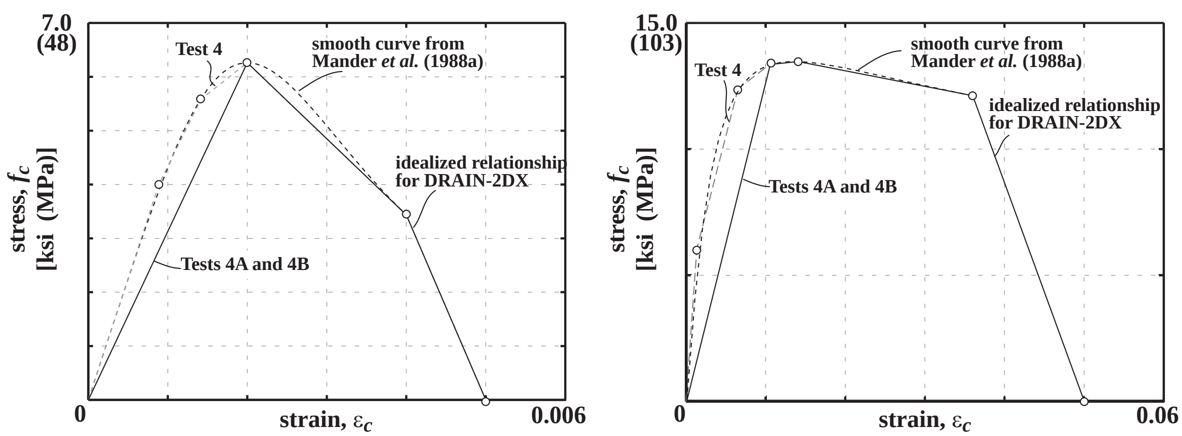

(a) (b)

Figure 9.17: Assumed concrete compressive stress-strain relationships for Tests 4A and 4B – (a) unconfined concrete; (b) confined concrete.

9.3.1 Beam Shear Force versus Chord Rotation Behavior

Figures 9.18 – 9.23 show the measured (left) and predicted (right) hysteretic beam shear force versus beam chord rotation behaviors for Tests 2, 3, 3B, 4, 4A, and 4B, respectively. It is observed that the analytical model predicts the measured behavior of the test specimens reasonably well, including stiffness, strength, energy dissipation, and self-centering characteristics. The small amount of energy dissipation (mostly due to concrete damage) for the non-virgin specimen with no angles in Test 4A is not captured well by the model; however, this effect becomes relatively small once angles are introduced at the beam ends.

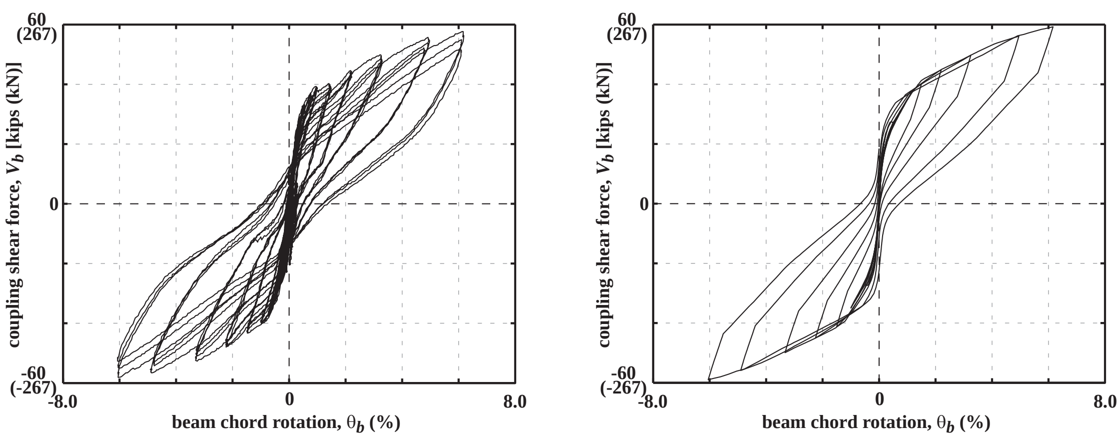

Figure 9.18: Experimental versus analytical V_b-θ_b behavior for Test 2.

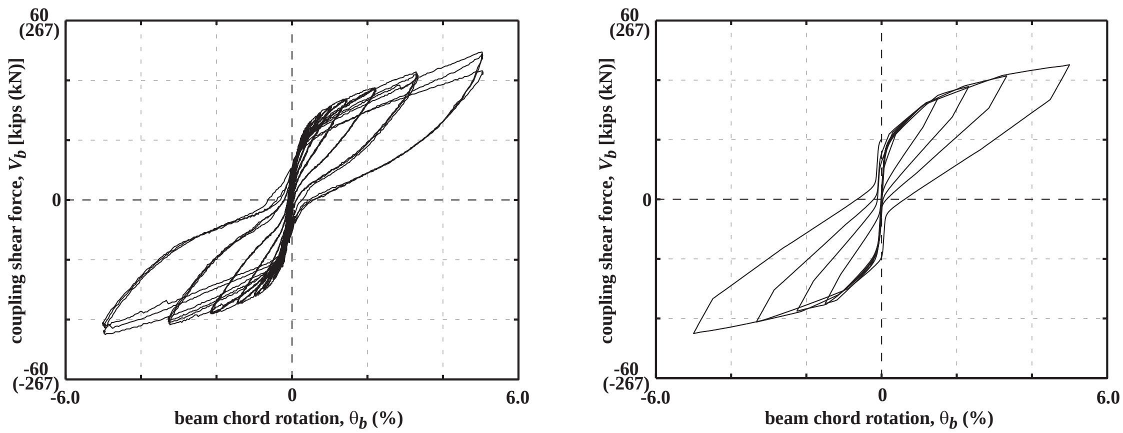

Figure 9.19: Experimental versus analytical V_b-θ_b behavior for Test 3.

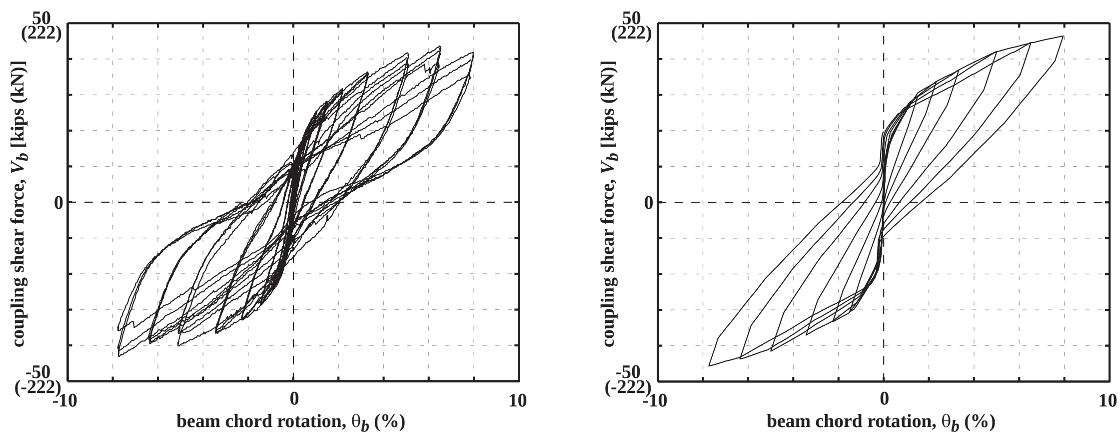

Figure 9.20: Experimental versus analytical V_b-θ_b behavior for Test 3B.

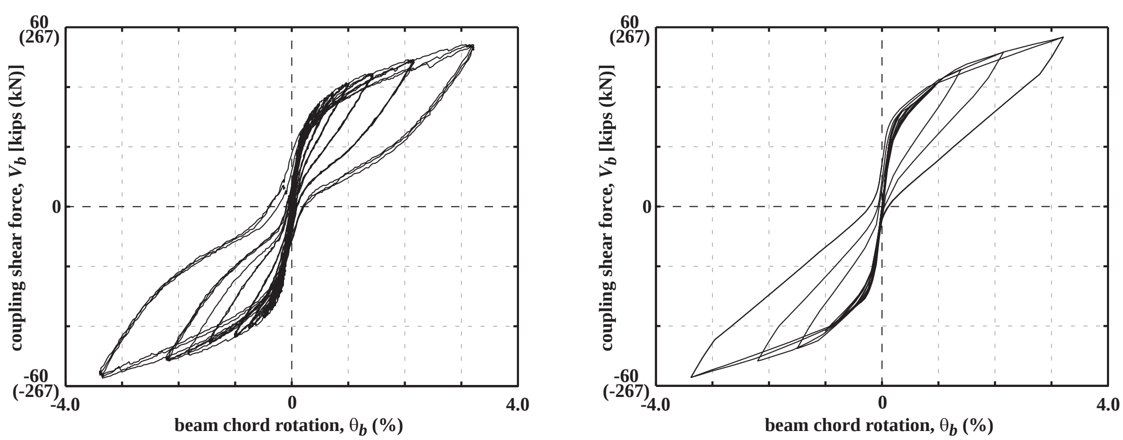

Figure 9.21: Experimental versus analytical V_b-θ_b behavior for Test 4.

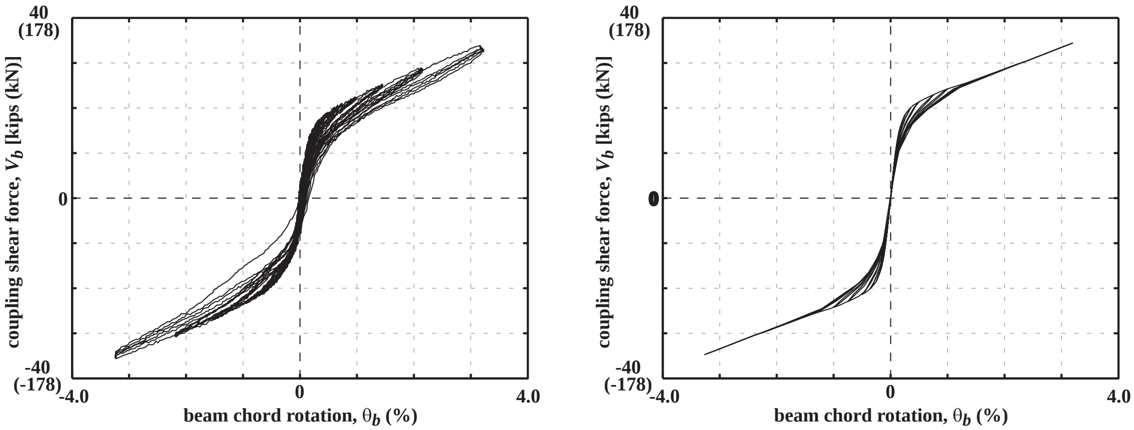

Figure 9.22: Experimental versus analytical V_b-θ_b behavior for Test 4A.

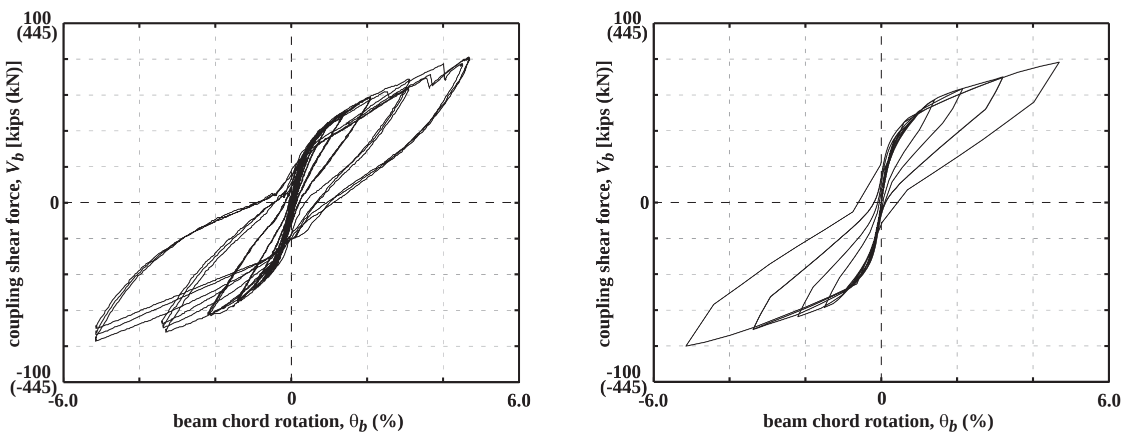

Figure 9.23: Experimental versus analytical V_b-θ_b behavior for Test 4B.

9.3.2 Beam Post-tensioning Force

Figure 9.24(a) shows the measured (left) and predicted (right) total beam post-tensioning force [normalized by the design maximum strength of the tendon, with f_{bpu} = 270 ksi (1862 MPa)] versus the beam chord rotation (P_{bp}-θ_b) behavior for the subassembly from Test 2. Similarly, Figure 9.24(b) compares the measured and predicted load block horizontal displacement versus the beam chord rotation from Test 2. The corresponding comparisons for Tests 3, 3B, 4, 4A, and 4B are given in Figures 9.25 –

9.29, respectively. It can be seen that the analytical model is able to predict the measured forces in the post-tensioning tendons quite well, including the increase in the post-tensioning forces as gaps open at the beam ends and the load block is displaced in the horizontal direction. The largest discrepancy is observed between the measured and predicted load block horizontal displacements from Test 3B. While the exact source of this discrepancy is unknown, it could have occurred due to the uncertainties involved in modeling a previously tested (i.e., non-virgin) beam. Note that the discrepancies between the measured and predicted post-tensioning forces are generally smaller than the discrepancies between the measured and predicted horizontal displacements of the load block. This is because the load block displacements only affect the increase in the post-tensioning force and not the initial force.

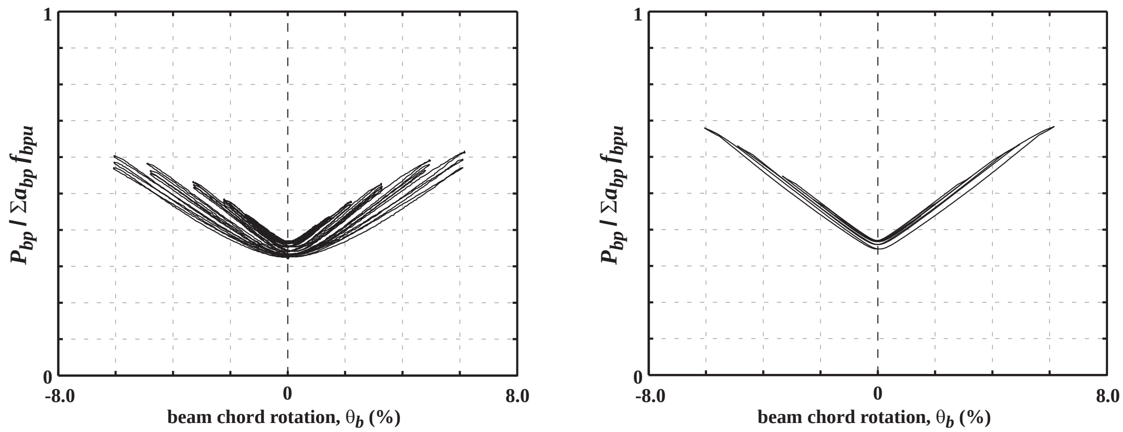

(a)

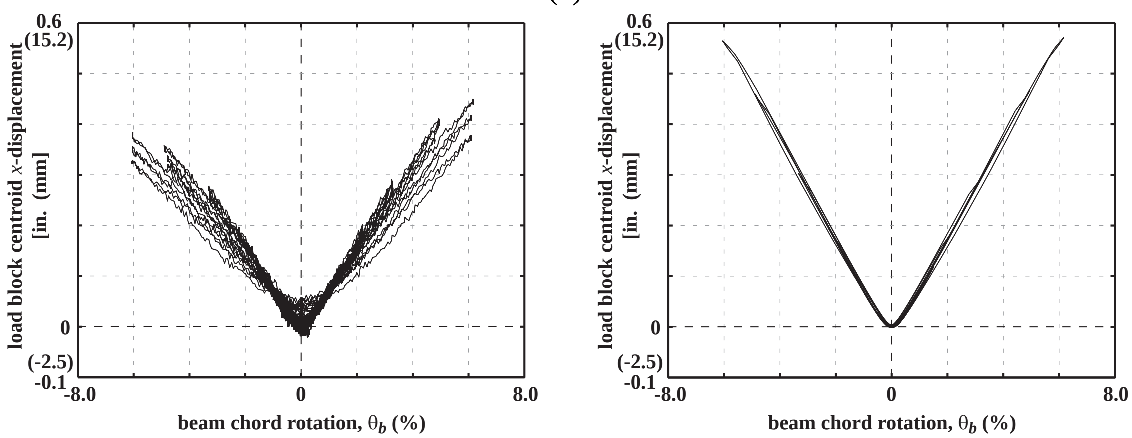

(b)

Figure 9.24: Experimental versus analytical beam post-tensioning behavior for Test 2 – (a) P_{bp}-θ_b behavior; (b) load block horizontal displacement.

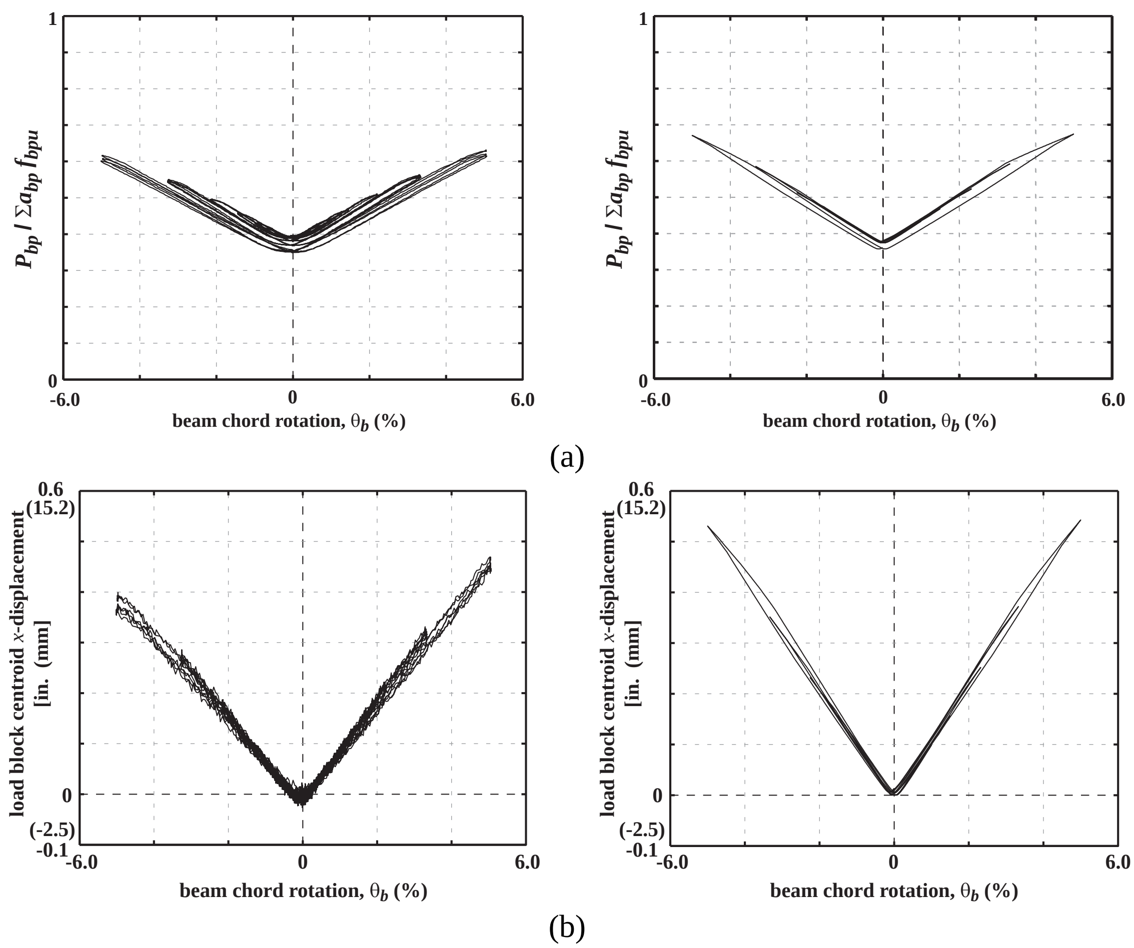

Figure 9.25: Experimental versus analytical beam post-tensioning behavior for Test 3 – (a) P_{bp}-θ_b behavior; (b) load block horizontal displacement.

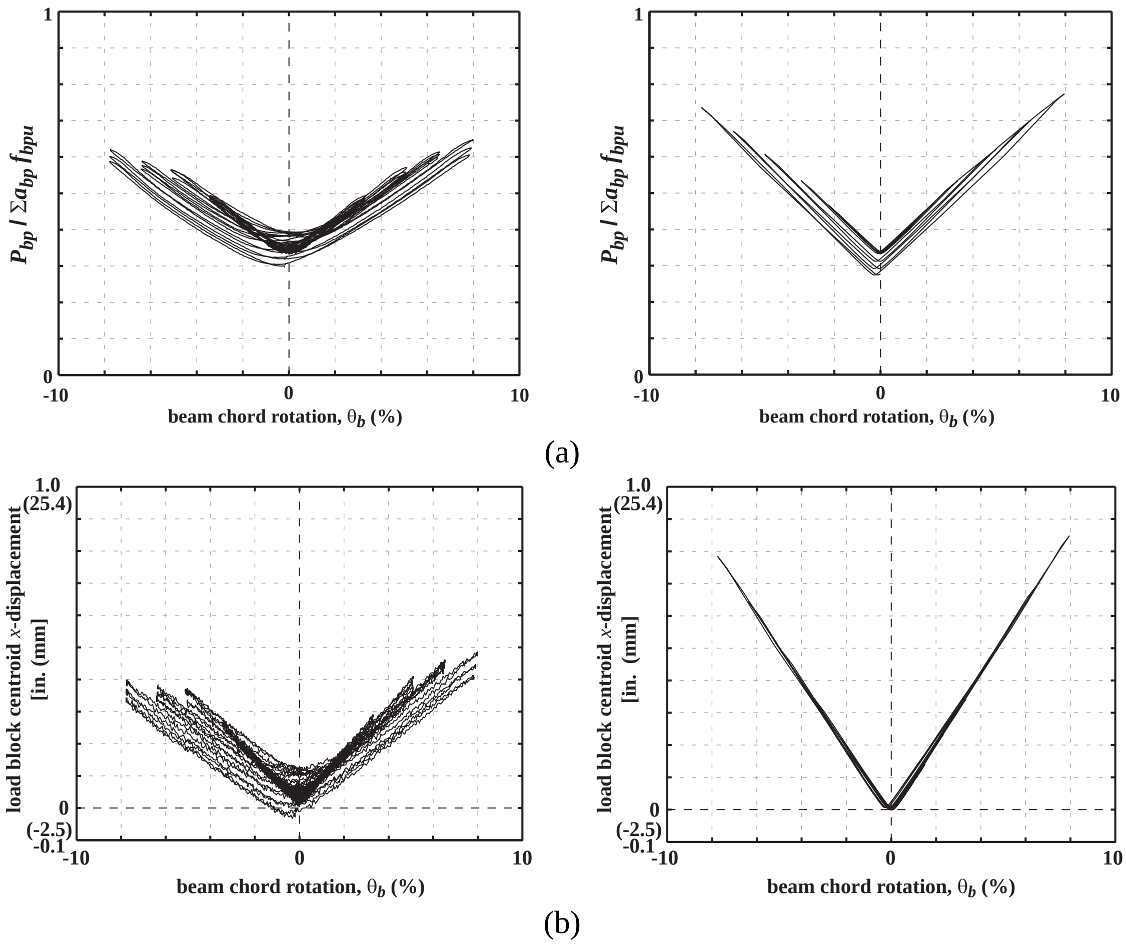

Figure 9.26: Experimental versus analytical beam post-tensioning behavior for Test 3B – (a) P_{bp}-θ_b behavior; (b) load block horizontal displacement.

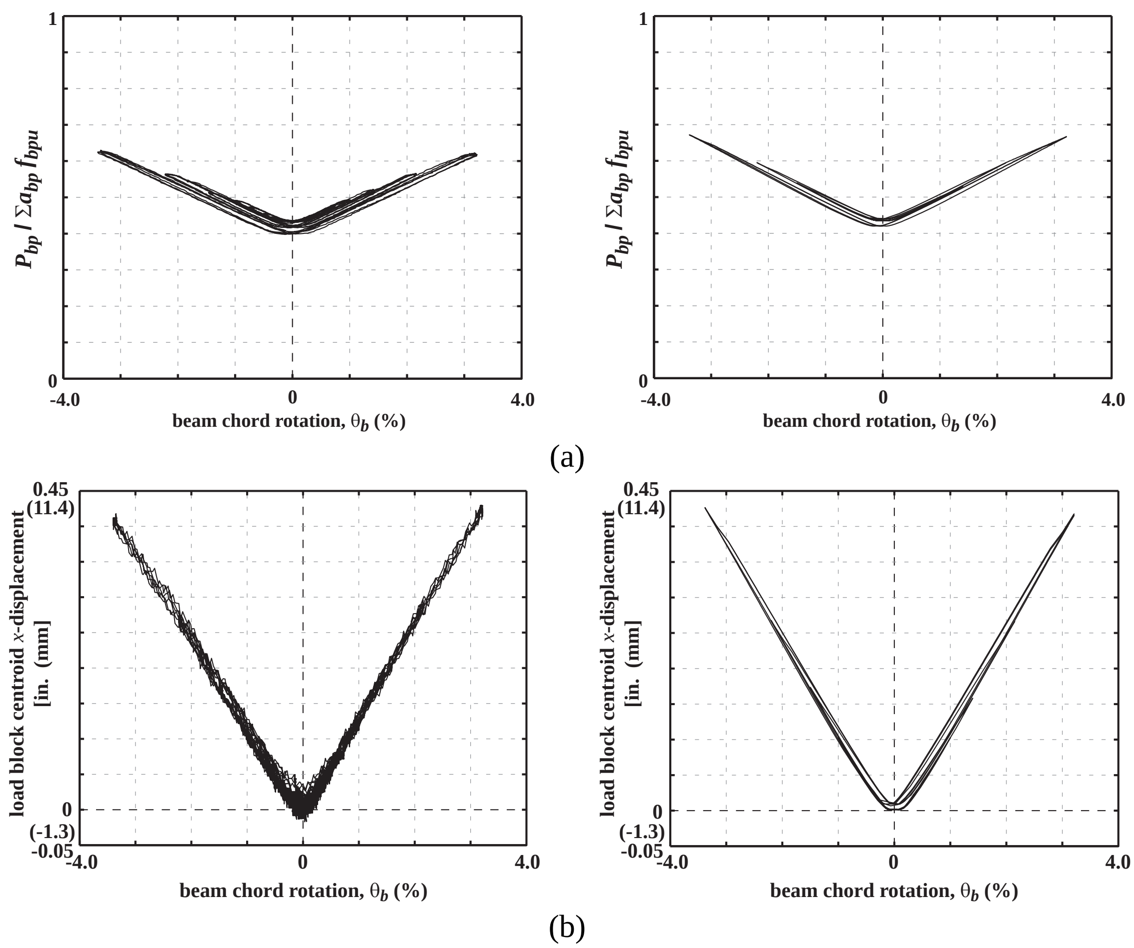

Figure 9.27: Experimental versus analytical beam post-tensioning behavior for Test 4 – (a) P_{bp}-θ_b behavior; (b) load block horizontal displacement.

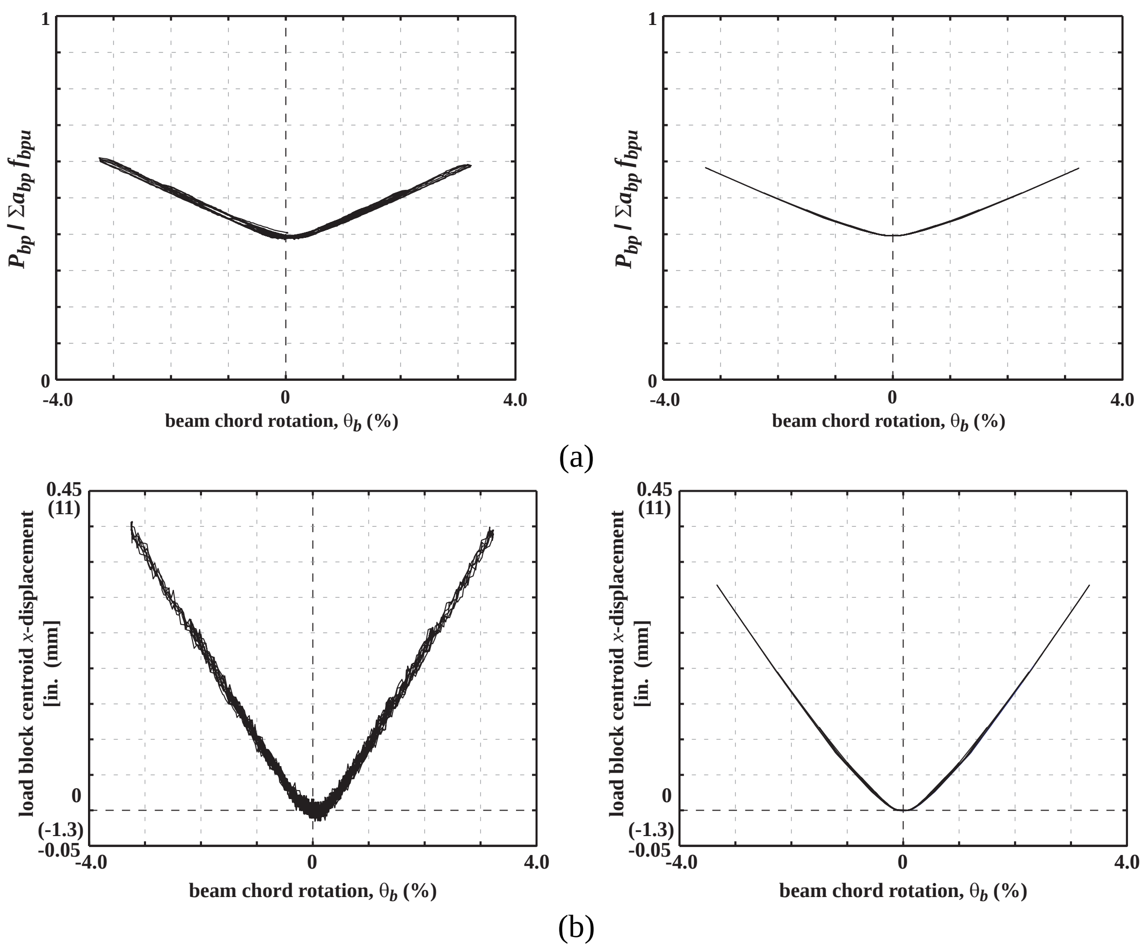

Figure 9.28: Experimental versus analytical beam post-tensioning behavior for Test 4A – (a) P_{bp}-θ_b behavior; (b) load block horizontal displacement.

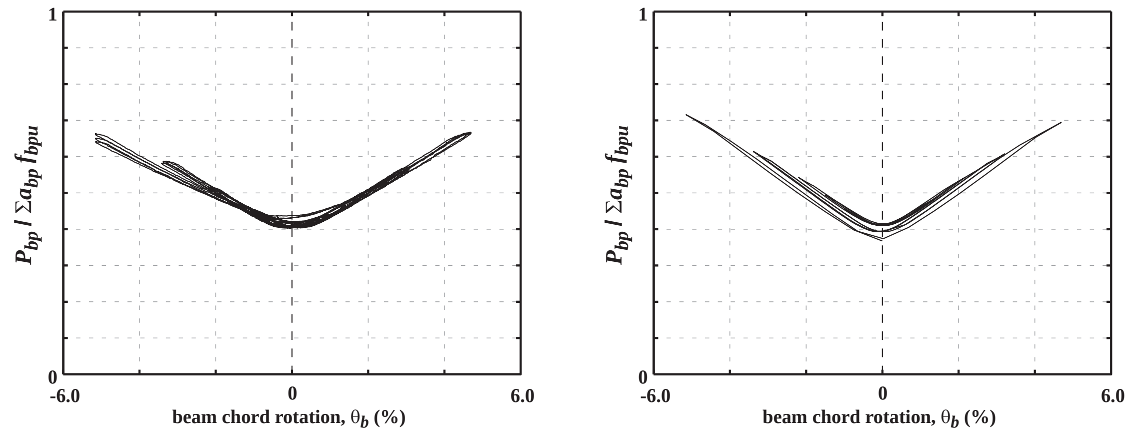

(a)

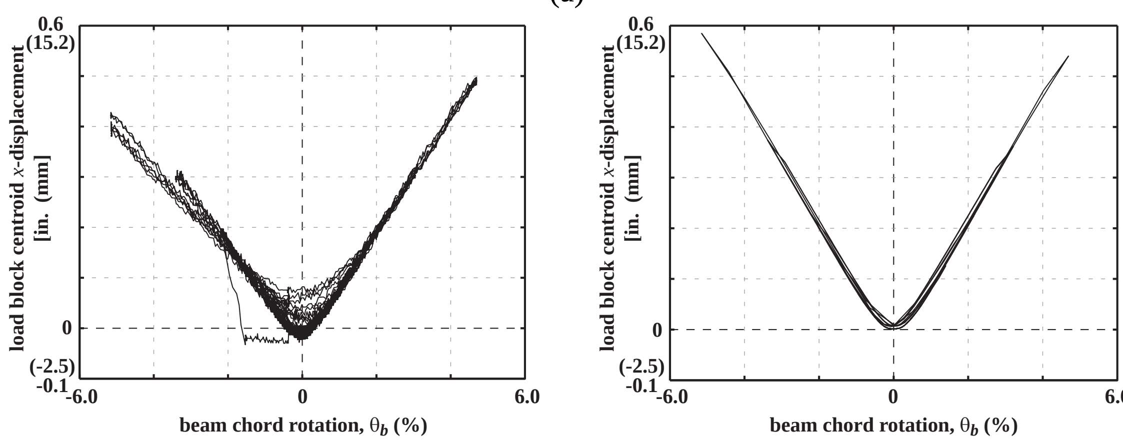

(b)

Figure 9.29: Experimental versus analytical beam post-tensioning behavior for Test 4B – (a) P_{bp}-θ_b behavior; (b) load block horizontal displacement.

9.3.3 Contact Depth at Beam-to-Reaction-Block Interface

Figure 9.30 shows the measured contact depth at the beam-to-reaction-block interface (circular markers) using the five methods described in Chapter 5 and the predicted contact depth from the analytical model (solid lines) for Test 2. Similar comparisons for Tests 3, 3B, 4, 4A, and 4B are given in Figures 9.31 – 9.35, respectively.

In general, the results from the analytical model show similar trends as the results from the measured data. The comparisons between the analytical and measured results are mixed depending on the method used to determine the measured contact depth. This finding is not unexpected given the difficulties in accurately modeling as well as accurately measuring the contact depth at the end of a concrete coupling beam. Loosening (due to damage to the surrounding concrete) of the embedded ferrule inserts supporting the sensors may have distorted some of the measurements, especially during the large nonlinear displacements of the beam.

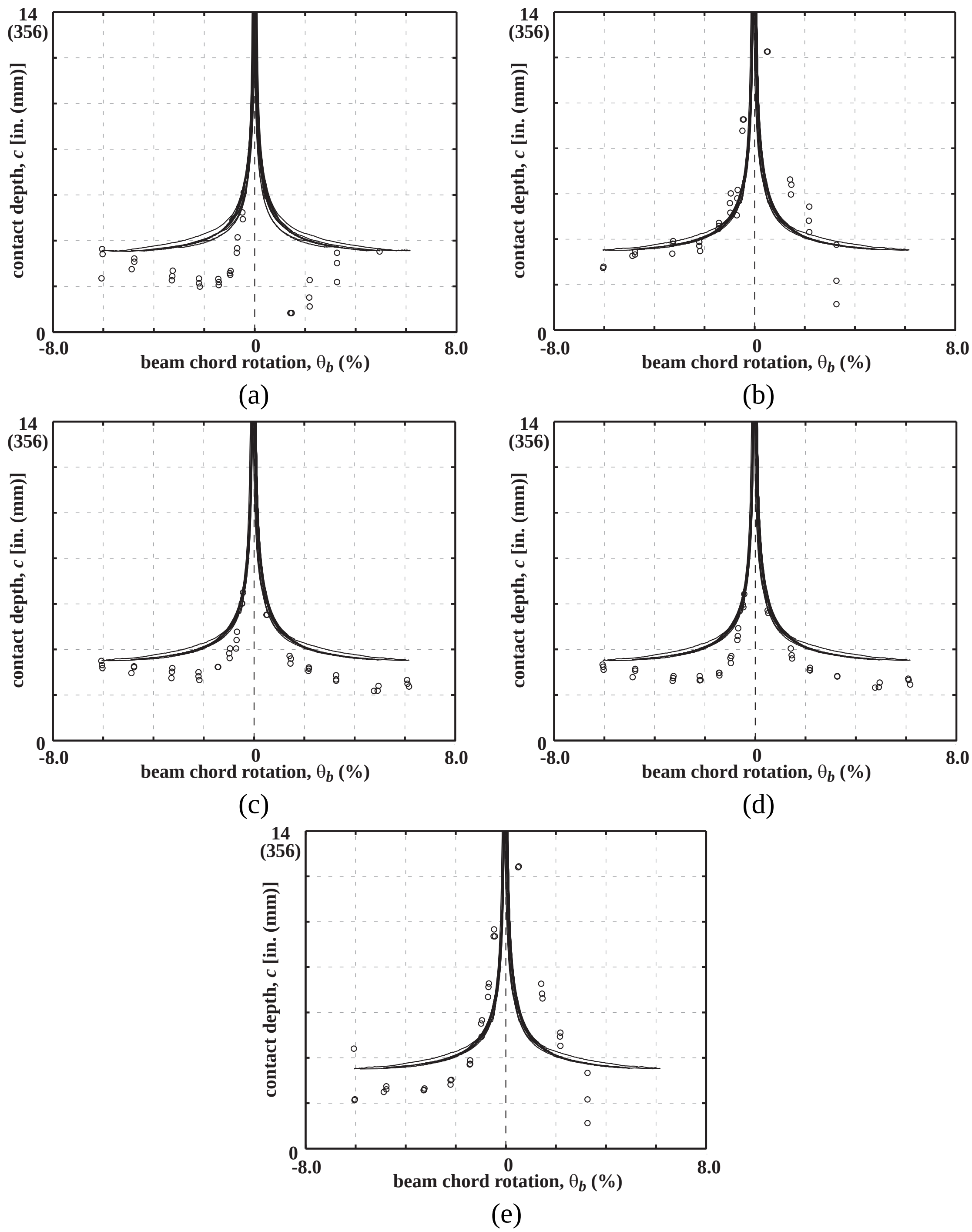

Figure 9.30: Experimental versus analytical contact depth at beam-to-reaction-block interface for Test 2 – (a) method 1 using DT11, DT12, and DT13; (b) method 2 using RT2, DT11, and DT13; (c) method 3 using RT2 and DT12; (d) method 4 using θ_b and DT12; (e) method 5 using θ_b, DT11, and DT13.

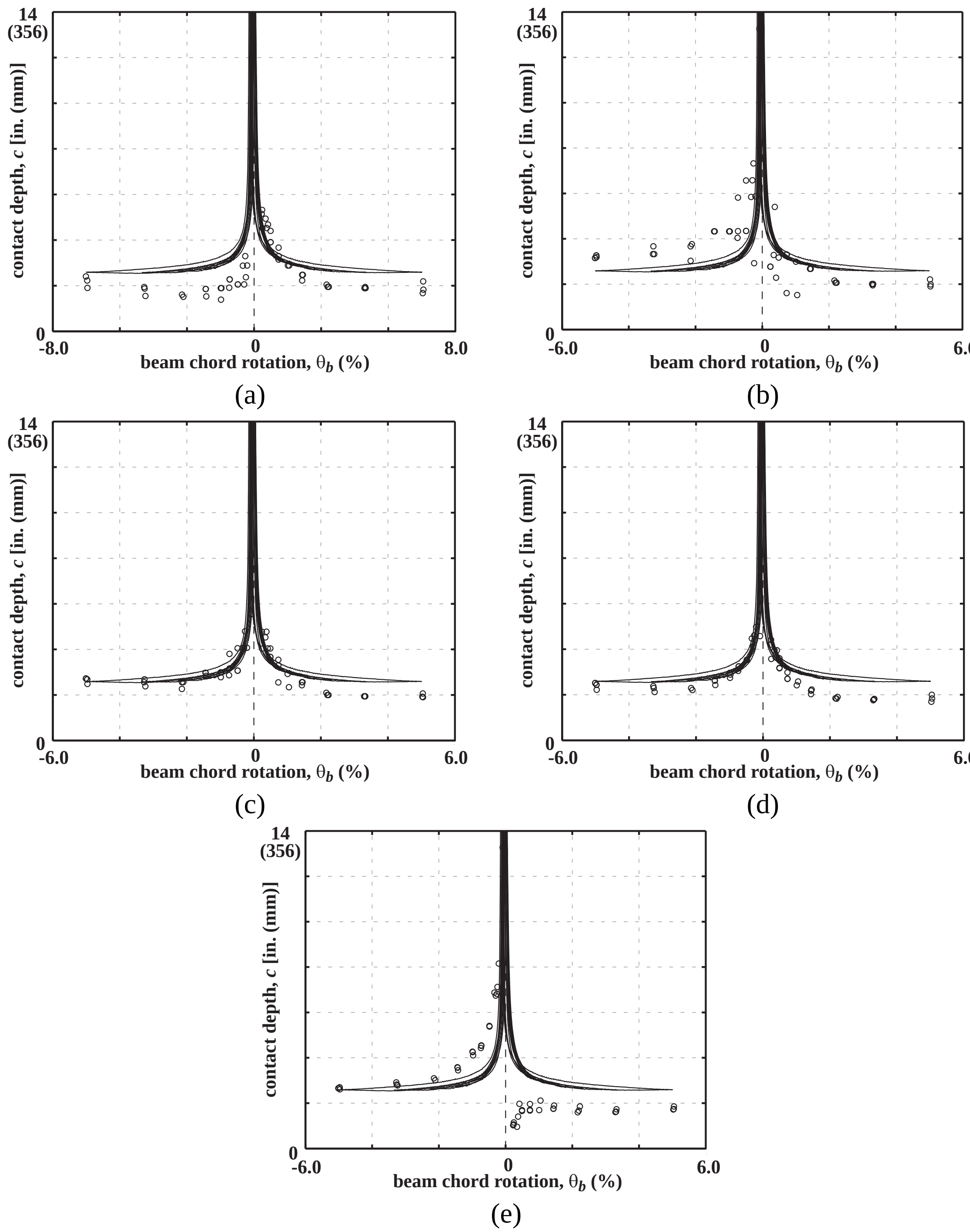

Figure 9.31: Experimental versus analytical contact depth at beam-to-reaction-block interface for Test 3 – (a) method 1 using DT11, DT12, and DT13; (b) method 2 using RT1, DT11, and DT13; (c) method 3 using RT1 and DT12; (d) method 4 using θ_b and DT12; (e) method 5 using θ_b, DT11, and DT13.

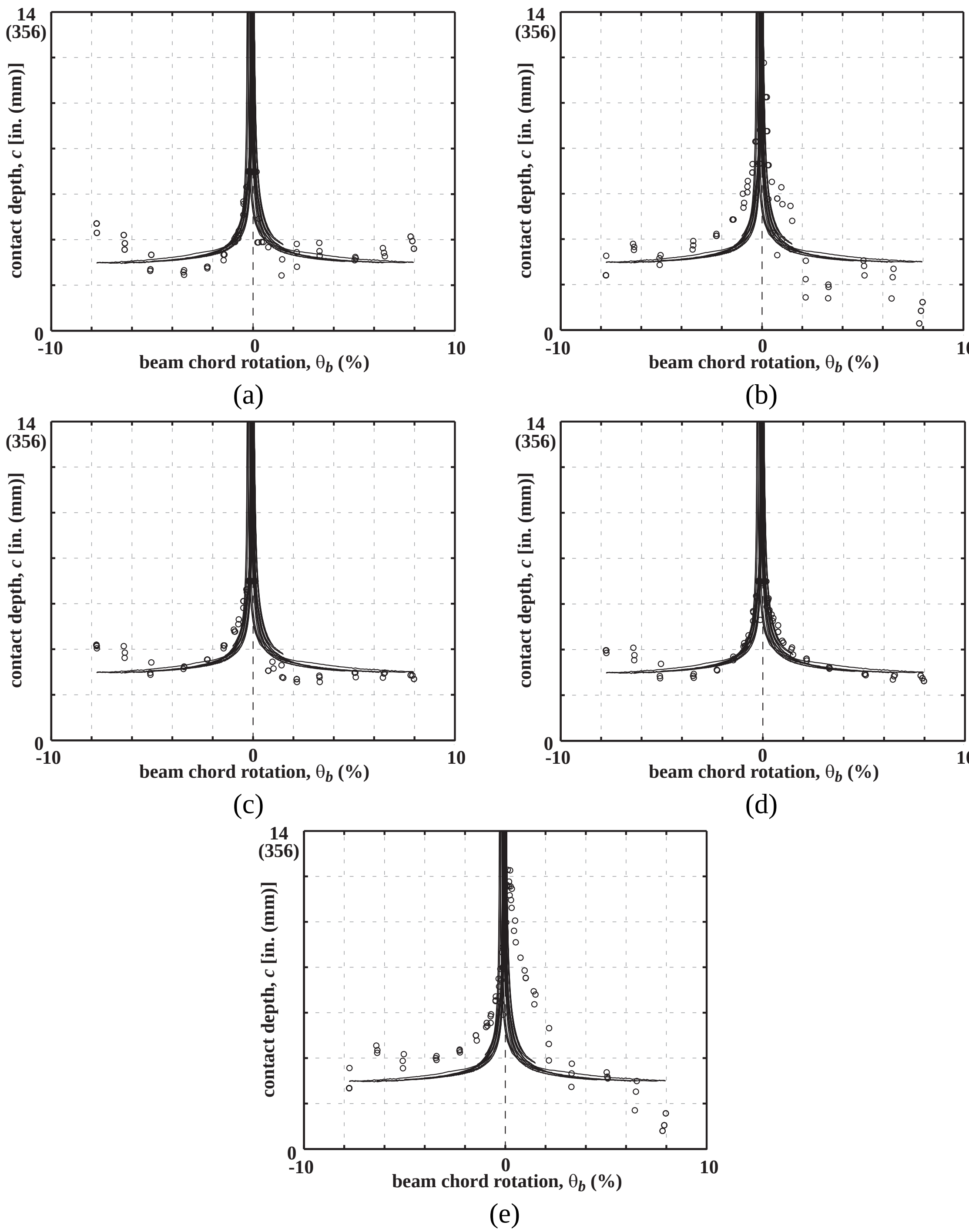

Figure 9.32: Experimental versus analytical contact depth at beam-to-reaction-block interface for Test 3B – (a) method 1 using DT11, DT12, and DT13; (b) method 2 using RT1, DT11, and DT13; (c) method 3 using RT1 and DT12; (d) method 4 using θ_b and DT12; (e) method 5 using θ_b, DT11, and DT13.

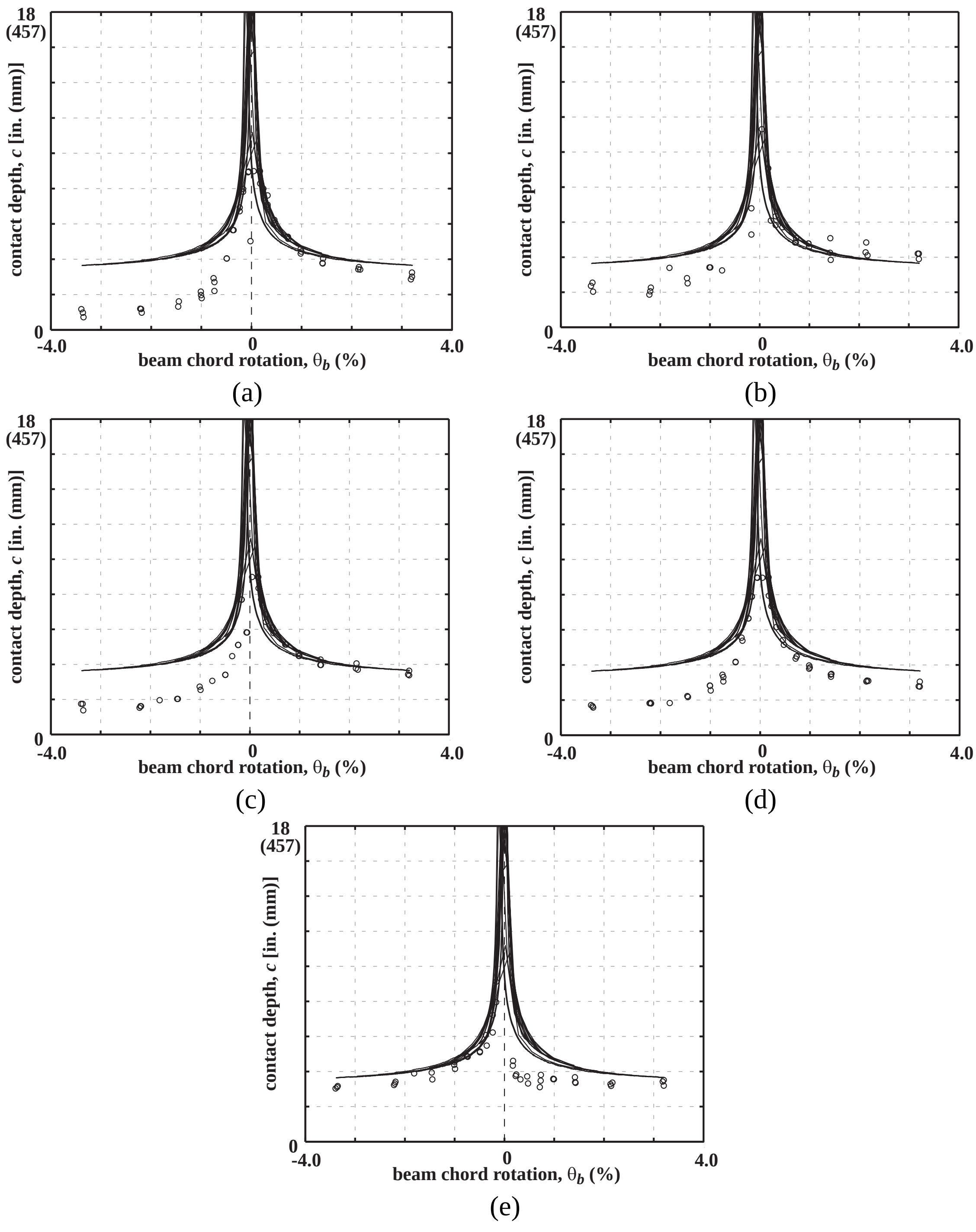

Figure 9.33: Experimental versus analytical contact depth at beam-to-reaction-block interface for Test 4 – (a) method 1 using DT11, DT12, and DT13; (b) method 2 using RT2, DT11, and DT13; (c) method 3 using RT2 and DT12; (d) method 4 using θ_b and DT12; (e) method 5 using θ_b, DT11, and DT13.

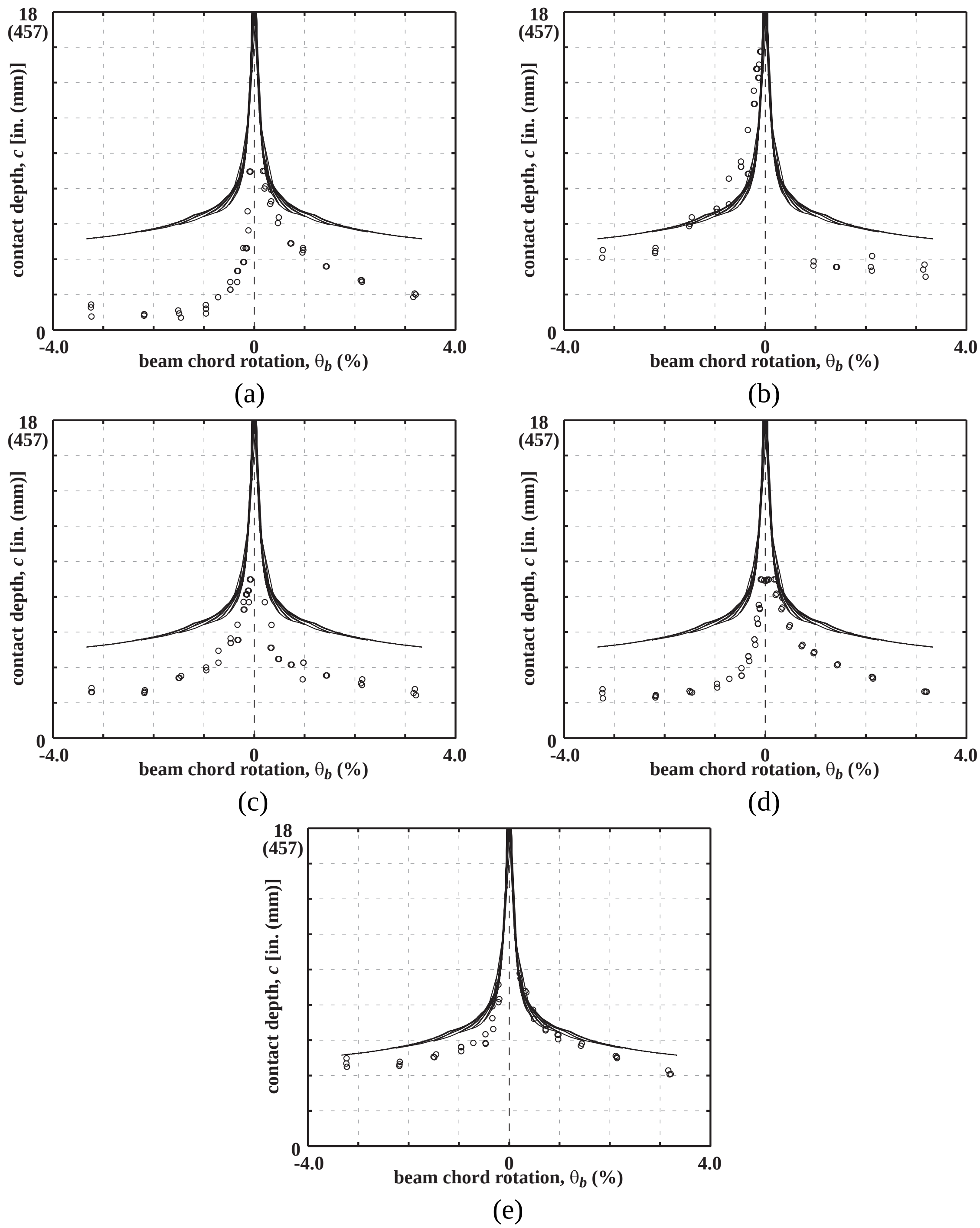

Figure 9.34: Experimental versus analytical contact depth at beam-to-reaction-block interface for Test 4A – (a) method 1 using DT11, DT12, and DT13; (b) method 2 using RT2, DT11, and DT13; (c) method 3 using RT2 and DT12; (d) method 4 using θ_b and DT12; (e) method 5 using θ_b, DT11, and DT13.

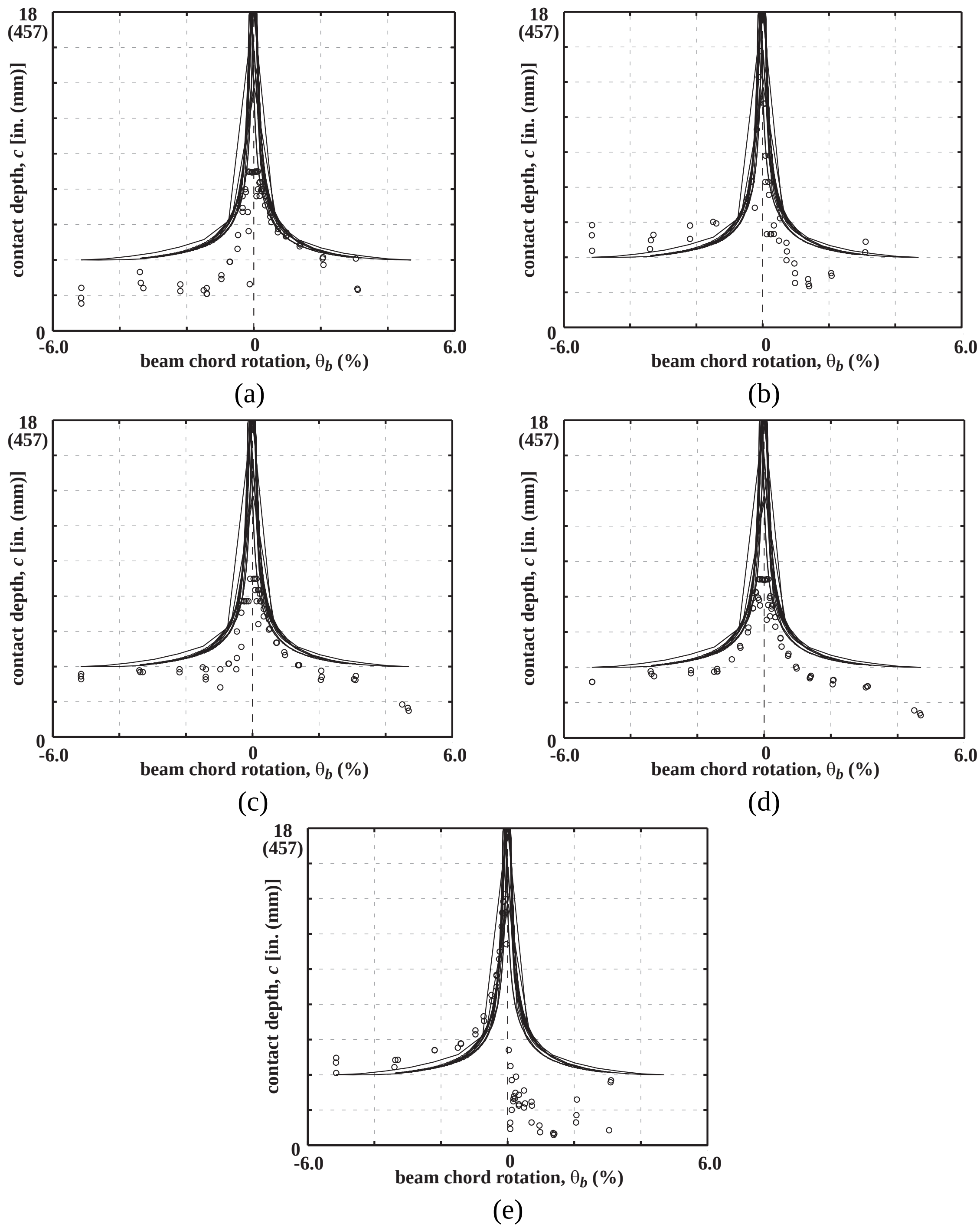

Figure 9.35: Experimental versus analytical contact depth at beam-to-reaction-block interface for Test 4B – (a) method 1 using DT11, DT12, and DT13; (b) method 2 using RT2, DT11, and DT13; (c) method 3 using RT2 and DT12; (d) method 4 using θ_b and DT12; (e) method 5 using θ_b, DT11, and DT13.

9.3.4 Gap Opening at Beam-to-Reaction-Block Interface

Figure 9.36 shows the measured gap opening at the beam-to-reaction-block interface (circular markers) using the five methods described in Chapter 5, ruler measurements taken during the test (+ markers), and the predicted gap opening from the analytical model (solid lines) for Test 2. Similar comparisons for Tests 3, 3B, 4, 4A, and 4B are given in Figures 9.37 – 9.41, respectively. The gap opening from the analytical model was determined by multiplying the tensile strains at the beam end (i.e., in the first slice adjacent to the wall contact region) by the length l_{cr}. In general, the analytical model is able to predict the measured behavior quite well, validating the length used for l_{cr} (i.e., the distance from the beam end to the centroid of the angle-to-beam connection). Similar to the comparisons for the contact depth at the beam-to-reaction-block interface, the comparisons between the analytical and measured results are mixed depending on the method used to determine the measured gap opening.

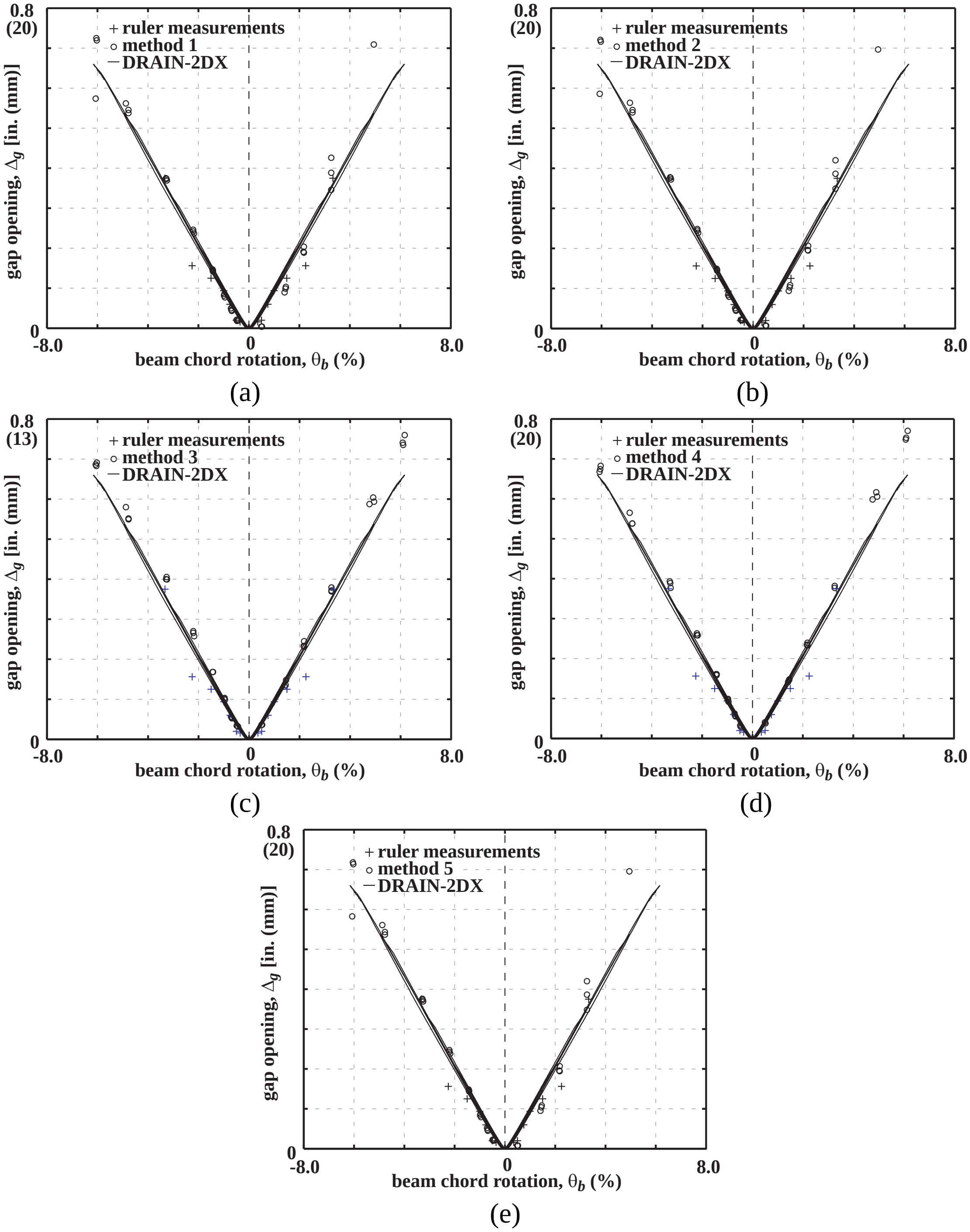

Figure 9.36: Experimental versus analytical gap opening at beam-to-reaction-block interface for Test 2 – (a) method 1 using DT11, DT12, and DT13; (b) method 2 using RT2, DT11, and DT13; (c) method 3 using RT2 and DT12; (d) method 4 using θ_b and DT12; (e) method 5 using θ_b, DT11, and DT13.

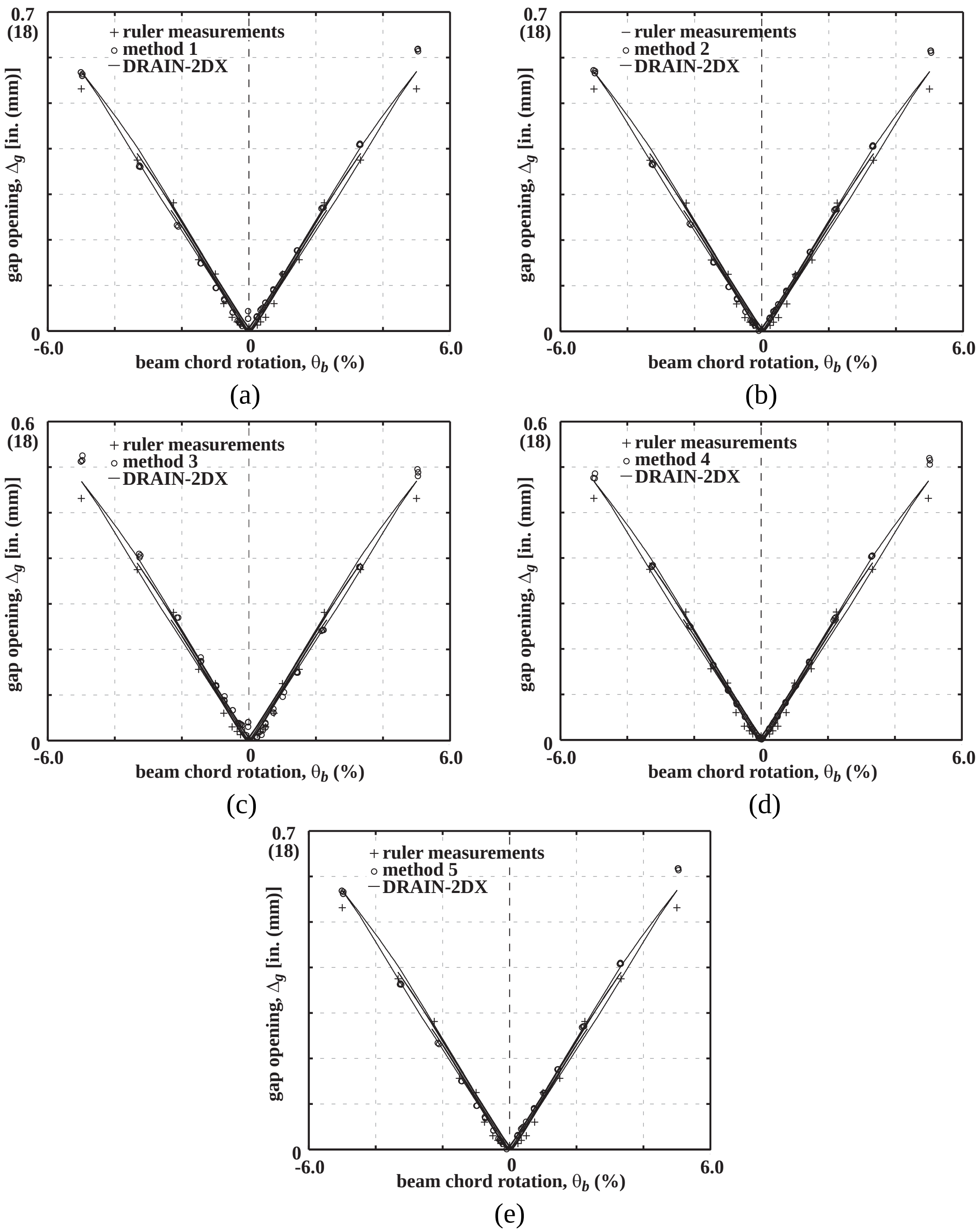

Figure 9.37: Experimental versus analytical gap opening at beam-to-reaction-block interface for Test 3 – (a) method 1 using DT11, DT12, and DT13; (b) method 2 using RT1, DT11, and DT13; (c) method 3 using RT1 and DT12; (d) method 4 using θ_b and DT12; (e) method 5 using θ_b, DT11, and DT13.

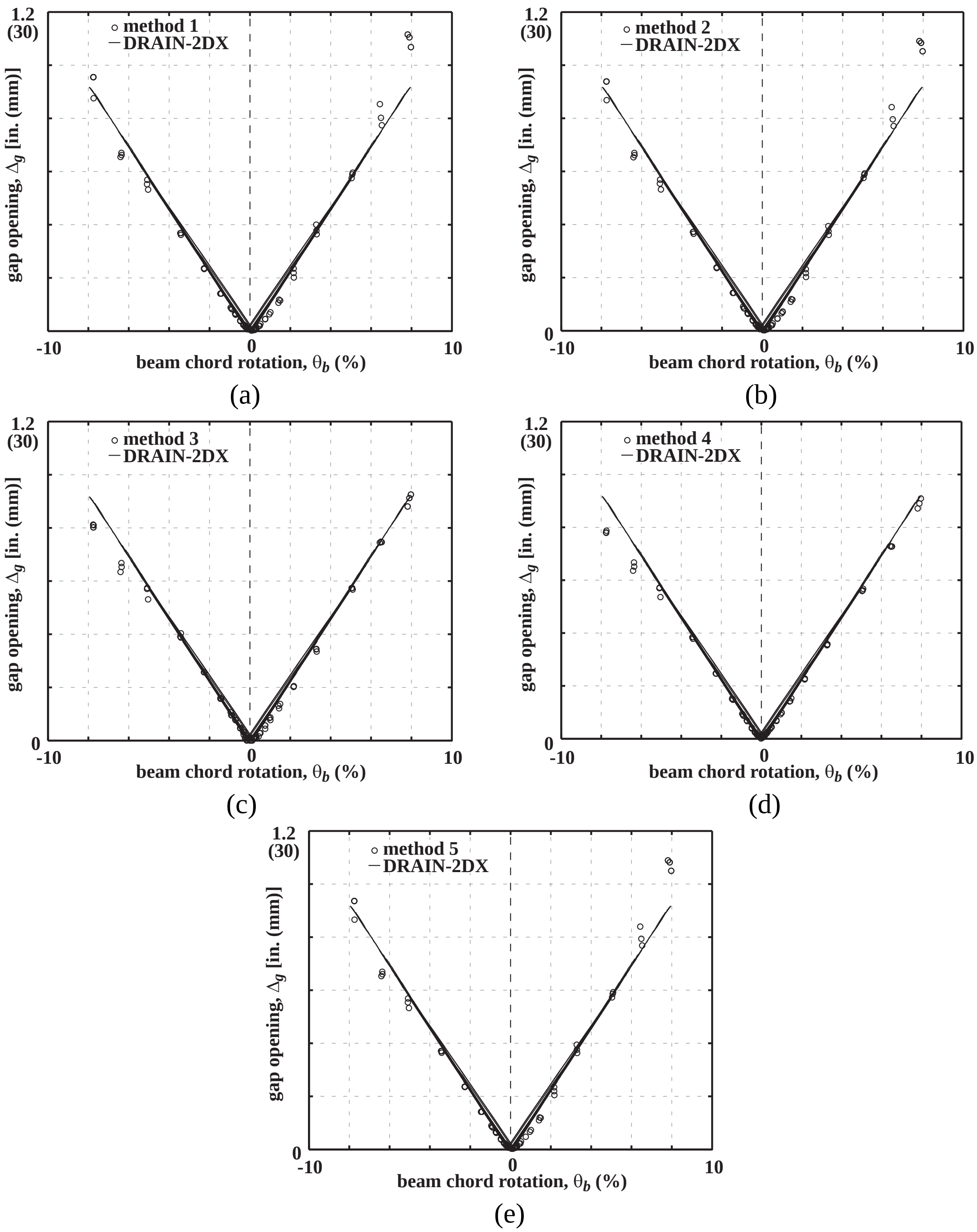

Figure 9.38: Experimental versus analytical gap opening at beam-to-reaction-block interface for Test 3B – (a) method 1 using DT11, DT12, and DT13; (b) method 2 using RT1, DT11, and DT13; (c) method 3 using RT1 and DT12; (d) method 4 using θ_b and DT12; (e) method 5 using θ_b, DT11, and DT13.

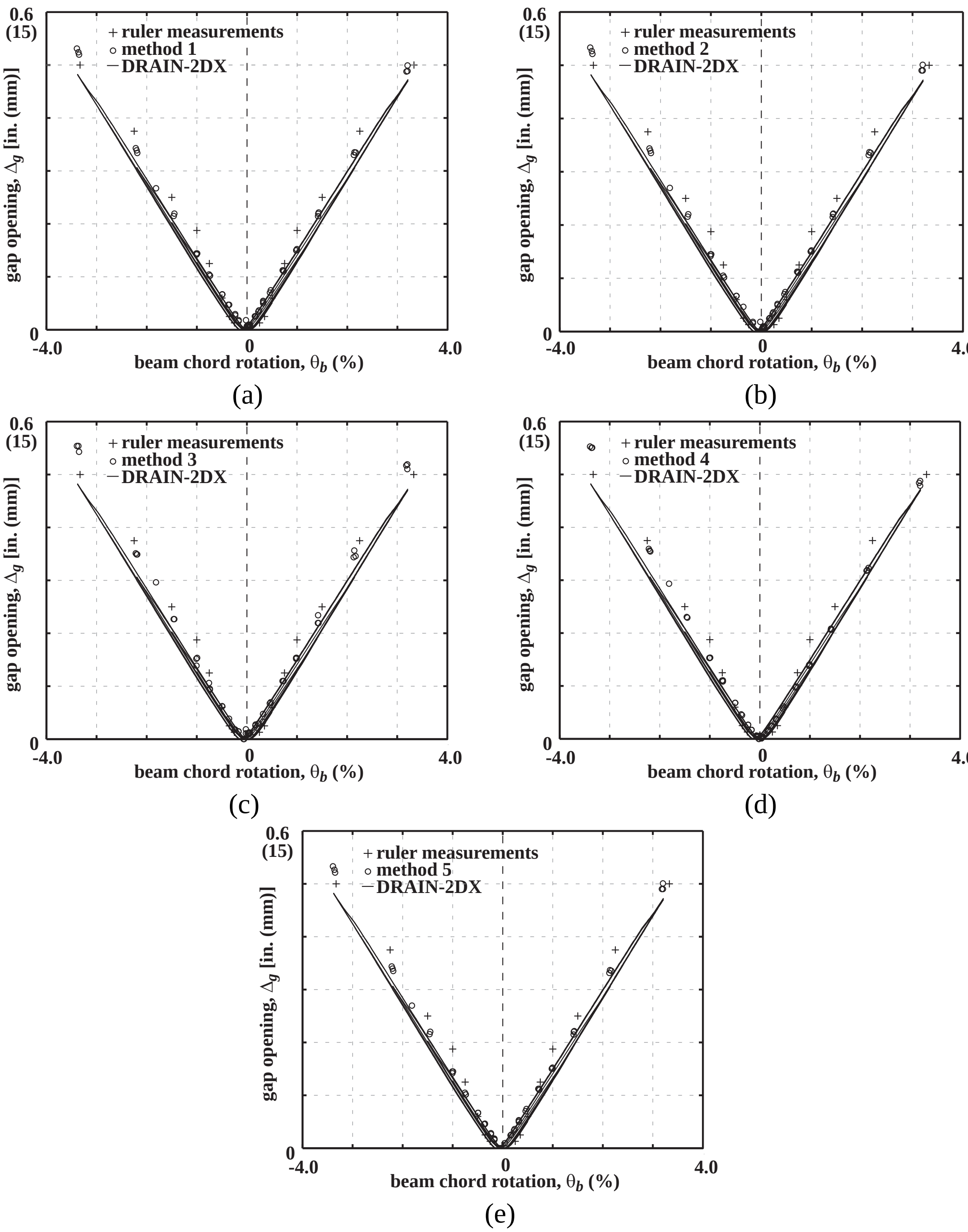

Figure 9.39: Experimental versus analytical gap opening at beam-to-reaction-block interface for Test 4 – (a) method 1 using DT11, DT12, and DT13; (b) method 2 using RT2, DT11, and DT13; (c) method 3 using RT2 and DT12; (d) method 4 using θ_b and DT12; (e) method 5 using θ_b, DT11, and DT13.

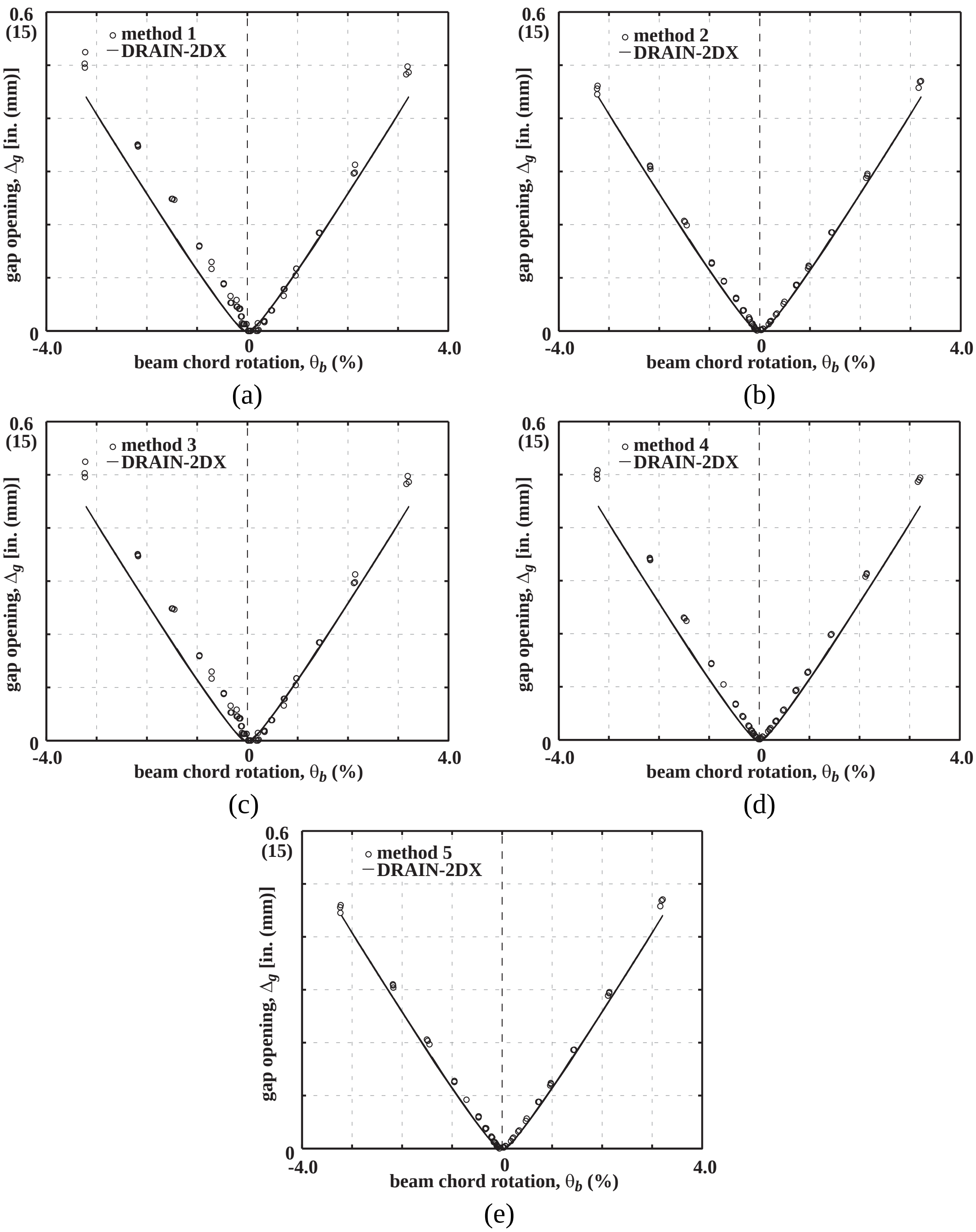

Figure 9.40: Experimental versus analytical gap opening at beam-to-reaction-block interface for Test 4A – (a) method 1 using DT11, DT12, and DT13; (b) method 2 using RT2, DT11, and DT13; (c) method 3 using RT2 and DT12; (d) method 4 using θ_b and DT12; (e) method 5 using θ_b, DT11, and DT13.

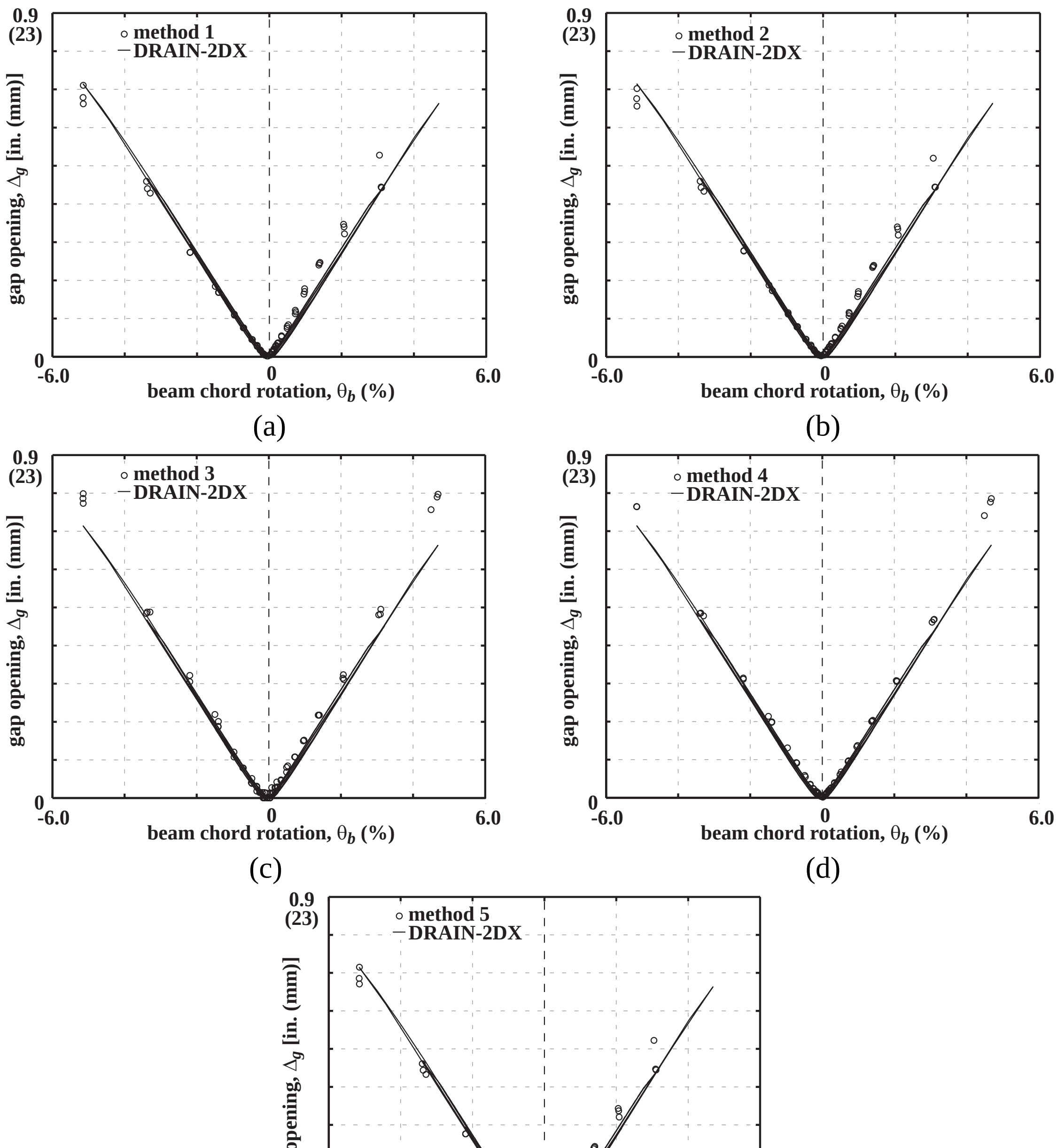

Figure 9.41: Experimental versus analytical gap opening at beam-to-reaction-block interface for Test 4B – (a) method 1 using DT11, DT12, and DT13; (b) method 2 using RT2, DT11, and DT13; (c) method 3 using RT2 and DT12; (d) method 4 using θ_b and DT12; (e) method 5 using θ_b, DT11, and DT13.

9.3.5 Concrete Compressive Strains at Beam End

Figure 9.42 shows the analytical concrete compressive strains at the south end of each beam in Tests 2, 3, and 4. These strains were determined from the extreme concrete compression fiber of the first beam fiber slice adjacent to the beam-to-reaction-block interface, where the behavior was modeled using compression-only concrete fibers. It can be seen from the analytical results that the unconfined concrete crushing strain (i.e., dashed lines at an assumed strain of ε'_{cu} = -0.004) is reached at a beam chord rotation of approximately 0.5%, 1.25%, and 0.5% for Tests 2, 3, and 4, respectively. These rotation values are smaller than the values observed from the experimental damage progression plots in Chapter 6 (i.e., Figures 6.78, 6.140, and 6.202 for Tests 2, 3, and 4, respectively), which may indicate that the analytical model is not able to accurately capture the concrete compression strains at the beam ends. Note that the concrete compressive strains were not measured during the experiments, and thus, could not be compared directly with the analytical results. The observed differences could also be attributed to the analytical model not capturing the clamping forces of the angle-to-beam connection bolts (which may have confined the concrete at the beam ends, thus, delaying crushing) or the reduced stiffness of the grout at the beam-to-wall interfaces (which may have also delayed the crushing of the beam concrete). In all three tests, the analytical concrete compressive strains do not reach the expected confined concrete crushing strain of ε_{ccu} = 0.030, 0.032, and 0.036 for Tests 2, 3, and 4, respectively.

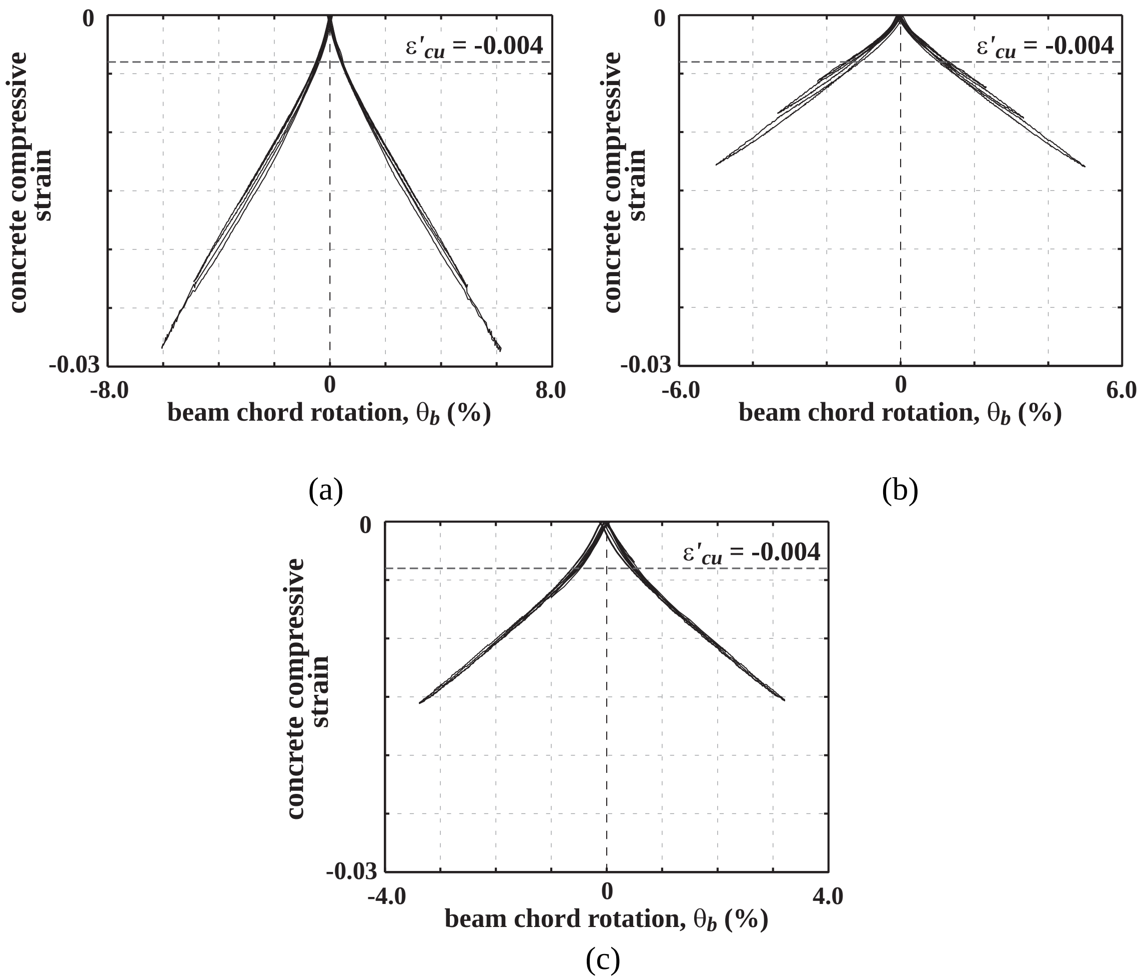

Figure 9.42: Concrete compressive strains at beam end – (a) Test 2; (b) Test 3; (c) Test 4.

9.3.6 Longitudinal Mild Steel Strains at Beam End

This section compares the measured and predicted results for the average strains in the longitudinal legs of the No. 6 looping mild steel reinforcement at the south end of each beam near the critical angle-to-beam connection. As illustrated in Figure 9.43, the measured average strains for each test were determined at two locations: (1) average strain at 5.75 in. (146 mm) from the beam end (e.g., gauges 6(1)T-E and 6(1)T-W); and (2) average strain at 11.50 in. (292 mm) from the beam end (e.g., gauges 6(2)T-E and

6(2)T-W). The average strains were calculated separately for the top and bottom longitudinal legs of the No. 6 looping reinforcing bars. Strain gauges with no reliable data were excluded from the averaging process, in which case, a direct comparison was made with a single strain gauge measurement.

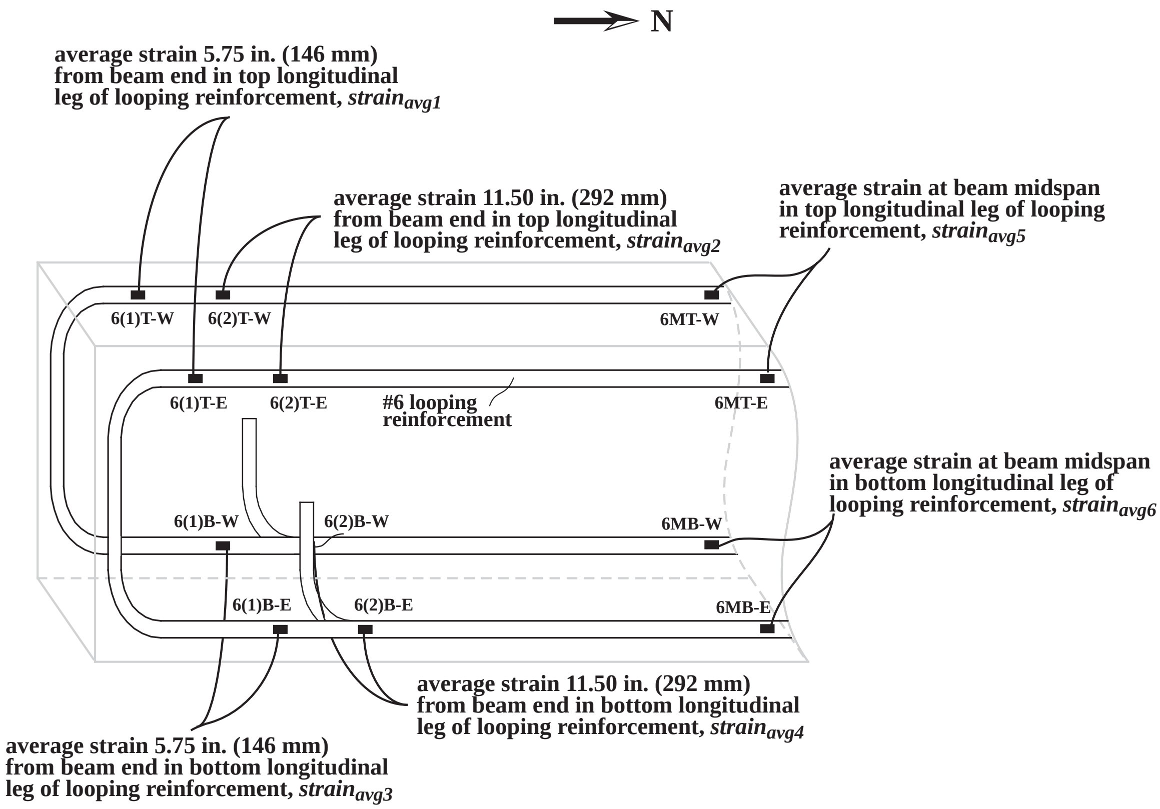

Figure 9.43: Measured average strain calculations.

In the DRAIN-2DX models, fiber element slices were placed at the same locations as the strain gauges, thus enabling strain predictions to be made from the slice deformations (Figure 9.44). Comparisons between the measured (left) and predicted (right) average strains for Tests 2, 3, 3B, 4, 4A and 4B are given in Figures 9.45 – 9.55, respectively. It can be seen that while there are general similarities between the measured and predicted average strains, various levels of discrepancies, some very significant, exist in the comparisons for each test specimen. The sources of these discrepancies, which tend to be larger for the tensile strains, are unknown and could include modeling inaccuracies as well as experimental difficulties such as loss of bond between the steel bar and the surrounding concrete. It is further noted that the initial (i.e., before the application of lateral loads) strain values are different for the measured and predicted strains causing some of the differences in the comparisons. As described in Chapter 7, the initial strain readings for the non-virgin beam specimens were especially affected by the residual strains from the previous test(s). It was not possible to include these residual strains in the analytical models.

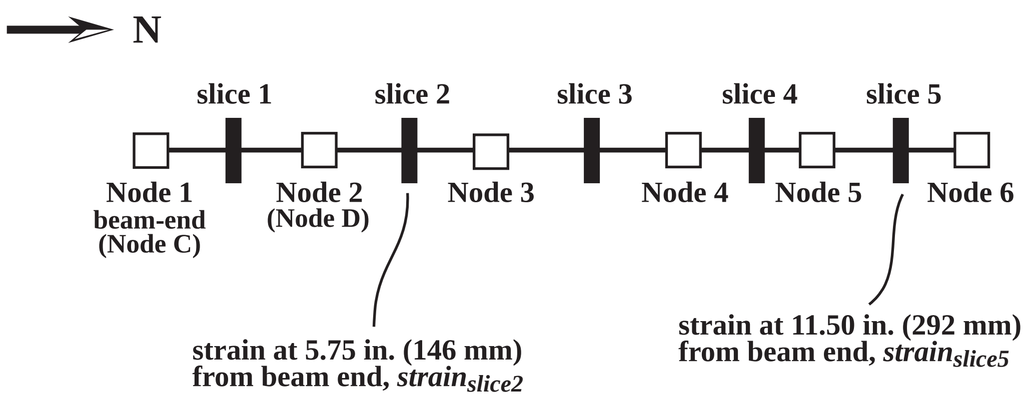

Figure 9.44: Fiber element slice locations used in strain predictions.

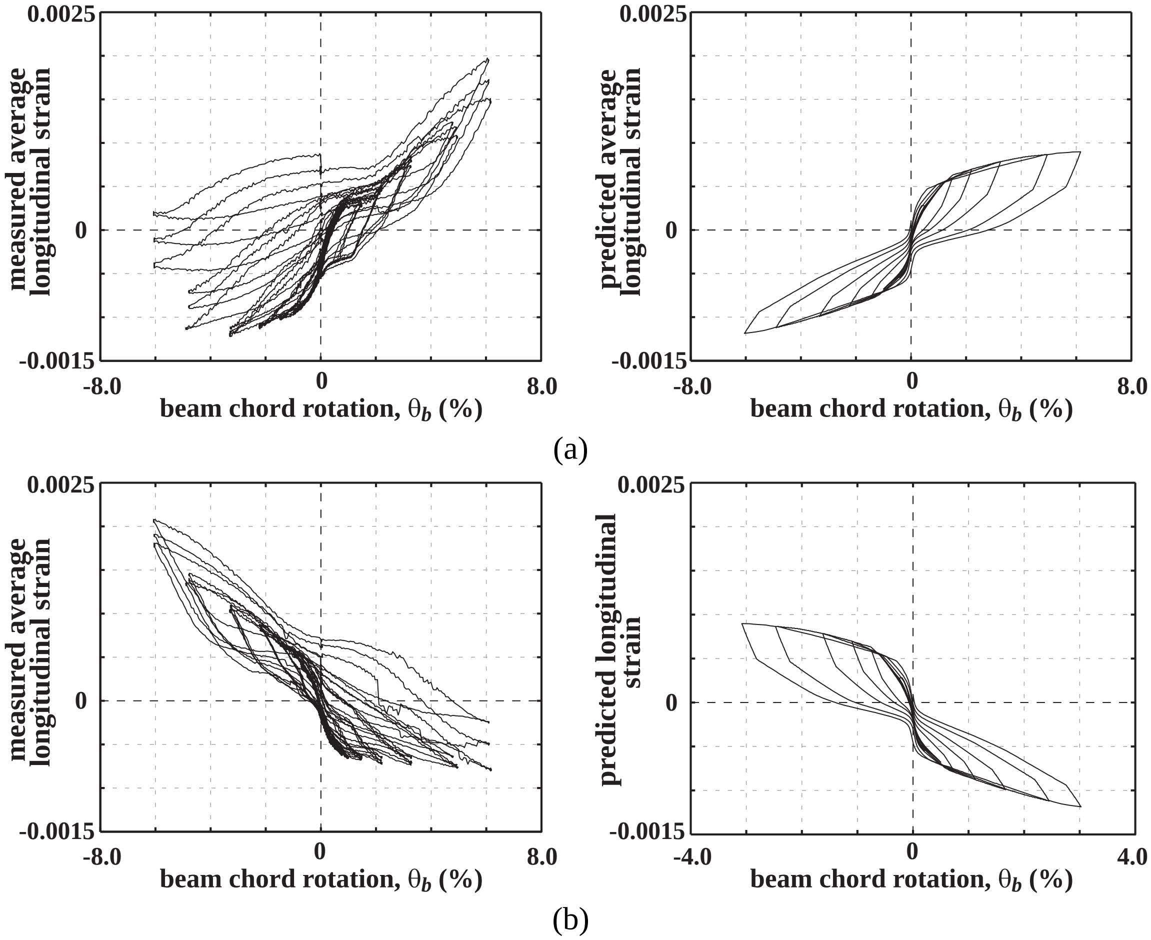

Figure 9.45: Experimental versus analytical beam end longitudinal reinforcement strains for Test 2 at 5.75 in. (146 mm) – (a) top leg; (b) bottom leg.

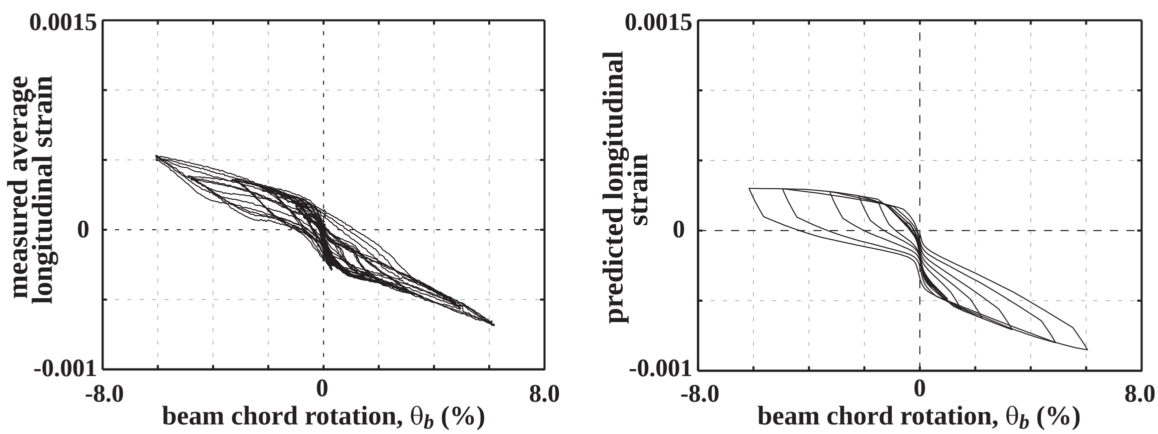

Figure 9.46: Experimental versus analytical beam end longitudinal reinforcement strains at 11.50 in. (292 mm) for Test 2 – bottom leg.

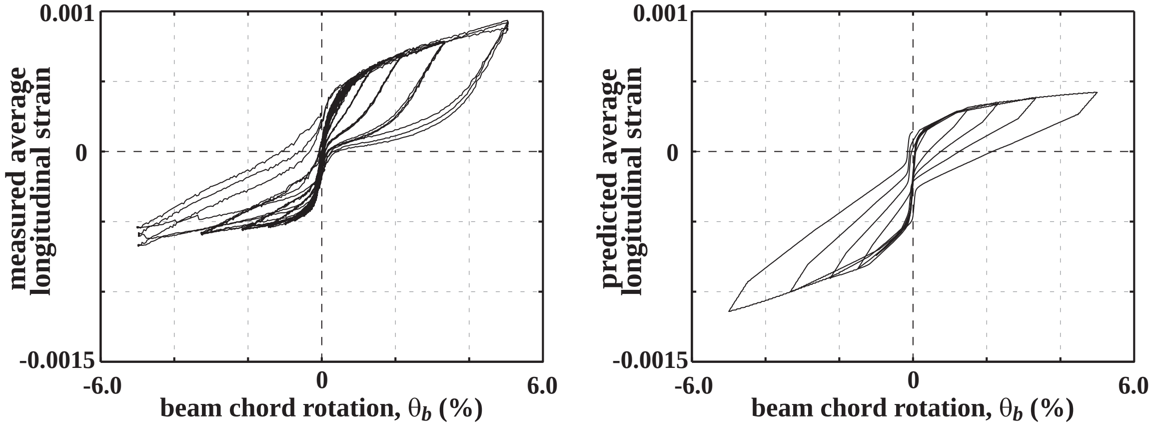

(a)

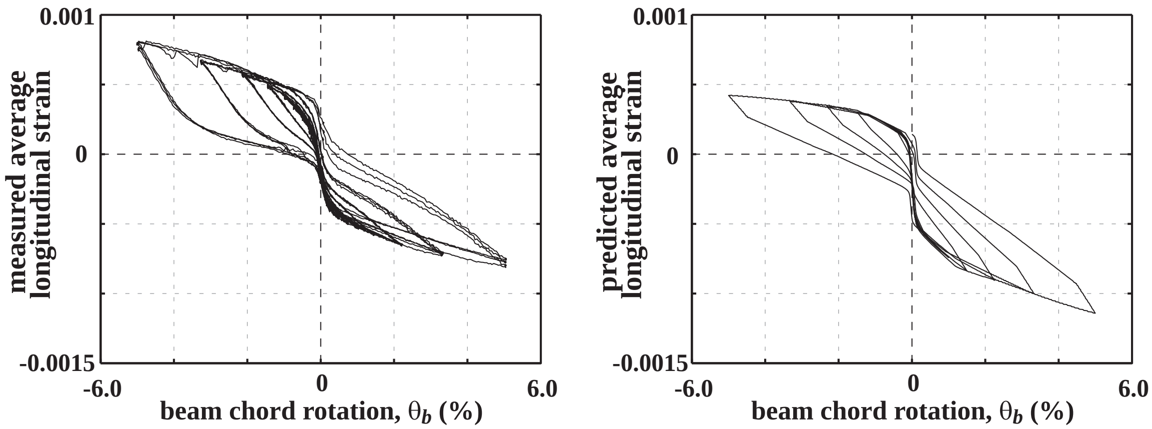

(b)

Figure 9.47: Experimental versus analytical beam end longitudinal reinforcement strains at 5.75 in. (146 mm) for Test 3 – (a) top leg; (b) bottom leg.

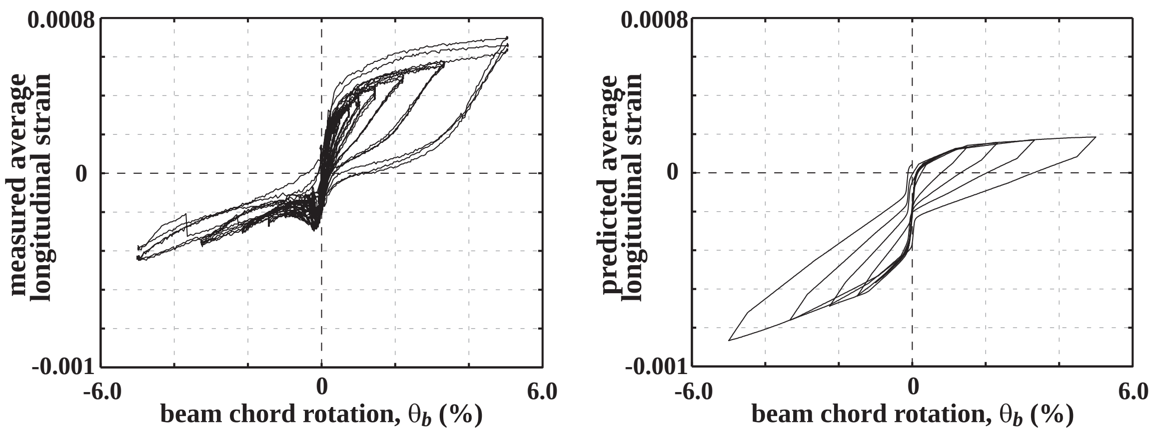

Figure 9.48: Experimental versus analytical beam end longitudinal reinforcement strains at 11.50 in. (292 mm) for Test 3 – top leg.

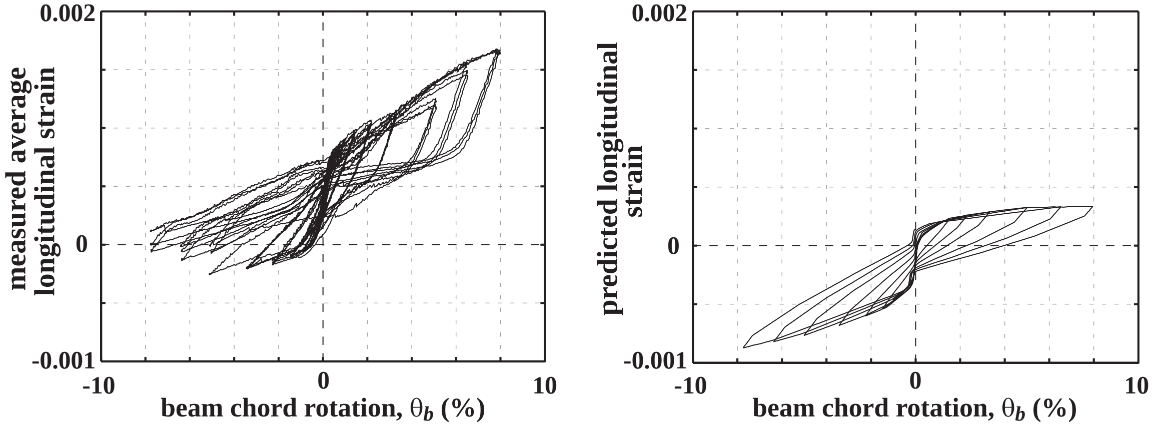

(a)

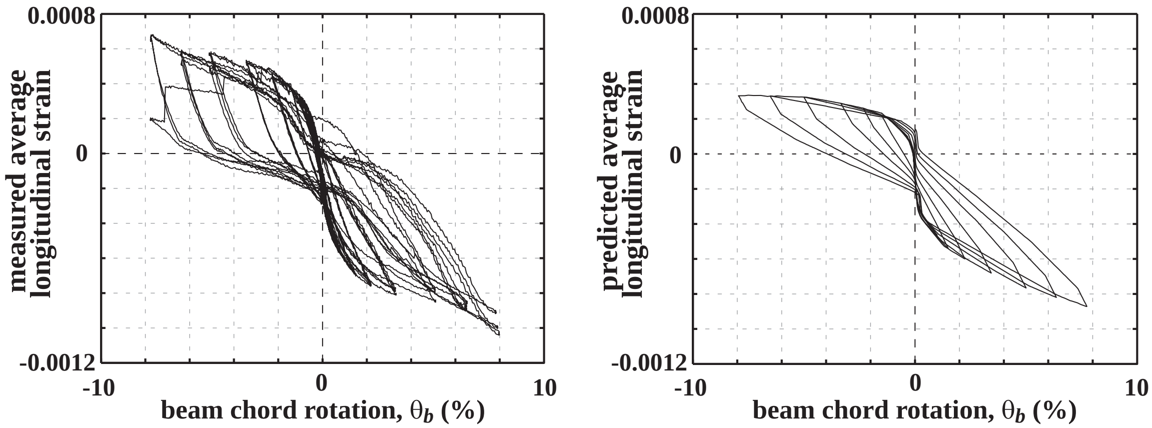

(b)

Figure 9.49: Experimental versus analytical beam end longitudinal reinforcement strains at 5.75 in. (146 mm) for Test 3B – (a) top leg; (b) bottom leg.

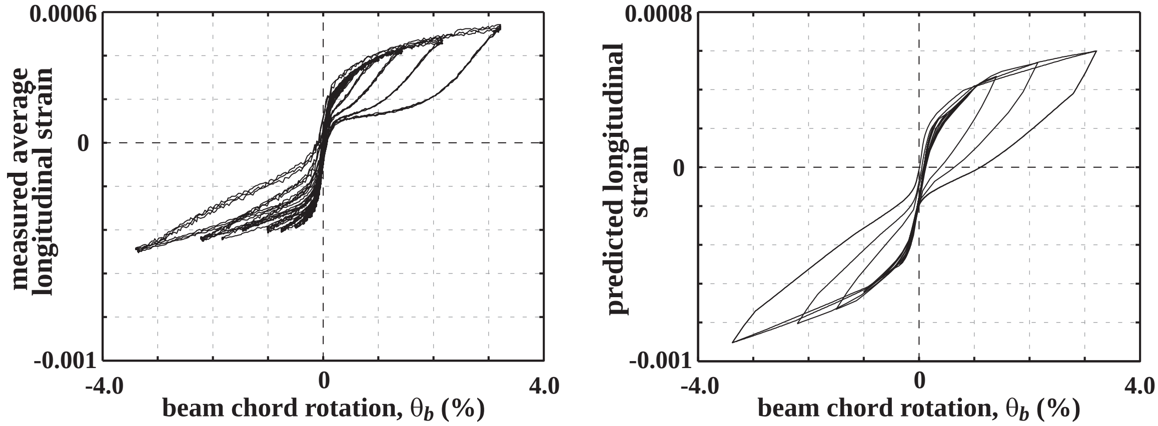

(a)

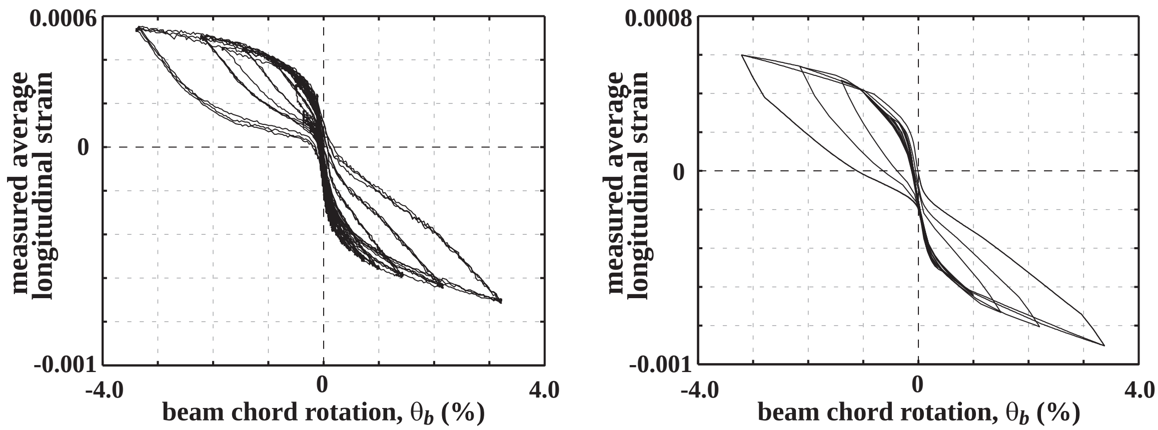

(b)

Figure 9.50: Experimental versus analytical beam end longitudinal reinforcement strains at 5.75 in. (146 mm) for Test 4 – (a) top leg; (b) bottom leg.

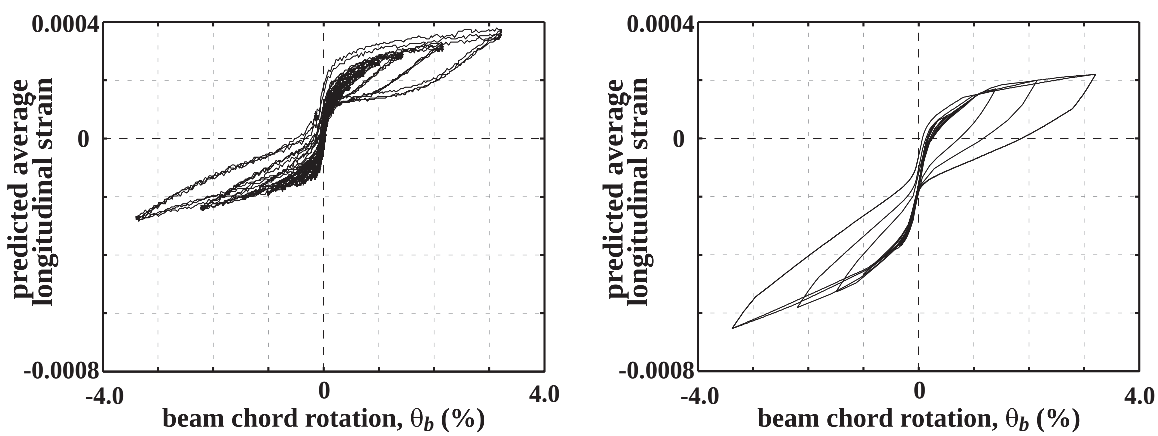

Figure 9.51: Experimental versus analytical beam end longitudinal reinforcement strains at 11.50 in. (292 mm) for Test 4 – top leg.

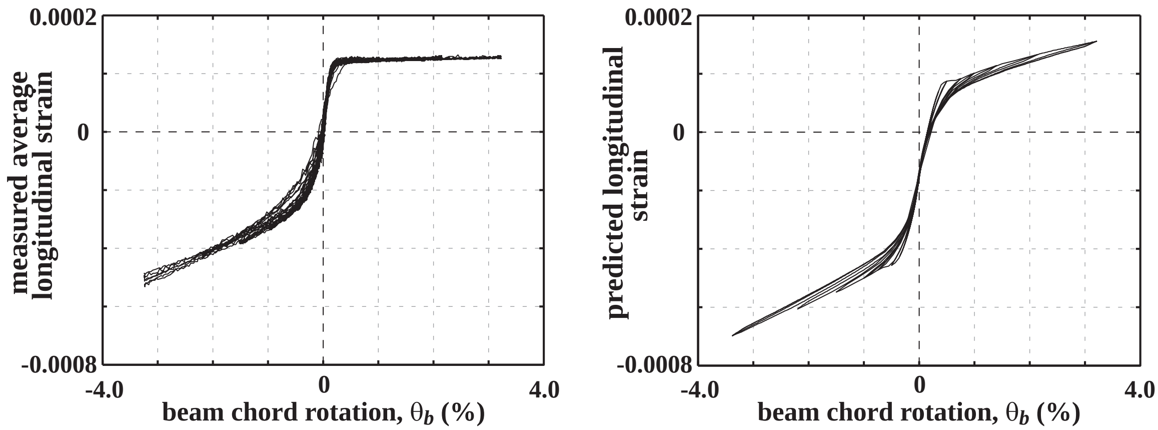

(a)

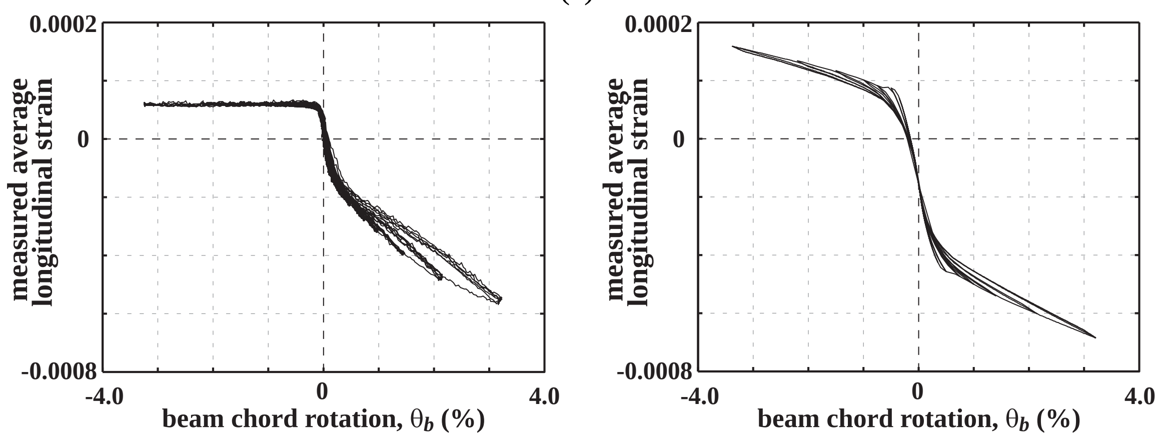

(b)

Figure 9.52: Experimental versus analytical beam end longitudinal reinforcement strains at 5.75 in. (146 mm) for Test 4A – (a) top leg; (b) bottom leg.

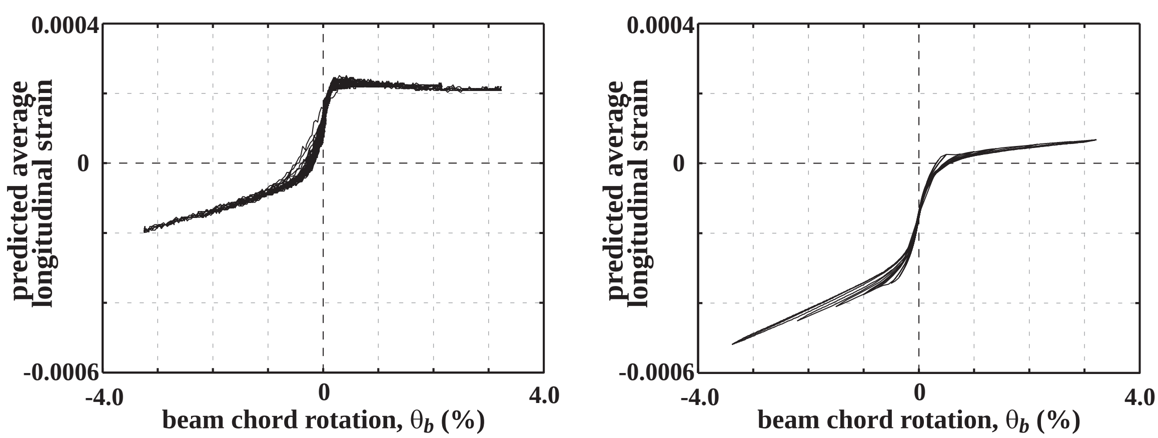

Figure 9.53: Experimental versus analytical beam end longitudinal reinforcement strains at 11.50 in. (292 mm) for Test 4A – top leg.

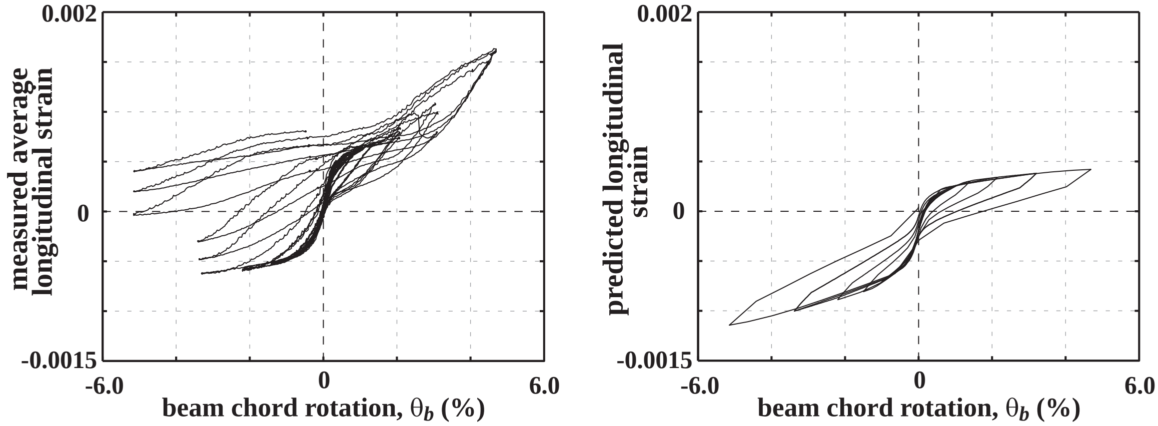

(a)

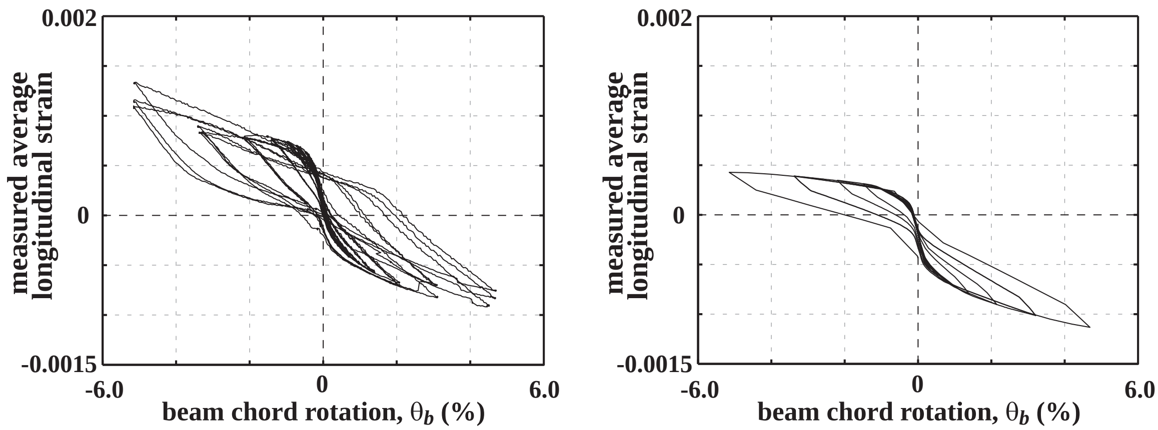

(b)

Figure 9.54: Experimental versus analytical beam end longitudinal reinforcement strains at 5.75 in. (146 mm) for Test 4B – (a) top leg; (b) bottom leg.

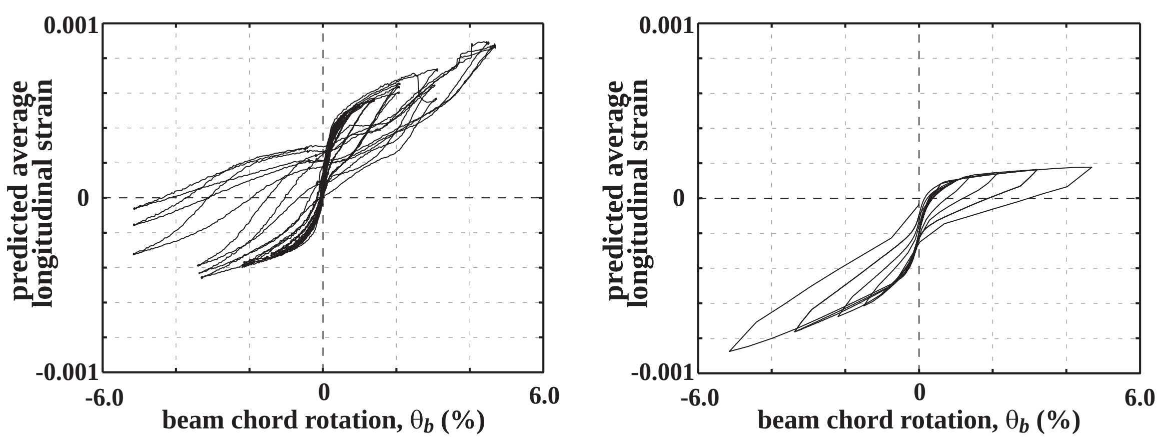

Figure 9.55: Experimental versus analytical beam end longitudinal reinforcement strains at 11.50 in. (292 mm) for Test 4B – top leg.

9.3.7 Longitudinal Mild Steel Strains at Beam Midspan

This section compares the measured (from gauges SG6MT-E, SG6MT-W, SG6MB-E, and SG6MB-W) and predicted results for the strains in the top and bottom longitudinal legs of the No. 6 looping mild steel reinforcement at the midspan of each beam. When reliable strain measurements were available from the east and west legs of the longitudinal reinforcement, then, these measurements were averaged. If only one strain measurement was available, a direct comparison between the measured and predicted strains was made. The strain measurements for the top and bottom legs of the reinforcement were kept separate.

Comparisons between the measured (left) and predicted (right) average strains for Tests 2, 3, 3B, 4, 4A and 4B are given in Figures 9.56 – 9.61, respectively. It can be seen that while discrepancies exist, the general trends between the measured and predicted strains are in reasonable agreement, especially considering that the strains are relatively small. Similar to the beam end strains described in the previous section, the initial measured and predicted strains are different, causing a significant portion of the discrepancy in some of the cases.

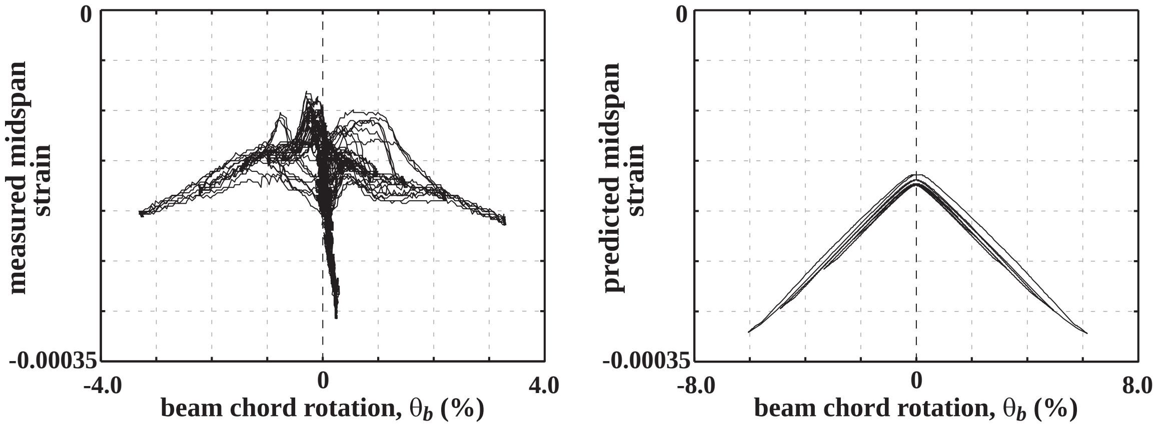

Figure 9.56: Experimental versus analytical longitudinal reinforcement strains at beam midspan for Test 2 – bottom leg.

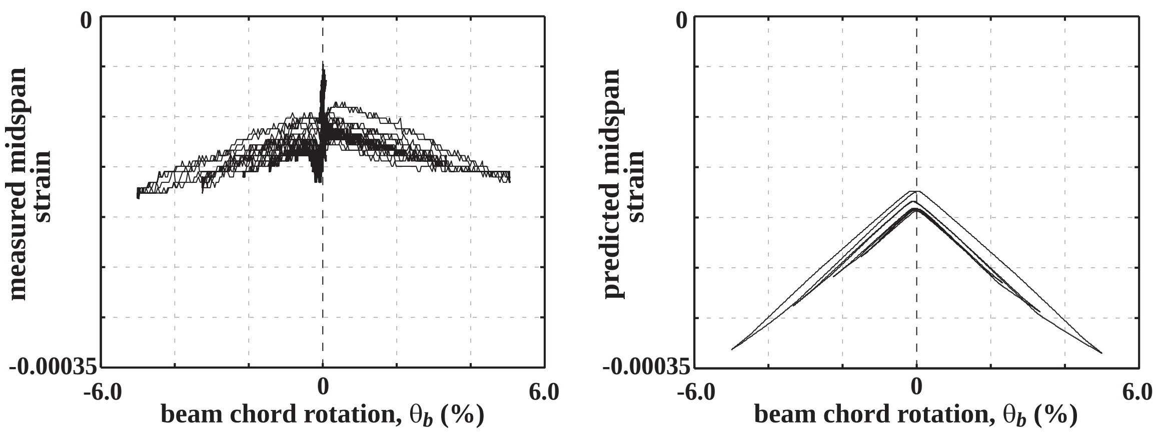

Figure 9.57: Experimental versus analytical longitudinal reinforcement strains at beam midspan for Test 3 – top leg.

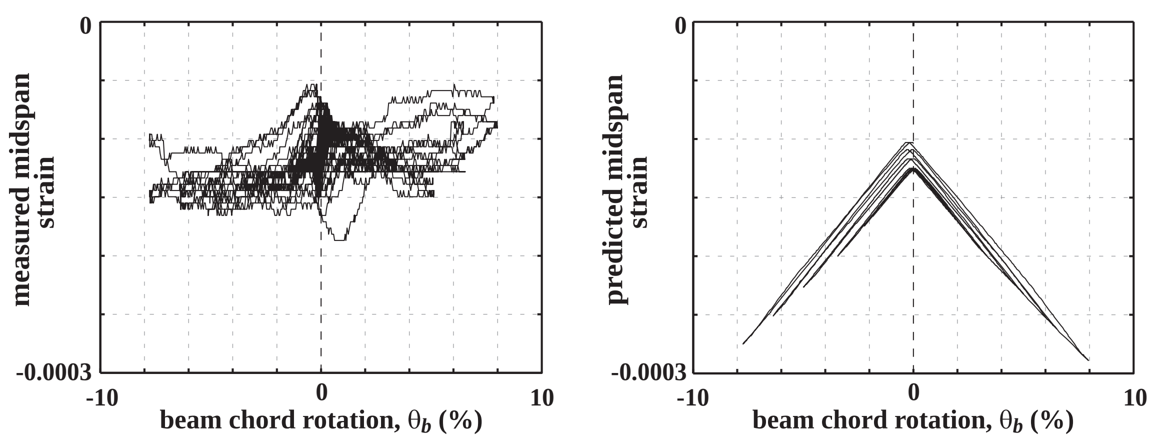

Figure 9.58: Experimental versus analytical longitudinal reinforcement strains at beam midspan for Test 3B – top leg.

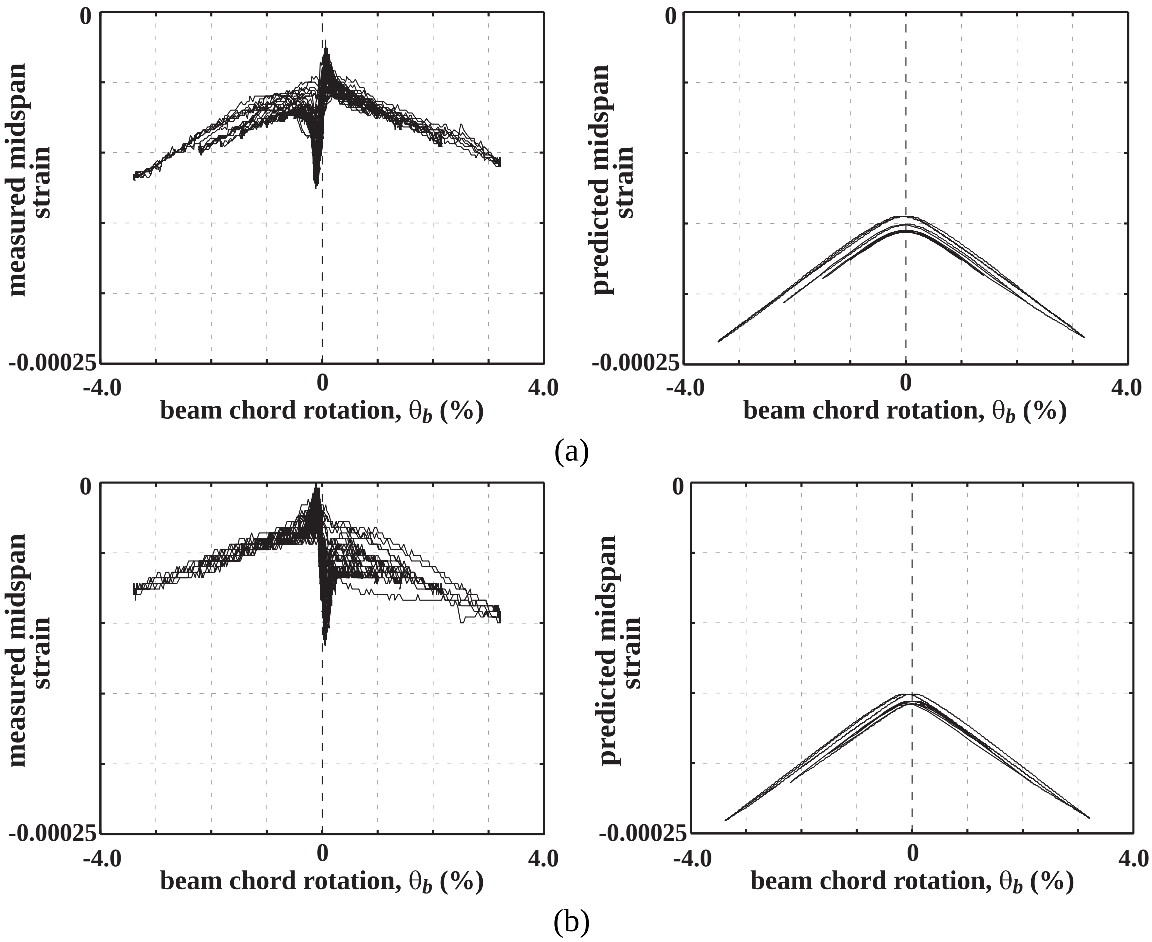

Figure 9.59: Experimental versus analytical longitudinal reinforcement strains at beam midspan for Test 4 – (a) top leg; (b) bottom leg.

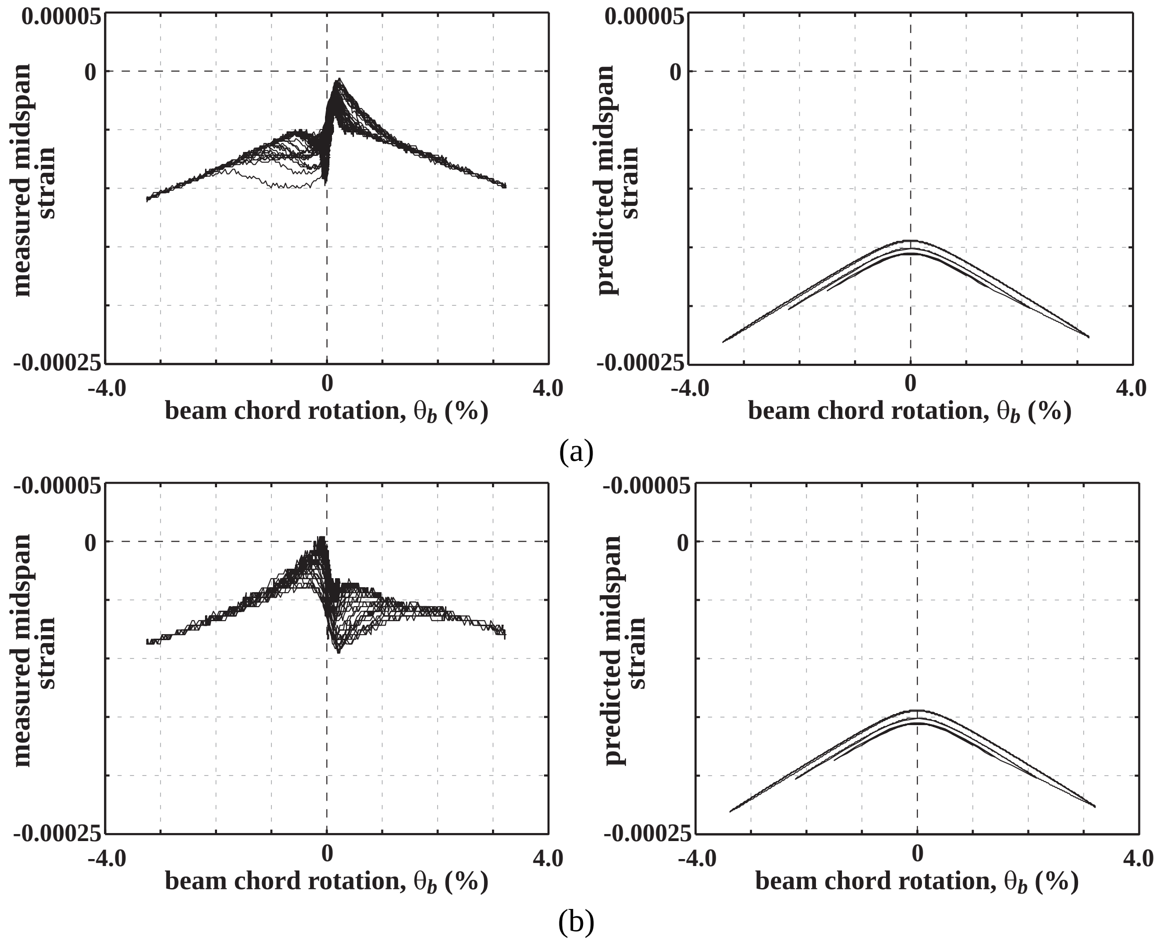

Figure 9.60: Experimental versus analytical longitudinal reinforcement strains at beam midspan for Test 4A – (a) top leg; (b) bottom leg.

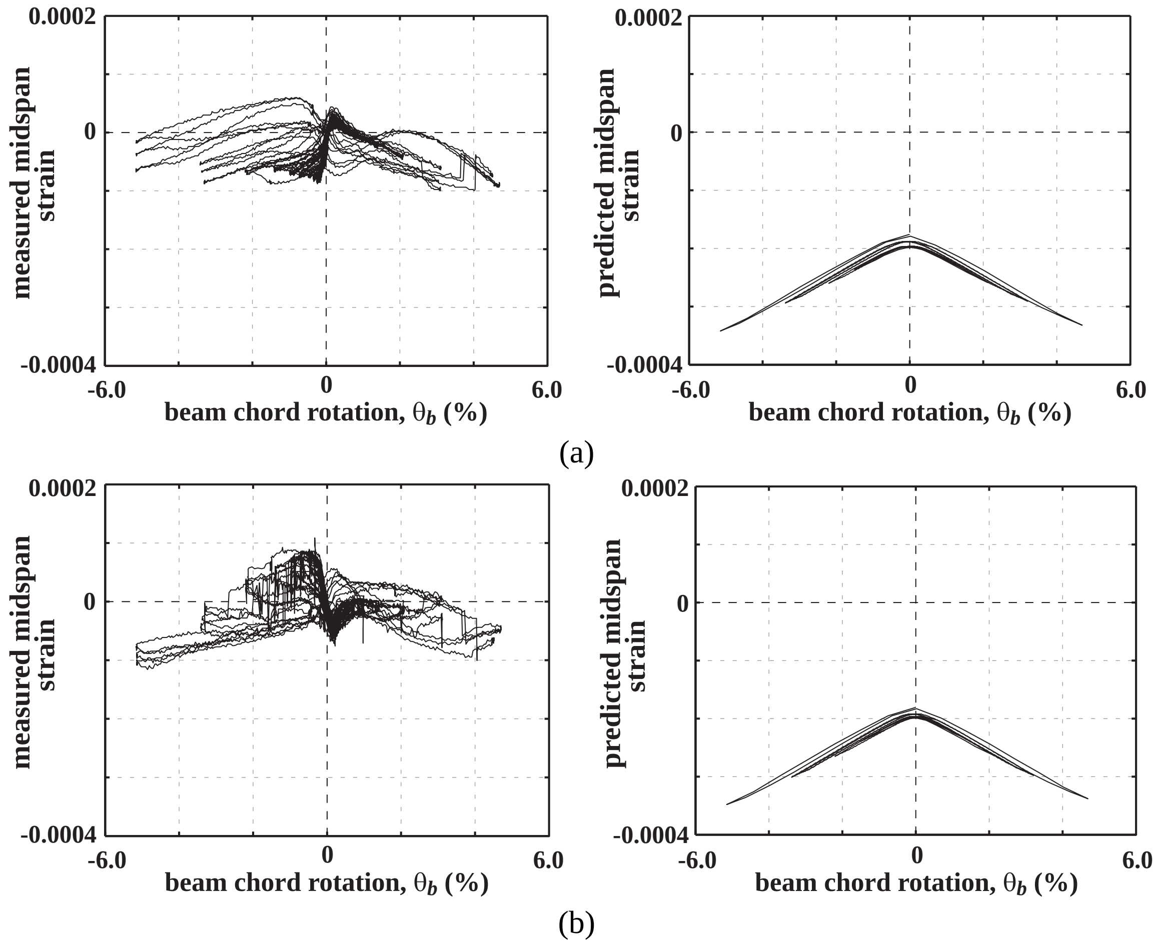

Figure 9.61: Experimental versus analytical longitudinal reinforcement strains at beam midspan for Test 4B – (a) top leg; (b) bottom leg.

9.3.8 Angle Behavior

As described in Chapters 6 and 7, the only significant difference between Tests 4 and 4A is the use of four top and seat steel angles at the beam ends. Figure 9.62 compares the last cycles of the coupling beam shear force versus chord rotation behaviors from the measured (left) and analytical (right) results for Tests 4 and 4A. As shown in Figure 9.63, the contribution of the top and seat angles to the behavior of the subassembly during this cycle can be determined by subtracting the coupling beam shear force of Test 4A from that of Test 4. The results indicate that the model captures the measured trends reasonably well; however, the predicted angle contribution is larger than the measured contribution. The overestimation of the angle forces in the analytical model may be due to an over-estimation of the tension angle displacements, which are affected (reduced) by the cracking of the concrete at the beam ends as well as by the loosening of the angle-to-beam connection bolts. As described earlier in this chapter, cracking of the beam concrete is not included in the analytical model.

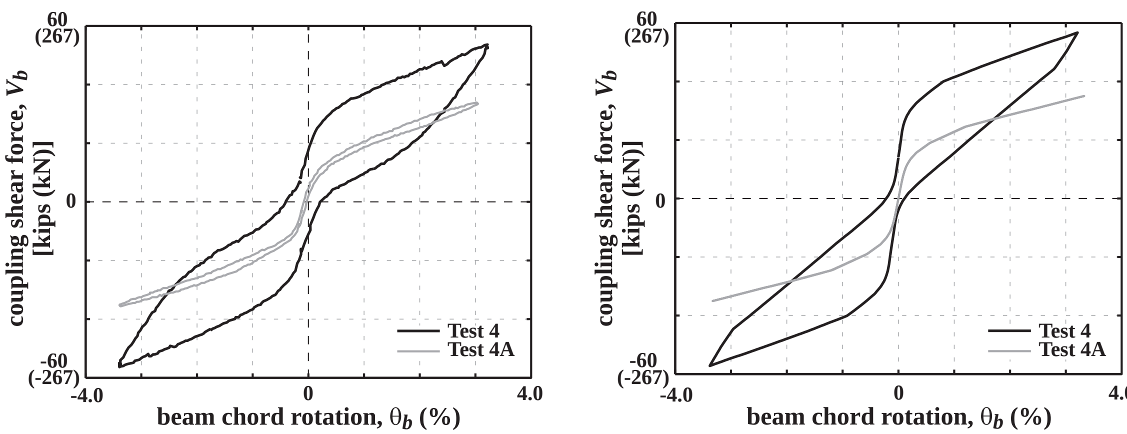

Figure 9.62: Comparison of last V_b-θ_b cycles from Tests 4 and 4A.

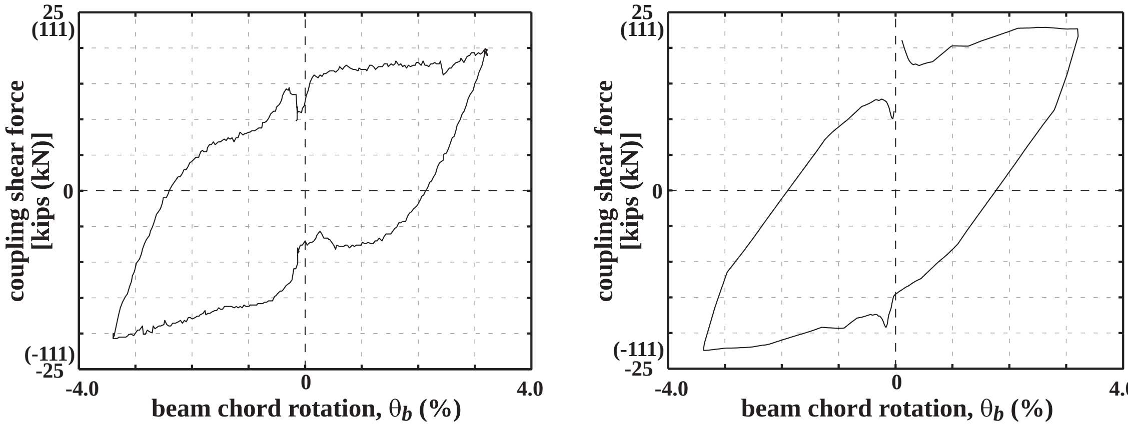

Figure 9.63: Difference between last V_b-θ_b cycles from Tests 4 and 4A.

9.4 ABAQUS Finite-Element Subassembly Model

A finite element model of the coupled wall subassembly was constructed using the ABAQUS Program (Hibbitt *et al.* 2001). This model served the following purposes: (1) verification of the DRAIN-2DX fiber-element model prior to the experimental test results; and (2) assessment of the stress distributions inside the coupling beam and the beam-to-wall contact regions.

As shown in Figure 9.64, the finite element model uses two-dimensional nonlinear rectangular plane stress elements to represent the wall regions and the coupling beam, truss elements to represent the unbonded post-tensioning tendon, and gap/contact surfaces to represent the gap behavior at the beam-to-wall interfaces. Note that the finite element model was constructed using full-scale dimensions of the structure (unlike the half-scale test specimens). A coupling beam with an increased depth (as compared with the prototype beam) of h_b = 36 in. (914 mm) and post-tensioning tendon area of A_{bp} = 3.47 in.^{2} (2240 mm^2) [sixteen 0.6 in. (15 mm) diameter strands] was used to result in larger bending and shear stresses in the structure. More information on the full-scale prototype structure can be found in Chapter 10.

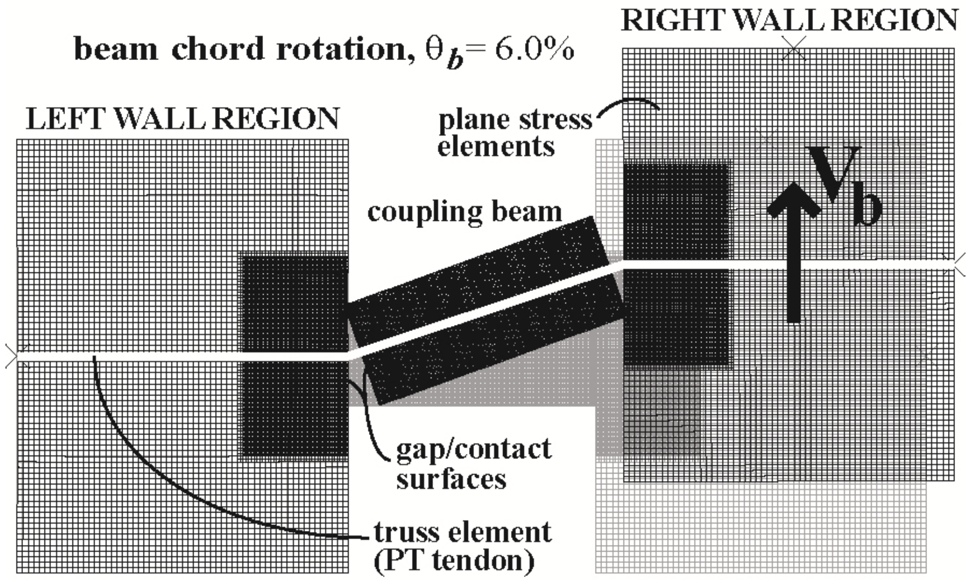

Figure 9.64: ABAQUS finite-element model.

The top and seat angles were not included in the finite-element model because of the difficulties in accurately representing the behavior of the angles, in particular the boundary conditions adjacent to the angle legs, prying, friction, slip, and interaction between the angles, bolts, and nuts (Sims 2000). Similar to the fiber-element model, the finite-element model assumes that:

(1) The beam is designed not to slip at the ends. Based on this assumption, adequate friction is provided to prevent slip at the beam-to-wall interfaces of the model.

(2) The bonded mild steel reinforcement used in the structure does not yield. Based on this assumption, significant tensile deformations are limited to the gap opening at the beam ends, and, the concrete is assumed to be linear elastic in tension. This allows great simplifications in the finite-element model, similar to the fiber-element model, since there is no need to model the mild steel.

(3) The post-tensioning tendon anchors are properly designed for the maximum post-tensioning forces. Based on this assumption, the post-tensioning anchors are modeled using rigid elements that share nodes with elements modeling the wall piers. Kinking of the post-tensioning tendon is modeled by constraining the vertical displacements of the tendon nodes at the beam-to-wall interfaces.

Since the subassembly deformations are concentrated in the beam-to-wall contact regions, a finer finite element mesh is used in these regions. The effect of the confinement steel is represented by using a confined concrete compressive stress-strain relationship in the plane stress elements for the confined regions of the walls and the coupling beam. As an example, the solid and dashed lines in Figure 9.65 show the smooth and idealized, respectively, multi-linear confined concrete compressive stress-strain relationships for the prototype subassembly (described in Chapter 10), as determined based on Mander *et al.* (1988). This multi-linear relationship was successfully used in the fiber-element model; however, numerical problems occurred in the ABAQUS model. The convergence problem was overcome by using a modified concrete stress-strain relationship as shown by the dotted line in Figure 9.65, which assumes that the compressive strength, f'_{cc} is reached at the crushing strain, ε_{ccu}. To prevent similar numerical problems due to the crushing of the cover concrete, the modified stress-strain relationship in Figure 9.65 was also used for the cover concrete. Due to the redistribution of nonlinear concrete stresses over the contact area, the approximations made in the modeling of the cover and confined concrete in compression are not expected to have a large effect on the finite-element analysis results.

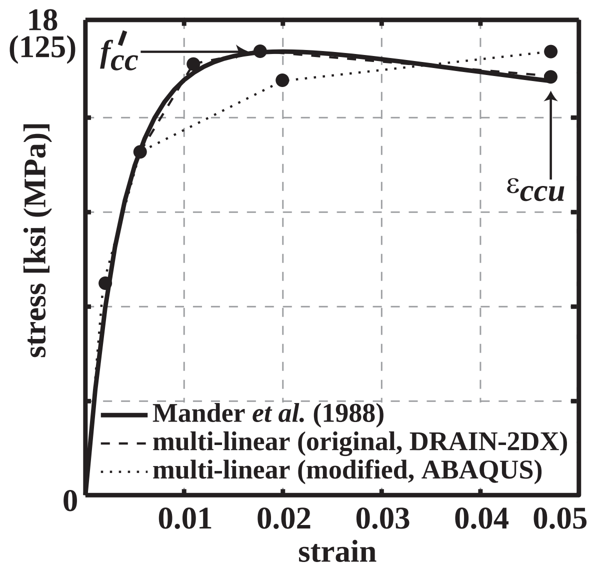

Figure 9.65: Confined concrete compressive stress-strain model.

9.5 Comparison of Fiber-Element and Finite-Element Models

Figure 9.66(a) compares the coupling beam shear force versus chord rotation plots from the fiber-element and finite-element models. The corresponding comparison plots for the contact depth (normalized with respect to the beam depth, h_b) at the beam-to-wall interfaces are shown in Figure 9.66(b). Note that the top and seat angles are excluded from the fiber-element model used in these comparisons since the finite-element model does not include the angles. Based on the results, it is concluded that both the fiber-element and the finite-element models are capable of capturing the primary response characteristics (e.g., lateral strength, stiffness, gap opening/contact behavior) of unbonded post-tensioned precast concrete coupling beam subassemblies. The fiber-element model was used to conduct the parametric analyses described in Chapter 10 because of its relative simplicity, including the modeling of the angles.

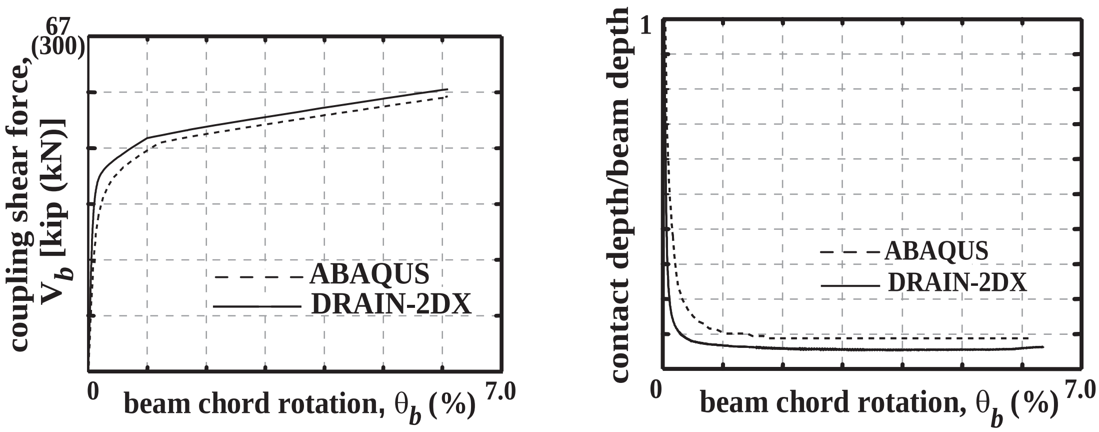

(a) (b)

Figure 9.66: Comparisons between fiber-element and finite-element model results – (a) coupling shear force versus chord rotation; (b) beam-to-wall contact depth.

9.5.1 Wall Pier and Coupling Beam Stresses

To assess the stress distributions inside the coupling beam and the beam-to-wall contact regions, Figure 9.67(a) shows the principal compression stresses in the left wall pier (due to symmetry, the right wall pier is not shown) and the coupling beam as the subassembly is displaced to a beam chord rotation of θ_b = 6.0%. Figure 9.67(b) shows a close up view of the principal compression stresses in the coupling beam. The regions of the beam and the wall pier with compression stresses larger than the design unconfined concrete strength of f'_c = 6.0 ksi (41.4 MPa) are shaded in red. It can be seen that the compression stresses are concentrated in the contact regions (i.e., the corners of the beam in contact with the wall piers) and spread out into the beam, creating a diagonal compression strut and developing the coupling forces. Similar compression stresses develop in the contact regions of the wall piers, and thus, confinement reinforcement is needed in both the coupling beam and the wall piers. The compression stresses away from the beam-to-wall contact regions are small, and thus, concrete confinement is only needed in the contact regions.

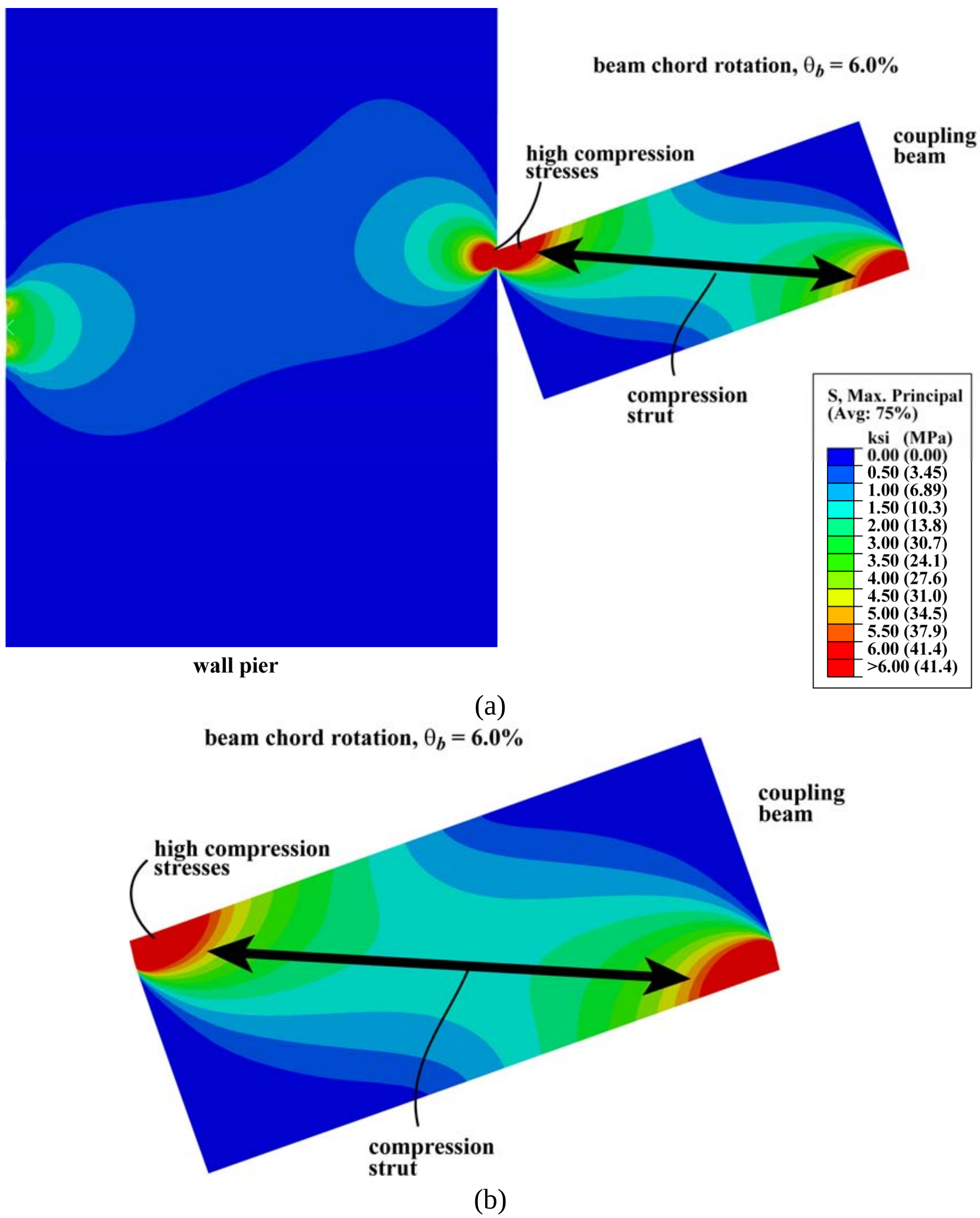

(a)

(b)

Figure 9.67: Principal compression stresses –
(a) wall pier and coupling beam; (b) close up view of coupling beam.

Similarly, Figure 9.68(a) shows the principal tension stresses that develop in the left wall pier and the coupling beam, and Figure 9.68(b) is a close up view of the coupling beam principal tension stresses at a beam chord rotation of θ_b = 6.0%. The red shaded regions [also shown in Figures 9.69(a) and 9.69(b)] depict the regions of the wall pier and the coupling beam where the principal tension stresses exceed the assumed cracking strength [0.581 ksi (4.0 MPa)] of the concrete. The gray shaded regions in Figure 9.69 indicate regions where cracking is not expected to occur. Since concrete is modeled as a linear elastic material in tension, stresses larger than the cracking strength develop in the finite element simulation (i.e., red shaded regions). The magnitudes of these tension stresses are not meaningful; and thus, they are not shown in Figures 9.68 and 9.69. The results demonstrate that, due to the opening of gaps at the beam ends and the development of a large diagonal compression strut, the tensile stresses along the length of the beam remain small under large nonlinear rotations. The most critical tensile regions of the beam are the ends where transverse mild steel reinforcement is needed. Note that, as discussed previously, additional tension stresses would develop at the top and bottom surfaces near the beam ends due to the transfer of the tension angle forces into the beam; however, these stresses are not shown in Figures 9.68 and 9.69 since the angles are not included in the ABAQUS model. Longitudinal mild steel reinforcement is needed to resist the tension stresses in the angle-to-beam connection regions.

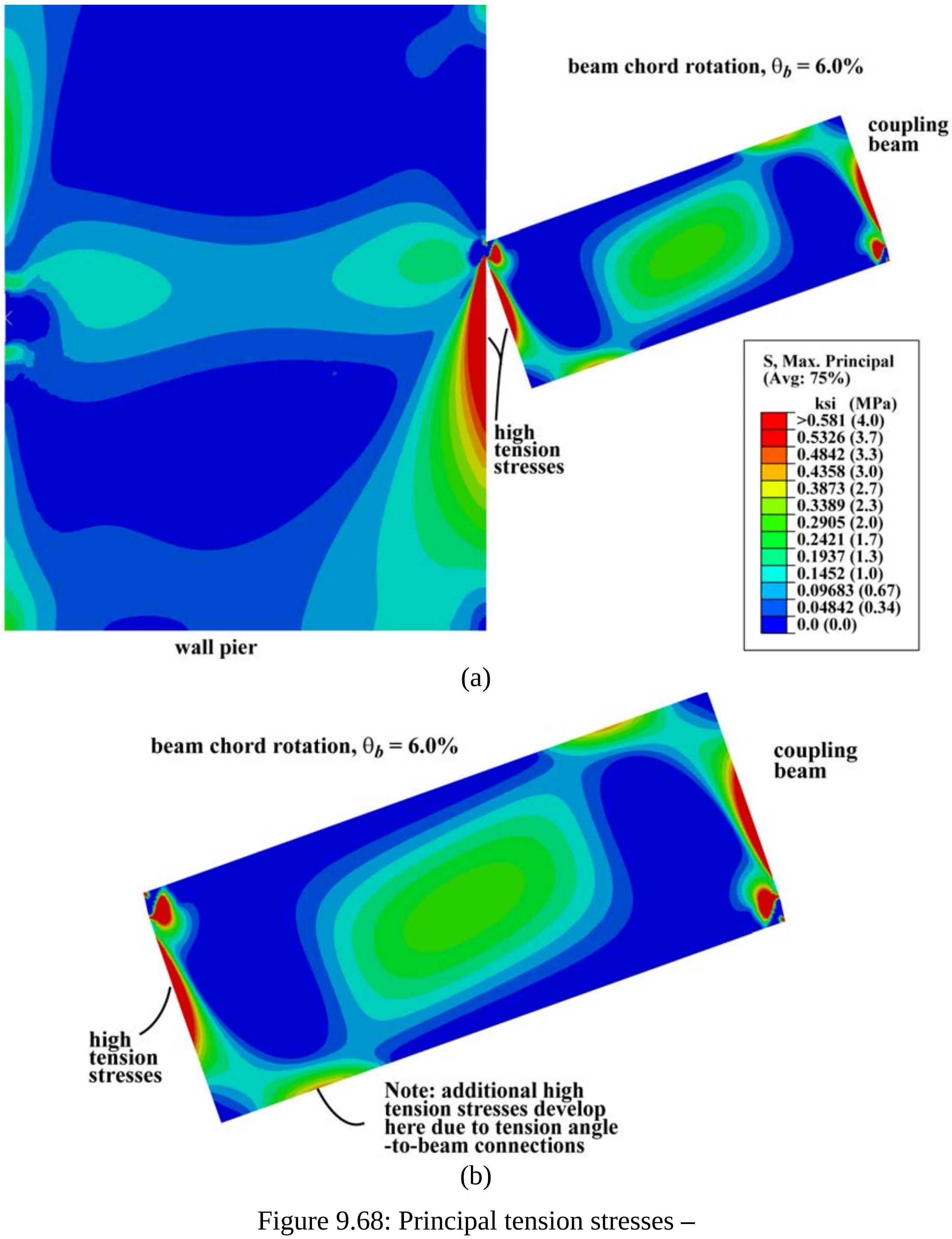

Figure 9.68: Principal tension stresses –
(a) wall pier and coupling beam; (b) close up view of coupling beam.

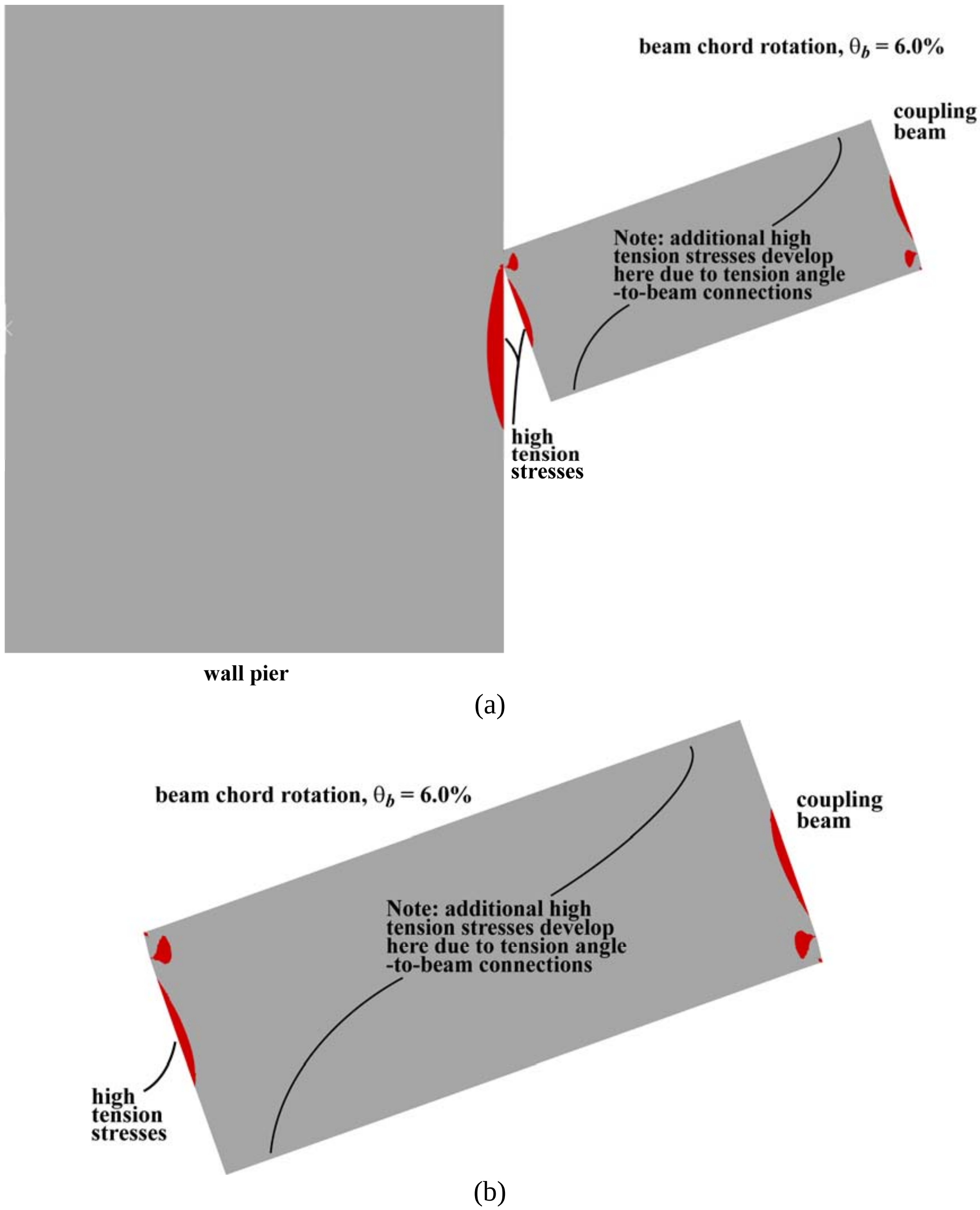

Figure 9.69: Regions where principal tension stresses are greater than assumed concrete cracking stress – (a) wall pier and coupling beam; (b) close up view of coupling beam.

9.6 Chapter Summary

This chapter describes two analytical models, a fiber beam-column element model using DRAIN-2DX and a finite-element model using ABAQUS, for floor-level coupled wall subassemblies with unbonded post-tensioned precast concrete coupling beams. The fiber-element model is verified by comparing the analytical results with experimental measurements for the test specimens described in Chapters 6 – 8. Based on these comparisons, it is concluded that the analytical model is able to capture the nonlinear hysteretic response characteristics of the structure reasonably well. The ABAQUS finite-element model is used for further verification of the fiber-element model as well as for the assessment of the stress distributions inside the coupling beam and the beam-to-wall contact regions.

CHAPTER 10

PARAMETRIC INVESTIGATION AND CLOSED FORM ESTIMATION OF THE BEHAVIOR OF UNBONDED POST-TENSIONED PRECAST COUPLING BEAMS

This chapter presents an analytical parametric investigation on the behavior and design of unbonded post-tensioned precast concrete coupling beams. In addition, a closed form procedure is developed to estimate the nonlinear lateral load versus displacement behavior of the beams under monotonic loading. The chapter is organized as follows: (1) prototype subassembly; (2) analytical modeling; (3) subassembly behavior under monotonic loading; (4) subassembly behavior under cyclic loading; (5) parametric investigation; (6) tri-linear estimation of subassembly behavior; (7) analytical verification of tri-linear estimation; and (8) experimental verification of tri-linear estimation.

10.1 Prototype Subassembly

The parametric analytical investigation in this chapter is based on a full-scale prototype precast concrete coupling beam subassembly as shown in Figure 10.1 and additional subassemblies obtained by varying the structural properties (e.g., beam depth, wall length, etc.) of the prototype subassembly. The prototype subassembly was designed to have a lateral strength that is similar to the strength of the unbonded post-tensioned steel coupling beam subassemblies investigated by Shen and Kurama (2002), Kurama and Shen (2004), and Shen *et al.* (2006). The structure has a wall pier length of l_w = 120 in. (3048 mm), uniform wall thickness of t_w = 15 in. (381 mm), beam width of b_b = 15 in. (381 mm), beam depth of h_b = 28 in. (711 mm), and beam length of l_b = 90 in. (2286 mm), resulting in a beam length to depth aspect ratio of 3.21. The beam dimensions were chosen to meet typical beam length to depth aspect ratios in coupled wall structures in the U.S.

Four L8x8x3/4 top and seat angles are used at the beam-to-wall interfaces of the full-scale subassembly, each with a length equal to the beam width of 15 in. (381 mm). The angle-to-wall connection gage length (i.e., the length from the heel of the angle to the center of the innermost angle-to-wall connectors) is l_{gv} = 5.0 in. (127 mm). The yield strength for the angle steel is taken as f_{ay} = 47 ksi (327 MPa). The design strength of unconfined concrete is f'_c = 6.0 ksi (41.4 MPa), with an assumed ultimate strain at crushing of ε_{cu} = 0.003. Closed hoops with cross-ties [No. 4 bars at 1.5 in. (38 mm) spacing] are used in the beam-to-wall contact regions to confine the concrete. The yield strength of the confinement steel is assumed as f_{hy} = 60 ksi (414 MPa). The strength of the beam confined concrete, estimated based on Mander *et al*. (1988), is equal to f'_{cc} = 16.8 ksi (116 MPa) with an ultimate strain of ε_{ccu} = 0.047.

The beam post-tensioning force of the full-scale structure is applied using a single tendon consisting of twelve 0.6 in. (15 mm) diameter high-strength strands with a total area of A_{bp} = 2.6 in.^{2} (1680 mm^2). The strands are post-tensioned to an initial stress of f_{bpi} = 0.50f_{bpu}, where f_{bpu} = 270 ksi (1862 MPa) is the design ultimate strength of the strands. The assumed design yield strength of the post-tensioning steel is f_{bpy} = 245 ksi (1689

MPa). The initial axial stress in the coupling beam (not excluding the post-tensioning duct area) due to the post-tensioning force is f_{bi} = 0.84 ksi (5.77 MPa) (equal to $0.14f'_c$).

Note that the overall dimensions of the test Specimens 1, 2, and 3 described in Chapter 3 are half-scale models of this full-scale prototype structure. Specimen 2 also provides a half-scale representation of the structure with respect to the tension strength of the top and seat angles and the initial beam post-tensioning tendon force (and initial beam concrete axial stress). However, due to the premature wire fractures of the post-tensioning strands in Test 1, the initial post-tensioning tendon force in Test 2 was achieved using an increased tendon area [four post-tensioning strands, A_{bp} = 0.868 in.^{2} (560 mm^2)] with lower initial stress ($f_{bpi} = 0.36 f_{bpu}$) rather than the half-scale tendon area [three strands, A_{bp} = 0.651 in.^{2} (420 mm^2)] at the design initial stress of $f_{bpi} = 0.50f_{bpu}$. These modifications are described in more detail in Chapter 6.

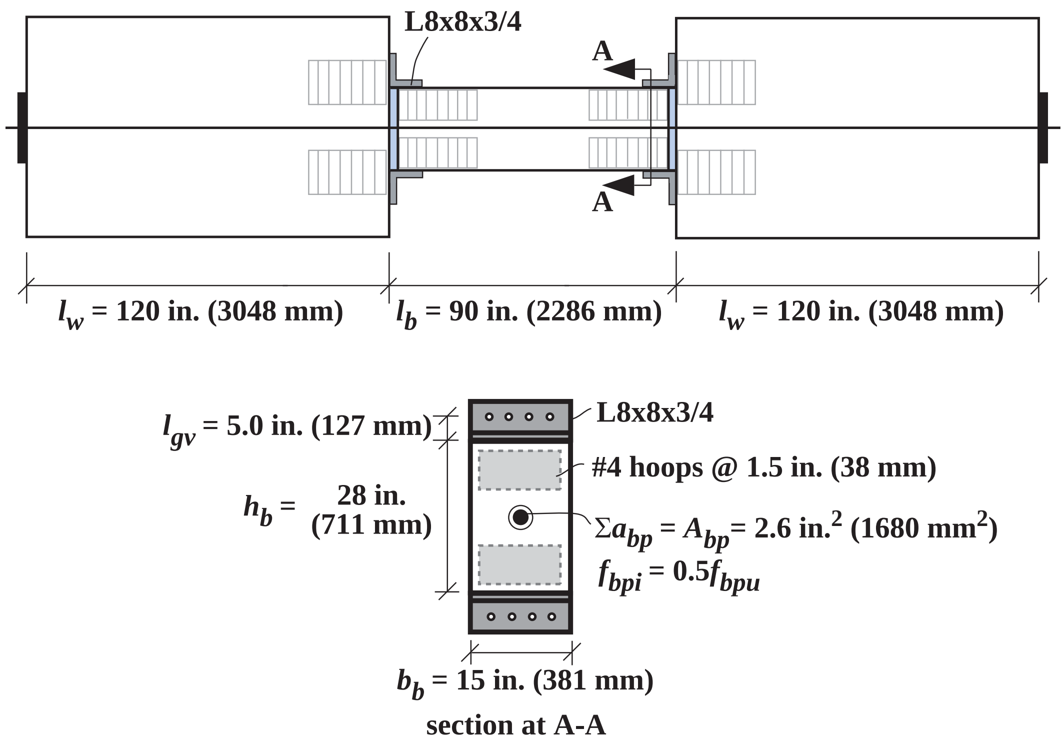

Figure 10.1: Full-scale prototype subassembly.

10.2 Analytical Modeling

The analytical modeling (see Figure 10.2) of the structures in the parametric investigation is done based on the DRAIN-2DX fiber element model in Chapter 9, except that the angles are modeled exactly as described in Shen *et al*. (2006), as shown in Figure 10.3, without the modifications in Chapter 9. Furthermore, it is assumed that the post-tensioning tendon duct is not oversized, and thus, the tendon Nodes I and J are kinematically constrained to corresponding wall pier nodes (i.e., Nodes B and G, respectively) in the vertical direction, without any gap/contact elements. Note again that the objective of the analytical model is to investigate the in-plane behavior of isolated coupling beam subassemblies under lateral loads. The gravity loads supported by the beam are not modeled and the out-of-plane behavior of the subassembly is not considered. The presence of a slab may affect the behavior of the beam; however, this is not investigated.

Similar to the analyses of the test specimens in Chapter 9, the left wall region of the model is fixed at Node B (ignoring the deformations in the wall-height elements, which are small), and the right wall region at Node G is allowed to translate in the horizontal and vertical directions, but not allowed to rotate. A vertical force *V* is applied at Node G in displacement control.

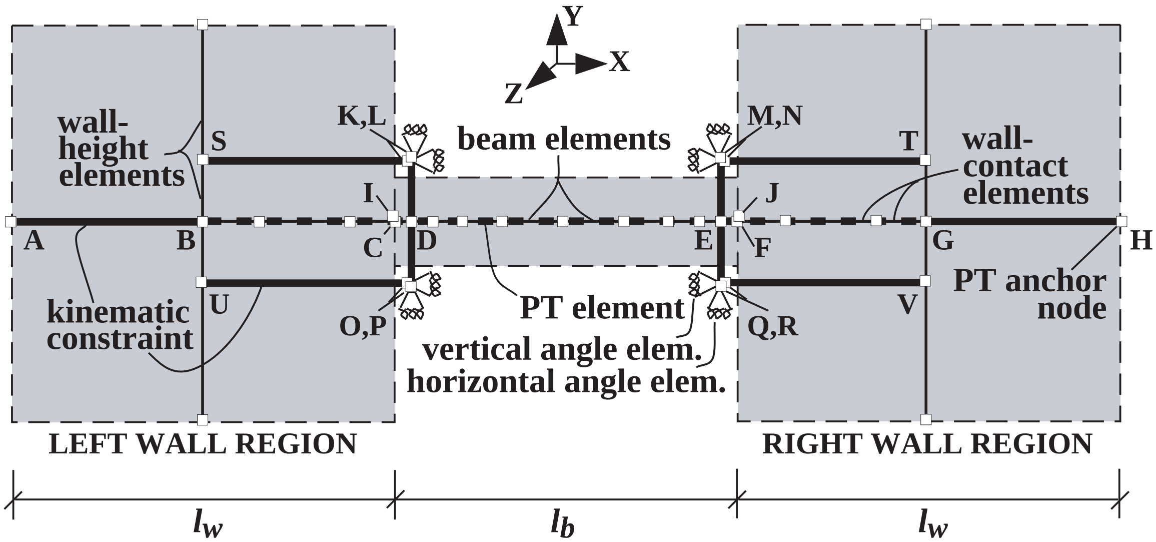

Figure 10.2: Subassembly analytical model used in the parametric investigation.

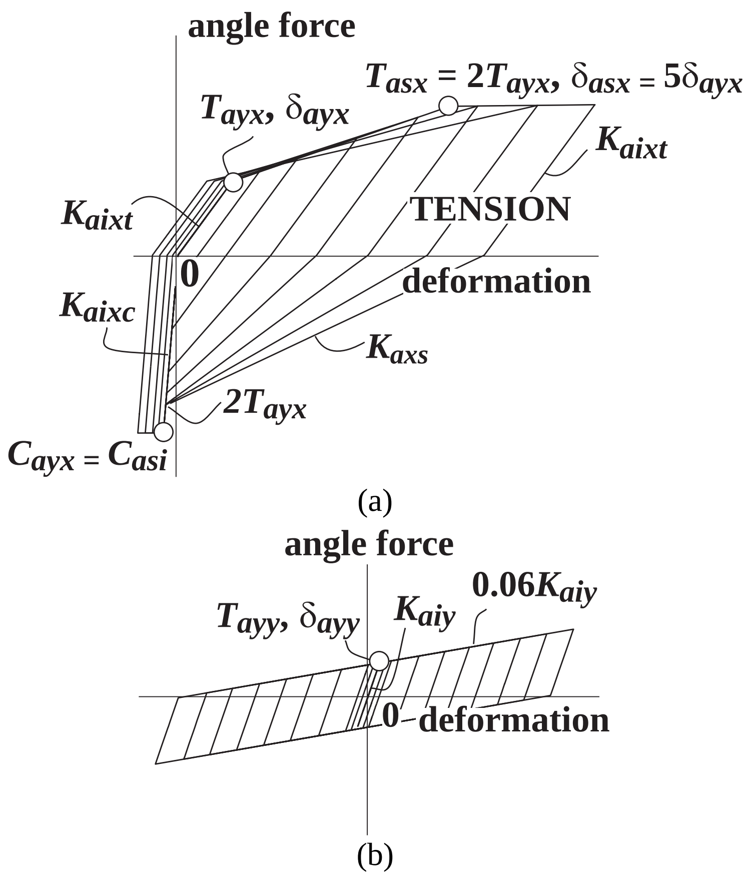

Figure 10.3: Assumed force versus deformation behaviors of the angle elements in the parametric investigation (from Shen *et al.* 2006) – (a) horizontal angle element; (b) vertical angle element.

10.3 Subassembly Behavior Under Monotonic Loading

Figure 10.4 shows the predicted (using the model in Figure 10.2) moment versus rotation (M_b-θ_b) behavior of the prototype coupling beam subassembly in Figure 10.1 under monotonic lateral loading. The beam moment M_b is equal to the coupling moment at the beam ends determined as:

$$M_b = \frac{Vl_b}{2} \tag{10.1}$$

The beam rotation θ_b is the chord rotation, calculated as the relative vertical displacement between the two ends of the beam divided by the beam length.

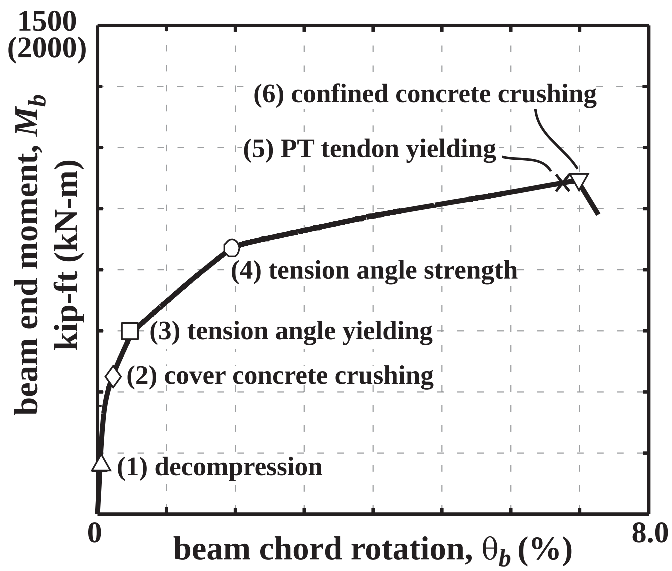

Figure 10.4: Behavior of prototype subassembly under monotonic loading.

As the prototype coupling beam subassembly is displaced, it goes through six response states as follows:

(1) Decompression (Δ marker) – This state represents the initiation of gap opening at the beam-to-wall interfaces when the pre-compression due to the post-tensioning force is overcome by the applied lateral load. Gap opening at the beam ends results in a reduction in the lateral stiffness, allowing the system to soften and undergo nonlinear rotations. Note that the effect of gap opening on the subassembly stiffness is small until the gap extends over a significant portion of the beam depth.

(2) Cover concrete crushing (◊ marker) – This state identifies the beginning of cover concrete crushing when the assumed ultimate strain of ε_{cu} = 0.003 is reached in the unconfined concrete at the compression corners of the beam. The subassembly stiffness continues to decrease due to increased gap opening in tension and deformation of the concrete in compression.

(3) Tension angle yielding (□ marker) – This state is reached at the first reduction in the stiffness of the assumed tri-linear tension angle force versus deformation relationship in Figure 10.3(a).

(4) Tension angle strength (○ marker) – This state is reached at the second reduction in the stiffness of the assumed tri-linear tension angle force versus deformation relationship in Figure 10.3(a), representing the full plastic capacity of the tension angles. A relatively large increase in the coupling beam moment resistance is observed between State 3 and State 4, after which the lateral stiffness of the structure is significantly reduced.

(5) Post-tensioning tendon yielding (X marker) – This state identifies the initiation of nonlinear straining [i.e., "yielding" at the assumed design yield strength of f_{bpy} = 245 ksi (1689 MPa)] of the beam post-tensioning tendon.

(6) Confined concrete crushing (▽ marker) – This state identifies the desired failure mode of the subassembly due to the crushing of the confined concrete at the beam ends, resulting in a drop in the coupling resistance of the structure. Note that other failure modes can also limit the nonlinear behavior of a subassembly, such as: (i) fracture of the top and seat angles; (ii) failure of the angle-to-beam or angle-to-wall connections; (iii) shear slip at the beam ends; (iv) diagonal tension failure of the beam; and (v) failure of the post-tensioning tendons or anchorages. These failure modes should be prevented by design, and thus, are not represented in Figure 10.4.

10.4 Subassembly Behavior Under Cyclic Loading

Figure 10.5(a) shows the hysteretic moment versus rotation (M_b-θ_b) behavior of the prototype subassembly under reversed-cyclic lateral loading. The thick curve represents the behavior under monotonic loading, shown previously in Figure 10.4. It can be seen that the subassembly is stable through large nonlinear cyclic rotations, while also dissipating a considerable amount of energy. The large self-centering capability of the structure indicates that the beam post-tensioning tendon provides a sufficient amount of restoring force to yield the tension angles back in compression and close the gaps at the beam ends. The total force in the post-tensioning tendon, P_b (normalized with $A_{bp}f_{bpu}$) corresponding to the hysteretic behavior in Figure 10.5(a) is shown in Figure 10.5(b). Almost all of the initial prestress is maintained throughout the analysis since the yielding of the post-tensioning steel is prevented due to the use of unbonded strands.

Figures 10.5(c) and 10.5(d) investigate the effect of the top and seat angles on the hysteretic behavior of the subassembly. The moment-rotation behavior in Figure 10.5(c) is for a system with thicker angles having L8x8x1 cross sections. The increased angle thickness results in increased strength and energy dissipation with slightly reduced self-centering capability. Similarly, Figure 10.5(d) shows the behavior of the prototype subassembly with the angles removed. As also demonstrated by the measured response of the specimen from Test 4A in Chapter 7, the cyclic behavior of the subassembly without angles is very close to nonlinear-elastic, indicating that the angles provide most of the energy dissipation in the structure. The angle size and post-tensioning force can be determined to achieve a good balance between the amount of energy dissipation and self-centering. It is important for the angles to provide a significant amount of energy dissipation; however, they should not prevent the closing of the gaps at the beam ends upon unloading.

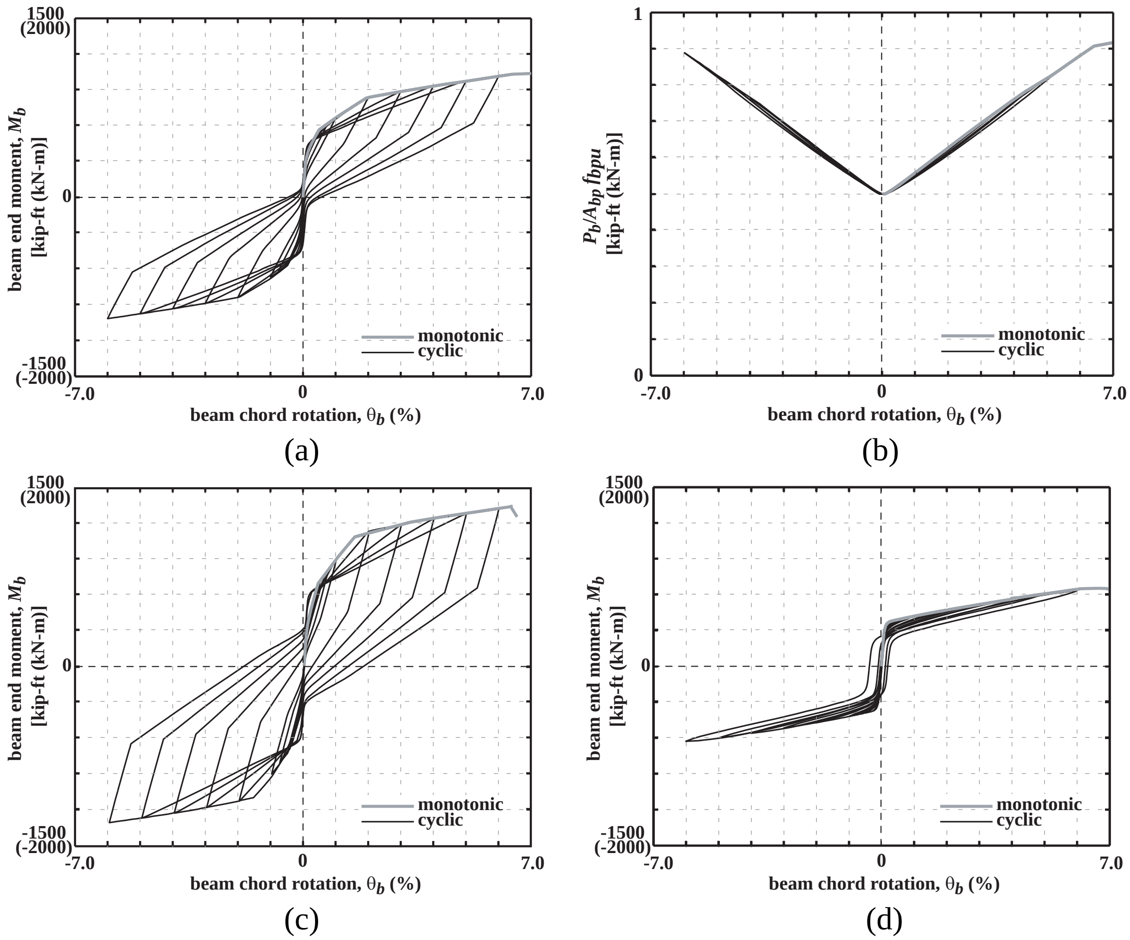

Figure 10.5: Behavior under cyclic loading – (a) prototype subassembly; (b) normalized beam post-tensioning force; (c) thicker angles; (d) no angles.

10.5 Parametric Investigation

This section describes a parametric analytical investigation on the monotonic lateral load behavior of the full-scale prototype coupling beam system by varying its structural properties. The results are used to determine how the behavior of the system can be controlled by design. The varied properties are: (1) thickness of the top and seat angles, t_a; (2) initial stress in the post-tensioning steel, f_{bpi}; (3) total area of the post-tensioning steel, A_{bp}; (4) f_{bpi} and A_{bp} varied simultaneously, with the total post-tensioning force kept constant; (5) wall length, l_w; (6) beam width, b_b; (7) beam depth, h_b; (8) beam length, l_b; (9) h_b and l_b varied simultaneously, with the beam length-to-depth aspect ratio kept constant; and (10) confined concrete crushing strain, ε_{ccu}. The parametric subassembly moment-rotation relationships are given in Figures 10.6(a)-(j). For each of the ten parameters investigated, two variations from the original prototype subassembly are made, while keeping all other parameters constant.

The markers in Figure 10.6 represent the response states identified in Figure 10.4. The beam end moment and chord rotation for the following states are shown in Figure 10.7 (solid lines) as functions of the varied parameters: (1) tension angle yielding (marker); (2) tension angle strength (○ marker); (3) post-tensioning tendon yielding (X marker); and (4) confined concrete crushing (▽ marker). The other response states from Figure 10.4 – decompression and cover concrete crushing – are not shown in Figure 10.7. The major observations for the parameter ranges investigated are summarized below.

From Figures 10.6(a) and 10.7(a), it is observed that an increase in angle thickness, t_a results in: (1) a large increase in the coupling resistance; (2) a small increase in the rotation at post-tensioning tendon yielding; and (3) a modest decrease in the rotation at confined concrete crushing.

Similarly, Figures 10.6(b) and 10.7(b) show that an increase in the post-tensioning steel initial stress, f_{bpi} results in: (1) a modest increase in the coupling resistance, without much change in the ultimate strength at confined concrete crushing; (2) a large decrease in the rotation at post-tensioning tendon yielding; and (3) a considerable decrease in the rotation at confined concrete crushing. Note that an initial post-tensioning steel stress that is too high can result in a loss of prestress under cyclic loading as well as tendon fracture.

From Figures 10.6(c) and 10.7(c), it is observed that an increase in the post-tensioning tendon area, A_{bp} results in: (1) a modest increase in the coupling resistance; (2) a small increase in the rotation at post-tensioning tendon yielding; and (3) a large decrease in the rotation at confined concrete crushing.

The total beam post-tensioning force varies as f_{bpi} and A_{bp} are varied in Figures 10.6(b), 10.6(c), 10.7(b) and 10.7(c). To investigate this effect, A_{bp} and f_{bpi} are varied simultaneously in Figures 10.6(d) and 10.7(d) such that the initial post-tensioning force, $P_{bi} = A_{bp}f_{bpi}$ remains constant. It is observed that the behavior up to the tension angle strength state is similar for the three subassemblies when P_{bi} is constant.

The next five parameters investigate the beam and wall geometry. Figures 10.6(e) and 10.7(e) show that an increase in the wall length, l_w results in: (1) a small decrease in the coupling strength at confined concrete crushing, with almost no effect on the behavior up to the tension angle strength state; (2) a large increase in the rotation at post-tensioning tendon yielding; and (3) a modest increase in the rotation at confined concrete crushing. The subassemblies in Figures 10.6(e) and 10.7(e) show no yielding of the post-tensioning tendon, except for Subassembly 1 for which tendon yielding occurs right before confined concrete crushing. The dotted line in Figure 10.7(e) depicts the effect of the wall length on the rotation at post-tensioning tendon yielding if the crushing of the confined concrete is suppressed.

From Figures 10.6(f) and 10.7(f), an increase in the beam width, b_b results in: (1) a small increase in the coupling strength at confined concrete crushing, with almost no effect on the behavior up to the tension angle strength state; (2) a considerable increase in the rotation at post-tensioning tendon yielding; and (3) a large increase in the rotation at confined concrete crushing.

Next, Figures 10.6(g) and 10.7(g) show that an increase in the beam depth, h_b results in: (1) a large increase in the coupling resistance; (2) a large decrease in the rotation at post-tensioning tendon yielding; and (3) a modest decrease in the rotation at confined concrete crushing. As discussed in Chapter 8, an increase in the beam depth can induce earlier fracture of the top and seat angles; however, angle fracture is not included in the analytical models developed in this dissertation.

Based on Figures 10.6(h) and 10.7(h), an increase in the beam length, l_b results in: (1) a small decrease in the coupling strength at confined concrete crushing, with almost no effect on the behavior up to the tension angle strength state; (2) a small increase in the rotation at post-tensioning tendon yielding; and (3) a modest decrease in the rotation at confined concrete crushing. The effect of the beam length on the rotation at post-tensioning tendon yielding is smaller than the effect of the wall length, since a change in wall length has double (for a structure with two wall piers) the effect on the unbonded length of the tendon than the same amount of change in beam length.

Note that the coupling beam length-to-depth aspect ratio varies as h_b and l_b are varied in Figures 10.6(g) and 10.6(h). To investigate this effect, h_b and l_b are varied simultaneously in Figures 10.6(i) and 10.7(i) such that the aspect ratio remains constant at a value of 3.21.

Finally, in Figures 10.6(j) and 10.7(j), the confined concrete crushing strain, ε_{ccu} is varied. The ε_{ccu} = 0.042 and 0.055 values for the parametric subassemblies were obtained by varying the spacing of the confinement reinforcement to 1.75 in. (48 mm) and 1.125 in. (29 mm), respectively. The smaller spacing of 1.125 in. (29 mm) may not be practical for actual design; however, the objective of this investigation is to observe the trends in structural behavior as selected parameters are varied. The results show that an increase in ε_{ccu} results in: (1) a small increase in the coupling strength at confined concrete crushing, with almost no effect on the behavior up to the tension angle strength state; (2) a small decrease in the rotation at post-tensioning tendon yielding; and (3) a large increase in the rotation at confined concrete crushing.

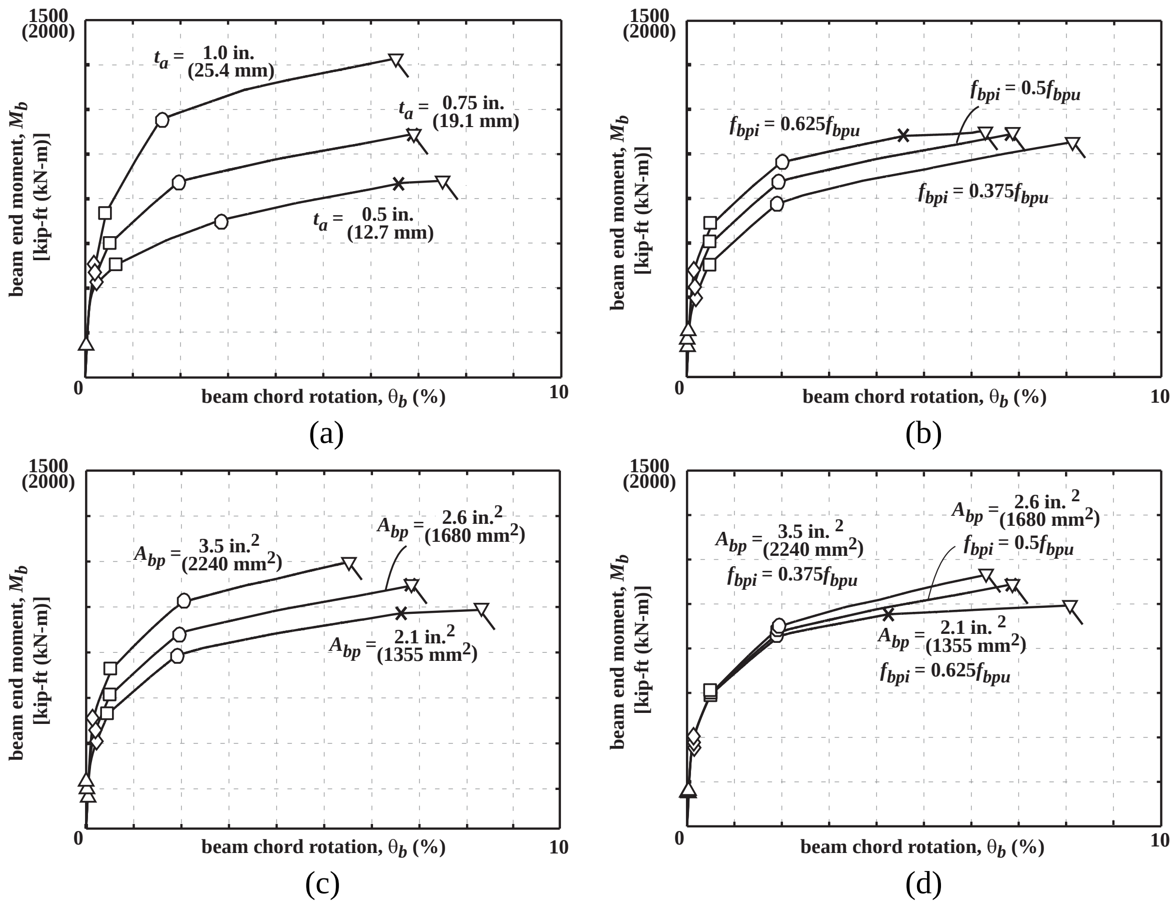

Figure 10.6: Behavior of parametric subassemblies –
(a) t_a; (b) f_{bpi}; (c) A_{bp}; (d) f_{bpi} and A_{bp}; (e) l_w; (f) b_b; (g) h_b; (h) l_b; (i) l_b and h_b; (j) ε_{ccu}.

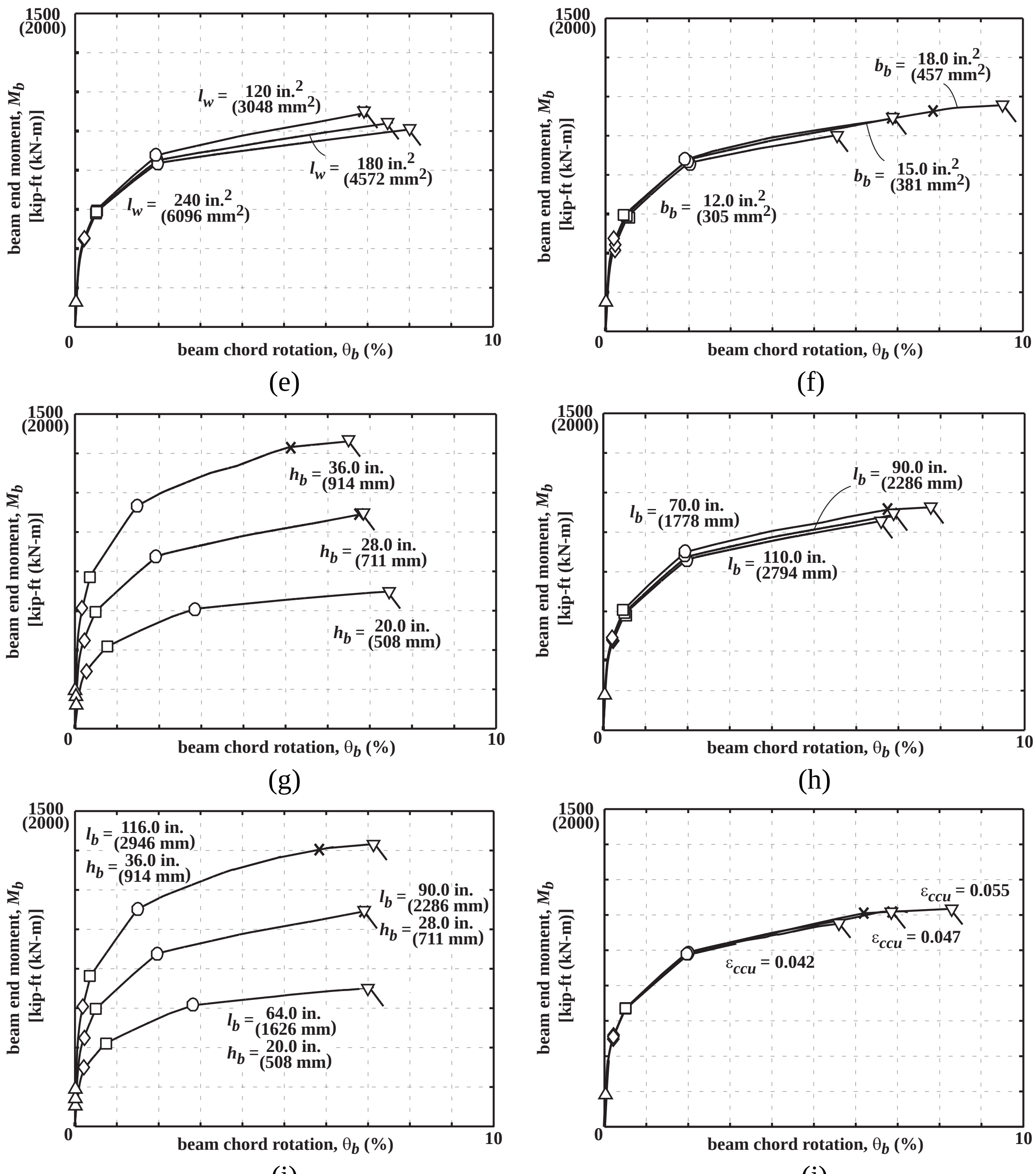

Figure 10.6 continued.

.

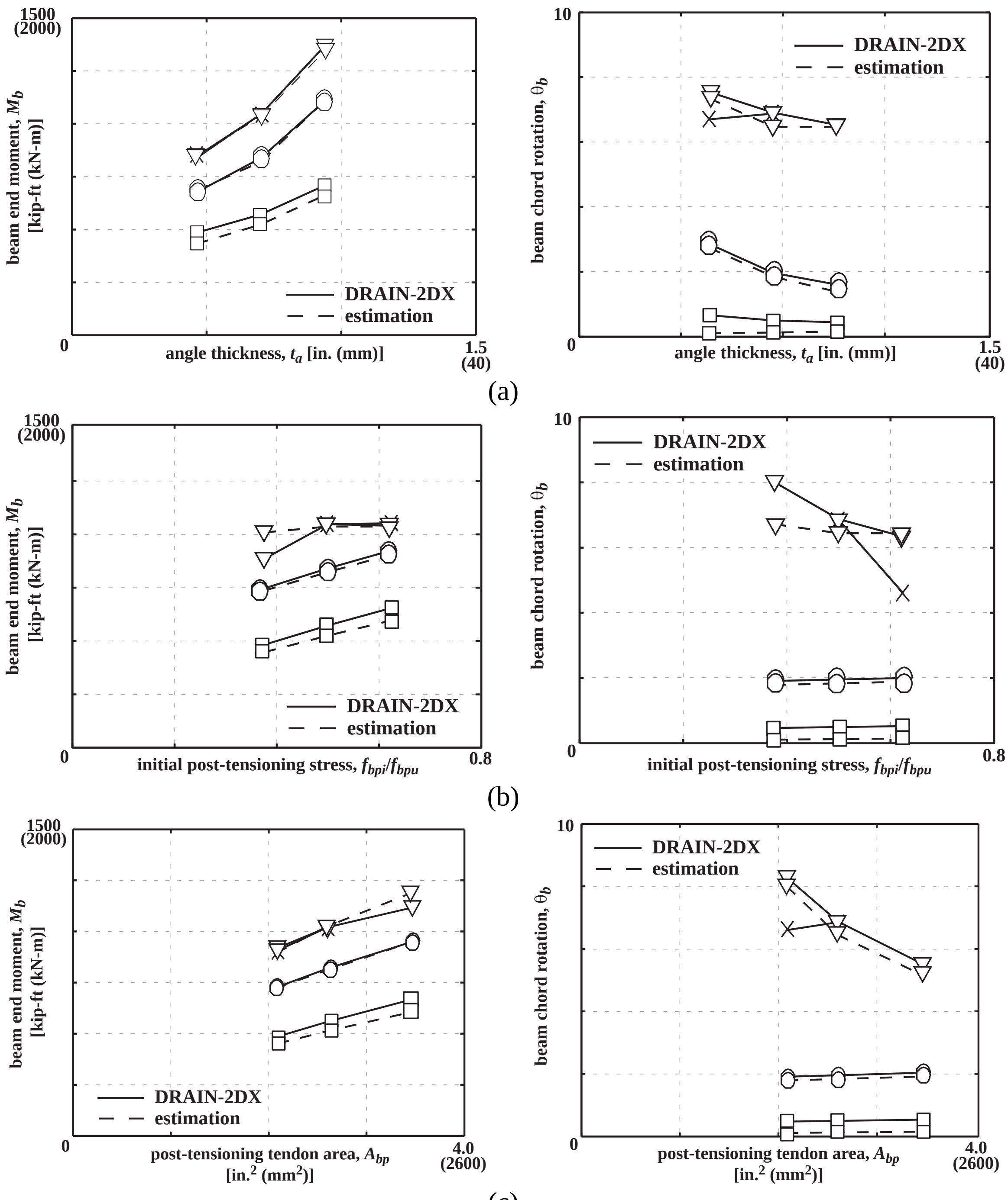

Figure 10.7: Behavior of parametric subassemblies –
(a) t_a; (b) f_{bpi}; (c) A_{bp}; (d) f_{bpi} and A_{bp}; (e) l_w; (f) b_b; (g) h_b; (h) l_b; (i) l_b and h_b; (j) ε_{ccu}.

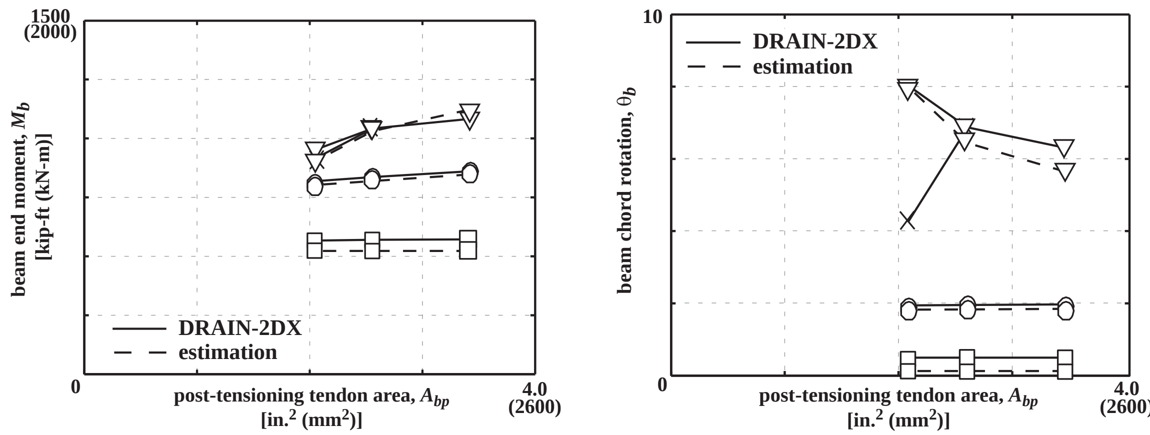

(d)

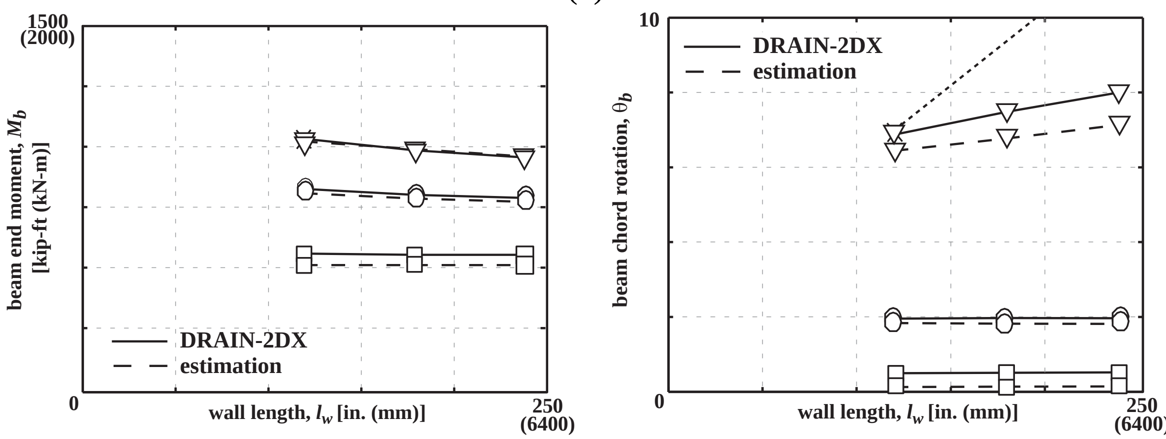

(e)

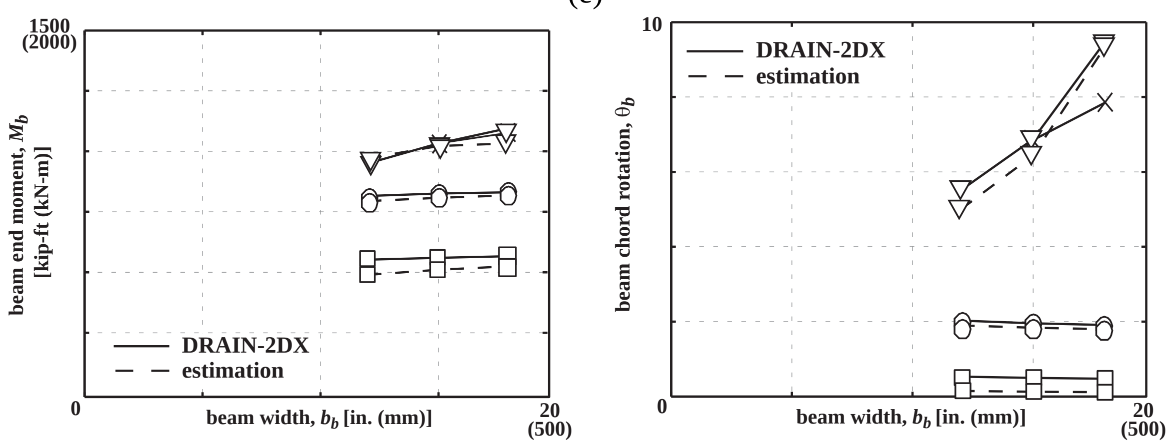

(f)

Figure 10.7 continued.

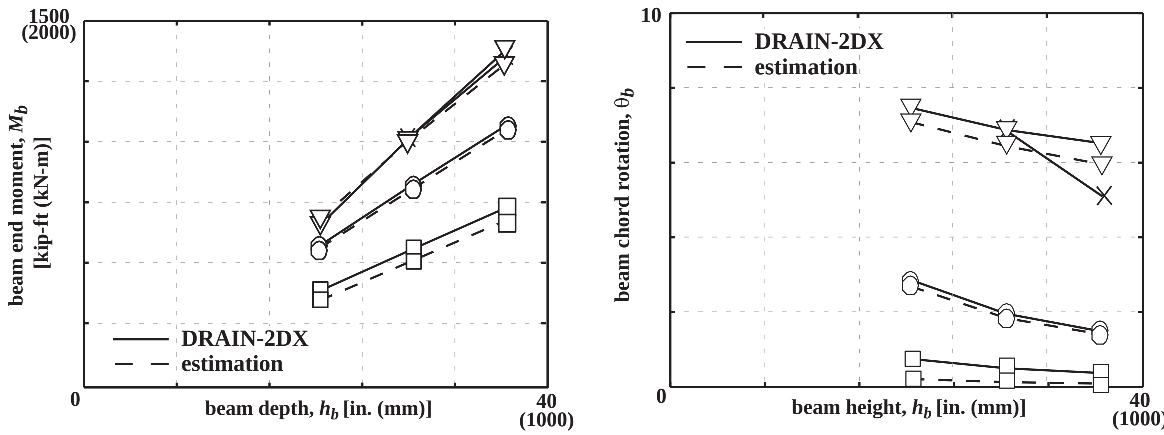

(g)

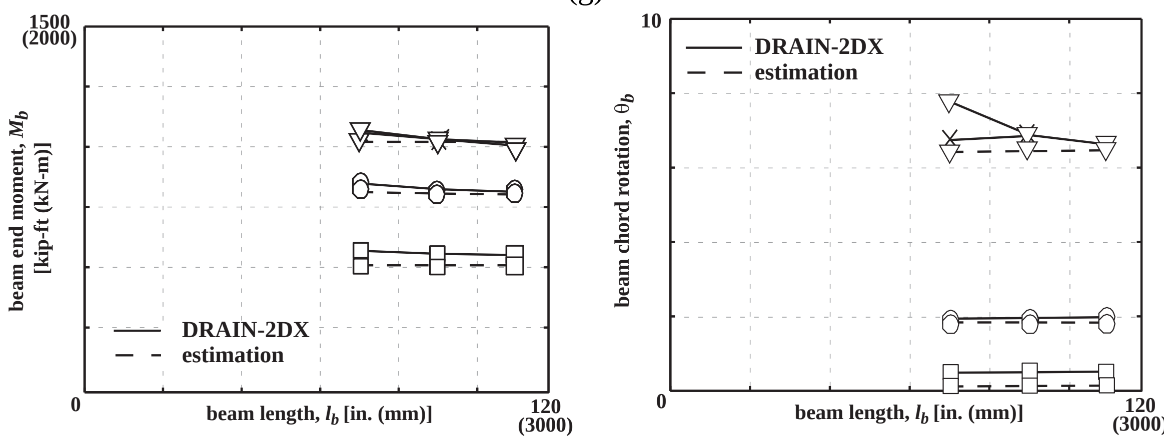

(h)

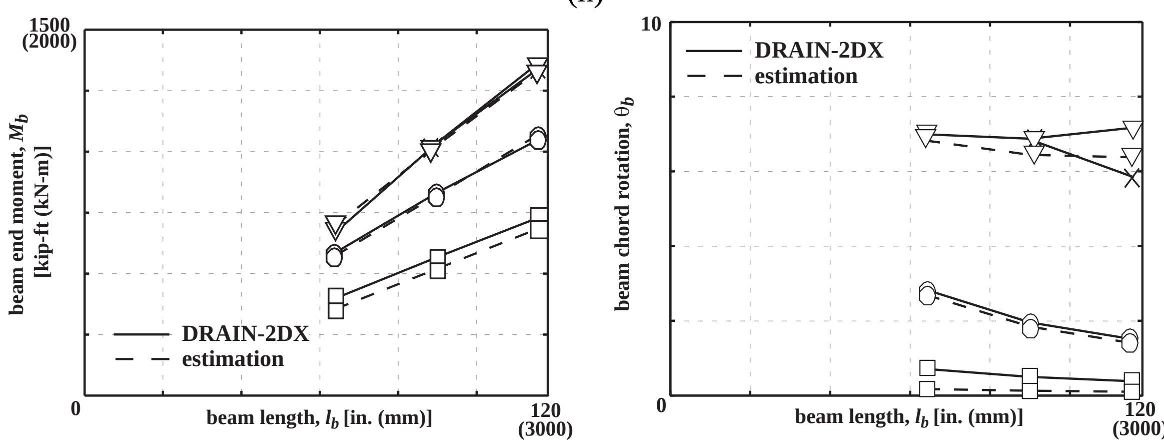

(i)

Figure 10.7 continued.

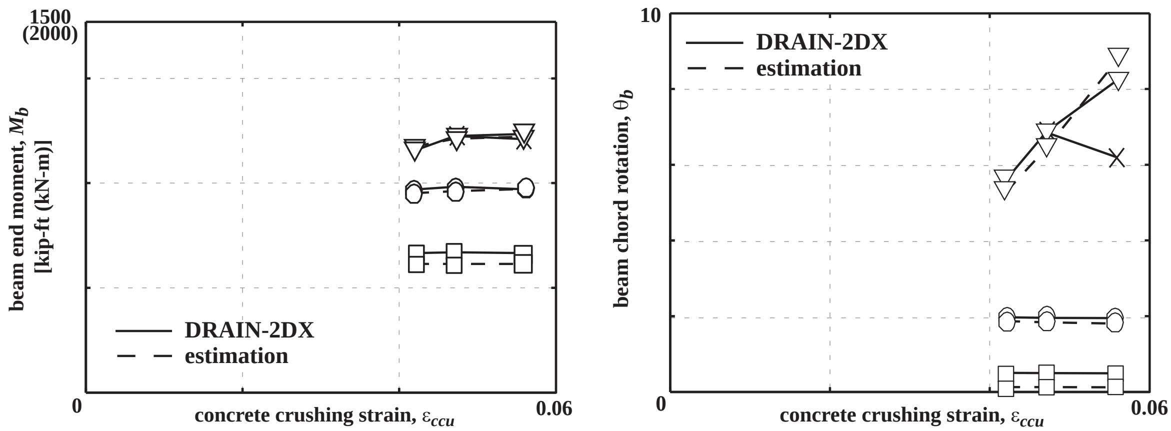

(j)

Figure 10.7 continued.

10.6 Tri-linear Estimation of Subassembly Behavior

This section presents a closed-form procedure to estimate the nonlinear beam end moment versus chord rotation behavior of unbonded post-tensioned precast coupling beam subassemblies under monotonic loading. The subassembly behavior is estimated using an idealized tri-linear relationship as shown in Figure 10.8, identified by the following three states: (1) tension angle yielding (M_{ay}, θ_{ay}); (2) tension angle strength (M_{as}, θ_{as}); and (3) confined concrete crushing (M_{ccc}, θ_{ccc}). Estimation procedures for M_{ay}, θ_{ay}, M_{as}, θ_{as}, M_{ccc}, and θ_{ccc} are developed using basic principles of equilibrium, compatibility, and constitutive relationships as described below.

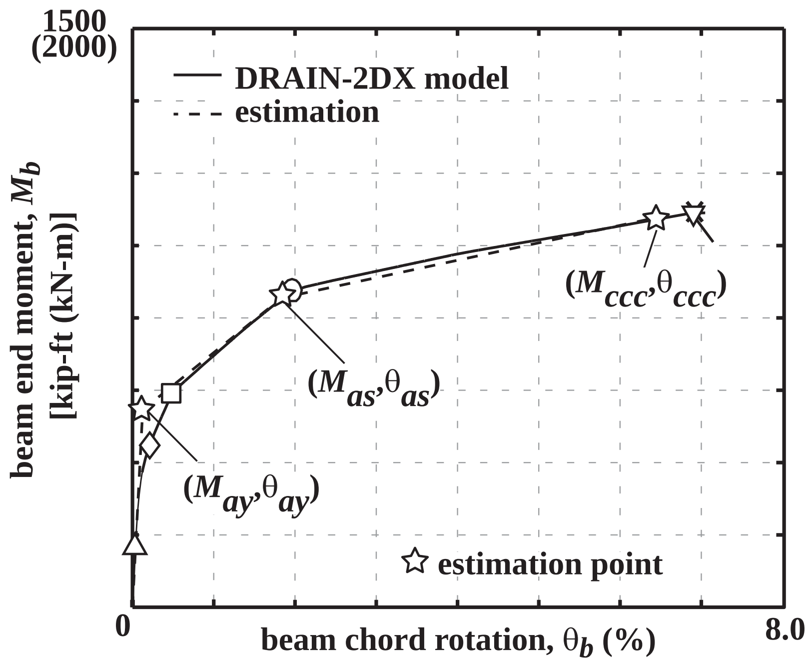

Figure 10.8: Tri-linear estimation of subassembly behavior.

10.6.1 Tension Angle Yielding State

The moment and rotation estimates for the tension angle yielding state are based on the following assumptions: (1) the force in the tension angles is equal to the yield force, T_{ayx} [e.g., see Figure 10.3(a)]; (2) the force in the compression angles is equal to $0.1 f_{ay} A_a \leq C_{ayx}$, where f_{ay} is the yield strength of the angle steel, A_a is the area of the angle leg cross-section, and C_{ayx} is the assumed slip capacity of the angle-to-beam connection bolts; (3) the stress in the beam post-tensioning tendon is equal to the initial stress, f_{bpi}; and (4) the compressive stresses in the beam at the beam-to-wall interfaces have a uniform (i.e., rectangular) distribution with a magnitude of f'_c. Figure 10.9(a) compares the assumed and "actual" beam end concrete compressive stress distributions at the tension angle yielding state. Since the resultant location of the assumed uniform stress distribution is lower than that of the actual distribution, the procedure described below is expected to underestimate M_{ay}.

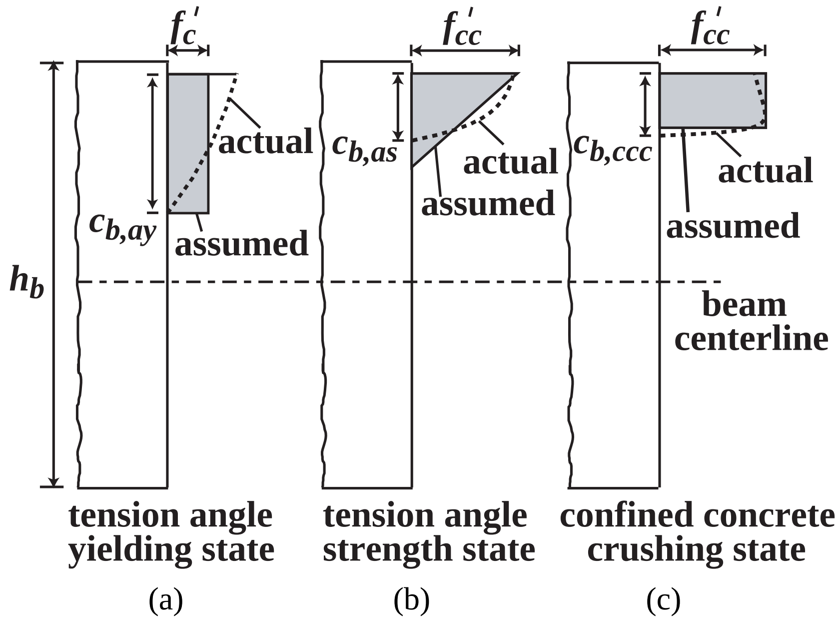

Figure 10.9: Concrete stress distributions at beam end – (a) tension angle yielding state; (b) tension angle strength state; (c) confined concrete crushing state.

The basis for Assumption (2) is described as follows. Under monotonic lateral loading of the structure, most of the post-tensioning force is transferred through the concrete contact regions at the beam corners while the compression forces in the angles remain small. Assumption (2) is used in the absence of a more reliable method to predict the forces in the compression angles. Note that the compression angle forces have a relatively small effect on the coupling beam moment and rotation at the tension angle yielding state; and thus, they can be ignored in the estimation procedure. Note also that, to maintain simplicity in the equations, possible crushing of the cover concrete is ignored below.

Step 1: Based on Assumptions 1 – 3, estimate the compression force at the end of the beam as:

$$C_{b,ay} = P_{bi} + T_{ayx} - 0.1 f_{ay} A_a \tag{10.2}$$

where $P_{bi} = A_{bp} f_{bpi}$ is the initial post-tensioning force and $0.1 f_{ay} A_a$ is limited to C_{ayx}.

Step 2: Use Assumption 4 to estimate the depth of the compression (i.e., contact) region at the beam-to-wall interfaces as:

$$c_{b,ay} = \frac{C_{b,ay}}{f_c' b_b} \tag{10.3}$$

Step 3: Estimate the moment M_{ay} by taking moments about the beam centerline as:

$$M_{ay} = C_{b,ay}\left(\frac{h_b}{2} - \frac{c_{b,ay}}{2}\right) + \frac{1}{2}\left[0.1 f_{ay} A_a + T_{ayx}\right]\left(h_b + t_a\right) \tag{10.4}$$

where, $0.1 f_{ay} A_a$ is limited to C_{ayx}.

Step 4: Determine the initial stiffness, K_{bi} of the subassembly using a linear elastic model. As shown in Figure 10.10(a), one half the length of the subassembly can be used due to symmetry, from the center of the reaction block (Node B) to the beam midspan. The effects of the angles and the beam post-tensioning tendon on the initial stiffness of the subassembly are ignored. The center of the reaction block is fixed and the beam midspan is free. A vertical force V is applied at the free end. The Y-translational degree of freedom of Node C, which represents the beam-to-wall interface, is restrained. Thus, the model is indeterminate to the first degree. Alternatively, a simpler linear-elastic model can be obtained by ignoring the deformations of the wall-contact elements as shown in Figure 10.10(b), resulting in a small overestimation of the initial stiffness. This model is statically determinate.

The stiffness K_{bi} of either model can be determined using an appropriate linear-elastic structural analysis procedure. Closed-form expression for K_{bi} can also be developed. The cross-sectional properties of the model are determined from the concrete properties of the coupling beam and the wall-contact regions (which can be obtained from the fiber element model described in Chapter 9), with linear-elastic concrete material properties in both tension and compression. Effective reduced stiffness properties for concrete can also be assumed to indirectly include the effects of small amounts of cracking/gap opening in the structure.

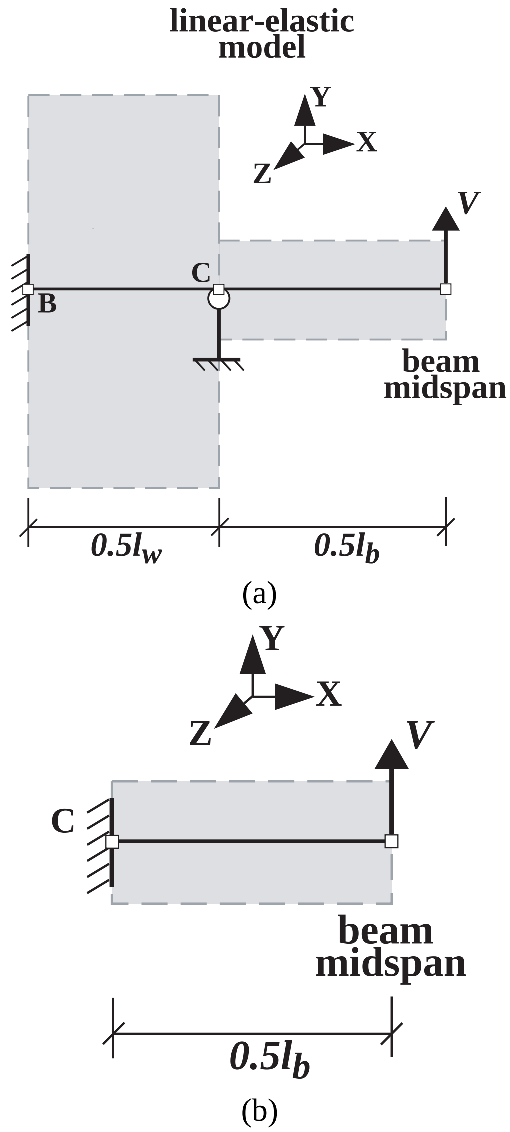

Figure 10.10: Linear-elastic subassembly model – (a) model with wall-contact elements; (b) model without wall-contact elements.

Step 5: Estimate the rotation θ_{ay} as:

$$\theta_{ay} = \frac{M_{ay}}{K_{bi}} \tag{10.5}$$

10.6.2 Tension Angle Strength State

The moment M_{as} and rotation θ_{as} at the tension angle strength state are estimated using an iterative procedure based on the following assumptions: (1) the force in the tension angles is equal to T_{asx}, reached at δ_{asx} [e.g., see Figure 10.3(a)]; (2) the force in the compression angles is equal to the assumed slip capacity, C_{ayx} of the angle-to-beam connection bolts; and (3) the compressive stresses in the beam at the beam-to-wall interfaces have a linear (i.e., triangular) distribution with the maximum stress equal to the confined concrete strength, f'_{cc}. The assumed and "actual" beam end concrete compressive stress distributions at the tension angle strength state are shown in Figure 10.9(b). Note that, similar to the tension angle yielding state, the procedure described below ignores the crushing of the cover concrete to maintain simplicity in the equations. Crushing of the cover concrete can be incorporated into these equations by assigning reduced or zero stresses to the beam end regions surrounding the confined concrete.

Step 1: Assume that the beam post-tensioning tendon force at the tension angle strength state is equal to the initial post-tensioning tendon force as:

$$P_{b,as} = P_{bi} \tag{10.6}$$

Step 2: Based on Assumptions 1 and 2, estimate the compression force at the end of the beam as:

$$C_{b,as} = P_{b,as} + T_{asx} - C_{ayx} \tag{10.7}$$

Step 3: Use Assumption 3 to estimate the depth of the compression region at the beam-to-wall interfaces as:

$$c_{b,as} = \frac{C_{b,as}}{0.5 f'_{cc} b_b} \tag{10.8}$$

Step 4: Estimate the coupling beam rotation at the tension angle strength state as:

$$\theta_{as} = \frac{\delta_{asx}}{h_b + \frac{t_a}{2} - c_{b,as}} \tag{10.9}$$

where, δ_{asx} is the deformation of the tension angle based on the assumed angle load-deformation relationship [e.g., Figure 10.3(a)] and the idealized beam end displacements in Figure 10.11.

Step 5: Using Figure 10.11 and the symmetry of the gap opening displacements at the centerline of the beam at the two ends, estimate the elongation of the beam post-tensioning tendon as:

$$u_{bp,as} = 2\theta_{as}\left(0.5h_b - c_{b,as}\right) \tag{10.10}$$

Step 6: Estimate the beam post-tensioning tendon force as:

$$P_{b,as} = P_{bi} + \left(\frac{u_{bp,as}}{l_{bp}}\right) E_{bp} A_{bp} \tag{10.11}$$

where, l_{bp} and E_{bp} are the length and the modulus of elasticity of the post-tensioning tendon.

Step 7: Iterate Steps 2 – 6 until satisfactory agreement on $P_{b,as}$ is achieved.

Step 8: Estimate the moment M_{as} by taking moments about the beam centerline as:

$$M_{as} = C_{b,as}\left(\frac{h_b}{2} - \frac{c_{b,as}}{3}\right) + \frac{1}{2}\left(C_{ayx} + T_{asx}\right)\left(h_b + t_a\right) \tag{10.12}$$

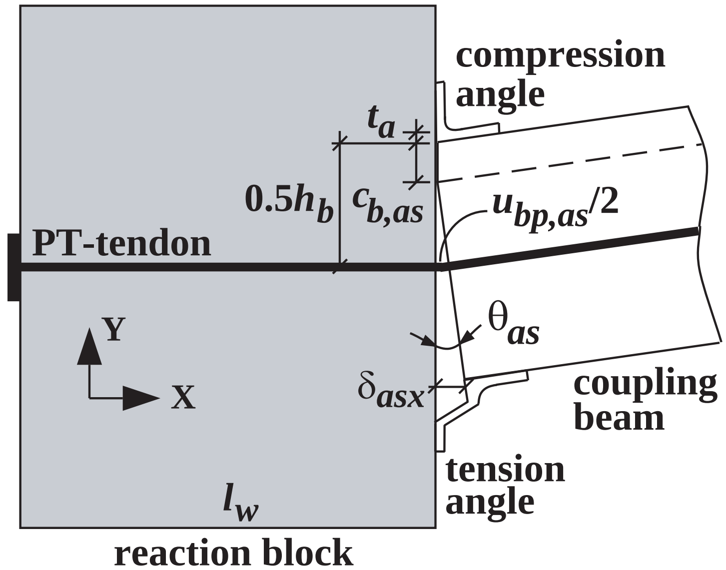

Figure 10.11: Beam end displacements at the tension angle strength state.

10.6.3 Confined Concrete Crushing State

The moment M_{ccc} and rotation θ_{ccc} at the confined concrete crushing state are estimated using an iterative process based on the following assumptions: (1) the force in the tension angles is equal to T_{asx}; (2) the force in the compression angles is equal to the assumed slip force, C_{ayx}; (3) the compressive stresses in the beam at the beam-to-wall interfaces have a uniform (i.e., rectangular) distribution with a magnitude of f'_{cc}; and (4) the length over which the "plastic" concrete compressive deformations at the ends of the beam take place, l_{pl} is equal to the larger of the contact depth at the confined concrete crushing state, $c_{b,ccc}$ and one-fourth the confined concrete width, b_c of the beam.

By definition, the confined concrete crushing state is reached when the extreme confined concrete compressive strain reaches the crushing strain, ε_{ccu}. The corresponding "actual" and assumed beam end concrete compressive stress distributions are shown in Figure 10.9(c). The assumed uniform distribution is expected to provide a reasonable representation of the confined concrete stresses at this state. Similar to the previous two states, the crushing of the cover concrete is ignored in the equations below. Note that the estimation of M_{ccc} and θ_{ccc} requires a "plastic hinge length." As given in Assumption (4) and shown in Figure 10.12, a plastic hinge length of $l_{pl} = 0.25b_c \geq c_{b,ccc}$ was determined to give good correlation with the fiber element analysis results for the parametric subassemblies.

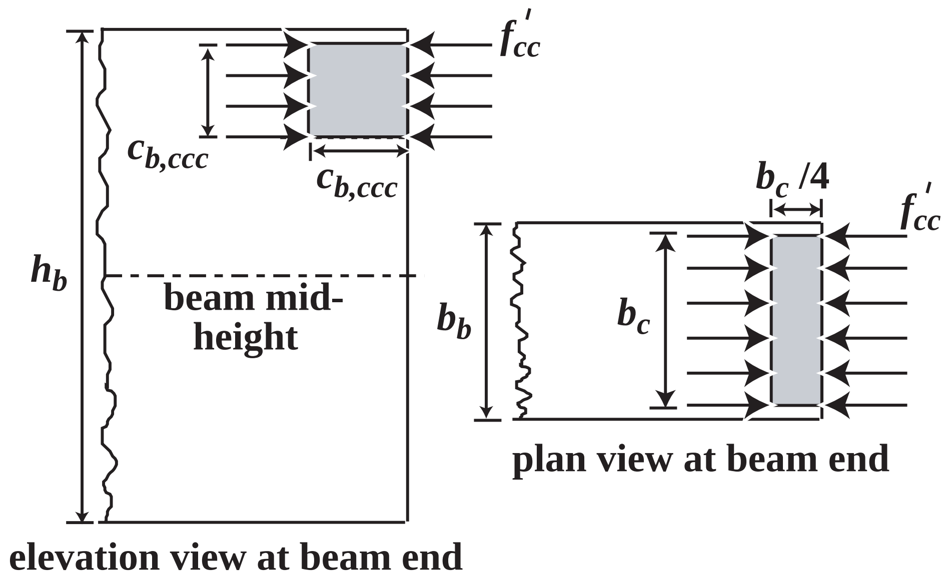

Figure 10.12: Estimation of plastic hinge length.

Step 1: Assume that the beam post-tensioning tendon force at the confined concrete crushing state is equal to the post-tensioning tendon force at the tension angle strength state as:

$$P_{b,ccc} = P_{b,as} \tag{10.13}$$

Step 2: Based on Assumptions 1 and 2, estimate the compression force at the end of the beam as:

$$C_{b,ccc} = P_{b,ccc} + T_{asx} - C_{ayx} \tag{10.14}$$

Step 3: Use Assumption 3 to estimate the depth of the compression region at the beam-to-wall interfaces as:

$$c_{b,ccc} = \frac{C_{b,ccc}}{f'_{cc} b_b} \tag{10.15}$$

Step 4: Estimate the moment M_{ccc} by taking moments about the beam centerline as:

$$M_{ccc} = C_{b,ccc}\left(\frac{h_b}{2} - \frac{c_{b,ccc}}{2}\right) + \frac{1}{2}\left(C_{ayx} + T_{asx}\right)\left(h_b + t_a\right) \tag{10.16}$$

Step 5: Estimate the plastic curvature at the beam ends as:

$$\varphi_{pi} = \frac{\varepsilon_{ccu}}{c_{b,ccc}} \tag{10.17}$$

Step 6: Estimate the plastic rotation as:

$$\theta_{pl} = \varphi_{pl} l_{pl} \tag{10.18}$$

where, $l_{pl} = 0.25 b_c \geq c_{b,ccc}$.

Step 7: Estimate the elastic rotation as:

$$\theta_{el} = \frac{M_{ccc}}{K_{bi}} \tag{10.19}$$

Step 8: Estimate the beam rotation at the confined concrete crushing state as:

$$\theta_{ccc} = \theta_{el} + \theta_{pl} \tag{10.20}$$

Step 9: Estimate the elongation of the beam post-tensioning tendon as:

$$u_{bp,ccc} = 2\theta_{ccc}\left(0.5 h_b - c_{b,ccc}\right) \tag{10.21}$$

Step 10: Estimate the post-tensioning tendon force as:

$$P_{b,ccc} = P_{bi} + \left(\frac{u_{bp,ccc}}{l_{bp}} \right) E_{bp} A_{bp} \leq P_{by} \tag{10.22}$$

where, $P_{by} = A_{bp}f_{bpy}$ is the assumed yield force of the beam post-tensioning tendon. If the post-tensioning steel yields before the confined concrete crushing state (i.e., $P_{b,ccc} > P_{by}$), Equation (10.22) can be revised using an idealized bilinear steel stress-strain relationship.

Step 11: Iterate Steps 2 – 10 until satisfactory agreement on $P_{b,ccc}$ is achieved.

10.7 Analytical Verification of Tri-Linear Estimation

The tri-linear estimation of the subassembly moment-rotation behavior above is verified by comparing the estimated moment and rotation values corresponding to the tension angle yielding, tension angle strength, and confined concrete crushing states with values determined using the DRAIN-2DX fiber element model. The dashed lines in Figures 10.7(a)-(j) show the estimated results for the parametric subassemblies in Figures 10.6(a)-(j). The comparisons indicate that the moment and rotation estimations are close to the results from the fiber element model for a wide range of parameters. Thus, the proposed procedures can be used to conduct approximate, simplified analyses of unbonded post-tensioned precast coupling beam subassemblies with different properties.

10.8 Experimental Verification of Tri-linear Estimation

This section provides an experimental verification of the tri-linear coupling beam end moment versus chord rotation behavior described above by comparing the estimated results with the measured behavior of the test specimens in Chapters 6 – 8. Different from the estimations of the parametric subassembly behavior in Section 10.7, the behaviors of the test specimens were estimated using the measured geometric and material properties of each subassembly, including any adjustments that were made to the material models as described in Chapter 9 (e.g., reduced stiffness of concrete in the non-virgin tests, and reduced concrete stiffness of the damaged area of the wall test region). The behaviors of the post-tensioning steel and the top and seat angles were also taken from the models in Chapter 9.

Comparisons between the measured and estimated behaviors of the test specimens are shown on the coupling beam shear force versus beam chord rotation plots in Figure 10.13. Note that no comparisons are provided for Tests 1 and 3A because of the difficulty in estimating the behavior of the patched beam end in Test 1 and the difficulty in estimating the strength of the top and seat angles in Test 3A. Note also that in Test 4A, due to the removal of the top and seat angles, no estimation could be made for the tension angle yielding and tension angle strength states. Instead, a "softening" point (corresponding to a significant change in the stiffness of the structure) is estimated for this test by using the same procedure as the tension angle yielding state described previously, but with the angle forces set to zero.

As shown in Figure 10.13, the estimated tri-linear behaviors of the test specimens are generally in reasonable agreement with the test results. The differences seem to be greater for Test 4A, which had no top and seat angles, and therefore required the estimation procedures to be modified outside their practical ranges. The beam chord rotation estimations corresponding to the tension angle strength state of the test specimens are θ_{as} = 4.23%, 4.57%, 4.87%, 3.86%, and 4.03% for Tests 2, 3, 3B, 4, and 4B, respectively. When compared to the initiation of angle fracture in each test (which was recorded through visual inspection of the angles during testing), the estimated rotations for the tension angle strength state make sense, with the exception of Test 2, which had no visible angle fracture since the gap opening remained small due to the relatively large concrete damage.

In Test 3, the initiation of angle fracture occurred at approximately 5.0% rotation as compared with 4.57% from the tri-linear estimation. Visible angle fracture was observed at 6.4% rotation in Test 3B, with surface cracks appearing during the 5.0% rotation cycle. These values are slightly higher than the 4.87% rotation from the tri-linear estimation. Test 4 was displaced to a smaller rotation that the estimated rotation for the tension angle strength state, and as would be expected, no visible initiation of angle fracture was observed during this test. Finally, in Test 4B, the initiation of angle fracture occurred at 5.0% rotation, which is slightly larger than the estimated rotation of 4.03%. It should be noted that the observed beam rotation at the initiation of angle fracture was taken when the displacement of the structure was paused, and thus, the angle fracture could have initiated at any rotation between the previous cycle and the current cycle. Furthermore, the estimations do not take into account any material deformations (e.g., rounding of beam end edges, grout deformations, etc.) in the non-virgin tests.

No fracture of the concrete confinement hoops was observed in any of the tests; however, many of the tests had significant concrete damage at the beam ends. The estimated rotation values for the confined concrete crushing state for Tests 2, 3B, and 4B are θ_{ccc} = 5.10%, 6.55%, and 5.23%, respectively. For Tests 2 and 3B, this value is less than the measured sustained rotation, however, it coincides well with the initiation of failure in the specimen (i.e., the subsequent cycle of each hysteretic loop has a decrease in strength). For Test 4B, the estimated rotation for the confined concrete crushing state coincides exactly with the sustained rotation; however, it should be noted that this test was stopped due to grout damage. Note that Tests 3, 4, and 4A were not displaced to failure; and thus, no comparisons can be made with the estimated rotation at the confined concrete crushing state.

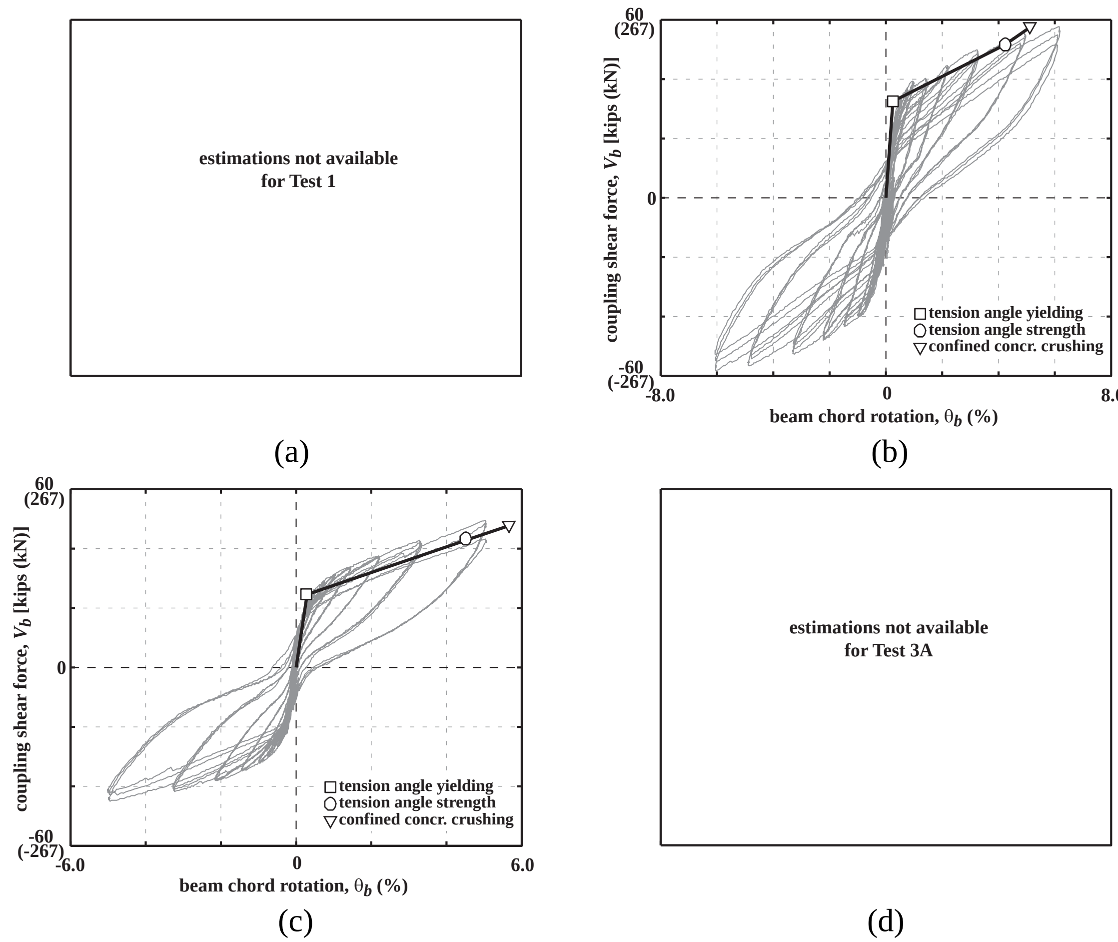

Figure 10.13: Tri-linear estimation of test subassembly behavior – (a) Test 1; (b) Test 2; (c) Test 3; (d) Test 3A; (e) Test 3B; (f) Test 4; (g) Test 4A; and (h) Test 4B.

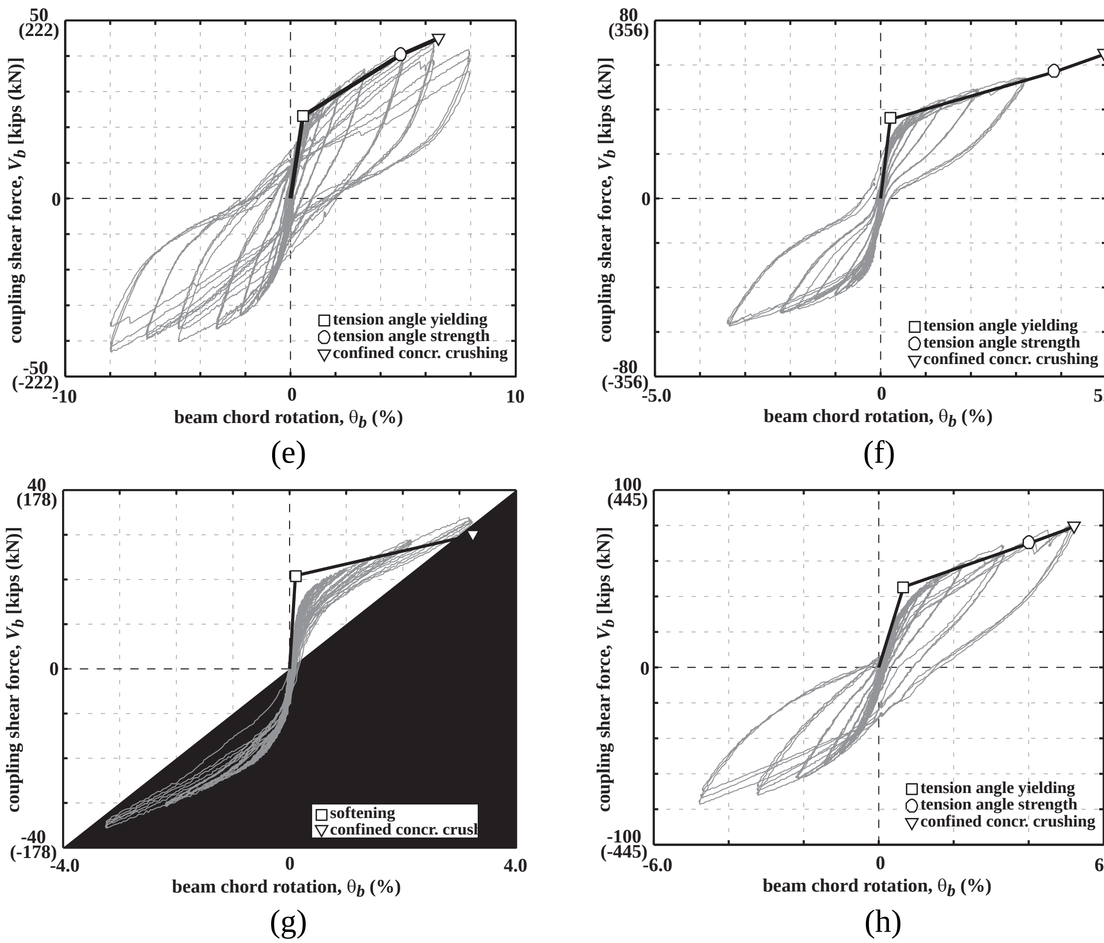

Figure 10.13 continued.

10.9 Summary

This chapter presents an analytical parametric investigation on the nonlinear lateral load behavior of unbonded post-tensioned precast coupling beam subassemblies. The effects of various design parameters (such as the beam post-tensioning steel area) on the moment versus rotation behavior of the coupling beams are quantified. It is shown that the coupling resistance can be controlled by varying the beam depth, the top and seat angle strength, and the beam post-tensioning force. The yielding of the post-tensioning tendons can be delayed by reducing the initial stress in the post-tensioning steel; and the crushing of the confined concrete at the beam ends can be delayed by reducing the total post-tensioning force and/or by increasing the amount of concrete confinement.

A closed-form procedure to estimate the nonlinear lateral load versus deformation behavior of unbonded post-tensioned precast coupling beam subassemblies is developed using basic principles of equilibrium, compatibility, and constitutive models. The subassembly moment-rotation behavior is estimated through an idealized tri-linear relationship, suitable for use in seismic design. Comparisons of the tri-linear relationship with the parametric analysis results as well as with the experimental results presented previously in the dissertation show that the closed-form procedure can be used to conduct approximate, simplified analyses of structures with different properties.

CHAPTER 11

SUMMARY, CONCLUSIONS, AND FUTURE WORK

11.1 Summary

This dissertation investigates the behavior, design, and analysis of unbonded post-tensioned precast concrete coupling beams for use in seismic regions. An experimental research program is conducted on the nonlinear lateral load versus deformation behavior of floor level coupled wall subassemblies. A total of eight half-scale tests are carried out with the following primary experimental parameters: (1) beam post-tensioning tendon area and initial stress; (2) initial beam concrete axial stress; (3) angle strength; and (4) beam depth. Four of the tests are conducted on virgin beam specimens and the other four tests are conducted on previously tested beams.

Two types of analytical models are developed and validated using the results from the experimental program. One of these models utilizes fiber beam-column elements to model the behavior of the coupling beams as well as gap opening at the beam-to-wall interfaces. The other model uses plane stress elements in a finite element program, with gap/contact surfaces modeling the behavior at the beam ends. Using the fiber element model, an analytical parametric investigation is conducted to expand the experimental results on the behavior and design of unbonded post-tensioned precast concrete coupling beams. Finally, a closed-form procedure is developed and validated as a design tool to estimate the nonlinear behavior of the beams under later loading.

11.2 Conclusions

The research described in this dissertation demonstrates that unbonded post-tensioned precast concrete coupling beams can be designed to provide an effective means to couple reinforced concrete wall piers in seismic regions. Important conclusions resulting from the research are as follows:

11.2.1 Experimental Program

- The experimental results show that unbonded post-tensioned precast beams can provide adequate lateral strength, stiffness, ductility, and energy dissipation under large reversed cyclic loading. The critical components of the structure that can limit this behavior include the post-tensioning anchors as well as the top and seat angles and their connections.
- The beam post-tensioning force creates a self-centered behavior minimizing the residual displacements of the structure upon unloading from a large nonlinear lateral displacement. The amount of self-centering can be controlled by varying the initial beam post-tensioning tendon force.
- Premature strand wire fractures of the beam post-tensioning tendon were observed during the experimental program. This undesirable behavior should be prevented

by pre-qualifying unbonded strand/anchorage systems to achieve the maximum expected strand stresses and strains without wire fracture.

- It was shown that the beam post-tensioning tendon force together with the top and seat connection angles provide adequate vertical support to the beam, preventing vertical slip at the beam-to-wall interfaces.
- The high-strength fiber-reinforced grout used at the beam-to-wall connection interfaces provided adequate strength, stiffness, toughness, and workability. The grout pads worked well, but the height of the pads needs to be slightly smaller than the full beam depth to prevent the angle heels from coming into contact with the pads as the structure is displaced laterally.
- The angle-to-beam connection bolts performed well through a beam chord rotation of approximately 3.33%; however, at larger rotations, some reduction in the bolt force was observed leading to slip of the top and seat angles. The reduction in the connection bolt force occurred due to the deterioration of the beam end concrete.
- The unbonded post-tensioned angle-to-wall connection strands worked well; however, a connection plate is recommended to help distribute the angle forces into the wall region if the angle length is less than the wall thickness.
- The energy dissipation provided by the top and seat angles can be controlled by varying the angle length, thickness, and gage length.
- An adequate area of bonded mild steel reinforcement is needed to transfer the angle forces into the beam as well as to confine the beam concrete at the ends. In

comparison, only a small amount of transverse reinforcement is needed in the beam midspan regions.

- The design procedures used for the coupling beams and the wall test region were shown to work well through the experimental program.
- Compliance of the measured behavior of the test specimens to the acceptance criteria provided by ACI ITG-5.1 (ACI 2008) validates the use of these structures in seismic regions as well as their analysis and design.
- As compared to previous experiments of conventional monolithic cast-in-place reinforced concrete coupling beams, the experiments described in this dissertation demonstrate larger sustained rotations of unbonded post-tensioned precast coupling systems.

11.2.2 Analytical Modeling and Parametric Investigation

- Comparisons between the experimental measurements and the analytical results, which include global response parameters such as the beam shear force versus chord rotation behavior as well as local parameters such as reinforcement strains, demonstrate that the fiber-element analytical model is able to capture the nonlinear hysteretic response characteristics of unbonded post-tensioned coupling beams reasonably well.
- The modeling of the top and seat angles was achieved by modifying a previous angle model to match the behavior of the experimental results.

- The modeling of the non-virgin beam test specimens was achieved by modifying the stress-strain relationships of the confined and unconfined concrete to account for the reduced stiffness from the previous loading of the structure.
- The finite-element model provided further verification of the fiber-element model as well as an assessment of the stress distributions inside the coupling beam and the beam-to-wall contact regions.
- Modified stress-strain relationships were used for the concrete to overcome convergence problems in the finite-element model. However, due to the unique behavior of the system, these modifications did not have a large effect on the results.
- The parametric analytical investigation showed that the lateral strength of the new coupling system can be controlled using the beam depth, top and seat angle strength, and the beam post-tensioning force. A reduction in the initial stress of the post-tensioning steel delays the yielding of the post-tensioning tendon.

11.2.3 Closed-form Estimations

- The lateral load versus deflection behavior of unbonded post-tensioned precast concrete coupling beams can be idealized as a tri-linear relationship.
- A closed-form procedure to estimate this relationship was developed as a design tool using basic principles of equilibrium, compatibility, and assumed constitutive models. Comparisons of the tri-linear approximations with the experimental results as well as with the parametric analytical results validate that the proposed

closed-form estimation procedure can be used to conduct approximate, simplified analyses of coupling beam structures with different design properties.

11.3 Future Work

Through the findings and conclusions from this research, the following recommendations are made to further the applicability of unbonded post-tensioned precast concrete coupling beams in seismic regions:

- Additional floor-level subassembly experiments are needed to further investigate the behavior and design of the beams, in particular, to study other beam detailing options such as the use of full-depth transverse reinforcement hoops at the beam ends as well as the use of fiber-reinforced concrete in the beams.
- Experiments of multi-story coupled wall systems, including the slab and out-of-plane effects, need to be conducted to provide a more complete assessment of the behavior of the structure.
- Analytical investigations of multi-story coupled wall systems, including nonlinear push-over and dynamic analyses, should be conducted to assess the wall, beam, and connection lateral force and deformation capacities and demands in multi-story structures.
- The behavior and design of the top and seat angles, including the angle-to-beam and angle-to-wall connections, need to be investigated further, especially for use in full-scale structures. The use of welded angle-to-beam and angle-to-wall

connections may be a feasible alternative to the connection types investigated in this dissertation.

- Additional research into the modeling of the top and seat angle behavior is also needed.
- The use of other energy dissipation devices and details utilizing the gap opening displacements at the beam ends should be studied.
- Reliable strand/anchorage systems need to be developed and validated for use in unbonded post-tensioned structural applications for seismic regions.

REFERENCES

ACI, "ITG-5.1-07 Acceptance Criteria for Special Unbonded Post-tensioned Precast Structural Walls Based on Validation Testing," American Concrete Institute Innovation Task Group 5, Farmington Hills, MI, 2008.

ACI Committee 318, "Building Code Requirements for Structural Concrete (ACI 318-05) and Commentary (ACI 318R-08)," American Concrete Institute, Farmington Hills, MI, 2008.

ACI Committee 318, "Building Code Requirements for Structural Concrete (ACI 318M-05) and Commentary (ACI 318RM-05)," American Concrete Institute, Farmington Hills, MI, 2005.

AISC, "Load and Resistance Factor Design Manual of Steel Construction," Third Edition, American Institute of Steel Construction, Chicago, IL, 2001.

Aktan, A, and Betero, V. V., "The Seismic Resistant Design of R/C Coupled Structural Walls," Report No. UCB/EERC-81/07, Earthquake Engineering Research Center, University of California, Berkeley, 1981.

Aktan, A. and Bertero, V., "Seismic Response of R/C Frame-Wall Structures," *Journal of Structural Engineering*, American Society of Civil Engineers, Vol. 110, No. 8, August 1984, pp. 1803-1821.

Aktan, A. and Bertero, V., "Evaluation of Seismic Response of RC Buildings Loaded to Failure," *Journal of Structural Engineering*, American Society of Civil Engineers, Vol. 113, No. 5, May 1987, pp. 1092-1108.

Aktan, A., Bertero, V., and Piazza, M., "Prediction of the Seismic Responses of R/C Frame-Coupled Wall Structures," Earthquake Engineering Research Center, Report No. UCB/EERC-82/12, Berkeley, CA, 1982, 182 pp.

Aktan, H.M., Yousef-Agha, W., and Olowokere, O.D., "Seismic Response of Low-Rise Steel Frames," *Journal of Structural Engineering,* American Society of Civil Engineers, Vol. 115, March 1989, pp. 594-607.

Aristizabal-Ochoa, J., "Seismic Behavior of Slender Coupled Wall Systems," *Journal of Structural Engineering*, American Society of Civil Engineers, Vol. 113, No. 10, October 1987, pp. 2221-2234.

ASTM, Annual Book of ASTM Standards, American Society for Testing and Materials, West Conshohocken, PA, 2001.

Azizinamini, A., “Cyclic Characteristics of Bolted Semi-Rigid Steel Beam-to-Column Connections,” Ph.D dissertation, University of South Carolina, 1985.

Backowski, B. J., Kuang, J. S., “A New Approach to Testing Concrete Coupling Beams Subjected to Reversed Cyclic Loading,” *Magazine of Concrete Research*, Vol. 60, No. 4, 2008, pp. 301-309.

Barney, G., Shiu, K., Rabbat, B., Fiorato, A., Russell, H., and Corley, W., “Earthquake Resistant Structural Walls – Tests of Coupling Beams,” Construction Technology Laboratories Report, Portland Cement Association, 1978.

Bernuzzi, C., “Predicition of the Behaviour of Top-and-Seat Cleated Steel Beam-to-Column Connections under Cyclic Reversal Loading,” *Journal of Earthquake Engineering*, Vol. 2, No. 1, 1998, pp. 419-430.

Bernuzzi, C., Calado, L., Castiglioni, C., “Ductility and Load Carrying Capacity Prediction of Steel Beam-to-Column Connections under Cyclic Reversal Loading,” *Journal of Earthquake Engineering*, Vol. 1, No. 2, April 1997, pp. 401-432.

Bristowe, S., “Seismic Response of Normal and High Strength Concrete Members,” Ph.D. Dissertation. Civil Engineering and Applied Mechanics, McGill University, Montreal, Canada, 2000.

Canbolat, B., Parra-Montesinos, G., and Wight, J., “Experimental Study on Seismic Behavior of High-Performance Fiber-Reinforced Cement Composite Coupling Beams,” *ACI Structural Journal.*, American Concrete Institute, Vol. 102, No. 1, 2005, pp. 159-166.

Chaallal, O., “Finite Element Model for Seismic RC Coupled Walls Having Slender Coupling Beams,” *Journal of Structural Engineering*, American Society of Civil Engineers, Vol. 118, No. 10, October 1992, pp. 2936-2943.

Chaallal, O., Gauthier, D., “Seismic Shear Demand on Wall Segments of Ductile Coupled Shear Walls,” *Canadian Journal of Civil Engineering*, Vol. 27, No. 3, 2000, pp. 506-522.

Chaallal, O., Gauthier, D., and Malenfant, P., “Classification Methodology for Coupled Shear Walls,” *Journal of Structural Engineering*, American Society of Civil Engineers, Vol. 122, No. 12, December 1996, pp. 1453-1458.

Chaallal, O., Guizani, L., and Malenfant, P., “Drift-Based Methodology for Seismic Proportioning of Coupled Shear Walls,” *Canadian Journal of Civil Engineering*, Vol. 23, No. 5, October, 1996, pp. 1030-1040.

Cheok, G. and Lew, H.S., “Performance of Precast Concrete Beam-to-Column Joints Subject to Cyclic Loading,” *PCI Journal*, Precast/Prestressed Concrete Institute, Vol. 36, No. 3, May-June 1991, pp. 56-67.

Cheok, G. and Lew, H.S., “Model Precast Concrete Beam-to-Column Joints Subject to Cyclic Loading,” *PCI Journal*, Precast/Prestressed Concrete Institute, Vol. 38, No. 4, July-August 1993, pp. 80-92.

Cheok, G. and Lew, H., “Model Precast Concrete Beam-to-Column Connections Subject to Cyclic Loading,” *PCI Journal*, Precast/Prestressed Concrete Institute, Vol. 38, No. 4, July-August 1993, pp. 80-92.

Cheok, G. and Stone, W., “Performance of 1/3 Scale Model Precast Concrete Beam-Column Connections Subjected to Cyclic Inelastic Loads – Report No. 4,” Report NISTIR 5436, National Institute of Standards and Technology, Gaithersburg, MD, 1994, 59pp.

Cheok, G., Stone, W., and Lew, H., “Performance of 1/3-Scale Model Precast Concrete Beam-Column Connections Subjected to Cyclic Inelastic Loads – Report No. 3,” NISTIR 5246, National Institute of Standards and Technology, Gaithersburg, MD, August 1993.

Cheok, G., Stone, W., and Nakaki, S., “Simplified Design Procedure for Hybrid Precast Concrete Joints,” *NISTIR-5765*, National Institute of Standards and Technology, Building and Fire Research Laboratory, Gaithersburg, Maryland, February 1996.

Cheok, G., Stone, W., and Kunnath, S., “Seismic Response of Precast Concrete Frames with Hybrid Joints,” *ACI Structural Journal*, American Concrete Institute, Vol. 95, No. 5, September-October 1998, pp. 527-539.

Christopoulos, C., Filiatrault, A., Uang, C., and Folz, B., “Posttensioned Energy Dissipating Connections for Moment-Resisting Steel Frames,” *Journal of Structural Engineering*, American Society of Civil Engineers, Vol. 128, No. 9, September, 2002, pp. 1111-1120.

Christopoulos, C., Filiatrault, A., and Folz, B., “Seismic Response of Self-Centering Hysteretic SDOF Systems,” *Earthquake Engineering and Structural Dynamics*, Vol. 31, No. 5, May, 2002, pp. 1131-1150.

Cosenza, E. and Pecce, M., “Shear and Normal Stresses Interaction in Coupled Structural Systems,” *Journal of Structural Engineering*, American Society of Civil Engineers, Vol. 127, No. 1, January 2001, pp. 84-88.

El-Sheikh, M., Sause, R., Pessiki, S., Lu, L.W., and Kurama, Y., “Seismic Analysis, Behavior, and Design of Unbonded Post-Tensioned Precast Moment Frames,” *Report No. EQ-97-02*, Department of Civil and Environmental Engineering, Lehigh University, Bethlehem, Pennsylvania, November 1997.

El-Sheikh, M., Sause, R., Pessiki, S., and Lu, L.W., "Seismic Behavior and Design of Unbonded Post-Tensioned Precast Concrete Frames," *PCI Journal*, Precast/Prestressed Concrete Institute, v. 44, No. 3, May-June 1999, pp. 54-71.

El-Sheikh, M., Sause, R., Pessiki, S., and Lu, L.W., "Moment Rotation Behavior of Unbonded Post-Tensioned Precast Concrete Beam-Column Joints," *ACI Structural Journal*, American Concrete Institute, v. 97, No. 1, January-February 2000, pp. 122-131.

El-Sheikh, M., Sause, R., Pessiki, S., and Lu, L.W., "Seismic Analysis, Behavior, and Design of Unbonded Post-Tensioned Precast Frames," Research Report No. EQ-97-02, Department of Civil and Environmental Engineering, Lehigh University, Bethlehem, PA 18015, November 1997, 316 pp.

El-Tawil, S., Kuenzli, C., and Hassan, M., "Pushover of Hybrid Coupled Walls I: Design and Modeling," *Journal of Structural Engineering*, Vol. 128, No. 10, 2002, pp. 1271-1281.

Ertas, O., Ozden, S., and Ozturan T., "Ductile Connections in Precast Moment Resisting Frames," *PCI Journal*, Precast/Prestressed Concrete Institute, Vol. 49, No. 4, May-June 2006, 12 pp.

FEMA-356, <u>Prestandard and Commentary for the Seismic Rehabilitation of Buildings</u>, American Society of Civil Engineers, Reston, Virginia, and Federal Emergency Management Agency (FEMA), Washington, D.C., November 2000.

Fintel, M. and Ghosh, S., "Seismic Resistance of a 31 Storey Frame-Wall Building Using Dynamic Inelastic Response History Analysis," *Proceedings*, 7th World Conference on Earthquake Engineering, Istanbul, 1980, pp. 379-386.

Fintel, M. and Ghosh, S., "Case Study of Aseismic Design of a 16 Storey Coupled Wall Structure Using Inelastic Dynamic Analysis," *ACI Structural Journal*, American Concrete Institute, Vol. 79, No. 3, May-June 1982, pp. 171-179.

Galano, L. and Vignoli, A., "Seismic Behavior of Short Coupling Beams with Different Reinforcement Layouts," *ACI Structural Journal*, American Concrete Institute, Vol. 97, No. 6, 2000, pp. 876-885.

Garlock, M., "Full-Scale Testing, Seismic Analysis, and Design of Post-Tensioned Seismic Resistant Connections for Steel Frames," Ph.D. Dissertation, Civil and Environmental Engineering Department, Lehigh University, Bethlehem, PA, 2002.

Garlock, M., Ricles, J., and Sause, R., "Influence of Design Parameters on Seismic Response of Post-Tensioned Steel MRF Systems," *Engineering Structures*, 2008, pp. 1037-1047.

Garlock, M., Ricles, J. and Sause, R., "Experimental Studies of Full-Scale Posttensioned Steel Connections," *Journal of Structural Engineering*, Vol. 131, No. 3, 2005, pp. 438-448.

Garlock, M., Ricles, J. and Sause, R., "Cyclic Load Tests and Analysis of Bolted Top-and-Seat Angle Connections," *Journal of Structural Engineering*, Vol. 129, No. 12, December 2003, pp. 1615-1625.

Goto, Y., Suzuki, S., and Chen, W. F., "Analysis of Critical Behavior of Semi-Rigid Frames with or without Load History in Connections," *International Journal of Solids and Structures*, Vol. 27, No. 4, 1991, pp. 467-483.

Harries, K., "Ductility and Deformability of Coupling Beams in Reinforced Concrete Coupled Walls," *Earthquake Spectra*, Volume 17, No. 3, August 2001, pp. 457-478.

Harries, K., Gong, B., and Shahrooz, B., "Behavior and Design of Reinforced Concrete, Steel, and Steel-Concrete Coupling Beams," *Earthquake Spectra*, Volume 16, No. 4, November 2000, pp. 775-799.

Harries, K., Mitchell, D., Redwood, R., and Cook, W., "Nonlinear Seismic Response Predictions of Walls Coupled with Steel and Concrete Beams," *Canadian Journal of Civil Engineering*, Vol. 25, No. 5, October 1998, pp. 803-818.

Hawileh, R., Tabatabai, H., Rahman, A., and Amro, A., "Non-Dimensional Design Procedures for Precast, Prestressed Concrete Hybrid Frames," *PCI Journal*, Precast/Prestressed Concrete Institute, September-October 2006, 22 pp.

Hibbitt, Karlsson, and Sorensen, ABAQUS User's Manual, Hibbitt, Karlsson, & Sorensen, Inc., Version 6.3, 2002

Kasai, K., Hodgson, I., and Blelman, D., "Rigid-Bolted Repair Method for Damaged Moment Connections," *Engineering Structures*, Vol. 20, Nos. 4-6, 1998, pp. 521-532.

Kim, H and Christopoulos, C., "Seismic Design Procedure and Seismic Response of Post-Tensioned Self-Centering Steel Frames," *Earthquake Engineering and Structural Dynamics*, Vol. 38, 2009, pp. 355-376.

Kishi, N., and Chen, W.F., "Moment-Rotation Relations of Semirigid Connections with Angles," *Journal of Structural Engineering*, American Concrete Institute, Vol. 116, No. 7, July 1990, pp. 1813-1834.

Kukreti, A. R. and Abolmaali, A., "Moment-Rotation Hysteresis Behavior of Top and Seat Angle Steel Frame Connections," *Journal of Structural Engineering*, American Society of Civil Engineers, Vol. 125, No. 8, 1999, pp. 810-820.

Kurama, Y. and Shen, Q., "Post-Tensioned Hybrid Coupled Walls under Lateral Loads." *Journal of Structural Engineering*, American Society of Civil Engineers, Vol. 130, No. 2, 2004, 297-309.

Kurama, Y., Weldon, B., and Shen, Q., "Experimental Evaluation of Post-Tensioned Hybrid Coupled Wall Subassemblages," *Journal of Structural Engineering*, American Society of Civil Engineers, Vol. 132, No. 7, 2006, pp. 1017-1029.

Kurama, Y., Weldon, B., and Shen, Q., "Experimental Evaluation of Unbonded Post-Tensioned Hybrid Coupled Wall Subassemblages," *13th World Conference on Earthquake Engin.*, Vancouver, BC, Canada, August 1-6, 2004, 15 pp. (CD-ROM)

Lee, J.-Y. and Wantanabe, F., "Predicting the Longitudinal Axial Strain in the Plastic Hinge Regions of Reinforced Concrete Beams Subjected to Reversed Cyclic Loading," *Engineering Structures*, 2003, pp. 927-939.

Leon, R.T., and Shin, K. J., "Seismic Performance of Semi-Rigid Composite Frames," *Proceeding of the 5USNCEE*, Vol. 1, Earthquake Engineering Research Institute, 1994, pp. 243-252.

Lorenz, R., Kato, B., and Chen, W., Semi-Rigid Connections in Steel Frames, Council on Tall Buildings and Urban Habitat, Committee 43, McGraw-Hill, Inc., 1993.

MacRae, G. and Priestley, M., "Precast Post-Tensioned Ungrouted Concrete Beam-Column Subassemblage Tests," *Report No. PRESSS-94/01*, Department of Applied Mechanics and Engineering Sciences, University of California, San Diego, California, March 1994.

Mander, J., Priestley, M., and Park, R., "Theoretical Stress-Strain Model for Confined Concrete," *Journal of Structural Engineering*, American Society of Civil Engineers, Vol. 114, No. 8, 1988, 1804–1826.

Mander, J., Chen, S. and Pekan, G., "Low-Cycle Fatigue Behavior of Semi-Rigid Top-and-Seat Angle Connections," *Engineering Journal*, Vol. 31, No. 3, 1994, pp.111-121.

Matsuoka, K., Kishi, N., Chen, W., and Goto, Y., "Analysis Program for the Design of Flexibly Jointed Frames," Computers and Structures, Vol. 49, Nov. 1993, pp. 705-713.

Morgen, B. and Kurama, Y., "A Friction Damper for Post-Tensioned Precast Concrete Moment Frames," *PCI Journal*, Precast/Prestressed Concrete Institute, 49(4), 2004, 112-133.

Morgen, B. and Kurama, Y., "A Friction Damper for Post-Tensioned Precast Concrete Beam-to-Column Joints," *PCI Journal*, Precast/Prestressed Concrete Institute, Vol. 49, No. 4, July-August 2004, pp. 112-133.

Morgen, B. and Kurama, Y., "An Innovative Friction-Damped Precast Concrete Frame Structure for Seismic Regions," *ASCE Structures Congress*, American Society of Civil Engineers, New York, NY, April 20-24, 2005, 12 pp.

Morgen, B. and Kurama, Y., "Seismic Design of Friction-Damped Precast Concrete Frame Structures," *Journal of Structural Engineering*, American Society of Civil Engineers, Vol. 133, No. 11, November 2007, pp. 1501-1511.

Morgen, B. and Kurama, Y., "Seismic Response Evaluation of Post-Tensioned Precast Concrete Frames with Friction Dampers," *Journal of Structural Engineering*, American Society of Civil Engineers, Vol. 134, No. 1, January 2008, pp. 132-145.

Morgen, B. and Kurama, Y., "Characterization of Two Friction Interfaces for Use in Seismic Damper Applications," *Materials and Structures*, Vol. 42, No. 1, January 2009, pp. 35-49.

Munshi, J. and Ghosh, S., "Displacement-Based Seismic Design for Coupled Wall Systems," *Earthquake Spectra*, Volume 16, No.3, August 2000, pp. 621-642.

Nakaki, S., Stanton, J., and Sritharan, S., "An Overview of the PRESSS Five-Story Precast Test Building," *PCI Journal*, Precast/Prestressed Concrete Institute, Vol. 44, No. 2, March-April 1999, pp. 26-39.

Park, H. and Eom, T., "Truss Model for Nonlinear Analysis of RC Members Subject to Cyclic Loading," *Journal of Structural Engineering*, American Society of Civil Engineers, Vol. 133, No. 10, October 2007, pp. 1351-1363.

Park, R. and Paulay,T., Reinforced Concrete Structures, John Wiley & Sons, New York, 1975.

Paulay, T., "Simulated Seismic Loading of Spandrel Beams," *Proceedings*, American Society of Civil Engineers Structural Journal, Vol. 97, No. ST9, September, 1971a, pp. 2407-2419.

Paulay, T., "Coupling Beams of Reinforced Concrete Shear Walls," *Proceedings*, American Society of Civil Engineers Structural Journal, Vol. 97, No. ST3, March, 1971b, pp. 843-862.

Paulay, T., "Ductility of Reinforced Concrete Shear Walls for Seismic Areas," in "Reinforced Concrete Structures in Seismic Zones", American Concrete Institute, SP-53, 1977, pp. 127-147.

Paulay, T. and Binney, J., "Diagonally Reinforced Coupling Beams of Shear Walls," in "Shear in Reinforced Concrete", American Concrete Institute, SP-42, Vol. 2, 1974, pp. 579-598.

Paulay, T., "A Displacement-Focused Seismic Design of Mixed Building Systems," *Earthquake Spectra*, Volume 18, No.4, November 2002, pp. 689-718.

Paulay, T. and Priestley, M., “Seismic Design of Reinforced Concrete and Masonry Buildings,” John Wiley & Sons, Inc., 1992, 744 pp.

Paulay, T. and Santhakumar, A., “Ductile Behavior of Coupled Shear Walls,” *Journal of Structural Engineering*, American Society of Civil Engineers, Vol. 102, No. ST1, January 1976, pp. 93-108.

PCI, PCI Design Handbook, Sixth Edition, Precast/Prestressed Concrete Institute, Chicago, IL, 2004.

Pekau, O. and Cistra, V., “Behavior of Nonlinear Coupled Shear Walls with Flexible Bases,” *Canadian Journal of Civil Engineering*, Vol. 18, February 1989, pp. 45-54.

Prakash, V., Powell, G., and Campbell, S., “DRAIN-2DX Base Program Description and User Guide; Version 1.10,” Rep. No. UCB/SEMM-93/17, Department of Civil Engineering, University of California, Berkeley, California, 1993.

Priestley, M., and MacRae, G., “Seismic Tests of Precast Beam-to-column Joint Subassemblages With Unbonded Tendons,” *PCI Journal*, Precast/Prestressed Concrete Institute, Vol. 41, No. 1, January-February 1996, pp. 64-81.

Priestley, M., Sritharan S., Conley J., Pampanin S., “Preliminary Results and Conclusions from the PRESSS Five-Story Precast Concrete Test Building,” *PCI Journal*, Precast/Prestressed Concrete Institute, Vol. 44, No.6, November-December 1999, pp. 42-67.

Priestley, M. and Tao, J.R., “Seismic Response of Precast Prestressed Concrete Frames with Partially Debonded Tendons,” *PCI Journal*, Precast/Prestressed Concrete Institute, v. 38, No. 1, January-February 1993, pp. 58-67.

PTI, “Specification for Unbonded Single Strand Tendons,” Post-Tensioning Institute, Phoenix, AZ, 2003.

Rahman, M. and Sritharan, S., “Performance-Based Seismic Evaluation of Two Five-Story Precast Concrete Hybrid Frame Buildings,” *Journal of Structural Engineering*, American Society of Civil Engineers, Vol. 133, No. 11, 2007, pp. 1489-1500.

Ricles, J., Sause, R., Peng, S., and Lu, L., “Experimental Evaluation of Earthquake Resistant Posttensioned Steel Connections,” *Journal of Structural Engineering*, American Society of Civil Engineers, Vol. 128, No.7, 2002, pp. 850-859.

Ricles, J., Sause, R., Garlock, M., and Zhao, C., “Posttensioned Seismic-Resistant Connections for Steel Frames,” *Journal of Structural Engineering*, American Society of Civil Engineers, Vol. 127, No. 2, February, 2001, pp. 113-121.

Rojas, P., Ricles, J. M., and Sause, R., "Seismic Performance of Post-tensioned Steel Moment Frames With Friction Devices," *Journal of Structural Engineering*, American Society of Civil Engineers, Vol. 131, No. 4, April 2005, pp. 529-540.

Saatcioglu, M., Derecho, A., and Corley, W., "Parametric Study of Earthquake-Resistant Coupled Walls," *Journal of Structural Engineering*, American Society of Civil Engineers, Vol. 113, No. 1, January 1987, pp. 141-157.

Sarraf, M. and Bruneau, M., "Cyclic Testing of Existing and Retrofitted Riveted Stiffened Seat Angle Connections," *Journal of Structural Engineering*, American Society of Civil Engineers, Vol. 122, No. 7, 1996, pp. 762-775.

Seo, C.-Y., and Sause, R., "Ductility Demands on Self-Centering Systems under Earthquake Loading," *ACI Structural Journal*, American Concrete Institute, Vol. 102, No. 2, 2005, pp. 275-285.

Shen, J. and Astaneh-Asl, A., "Hysteretic Model of Bolted Angle Connections," *Journal of Construction Steel Research*, Vol. 54, 1999, pp. 317-343.

Shen, J. and Astaneh-Asl, A., "Hysteretic Behavior of Bolted Angle Connections," *Journal of Construction Steel Research*, Vol. 51, No. 3, July, 1999, pp. 201-218.

Shen, Q. and Kurama, Y., "Lateral Load Behavior of Unbonded Post-Tensioned Hybrid Coupled Walls," *Sixth ASCCS Conference on Steel and Concrete Composite Structures*, Los Angeles, CA, March 22-24, 2000, 793-800.

Shen, Q. and Kurama, Y., "Coupling of Concrete Walls using Unbonded Post-Tensioning," *7th U.S. National Conference on Earthquake Engineering*, Earthquake Engineering Research Institute, Boston, MA, July 21-2, 2002a, 12 pp. (CD-ROM)

Shen, Q. and Kurama, Y., "Nonlinear Behavior of Post-Tensioned Hybrid Coupled Wall Subassemblages," *Journal of Structural Engineering*, American Society of Civil Engineers, Vol. 128, No. 10, 2002b, pp. 1290-1300.

Shen, Q., Kurama, Y., and Weldon, B., "Analytical Modeling and Design of Post-Tensioned Hybrid Coupled Wall Subassemblages," *Journal of Structural Engineering*, American Society of Civil Engineers, Vol. 132, No.7, 2006, pp. 1030-1040.

Sims, J., "Flange Angle Behavior in Semi-Rigid Connections for Steel PR Frames," MS thesis, Department of Civil Engineering and Geological Sciences, University of Notre Dame, Notre Dame, Indiana, April 2000, 187 pp.

Srichatrapimuk, T., "Earthquake Responses of Coupled Shear Wall Buildings," Earthquake Engineering Research Center, Report No. UCB/EERC-76/27, 1976, 117pp.

Stanton, J. and Nakaki, S., “Design Guidelines for Precast Concrete Seismic Structural Systems,” *Report No. PRESSS-01/03-09*, Department of Civil Engineering, University of Washington, Seattle, Washington, February 2002.

Stanton, J., Stone, W., and Cheok, G., “A Hybrid Reinforced Precast Frame for Seismic Regions”, *PCI Journal*, Precast/Prestressed Concrete Institute, v. 42, No. 2, March-April 1997, pp. 20-32.

Stone, W., Cheok, G., and Stanton, J., “Performance of Hybrid Moment-Resisting Precast Beam-Column Concrete Connections Subjected to Cyclic Loading,” *ACI Structural Journal*, American Concrete Institute, Vol. 91, No. 2, March-April 1995, pp. 229-249.

Subedi, N. K., “RC-Coupled Shear Wall Structures I – Ultimate Strength Calculations,” *Journal of Structural Engineering*, American Society of Civil Engineers, Vol. 117, No. 3, 1991b, pp. 681-698.

Subedi, N. K., “RC-Coupled Shear Wall Structures I – Analysis of Coupling Beams,” *Journal of Structural Engineering*, American Society of Civil Engineers, Vol. 117, No. 3, 1991a, pp. 667-680.

Swanson, J. and Leon, R., “SAC Steel Project.” <http://www.ce.gatech.edu/~sac/>, School of Civil and Environmental Engineering, Georgia Institute of Technology, GA, 1999.

Tassios, T., Moretti, M., and Bezas A., “On the Behavior and Ductility of Reinforced Concrete Coupling Beams of Shear Walls,” *ACI Structural Journal*, American Concrete Institute, V. 93, No. 6, November-December 1996, pp. 711-720.

Teshigawara, M., Sugaya, K., Kato, M., and Matsushima, Y., “Seismic Test on 12-Story Coupled Shear Wall with Flange Walls,” reprinted in *List of Technical Papers Written in English Authored by Japan-Side Researchers*, U.S.-Japan Cooperative Earthquake Research Program on Composite and Hybrid Structures, December 2000.

Wallace, J., “Modeling Issues for Tall Reinforced Concrete Core Wall Buildings,” *The Structural Design of Tall and Special Buidlings*, Vol. 16, 2007, pp. 615-632.

Walsh, K. and Kurama, Y., “Behavior of Unbonded Post-Tensioning Mono-Strand/Anchorage Systems under Monotonic Tensile Loading,” *PCI Journal*, Precast/Prestressed Concrete Institute, Vol. 55, No. 1, Winter 2010, pp. 97-117.

Walsh, K and Kurama, Y., “Behavior and Design of Unbonded Post-Tensioning Strand/Anchorage Systems for Seismic Applications,” Structural Engineering Research Report #NDSE-09-02, Department of Civil Engineering and Geological Sciences, University of Notre Dame, Notre Dame, Indiana, April 2009, 130 pp.

Weldon, B. and Kurama, Y., "Post-tensioned Precast Coupling Beam Systems," *8th National Conference on Earthquake Engineering*, San Francisco, CA, April 18-22, 2006, 10 pp.

Youssef-Agha, W., Aktan, H.M., and Olowokere, O. D., "Seismic Response of Low-Rise Steel Frames," *Journal of Structural Division*, American Society of Civil Engineers, Vol. 115, No. 3, 1989, pp. 594-607.

APPENDIX A

CONCRETE MIX DESIGN
GROUT MIX DESIGN

CONCRETE MIX DESIGN
2361 [25]
6,000 psi
1/25/2005

Contractor : StresCore
Project : Test pour
Source of Concrete : Aggregate Industries
Construction Type :
Placement :

Weights per Cubic Yard (Saturated, Surface-Dry)	Quantity	Density	Yield, ft^3
ASTM C150 Type 1 Cement, Lafarge, Alpena, lb	480	3.150	2.44
ASTM C618 Class C Fly Ash, ISG Resources, lb	85	2.600	0.52
Water, lb	266	1.000	4.26
INDOT #11 Limestone, Vulcan Q972053, lb	1,792	2.720	10.56
INDOT #23 Sand, Aggregate Ind. Q982081, lb	1,429	2.650	8.64
ASTM C494 Type A MRWR Grace Mira 92, oz (US)	28.3	1.000	0.03
Total Air, %	2.0 ± 1.0		0.54
		TOTAL	27.00

Water/Cement Ratio, lbs/lb	0.47
Slump, High, in	5.00
Low, in	5.00
Concrete Unit Weight, pcf	150.15
Yield, %	100.0

Exposure Condition : Severe exposure

Mr. Aaron Johnson:
The above mix design, #2361 6000 psi #11 limestone, is re-submitted for your approval. We recommend a minimum load of 2 cubic yards to assure proper batching & mixing. You may call 1-888-537-2050 to order concrete.

Prepared by :

Tom Atkins, Quality Control Manager

Concrete Mix Design

Grout Mix (final design mix, 10x fibers)

	Weight (g)	Specific Gravity	Volume (cc)	
Cement	4259.7	3.15	1352.29	
Water	1597.39	1.0	1597.39	
Sand	5112.77	2.6	1966.45	
Fiber	29.50			
		Total Volume =	4916.13	cc
			300.00	in^3
			0.17	ft^3

Normal Fiber content is 16.99 g/ft^3

Adjustment for Moisture Content of Sand:

Grout Mix Design

APPENDIX B

TEST SETUP
MA ANCHOR DETAILS

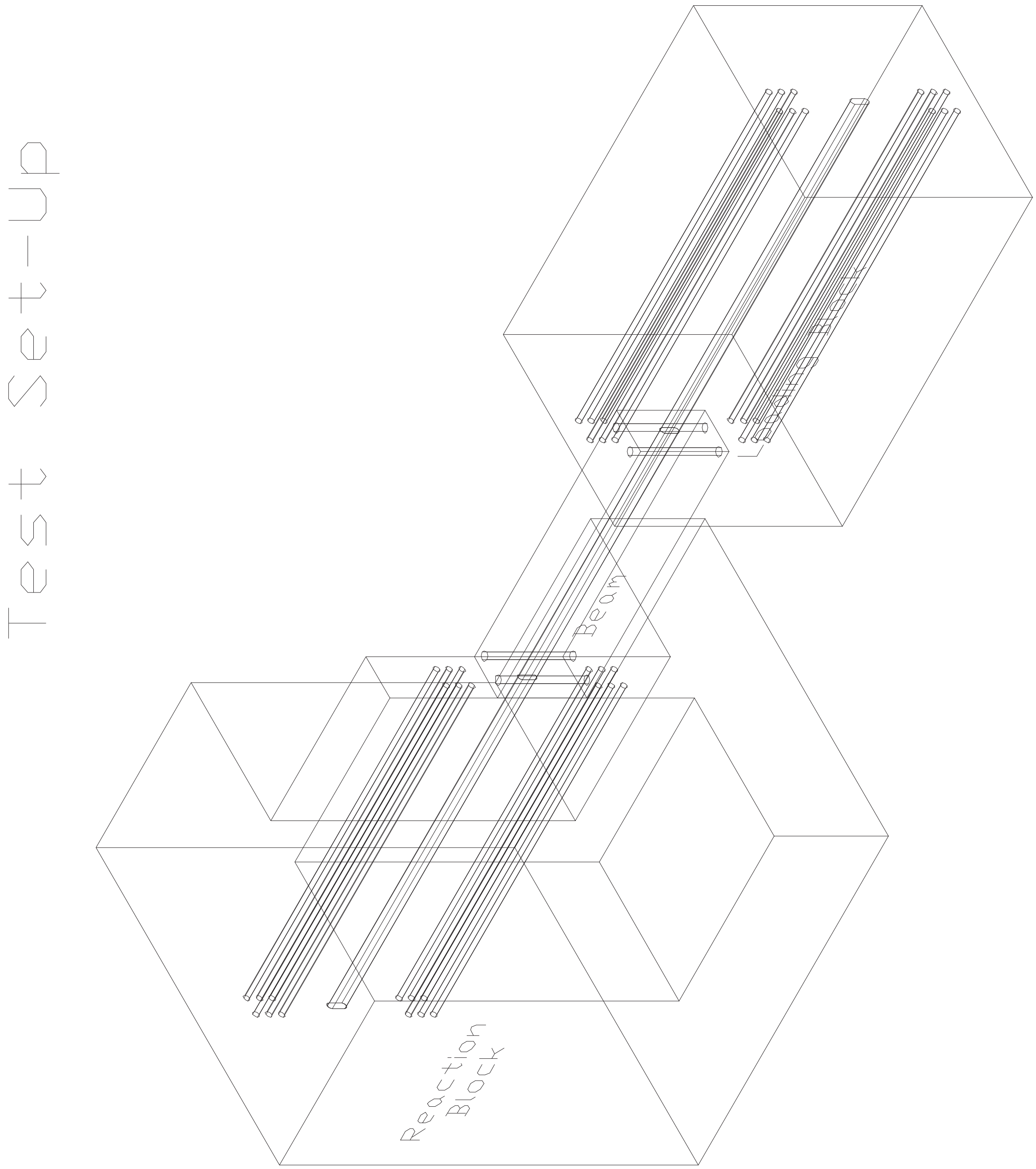

Figure B-1Test setup isometric view.

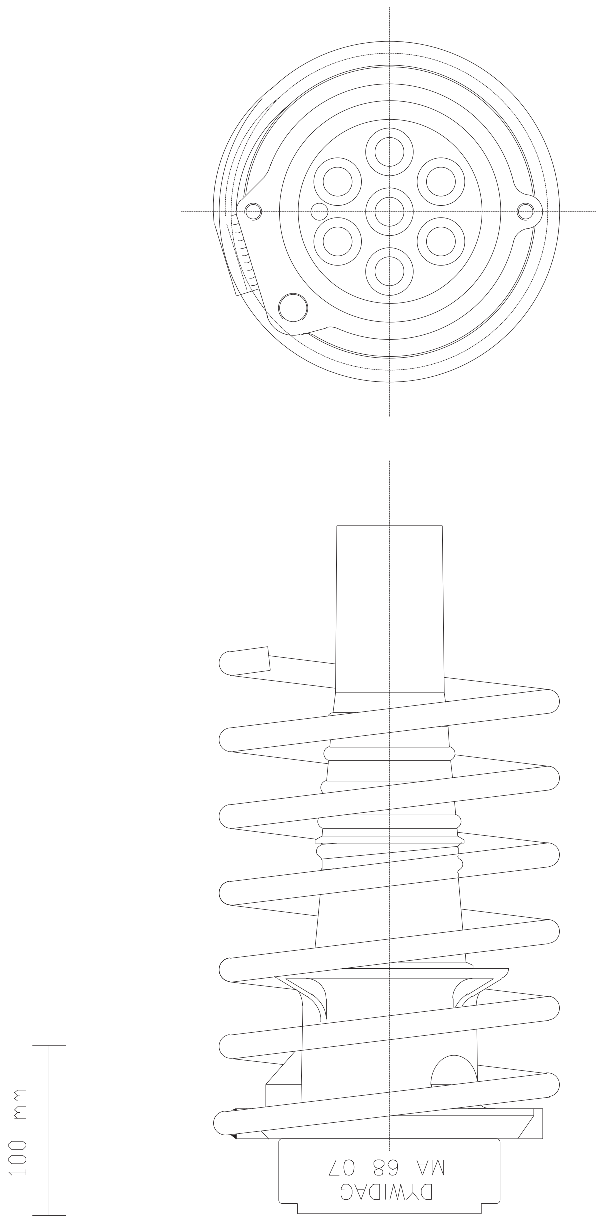

Figure B-2: MA Anchor details.

APPENDIX C

BEAMS 1-3 DESIGN DETAILS

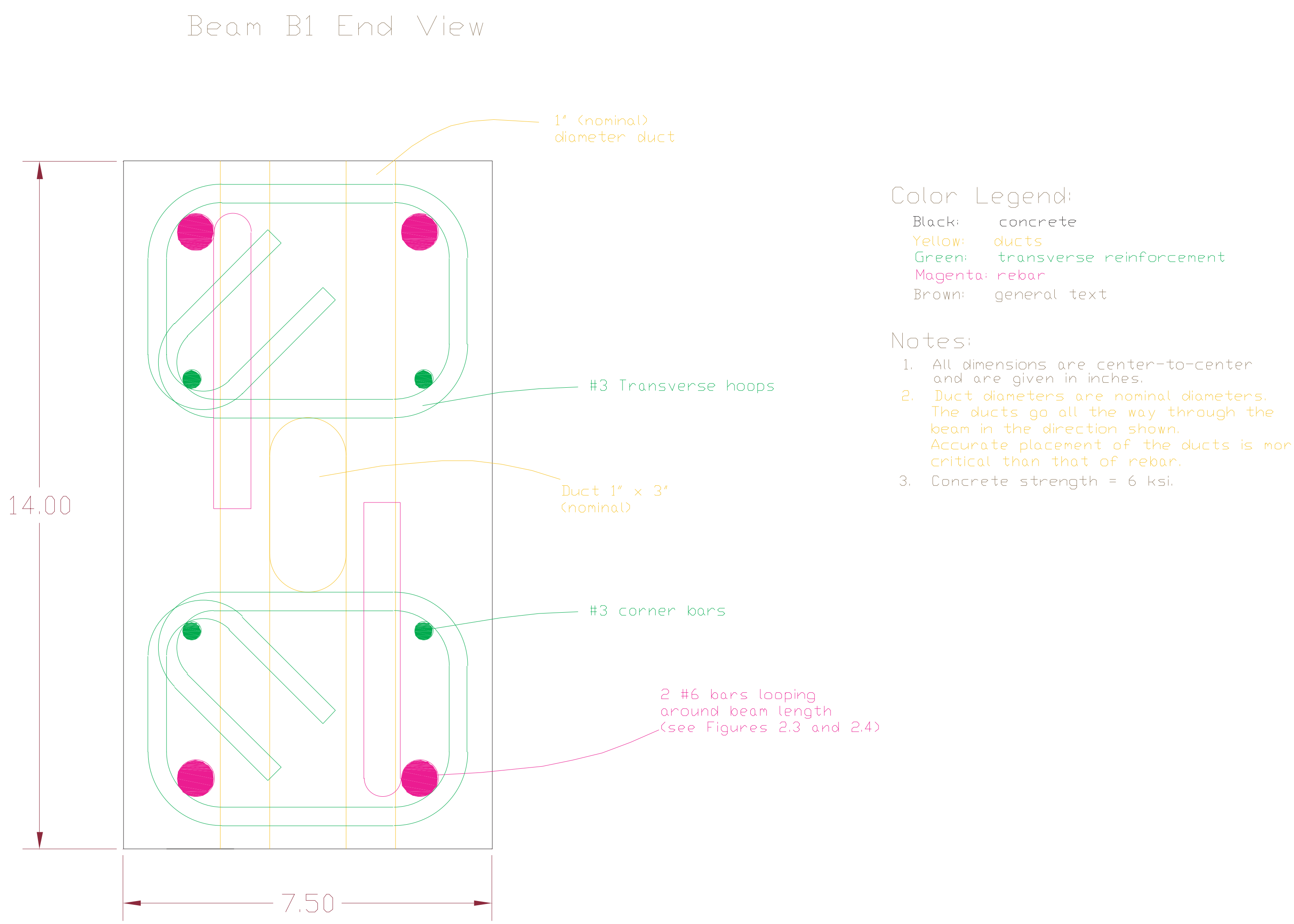

Figure C-1: Beams 1-3 end view – general properties.

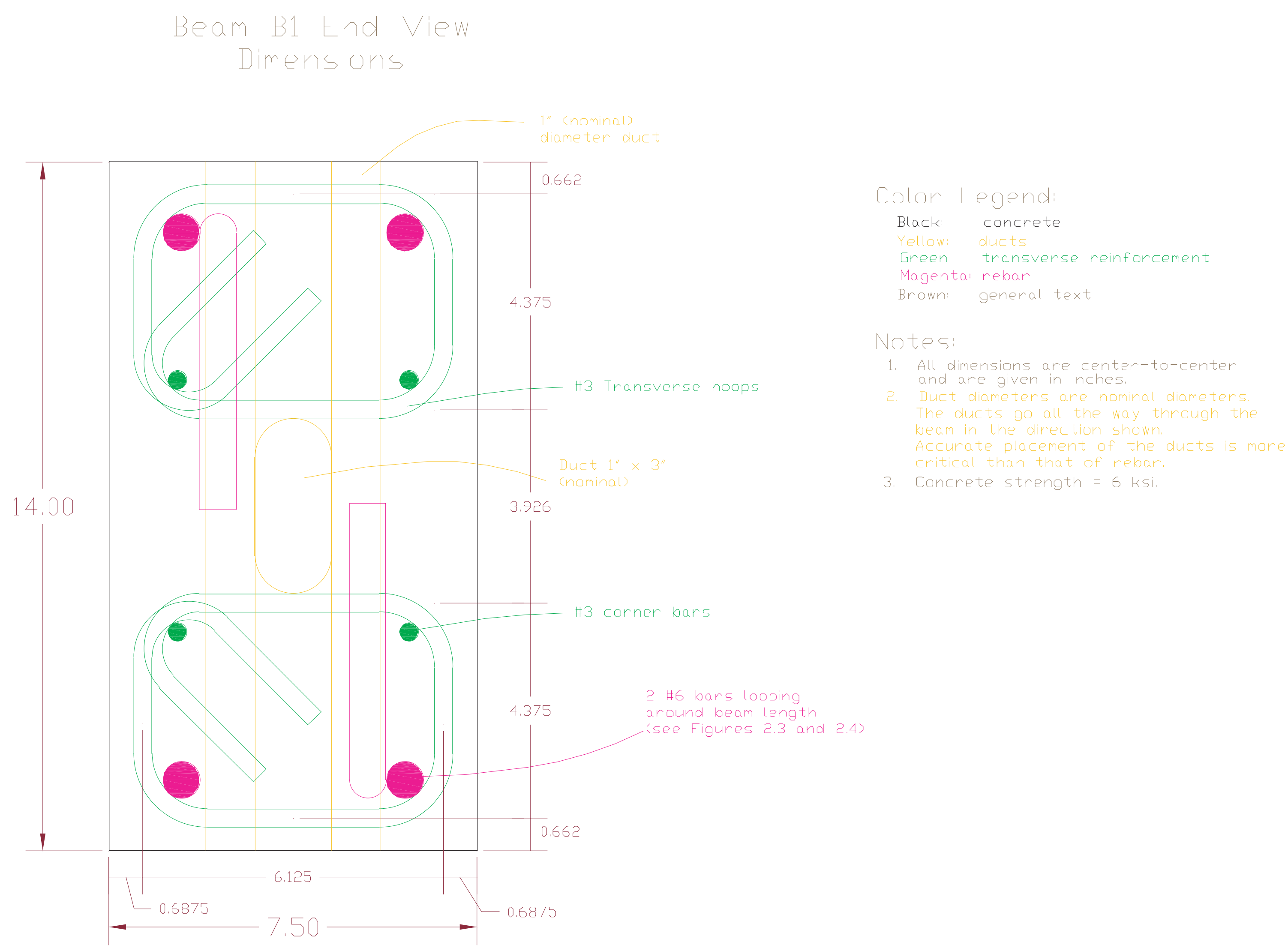

Figure C-2: Beams 1-3 end view – general dimensions.

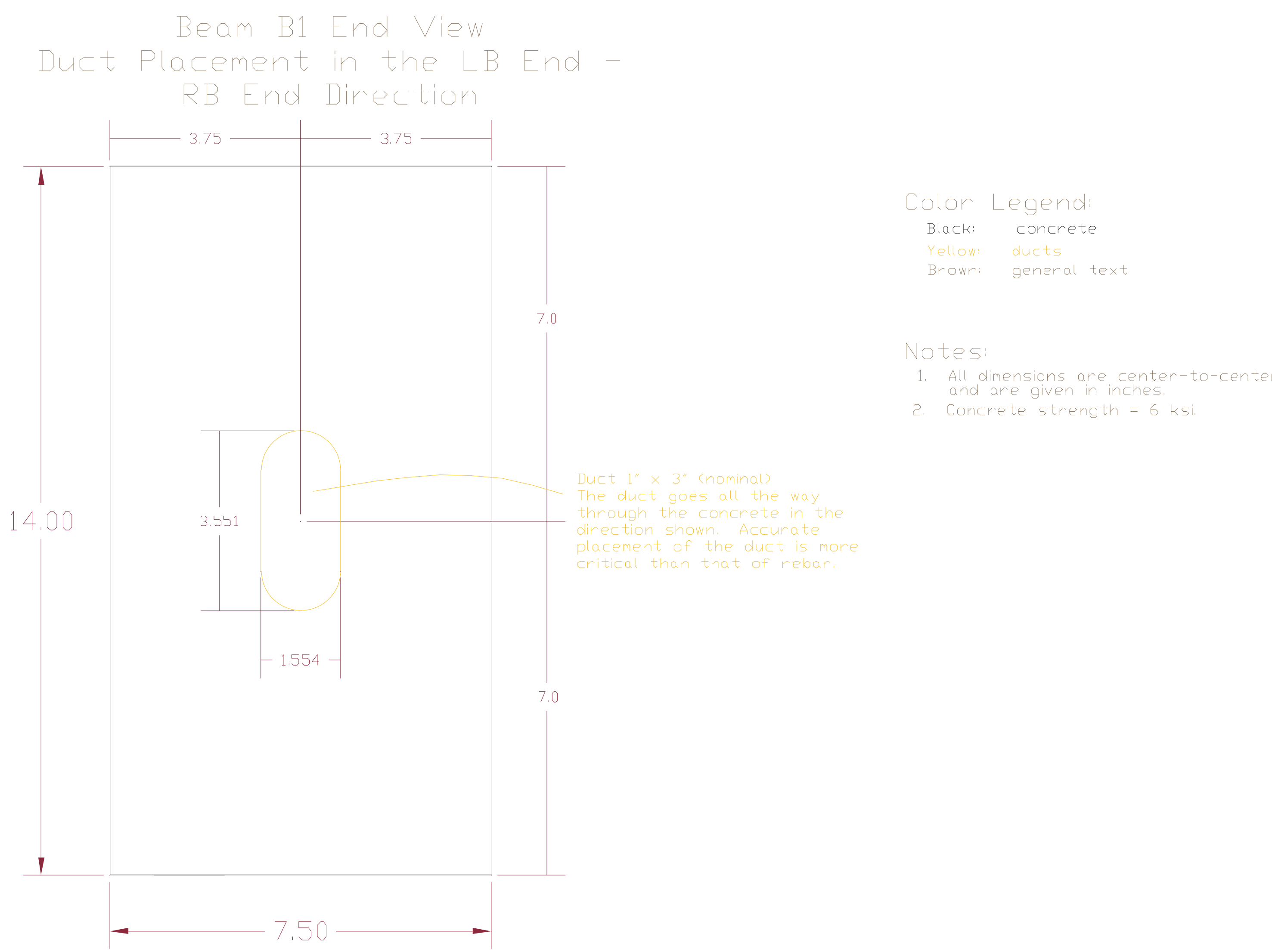

Figure C-3: Beams 1-3 end view – duct placement.

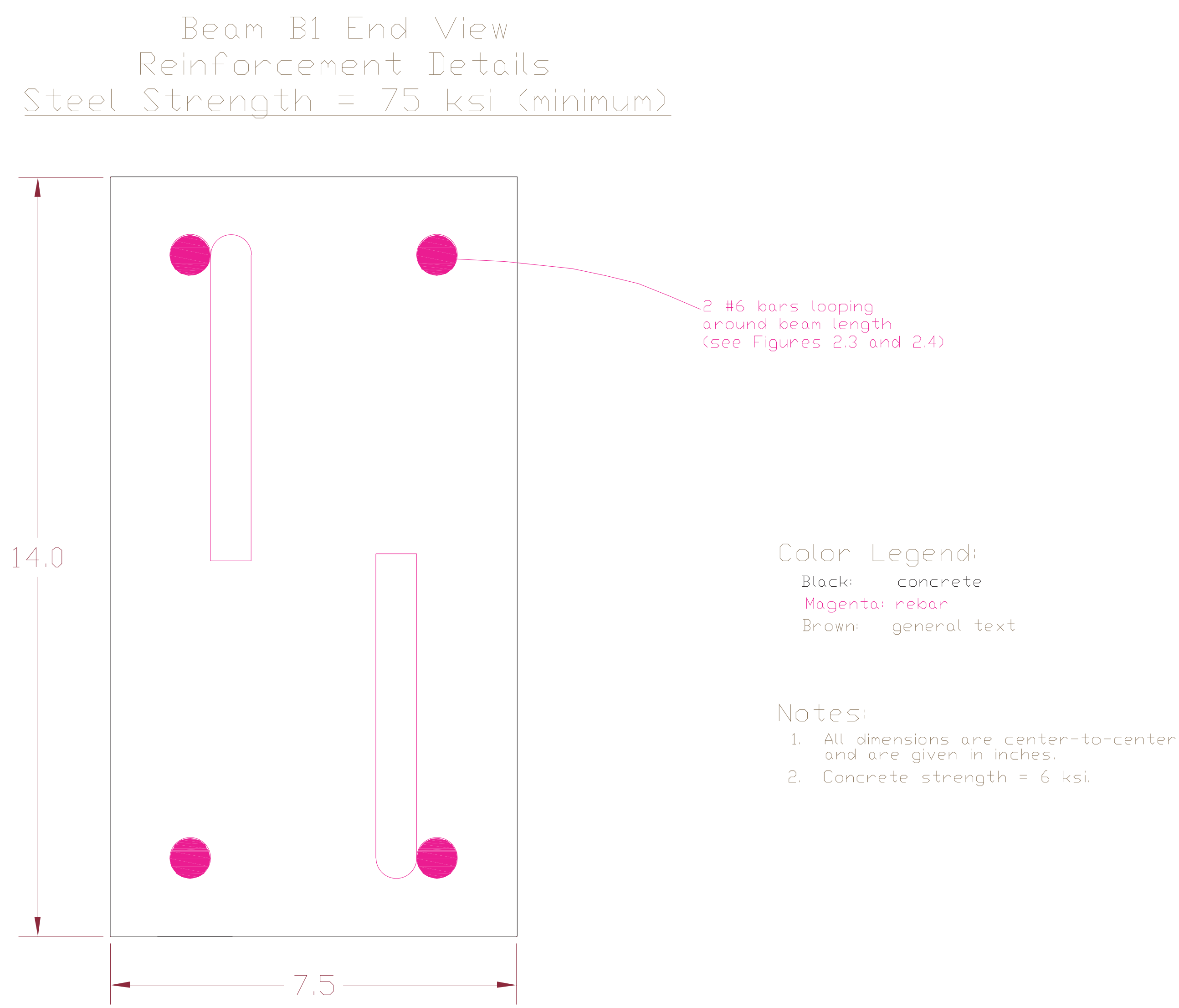

Figure C-4: Beams 1-3 end view – looping reinforcement details.

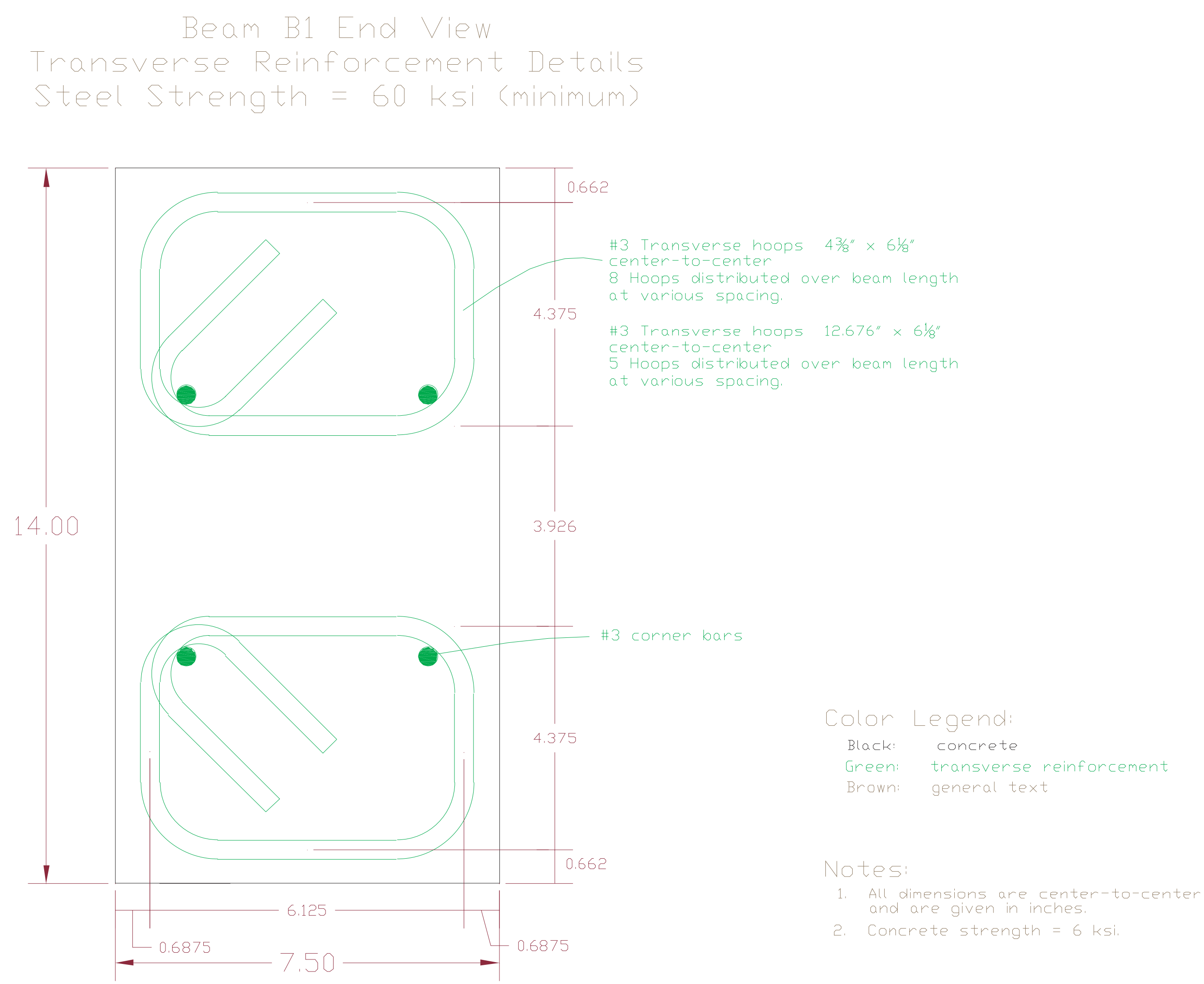

Figure C-5: Beams 1-3 end view – transverse reinforcement details.

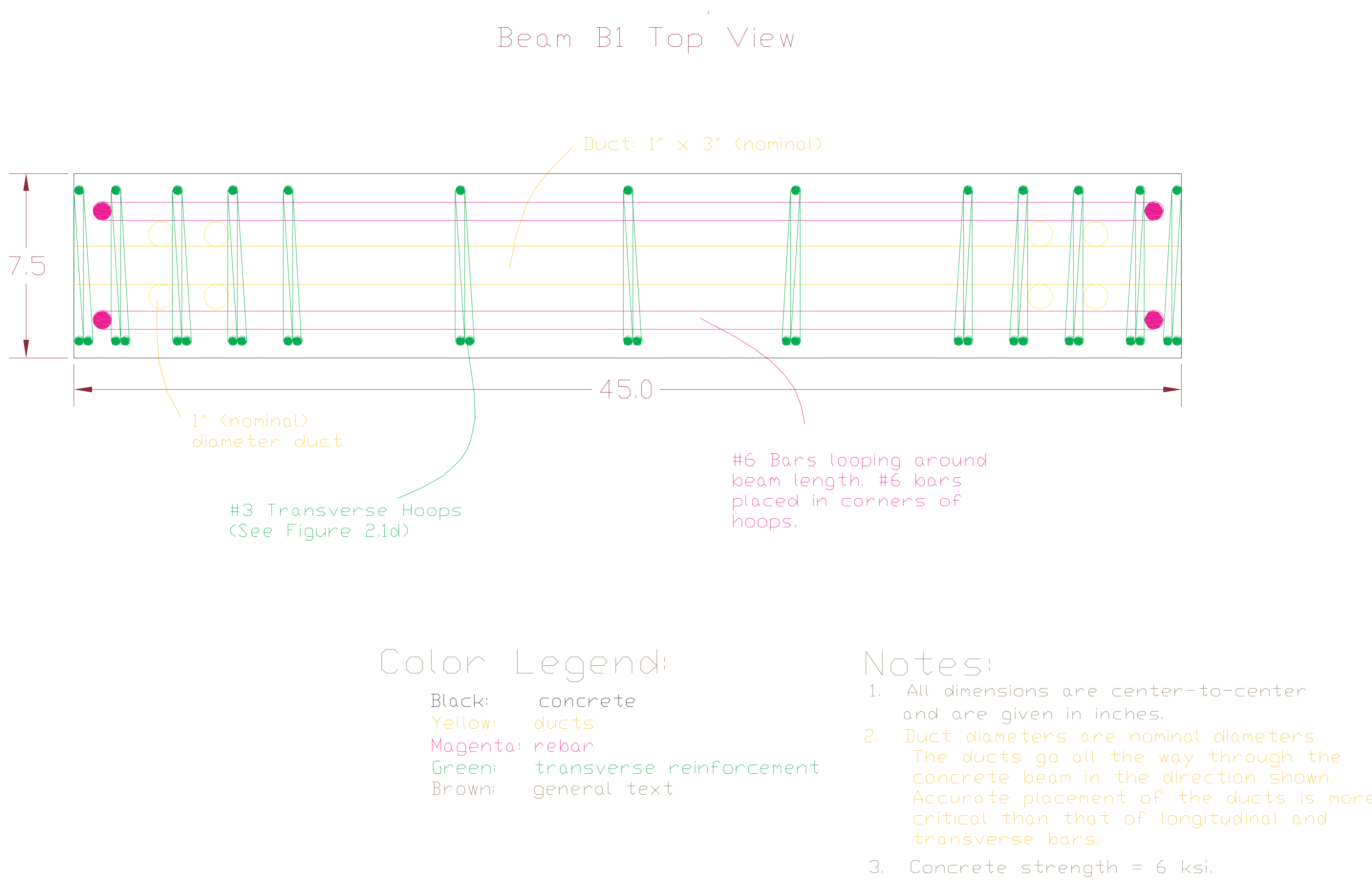

Figure C-6: Beams 1-3 top view – general properties.

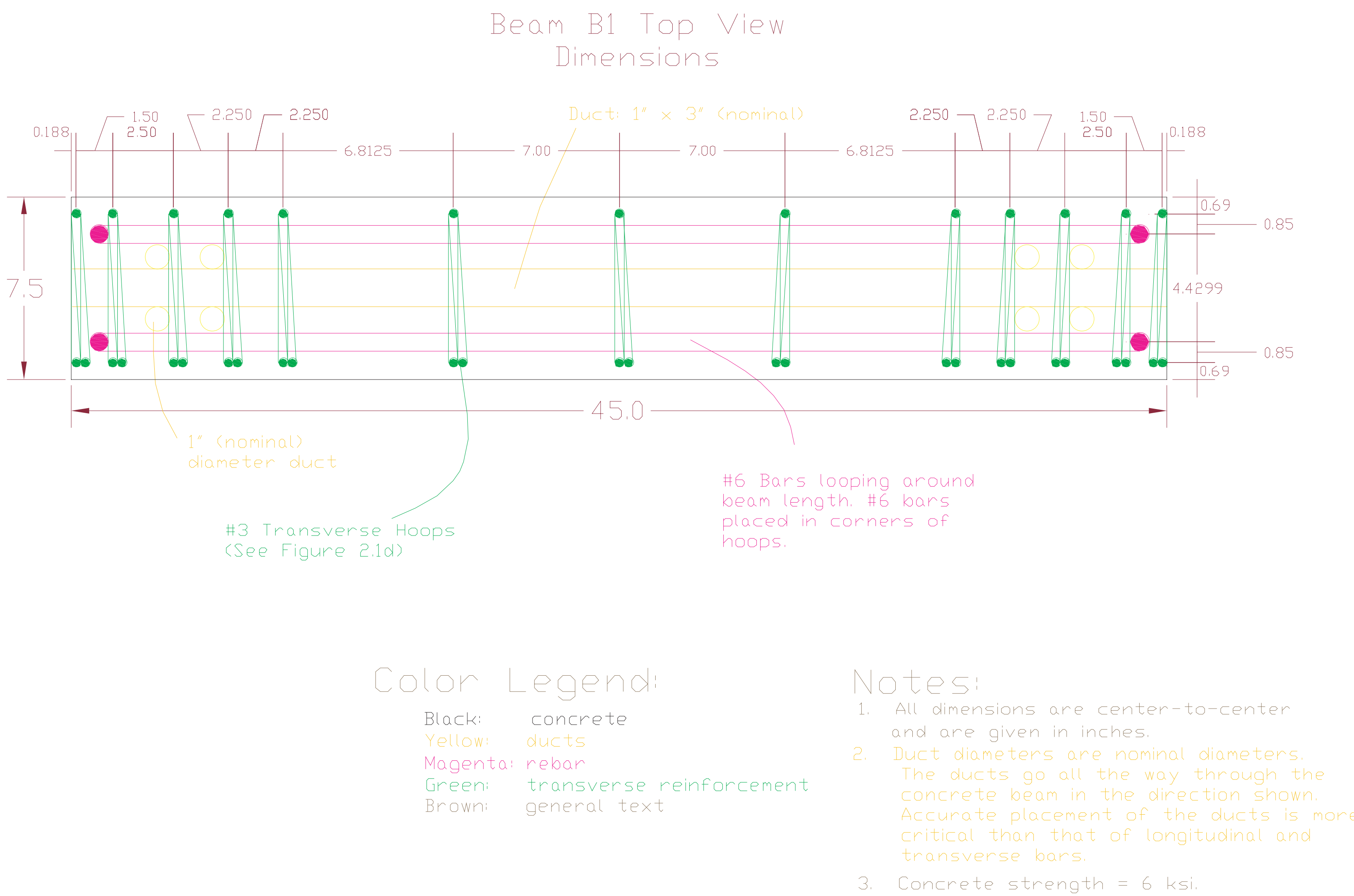

Figure C-7: Beams 1-3 top view – general dimensions.

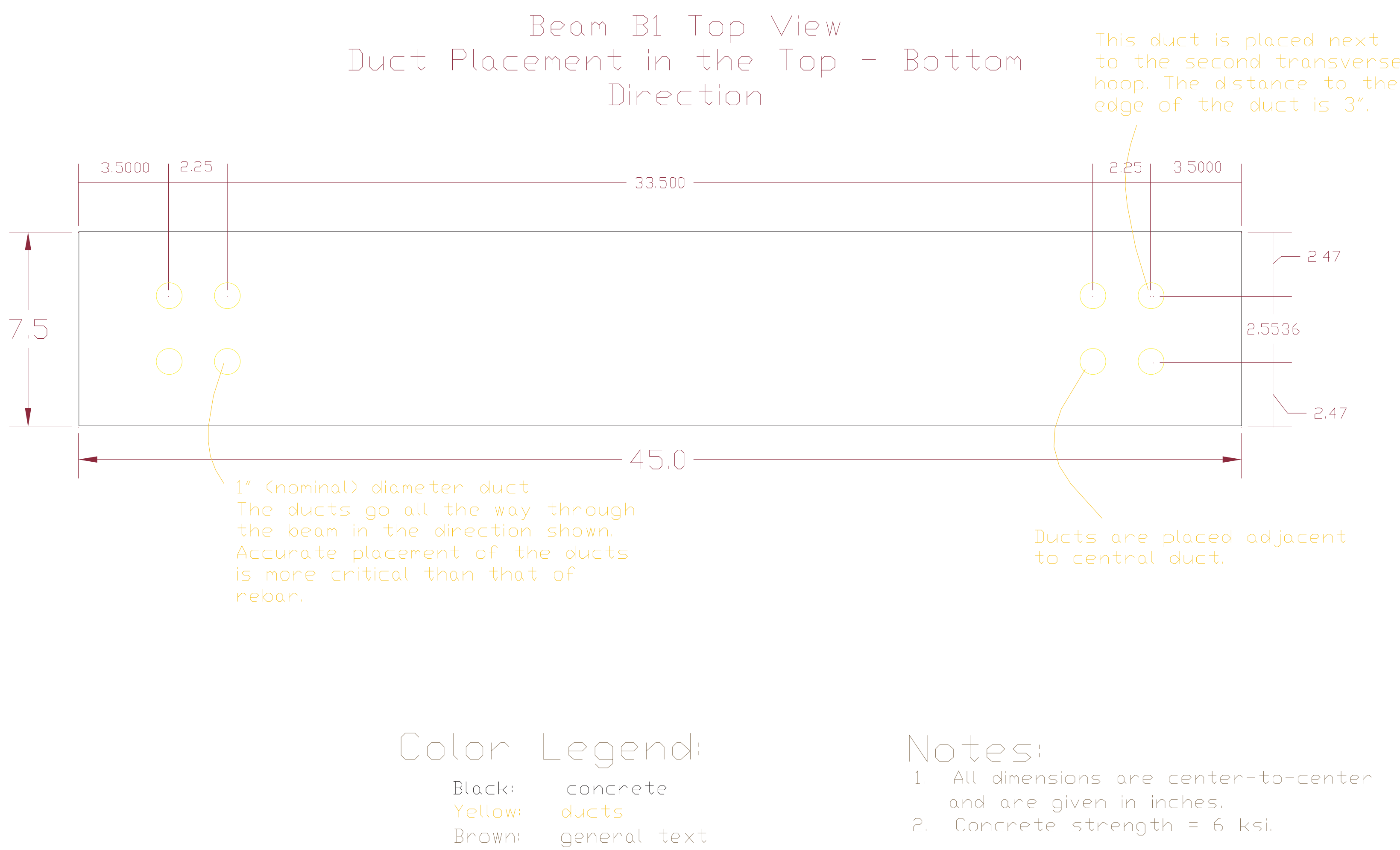

Figure C-8: Beams 1-3 top view – duct placement.

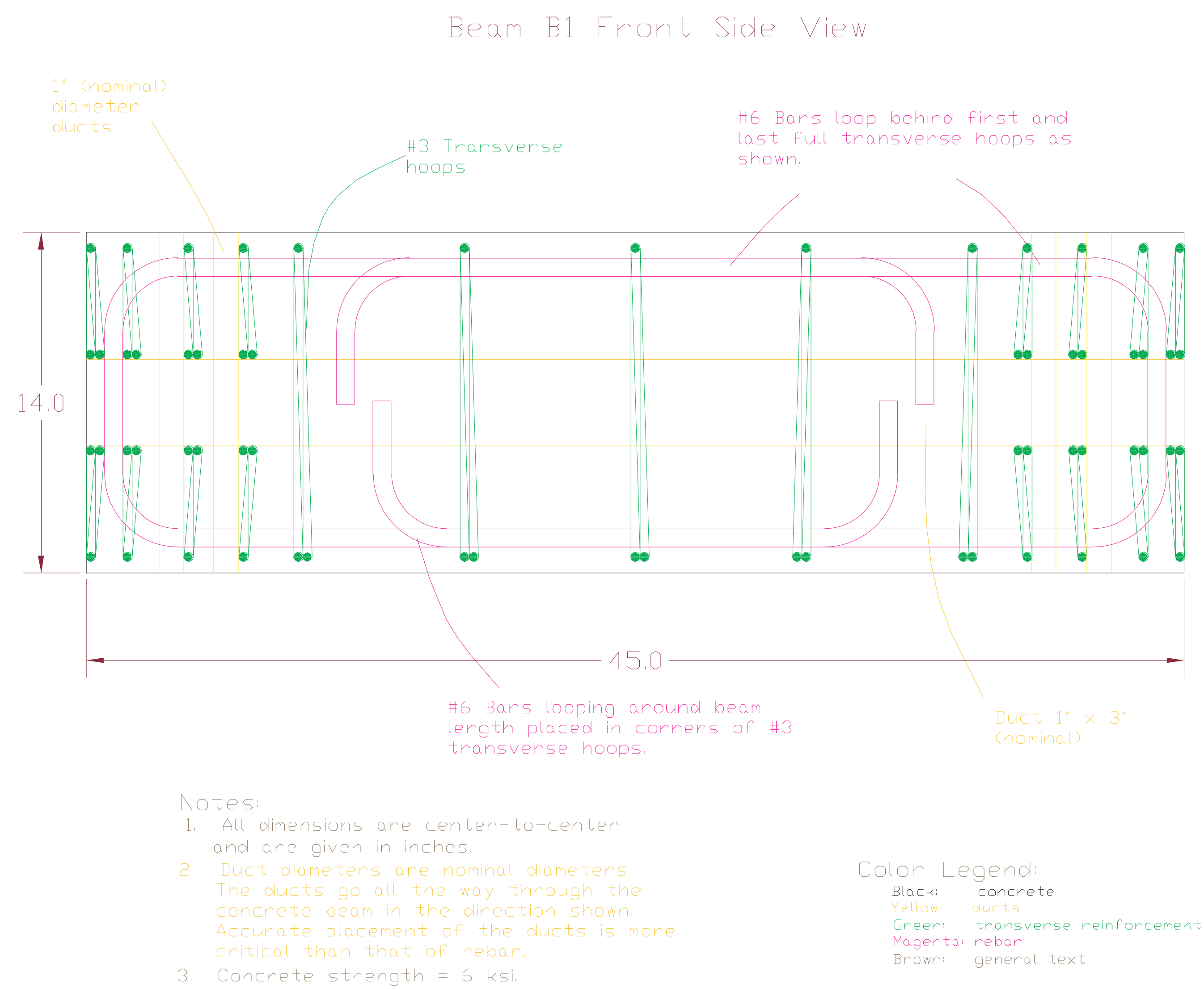

Figure C-9: Beams 1-3 front side view – general properties.

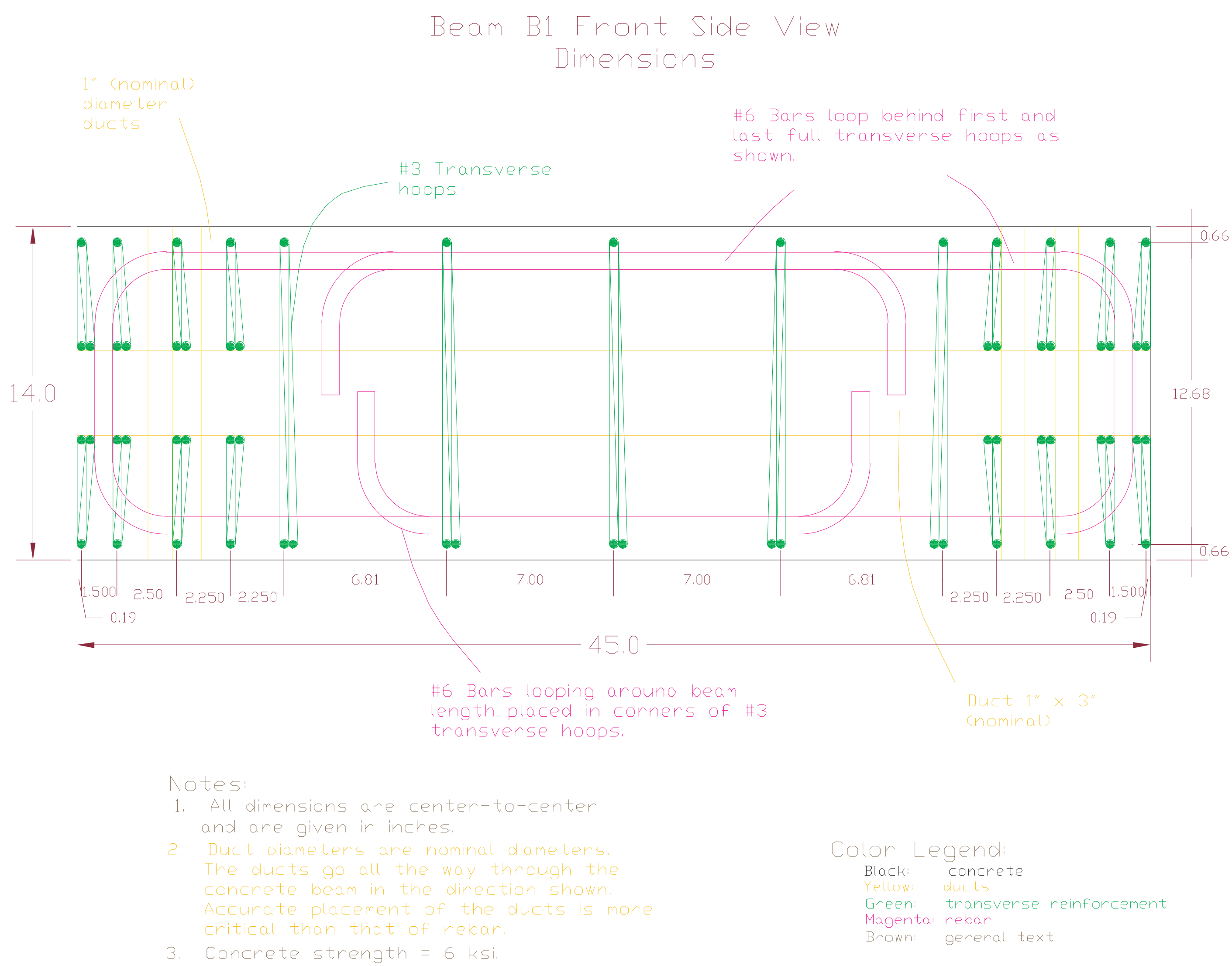

Figure C-10: Beams 1-3 front side view – general dimensions.

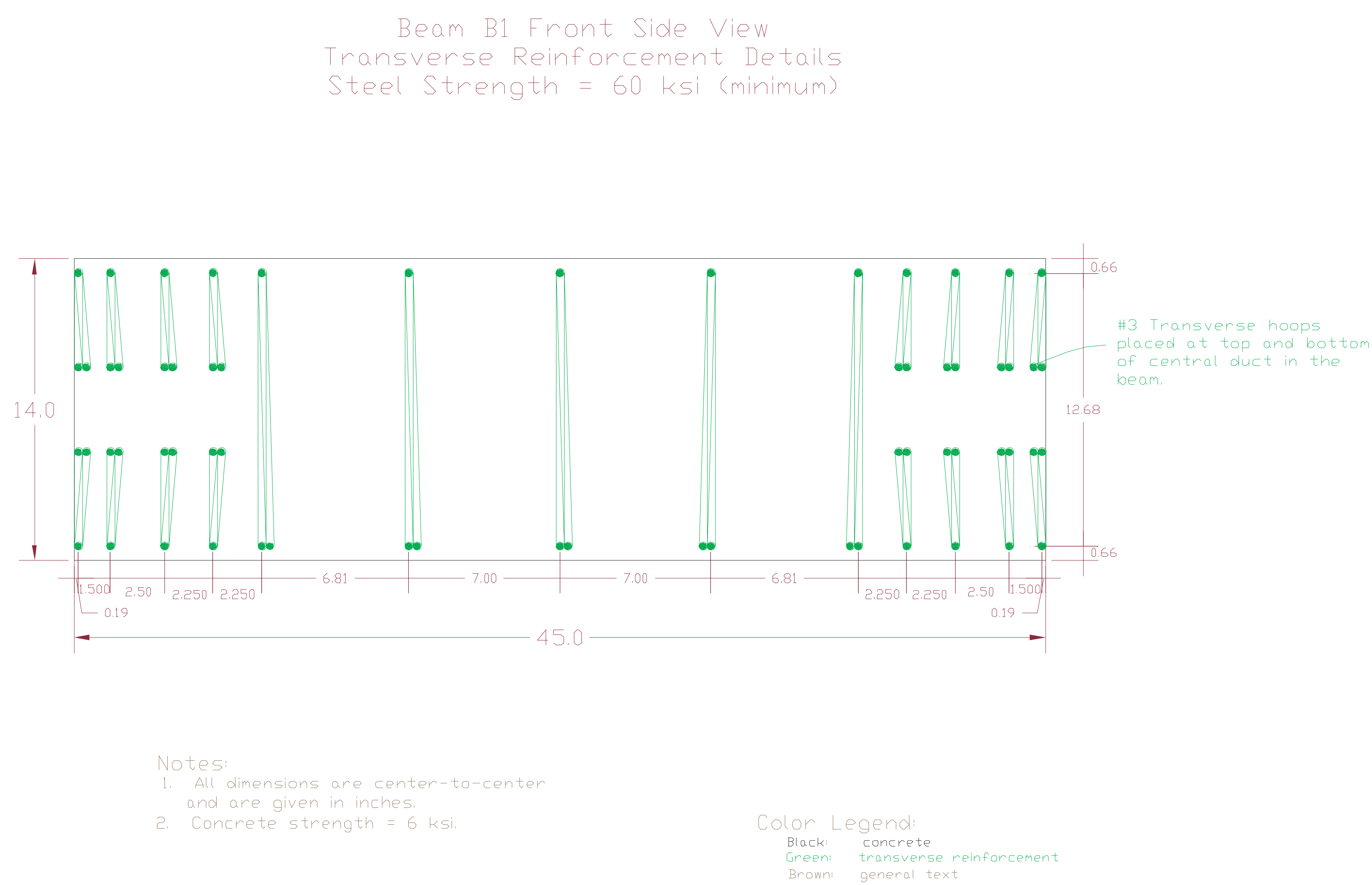

Figure C-11: Beams 1-3 front side view – transverse reinforcement details.

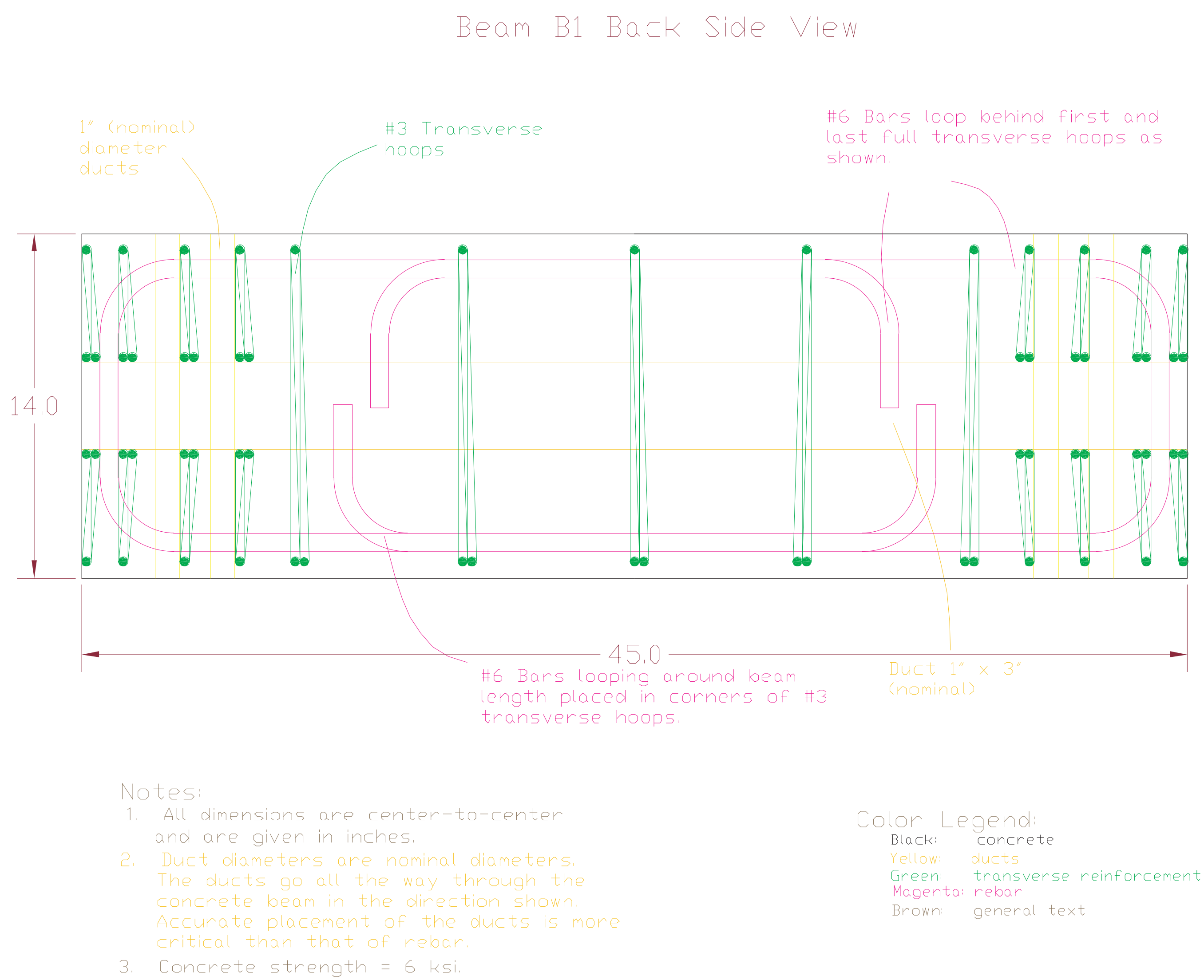

Figure C-12: Beams 1-3 back side view – general properties.

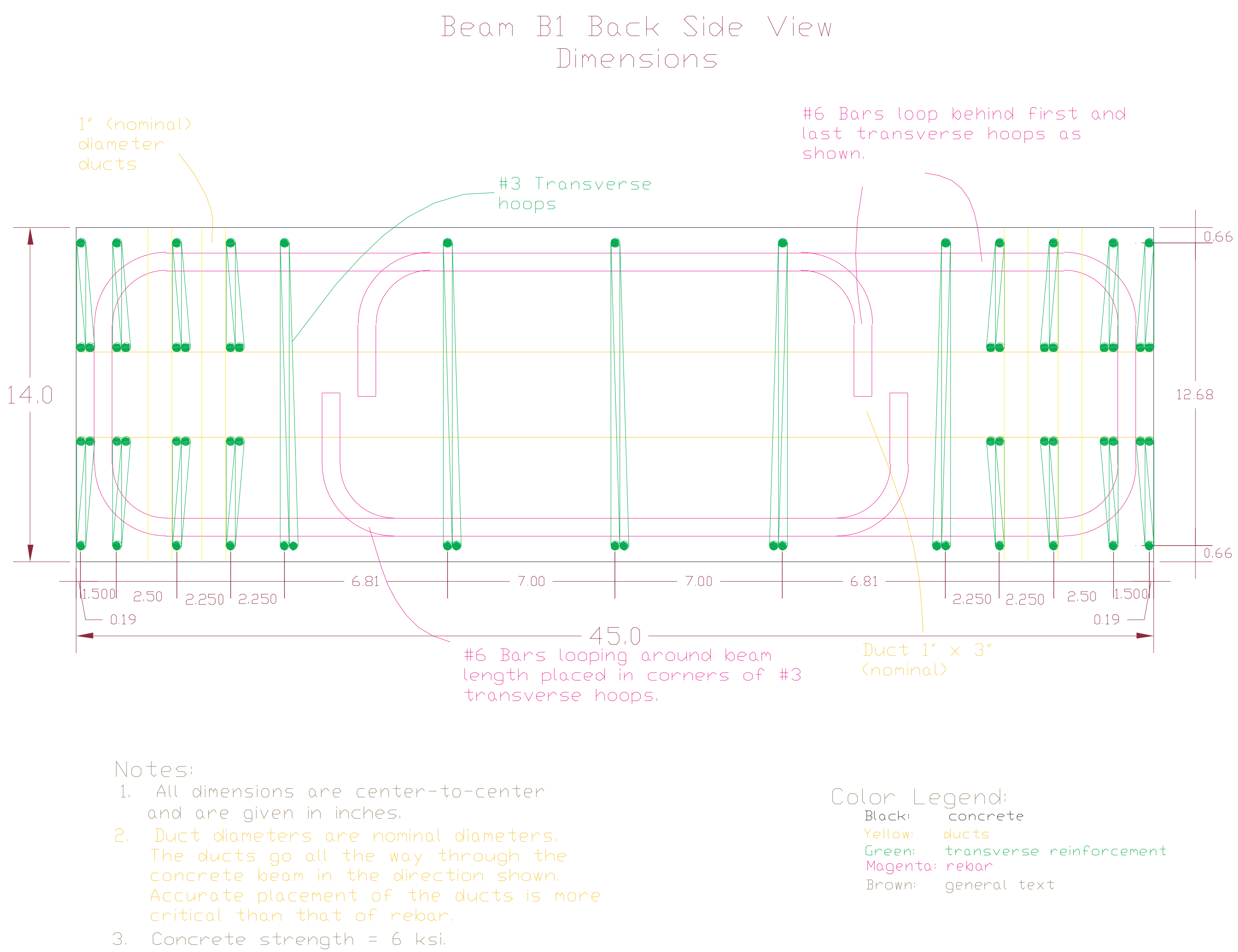

Figure C-13: Beams 1-3 back side view – general dimensions.

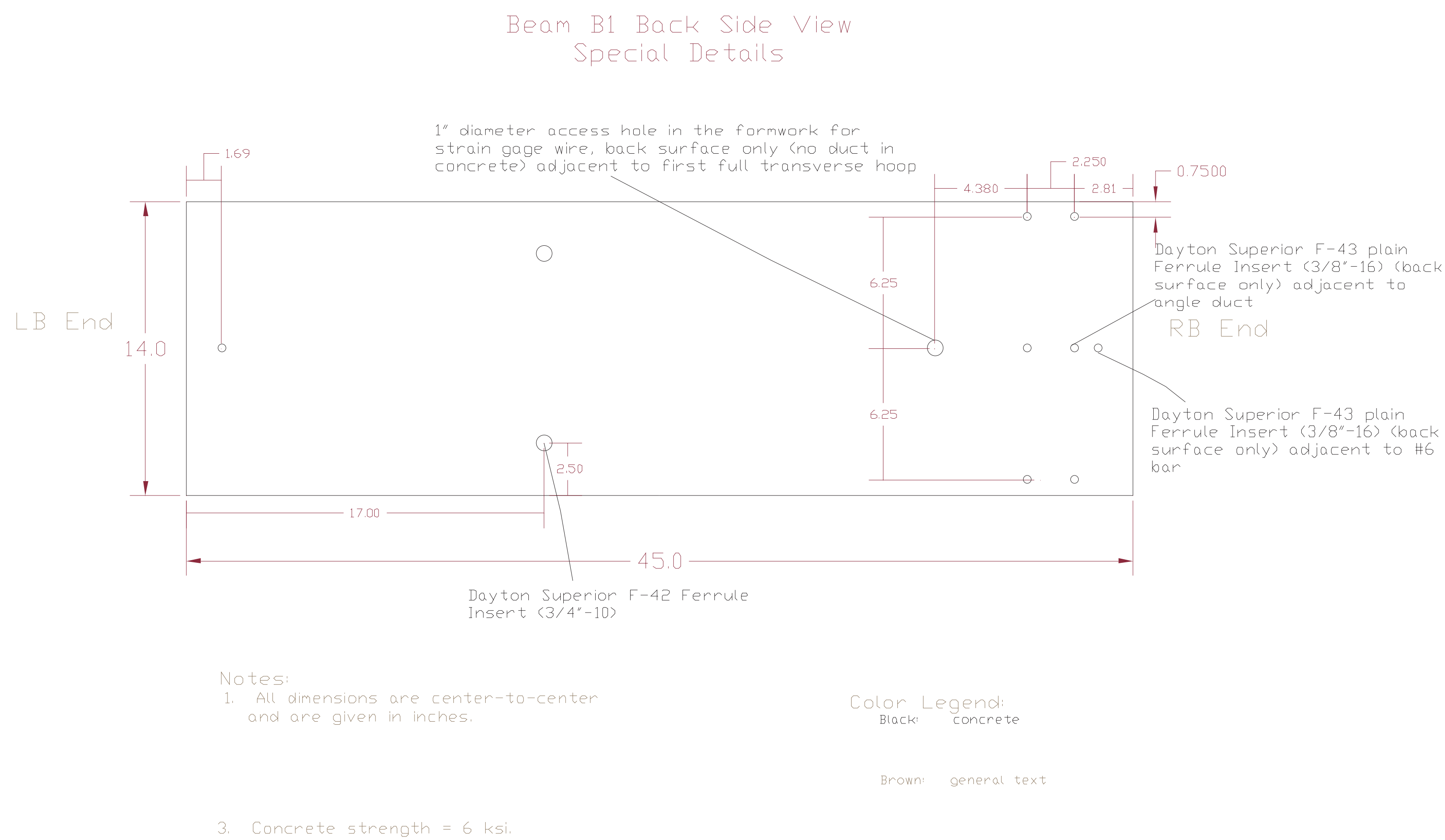

Figure C-14: Beams 1-3 back side view – special details.

APPENDIX D

REACTION BLOCK DESIGN DETAILS

Reaction Block R1

General Reaction Block Dimensions
Weight = 6.8 tons

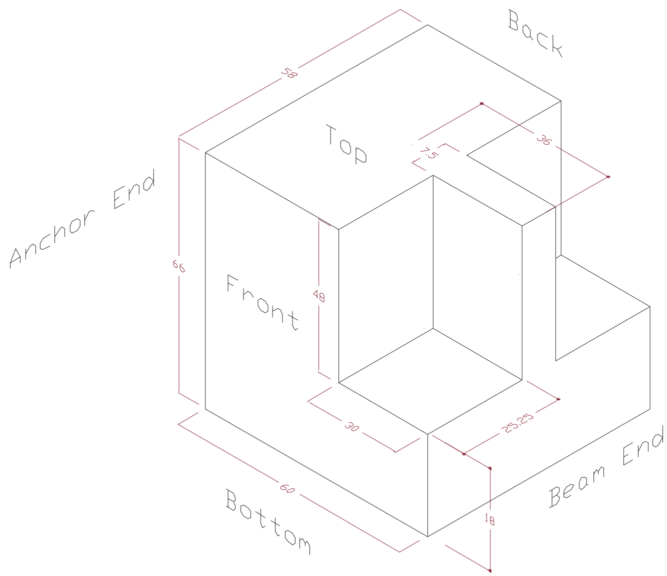

6 ksi Concrete
60 ksi Steel (minimum)
Tolerance = 1/16"

List of Figures:

Figure D-1: Reaction block isometric view and general properties.

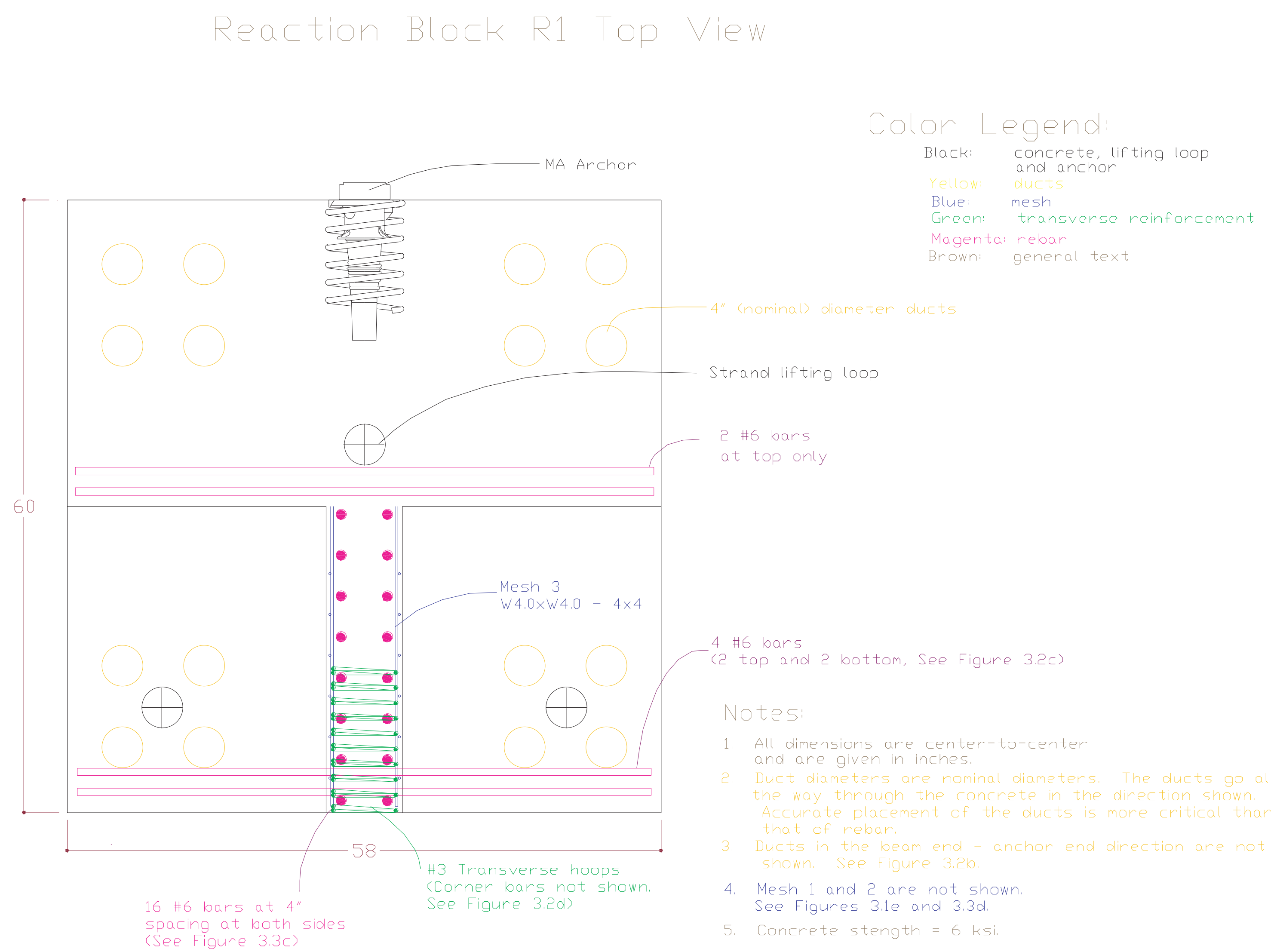

Figure D-2: Reaction block top view – general properties.

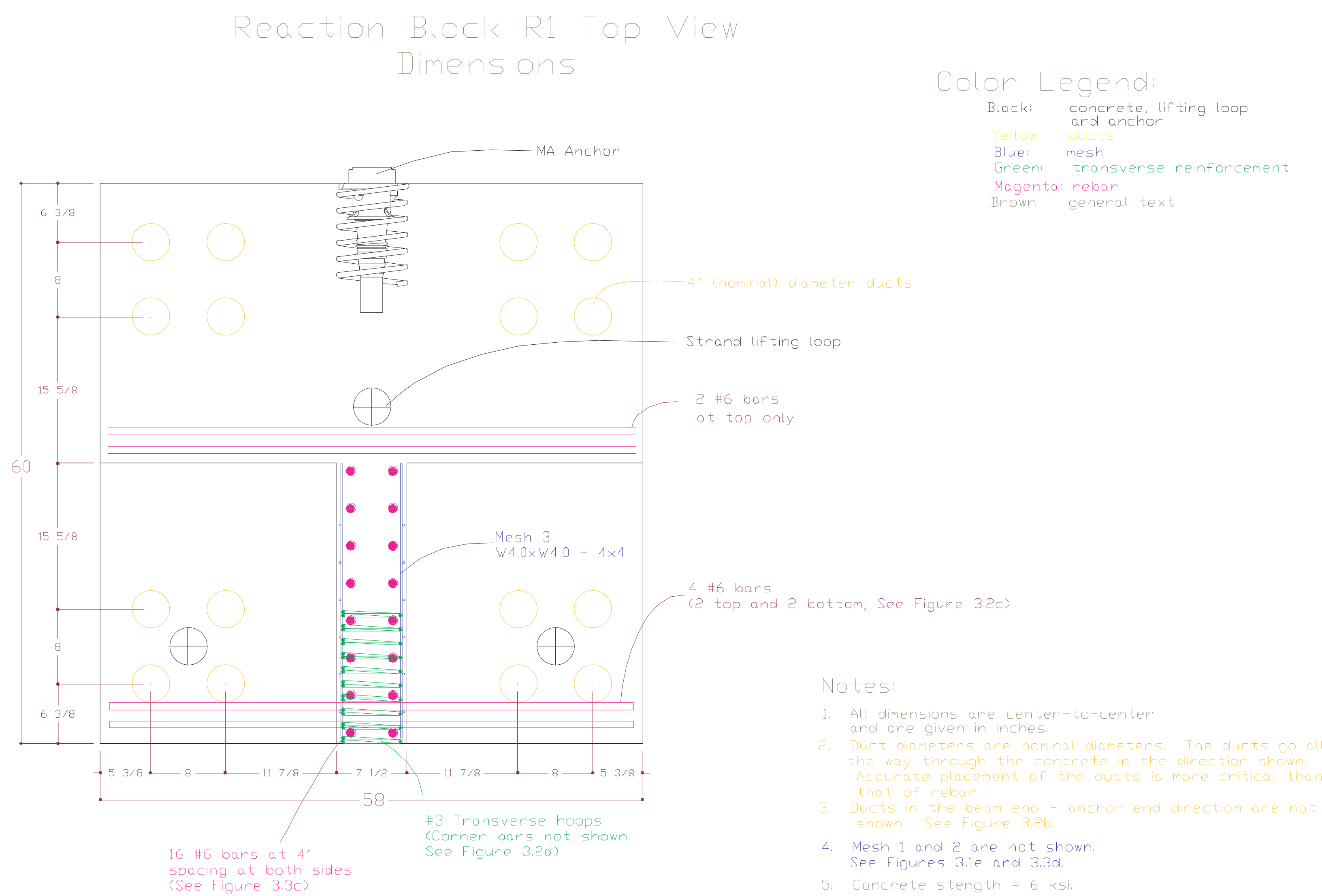

Figure D-3: Reaction block top view – general dimensions.

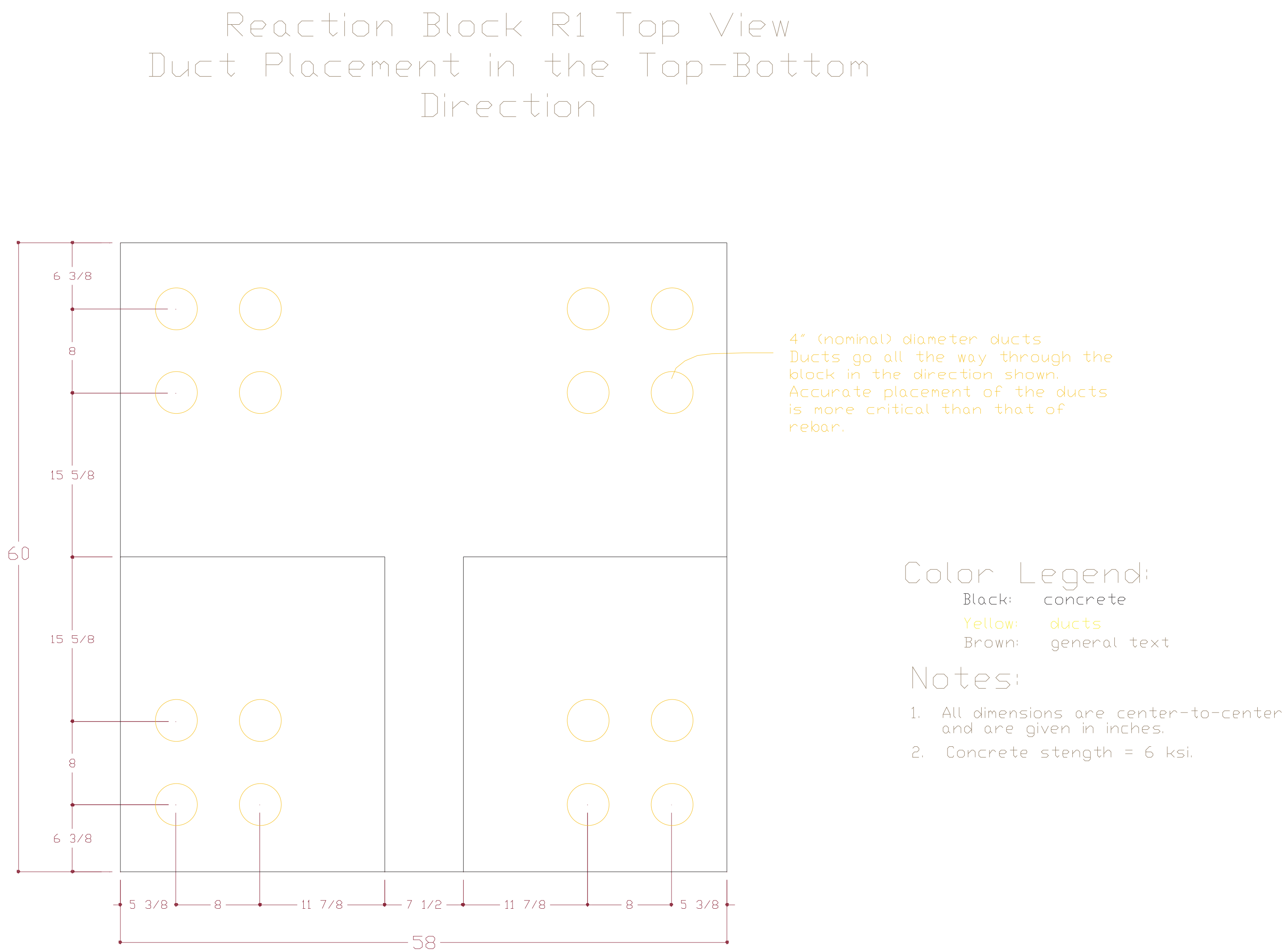

Figure D-4: Reaction block top view – duct placement.

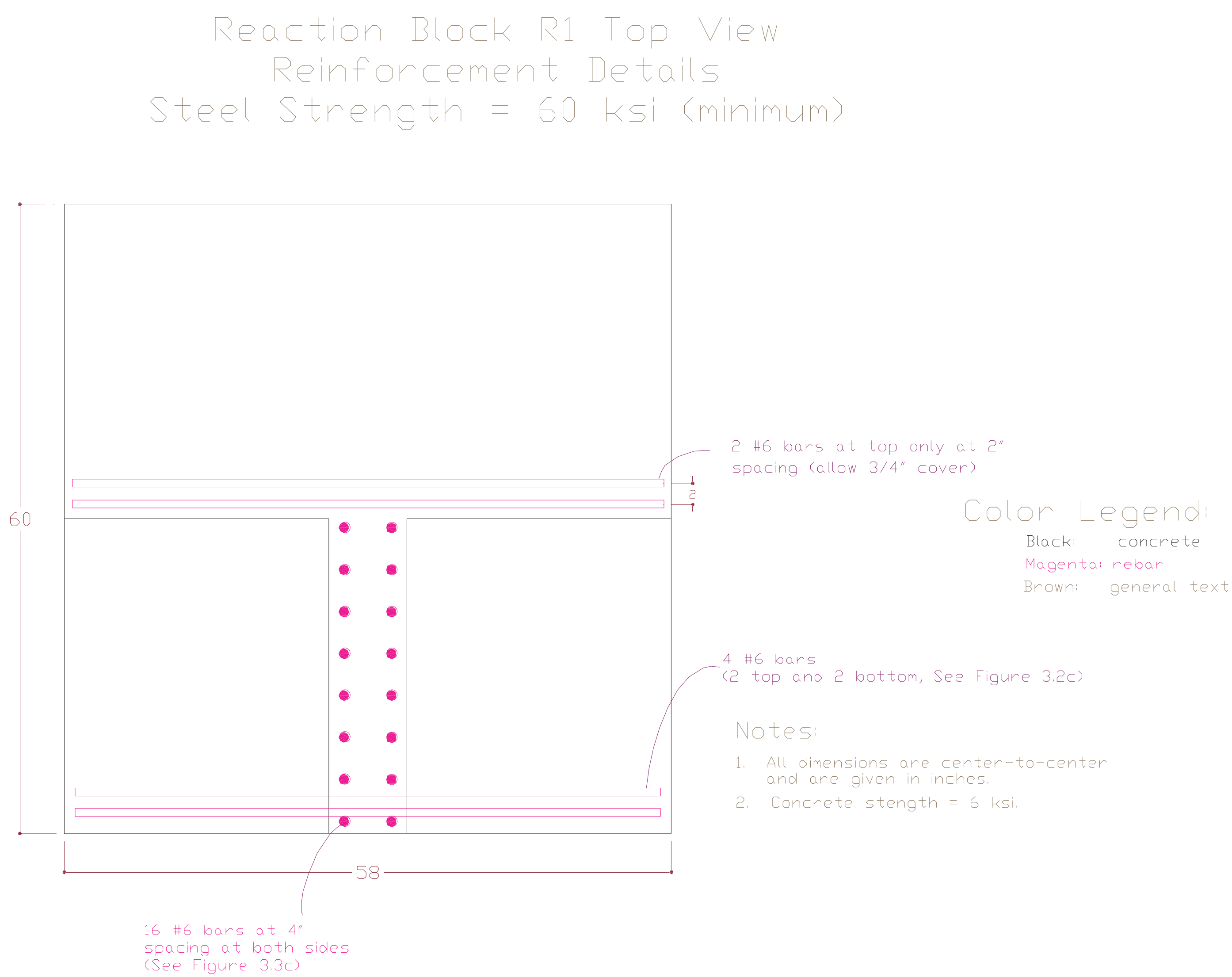

Figure D-5: Reaction block top view – No. 6 reinforcement details.

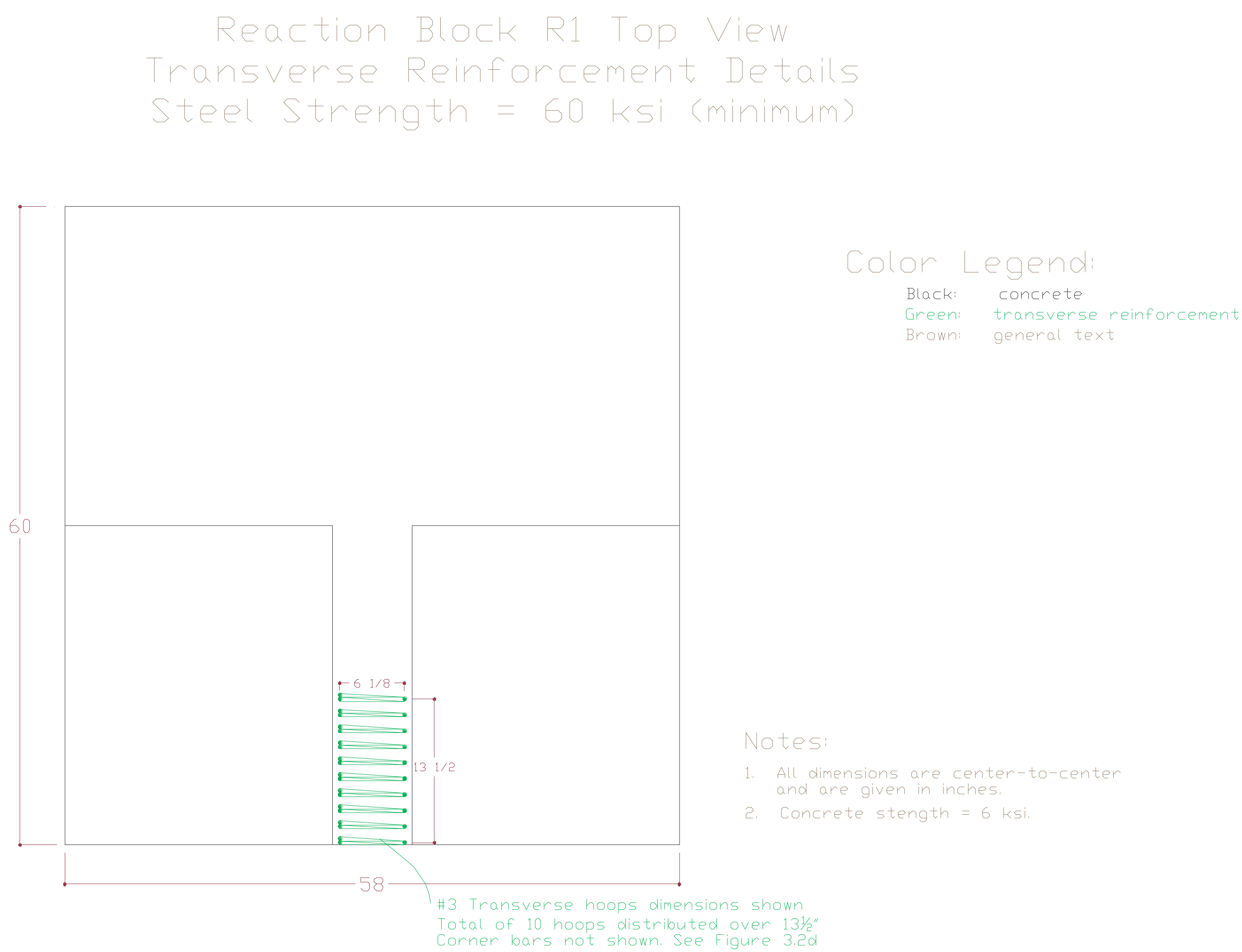

Figure D-6: Reaction block top view – transverse reinforcement details.

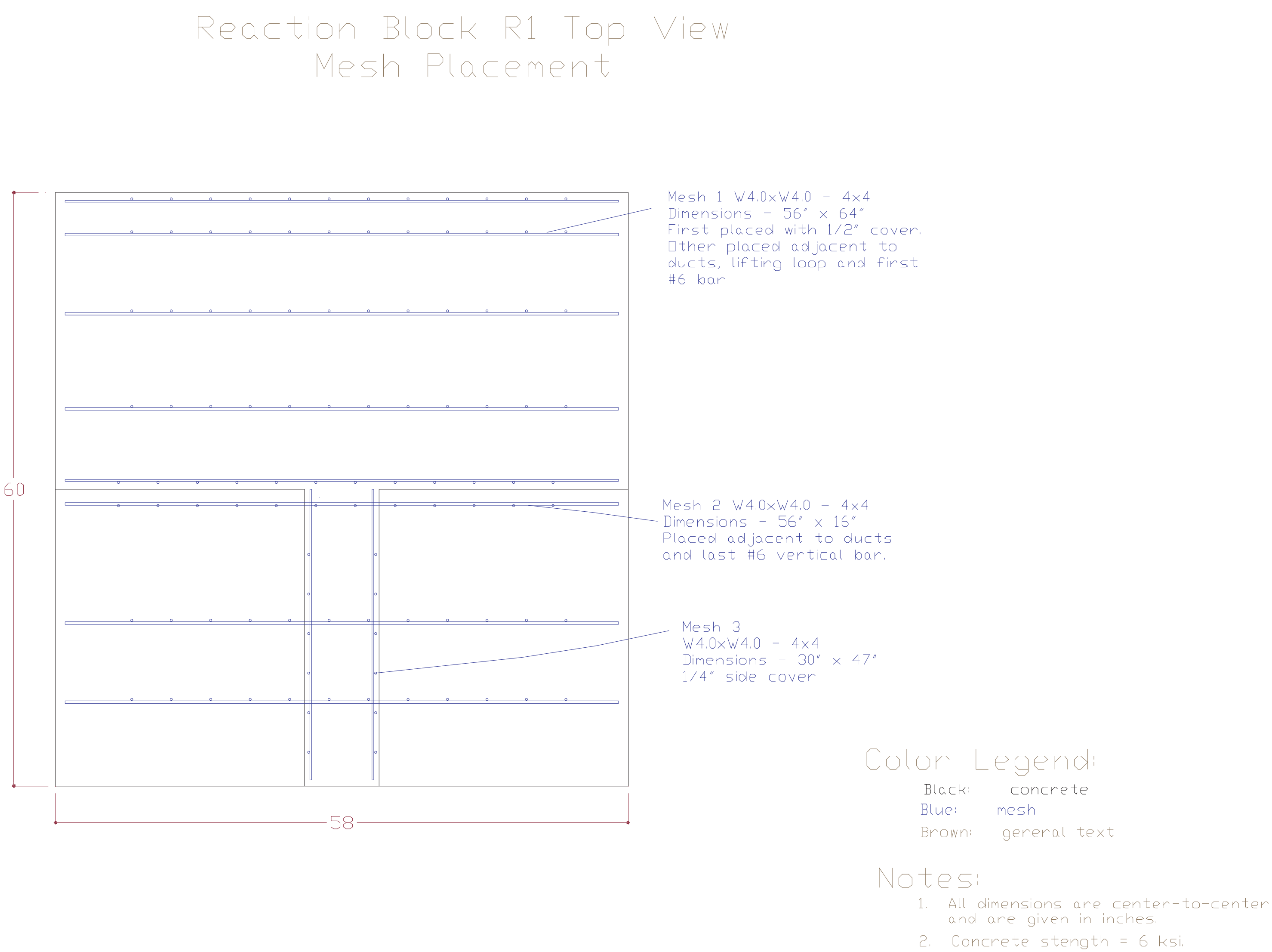

Figure D-7: Reaction block top view – mesh placement.

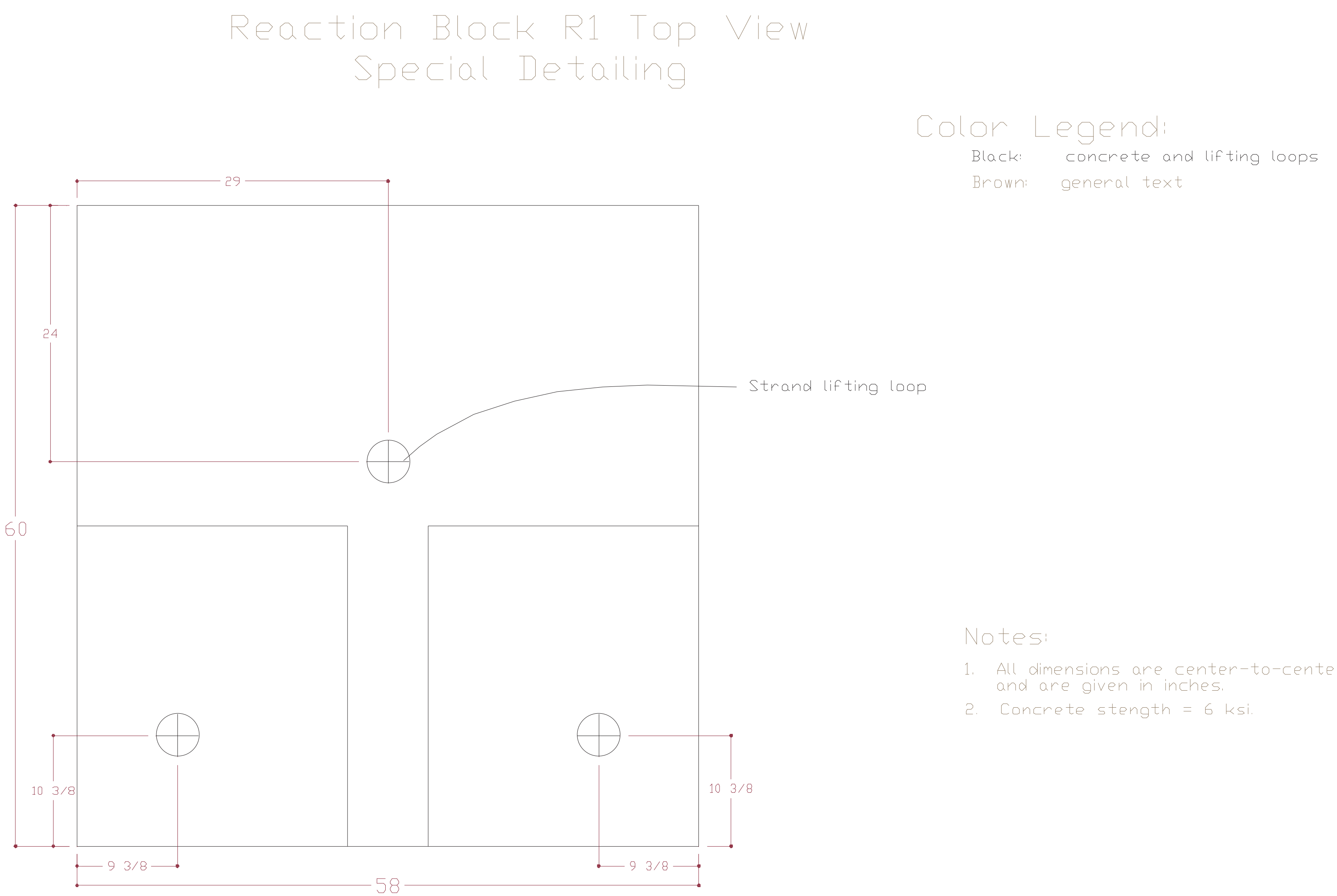

Figure D-8: Reaction block top view – special details.

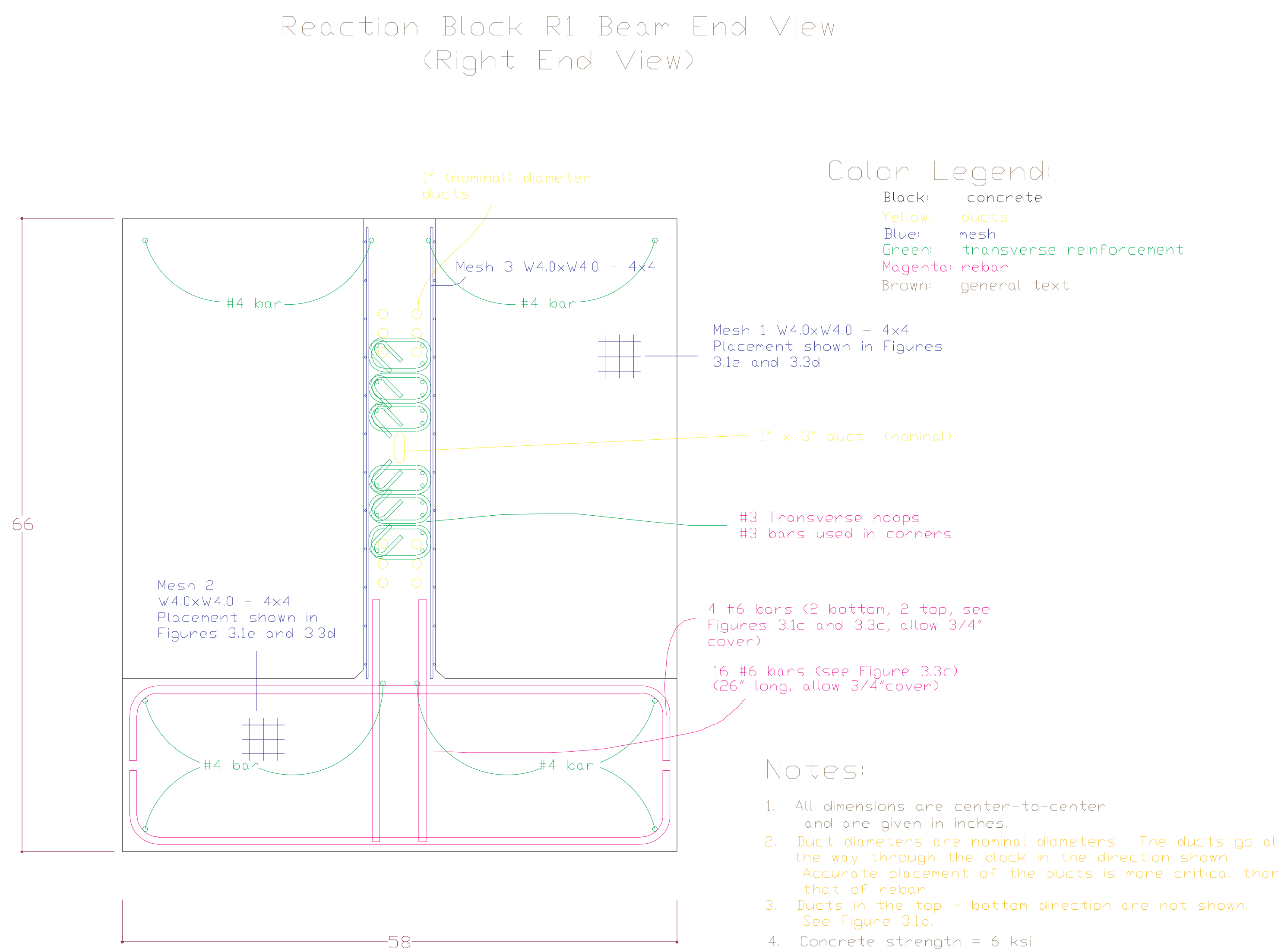

Figure D-9: Reaction block beam end view – general properties.

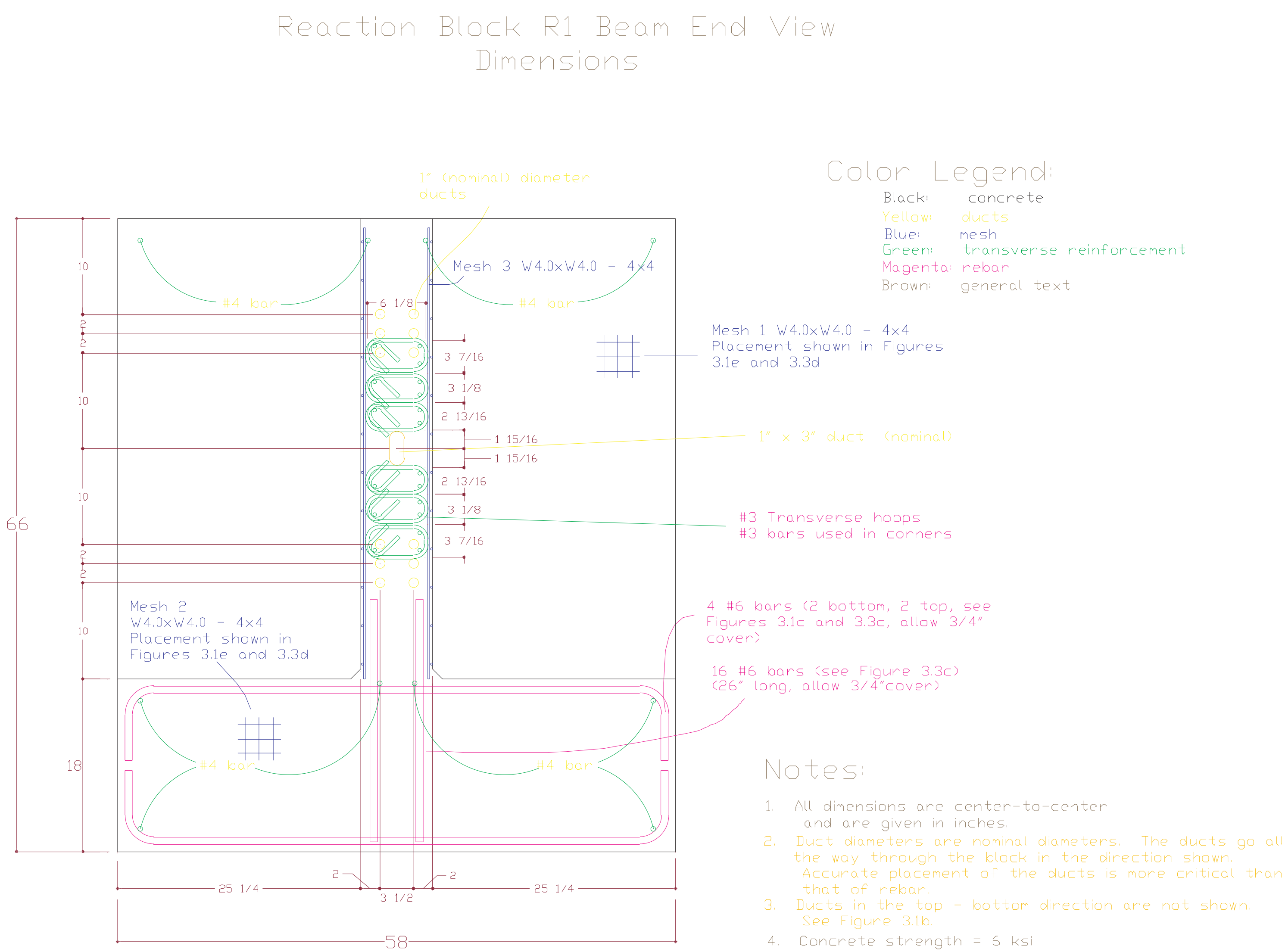

Figure D-10: Reaction block beam end view – general dimensions.

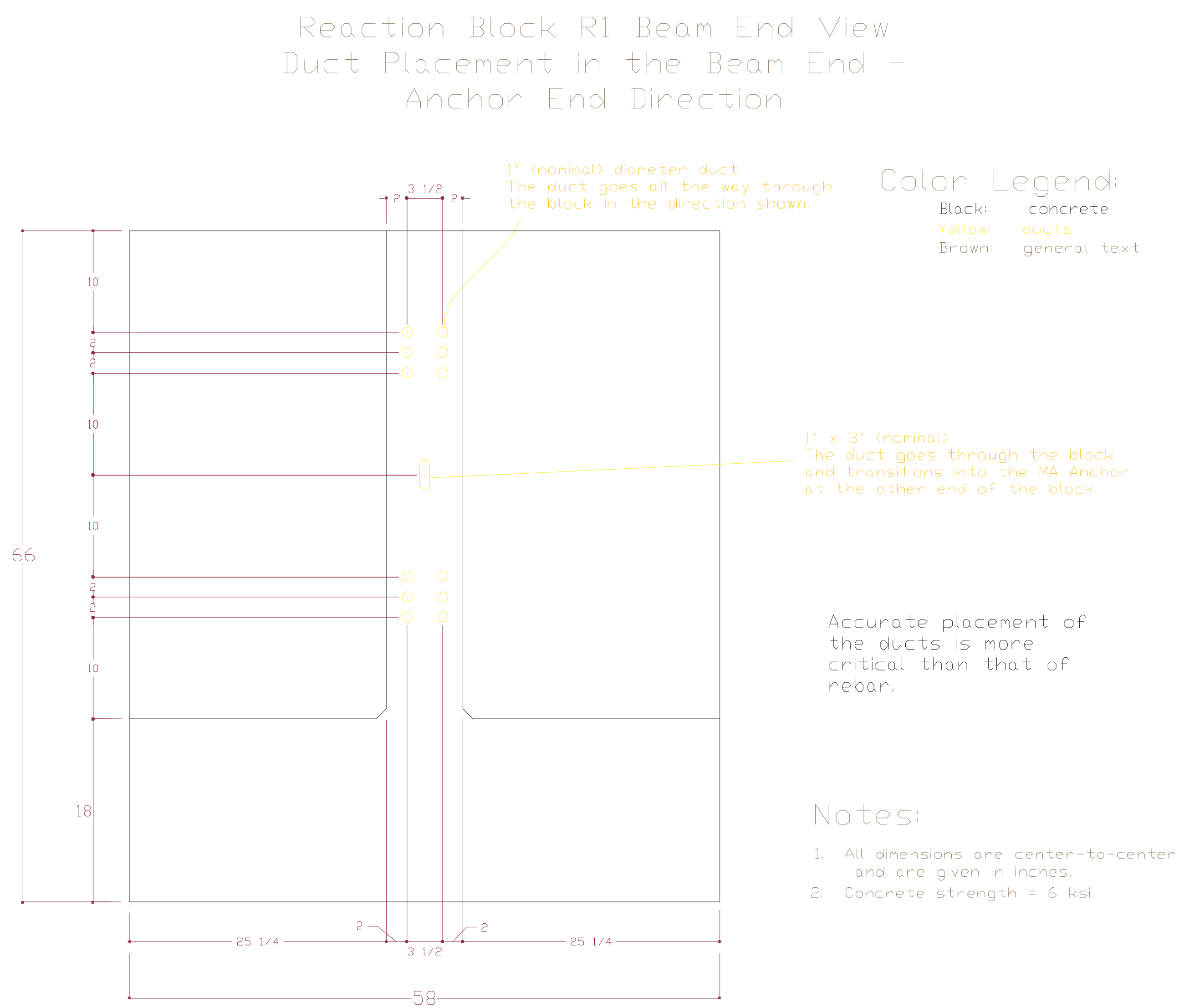

Figure D-11: Reaction block beam end view – duct placement.

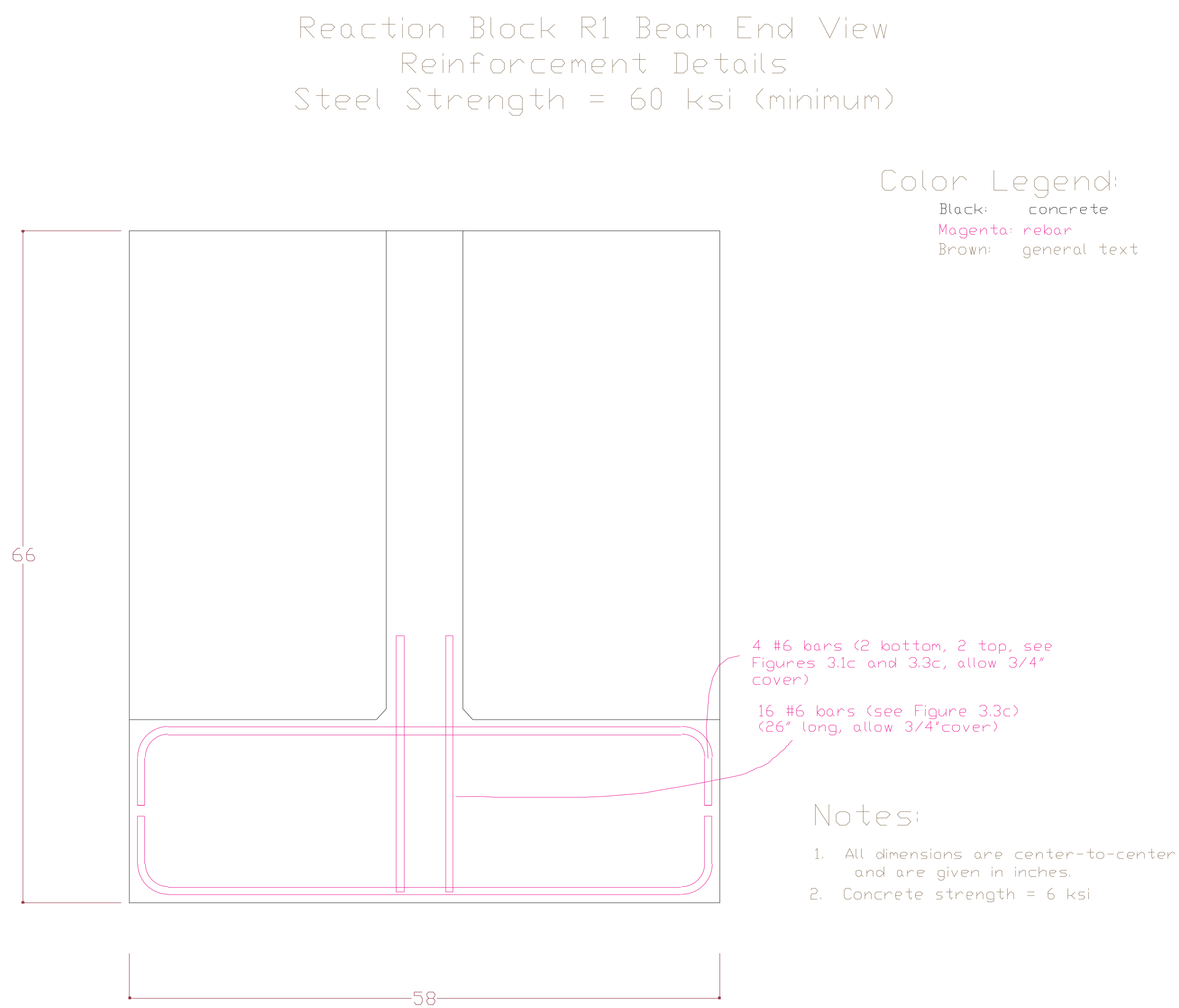

Figure D-12: Reaction block beam end view – No. 6 reinforcement details.

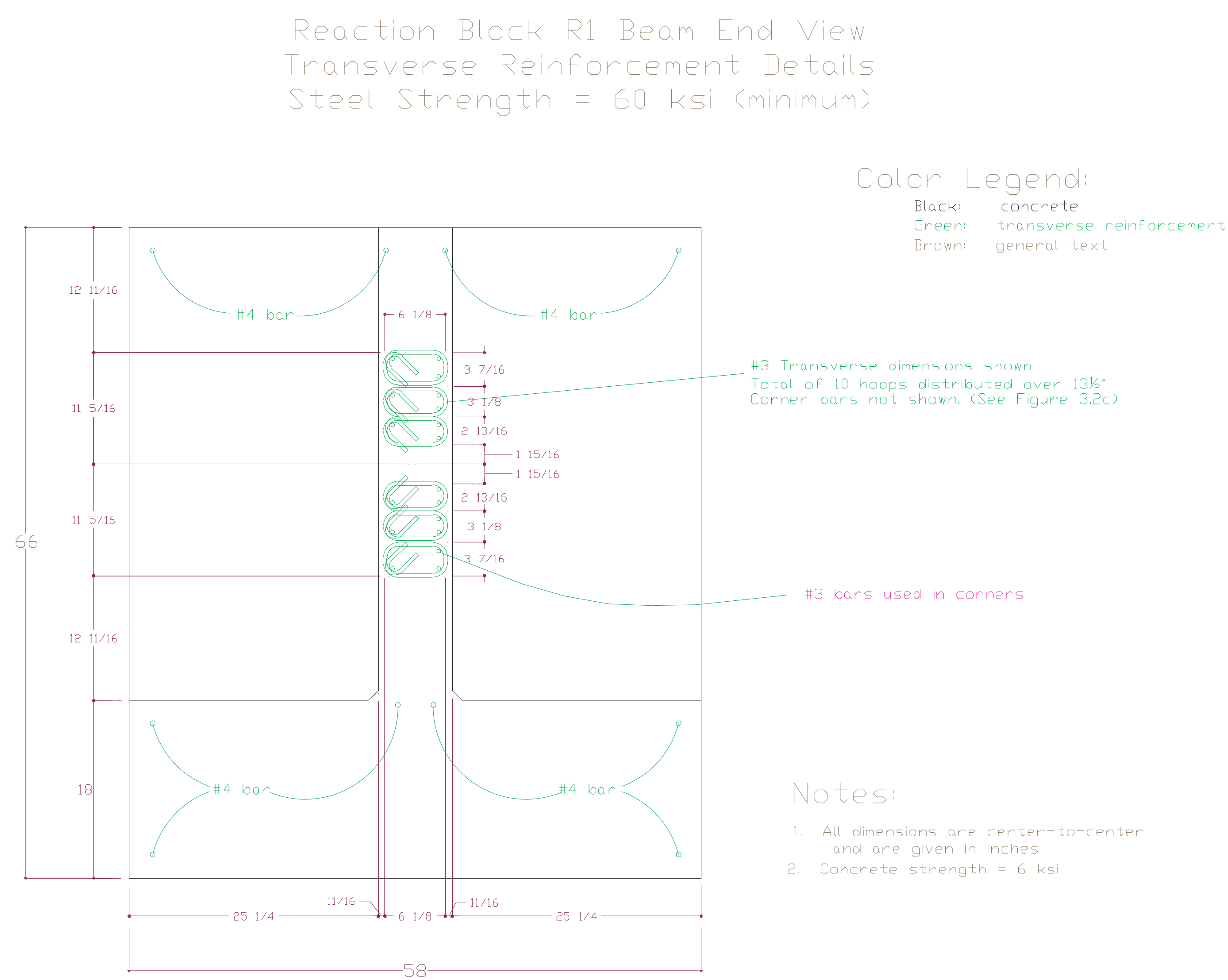

Figure D-13: Reaction block beam end view – transverse reinforcement details.

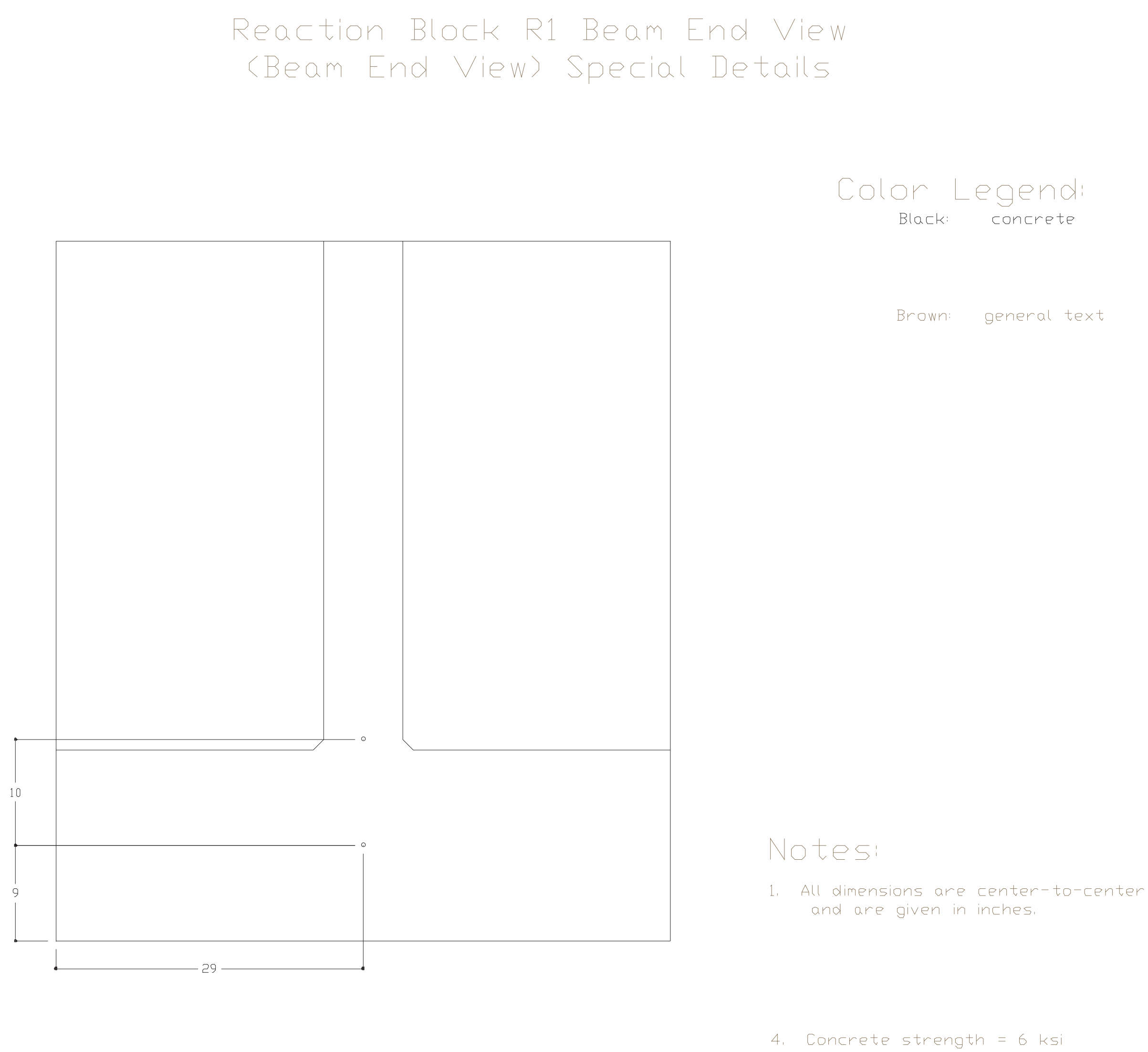

Figure D-14: Reaction block beam end view – special details.

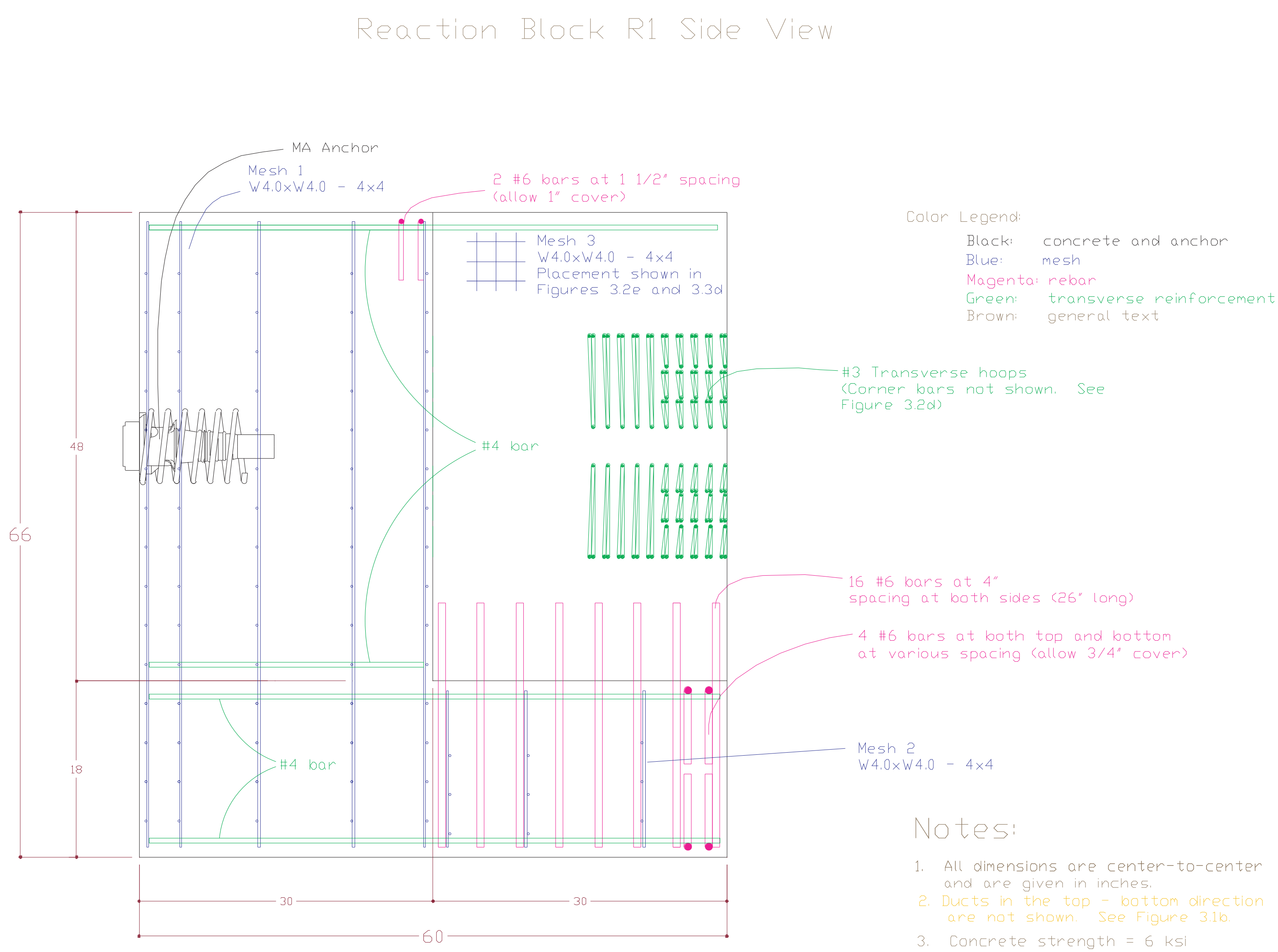

Figure D-15: Reaction block side view – general properties.

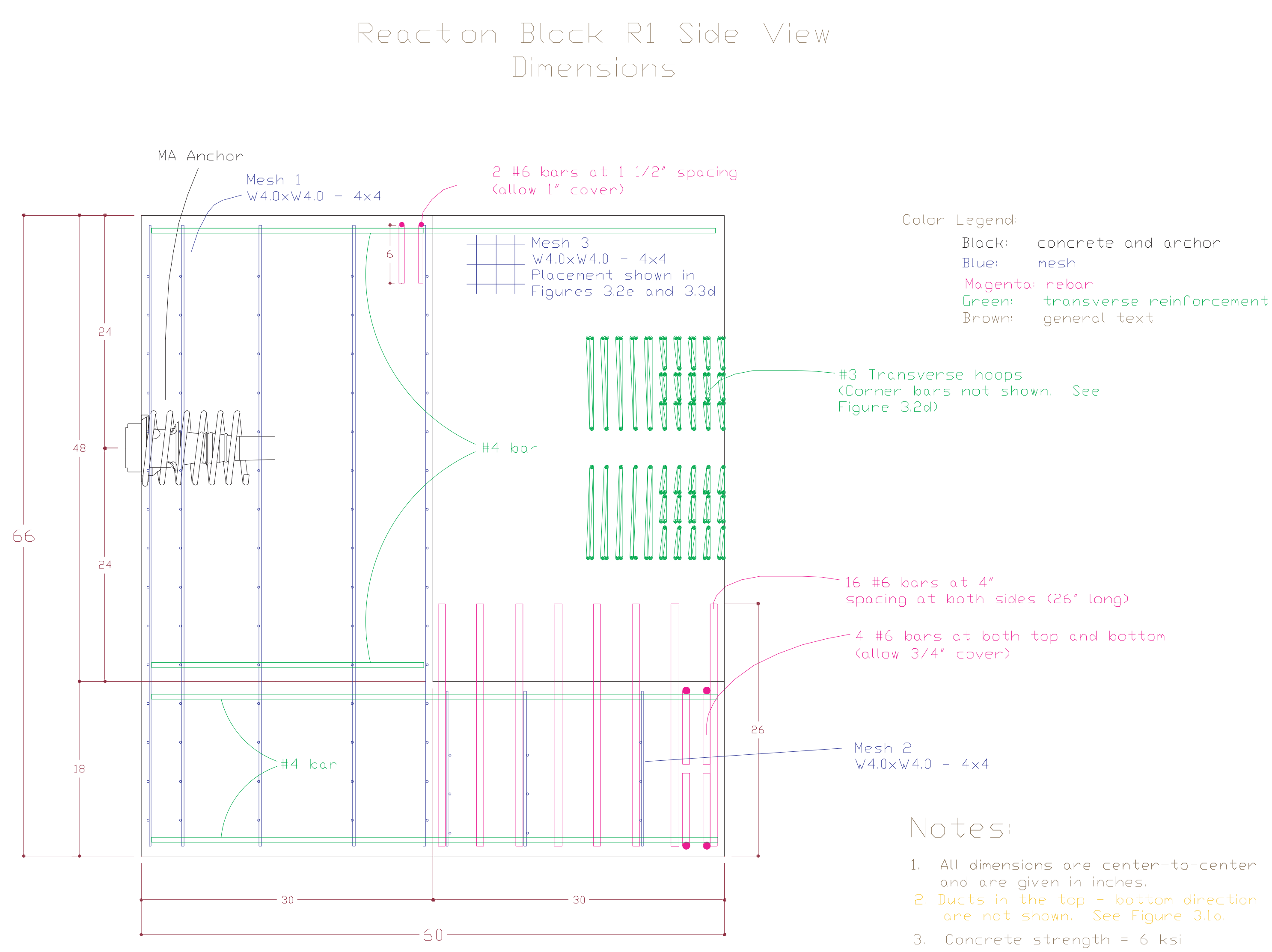

Figure D-16: Reaction block side view – general dimensions.

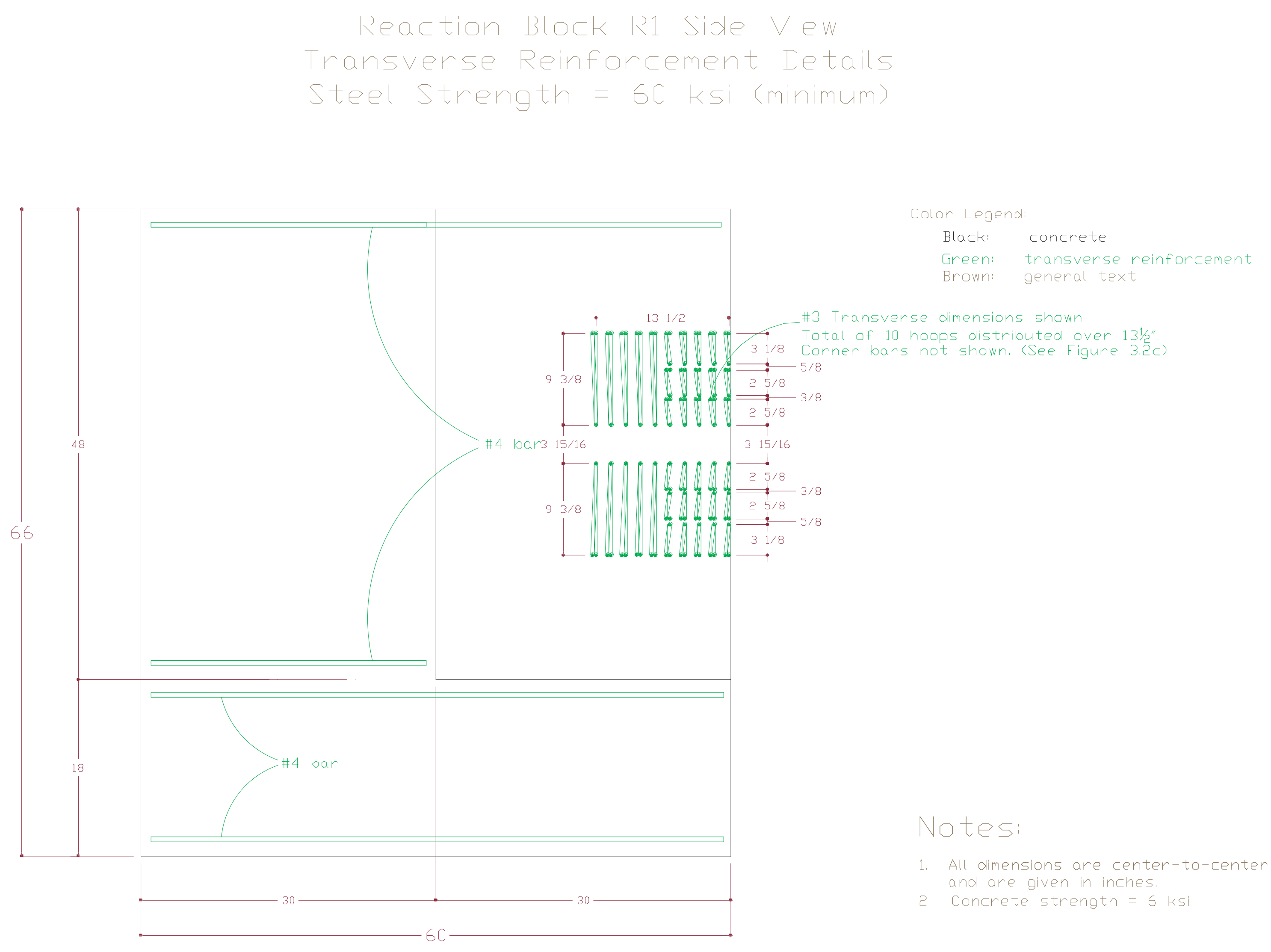

Figure D-17: Reaction block side view – transverse reinforcement details.

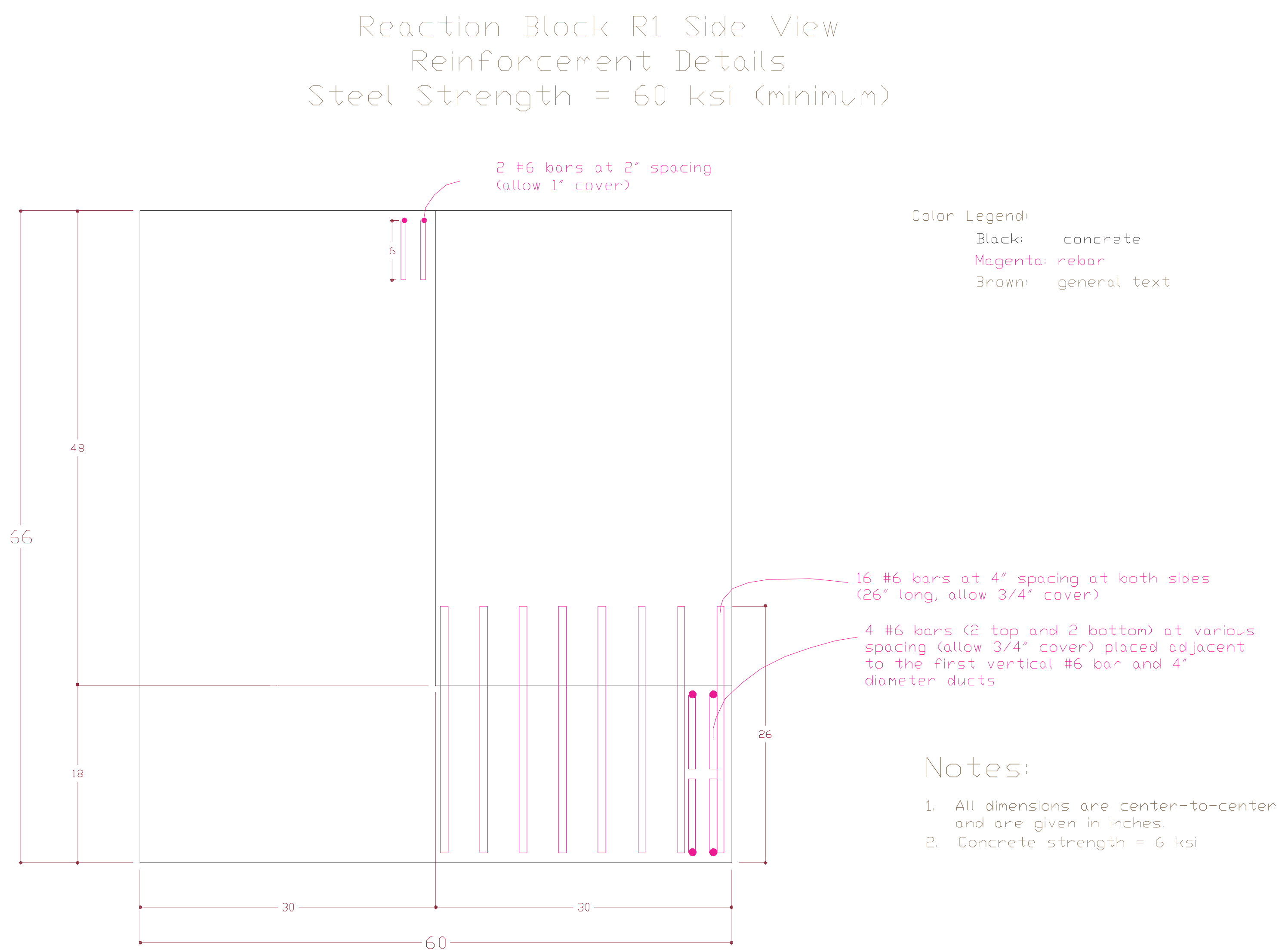

Figure D-18: Reaction block side view – No. 6 reinforcement details.

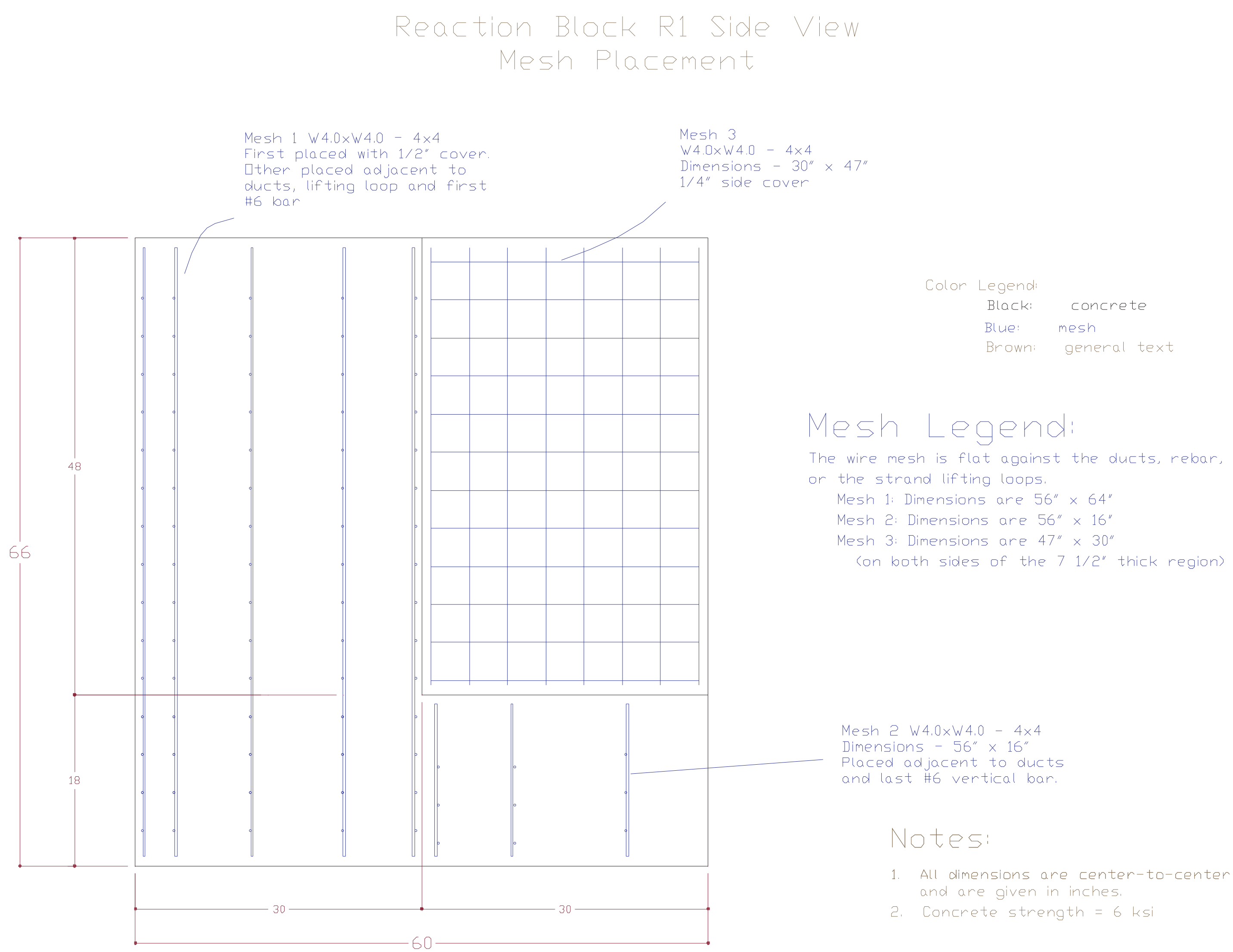

Figure D-19: Reaction block side view – mesh placement.

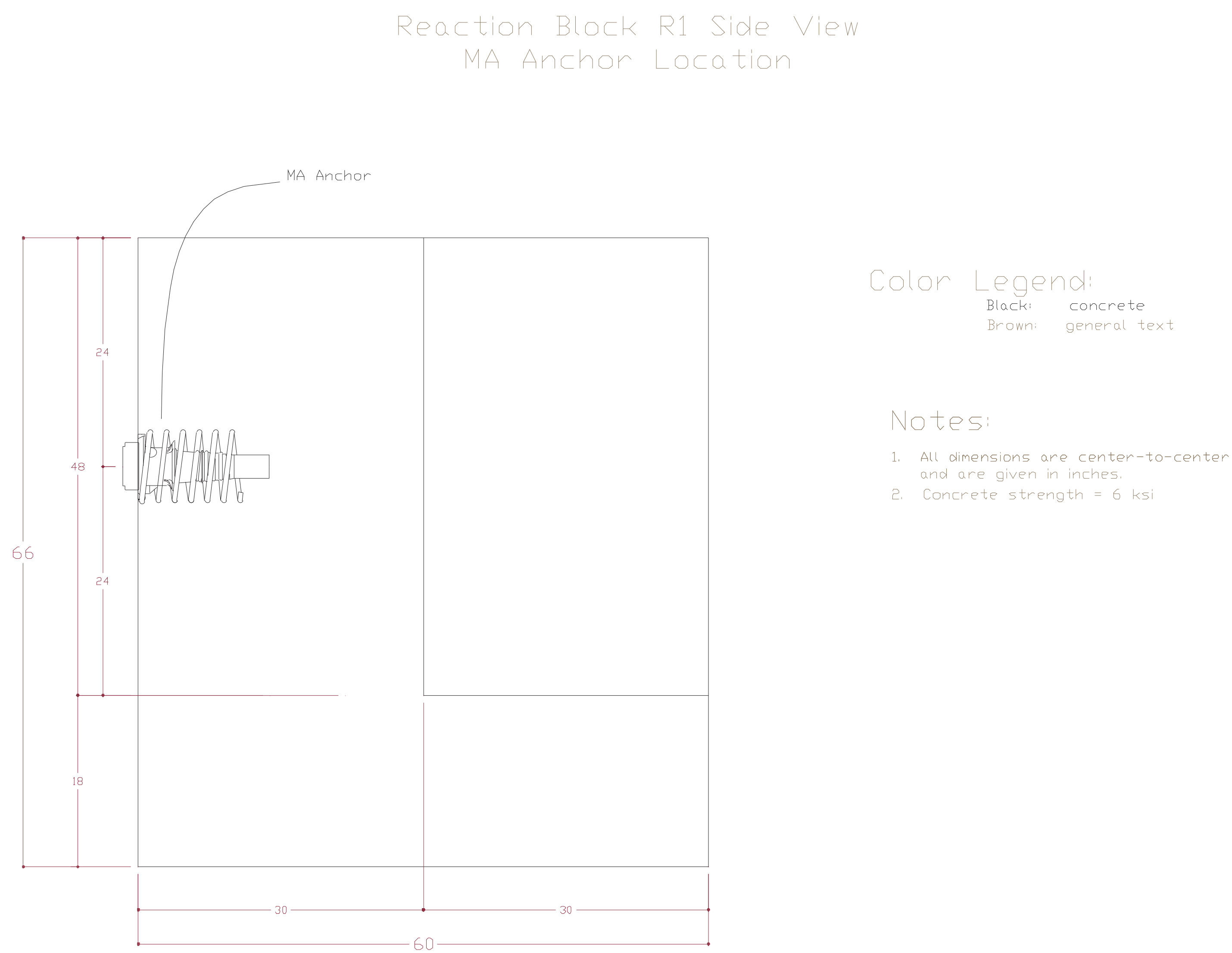

Figure D-20: Reaction block side view – MA anchor placement.

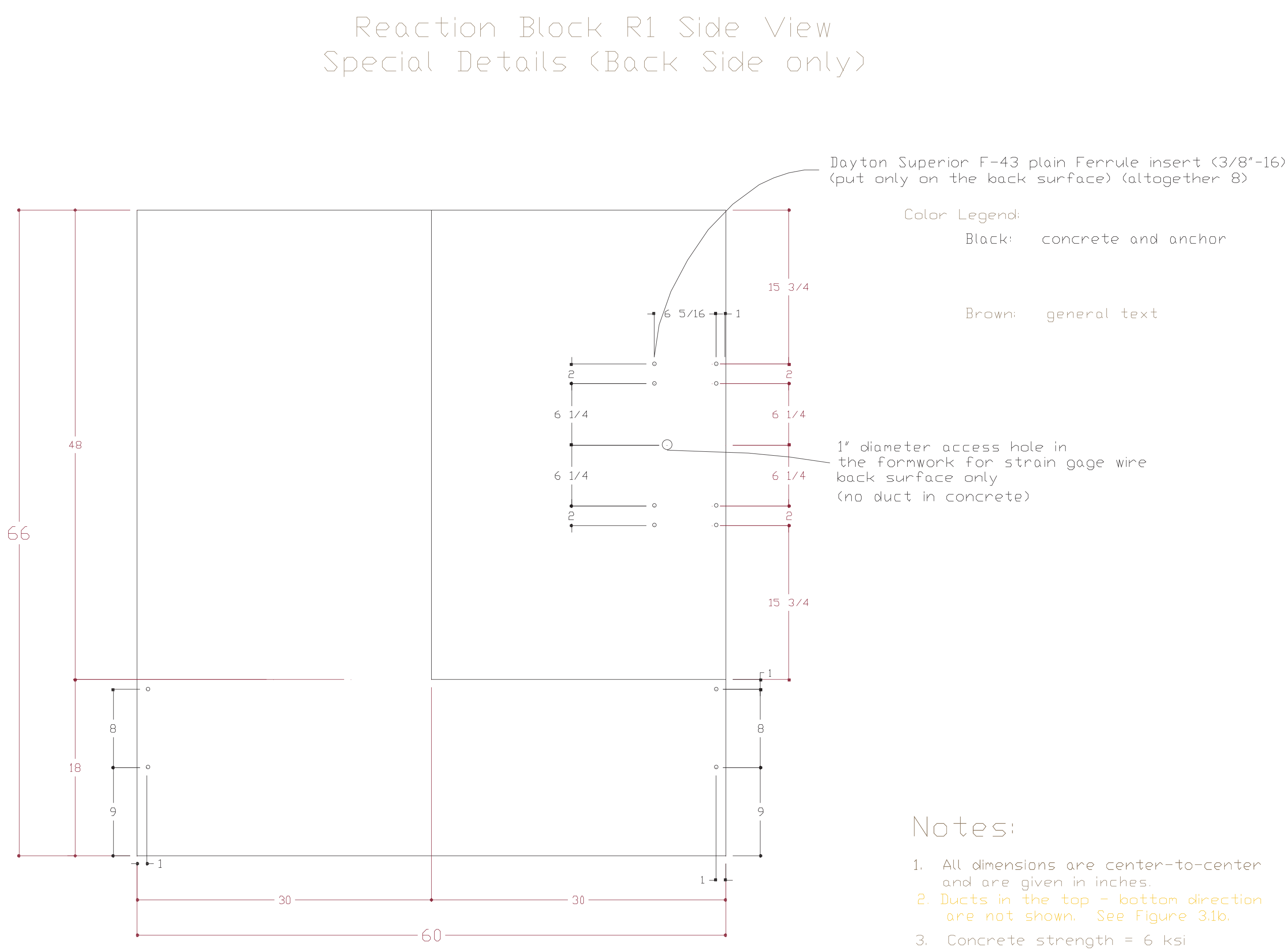

Figure D-21: Reaction block side view – special details.

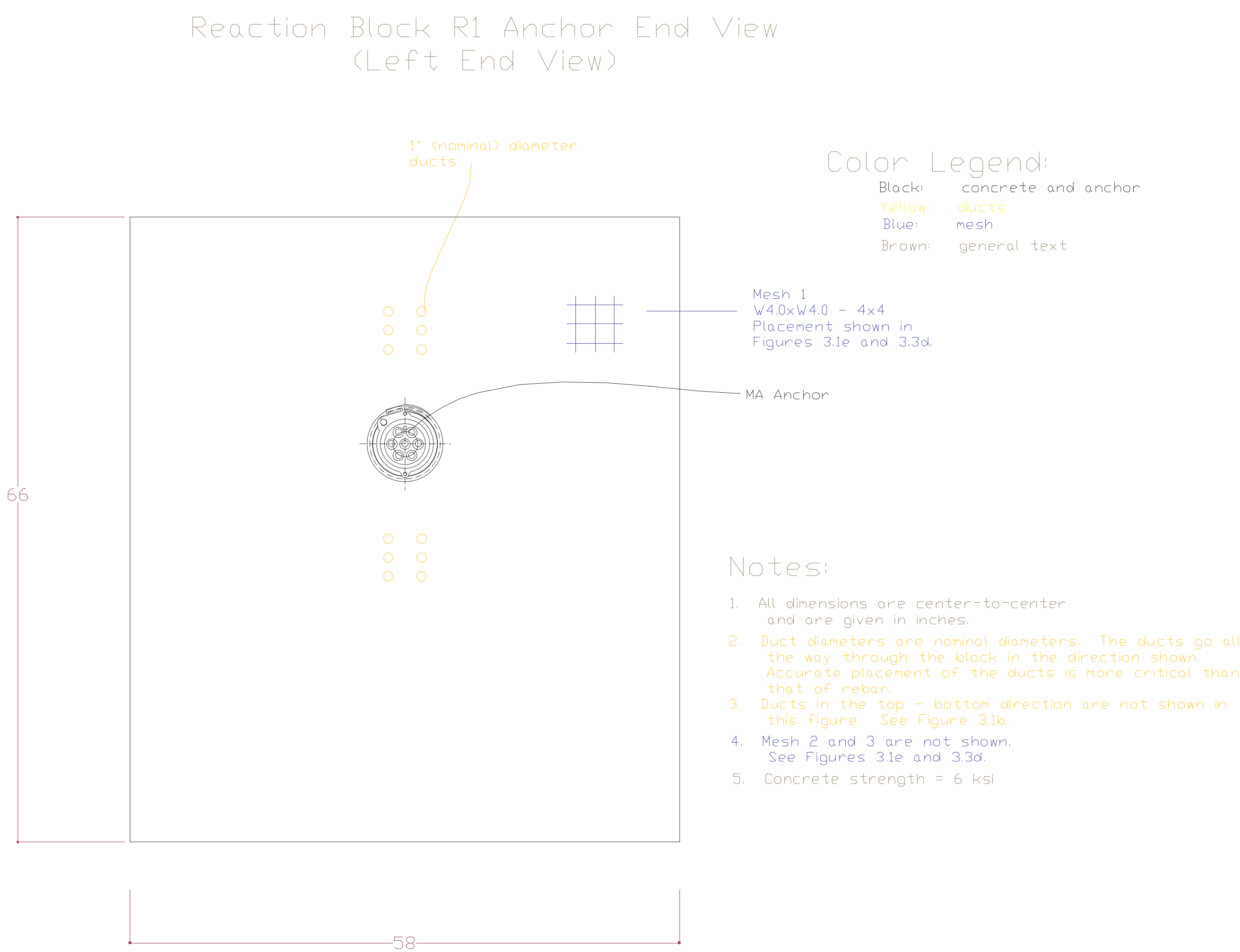

Figure D-22: Reaction block anchor end view – general properties.

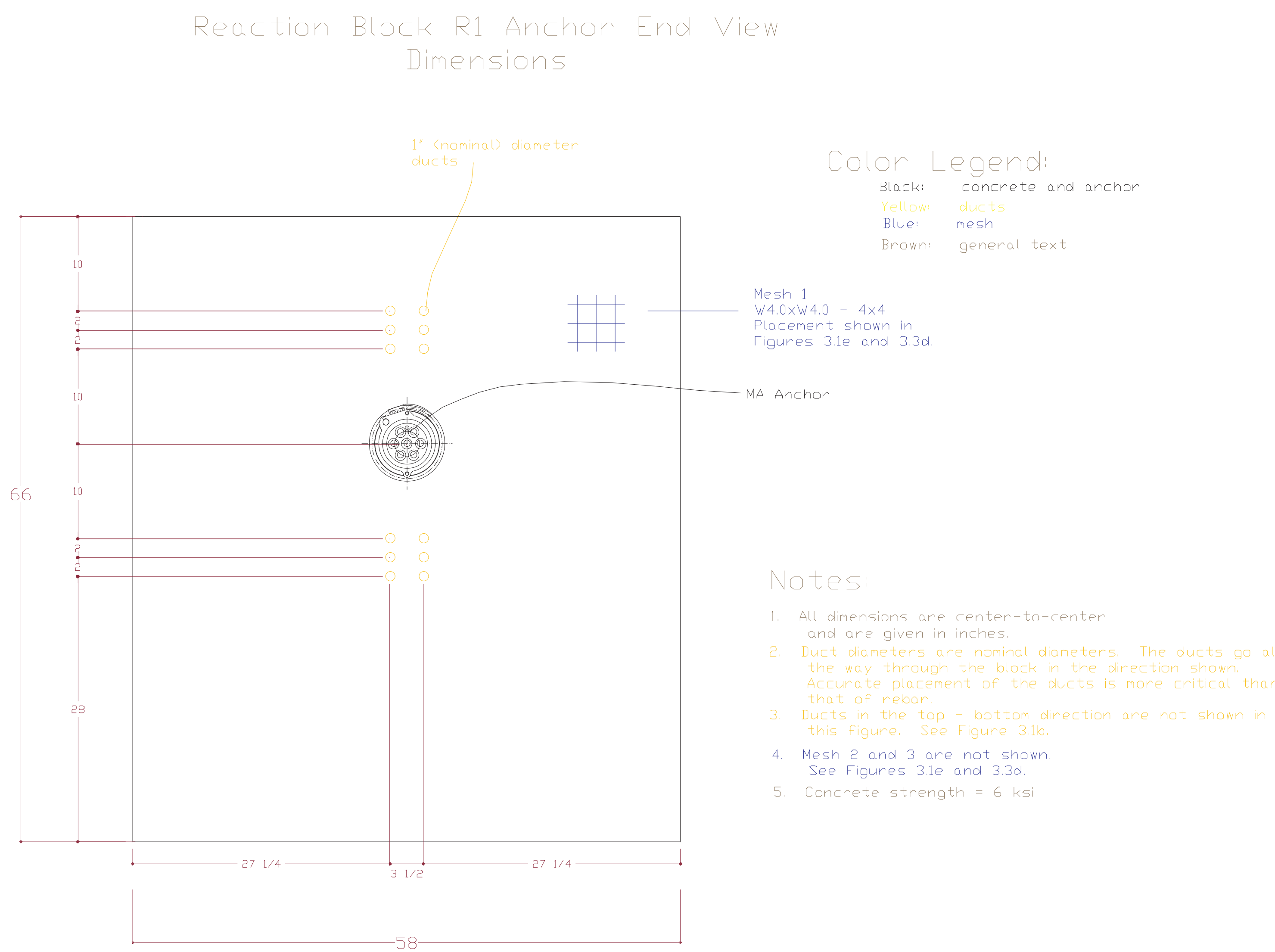

Figure D-23: Reaction block anchor end view – general dimensions.

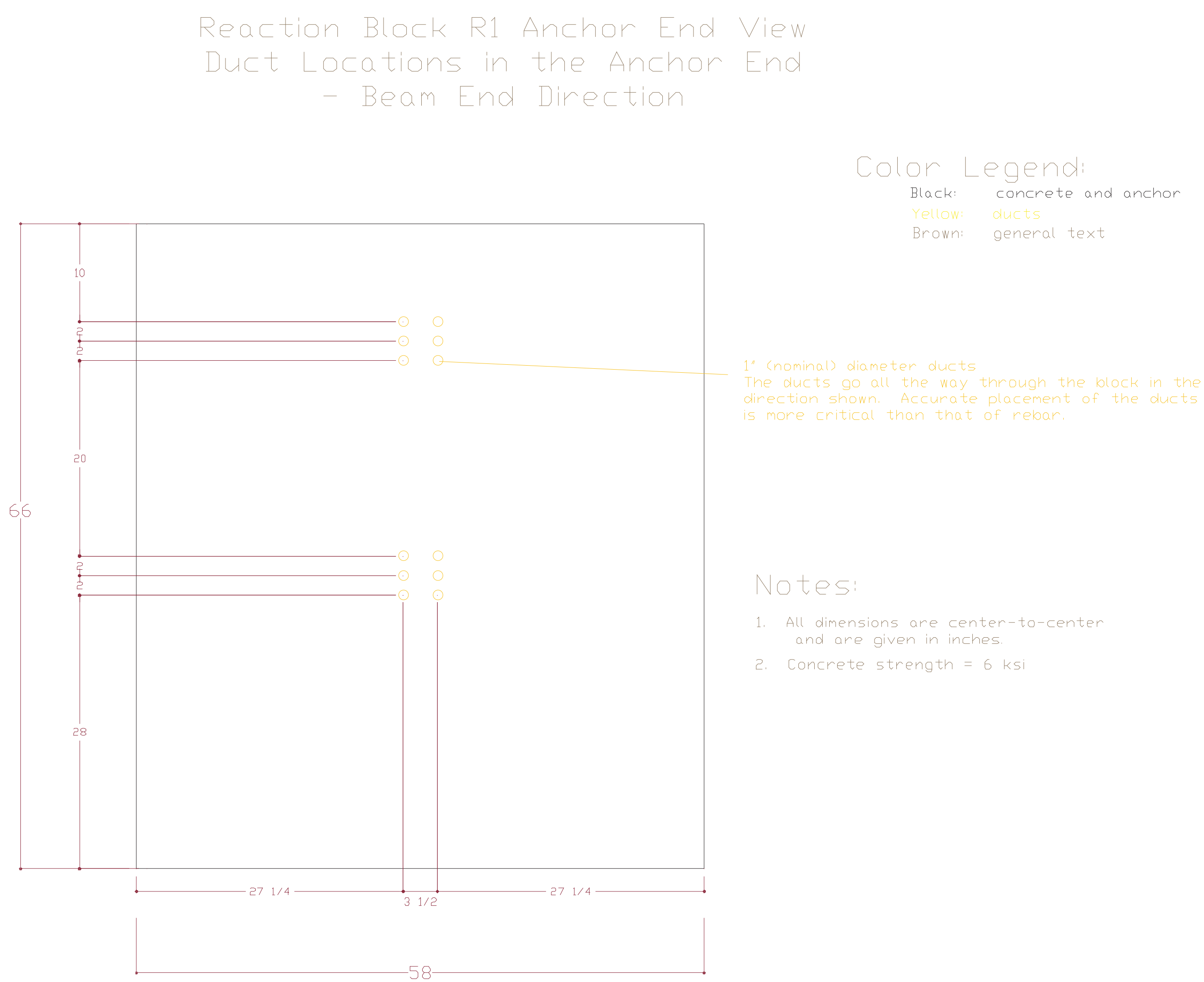

Figure D-24: Reaction block anchor end view – duct placement.

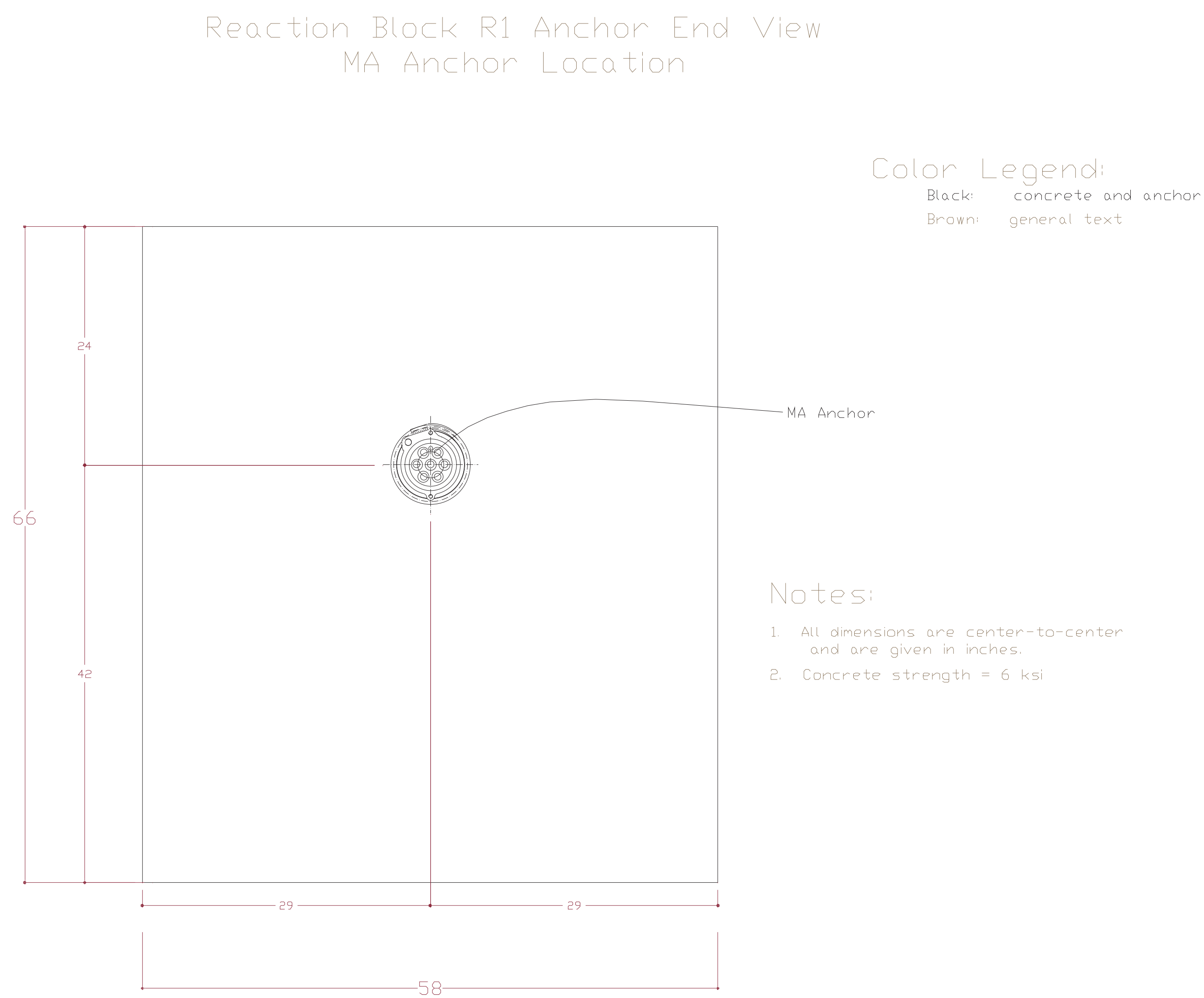

Figure D-25: Reaction block anchor end view – MA anchor placement.

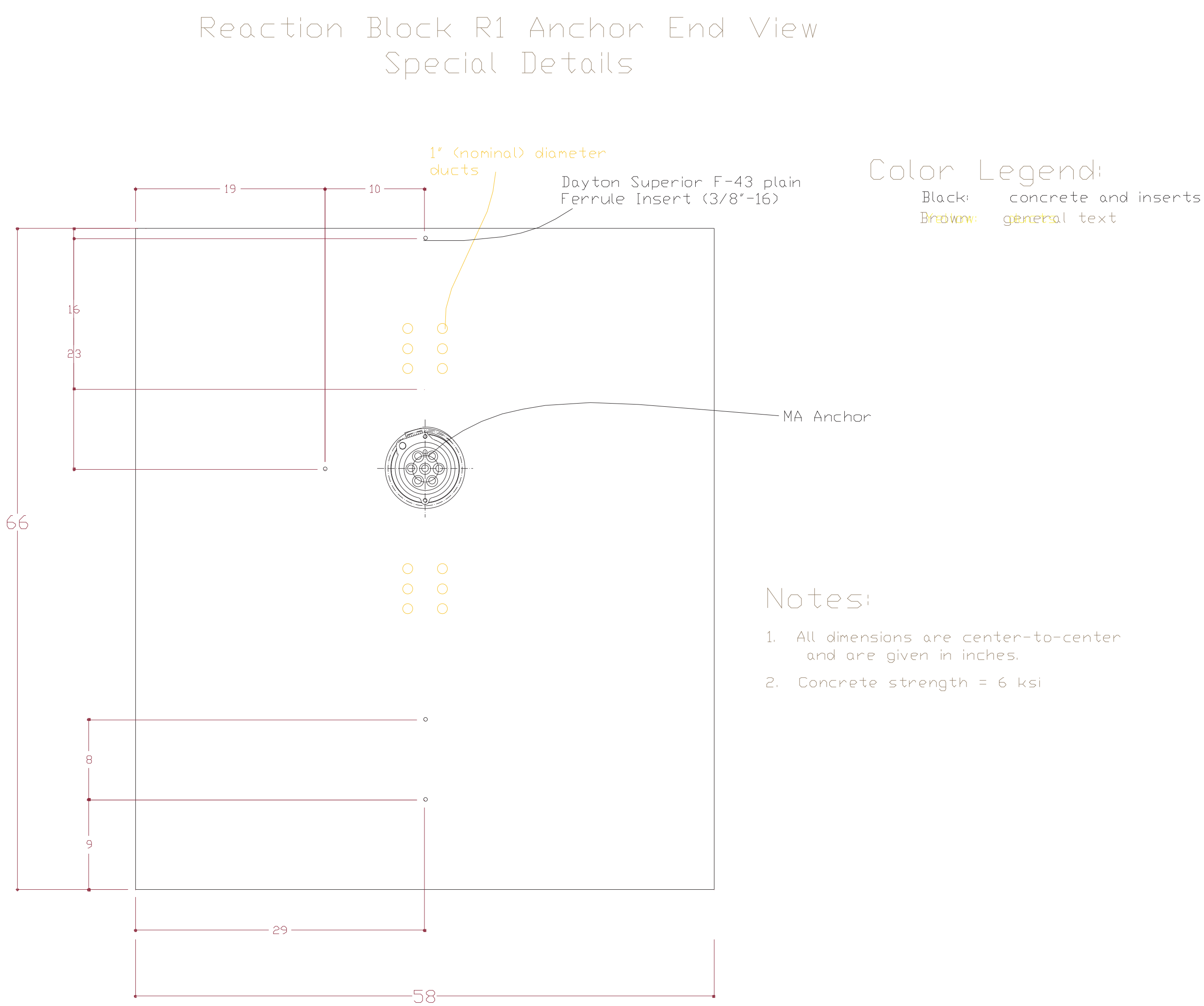

Figure D-26: Reaction block anchor end view – special details.

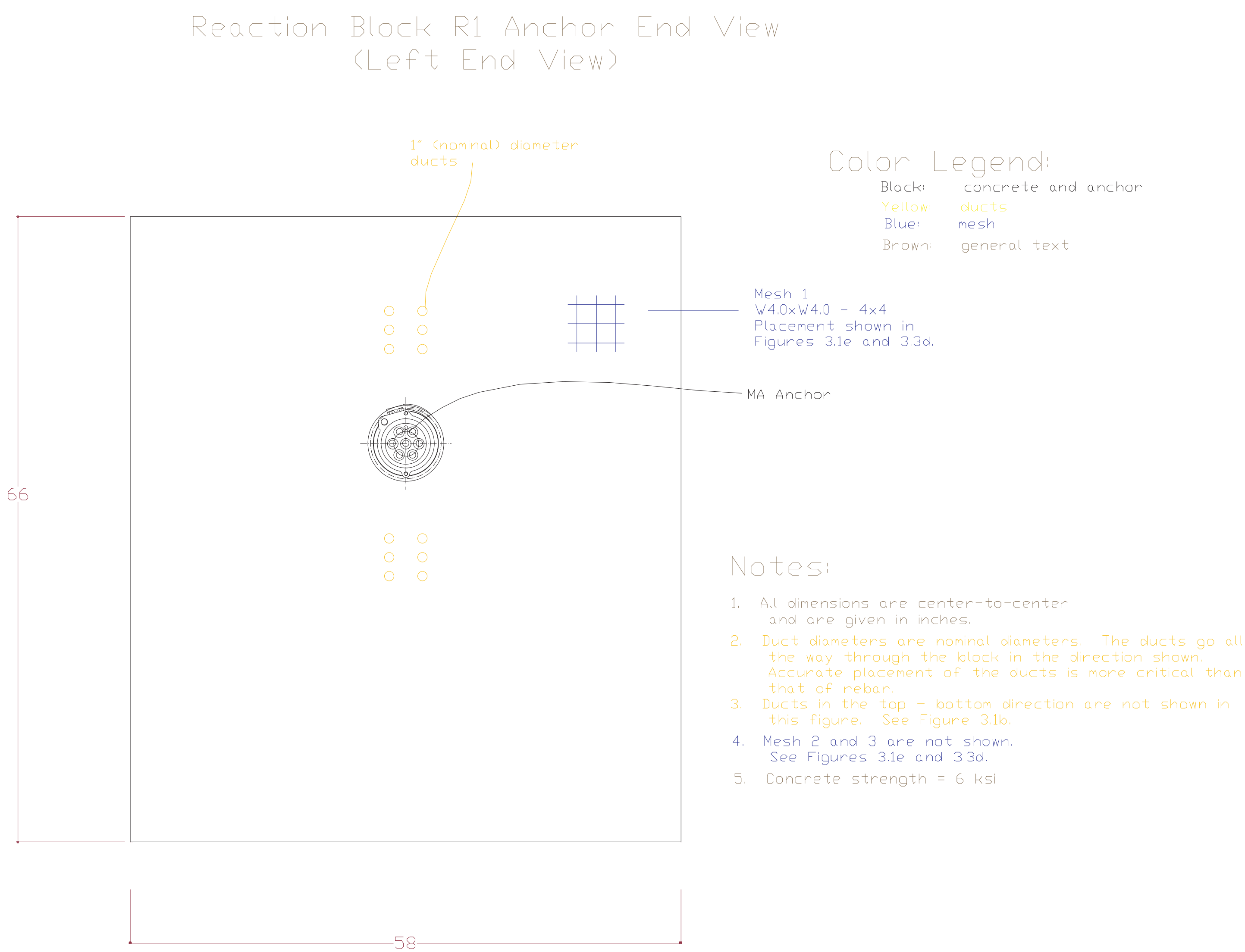

Figure D-14: Reaction block beam end view – special details.

APPENDIX E

LOAD BLOCK DESIGN DETAILS

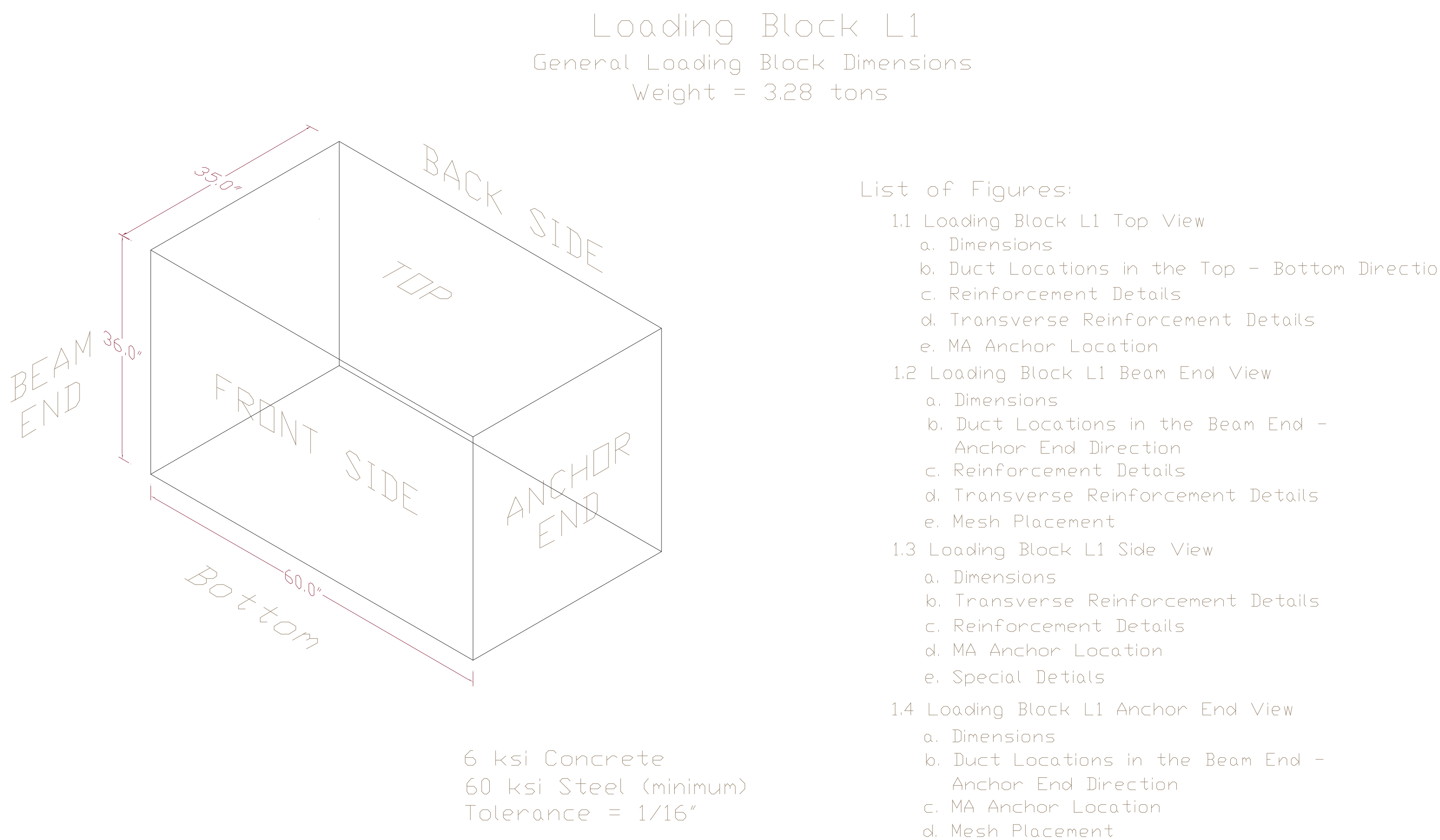

Figure E-1: Load block isometric view and general properties.

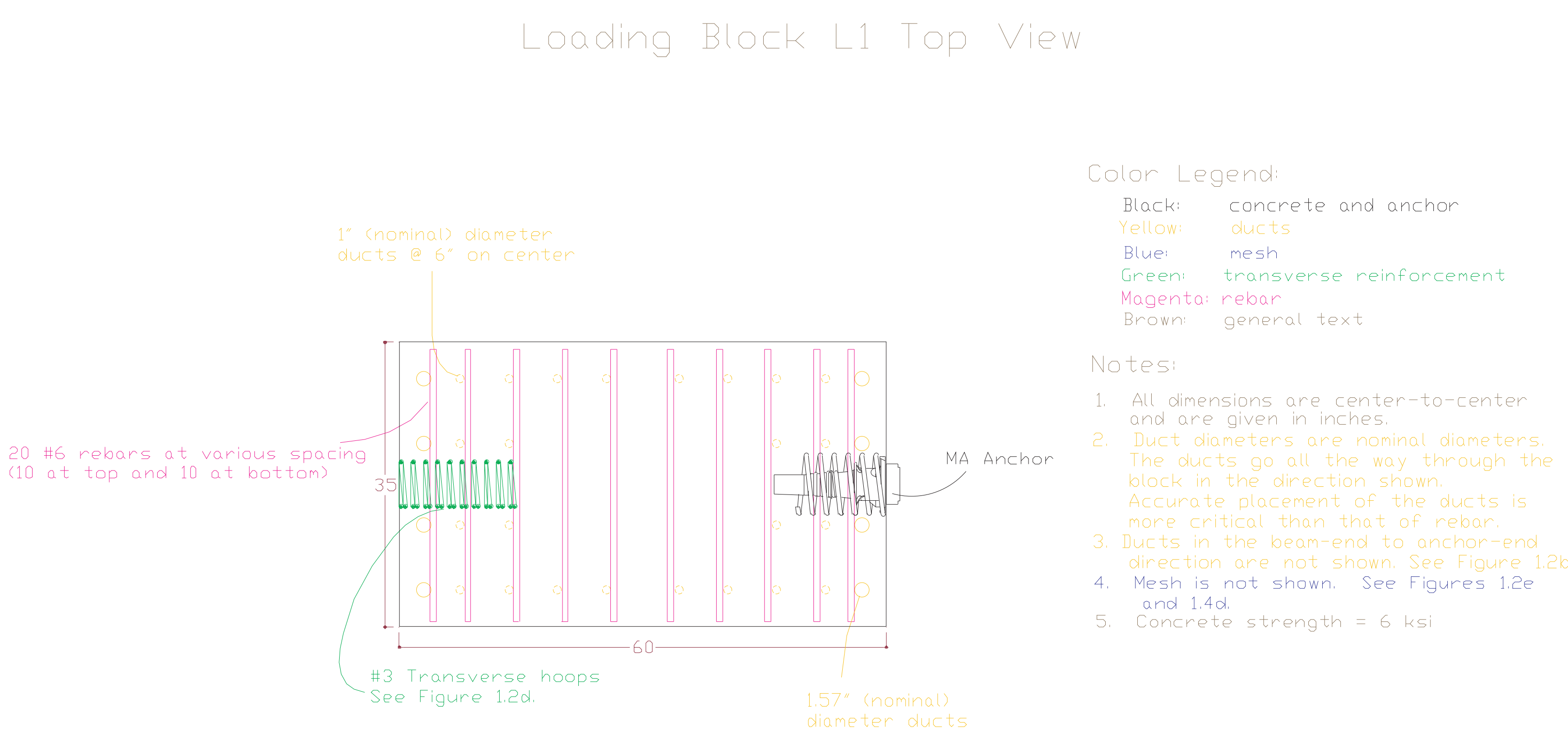

Figure E-2: Load block top view – general properties.

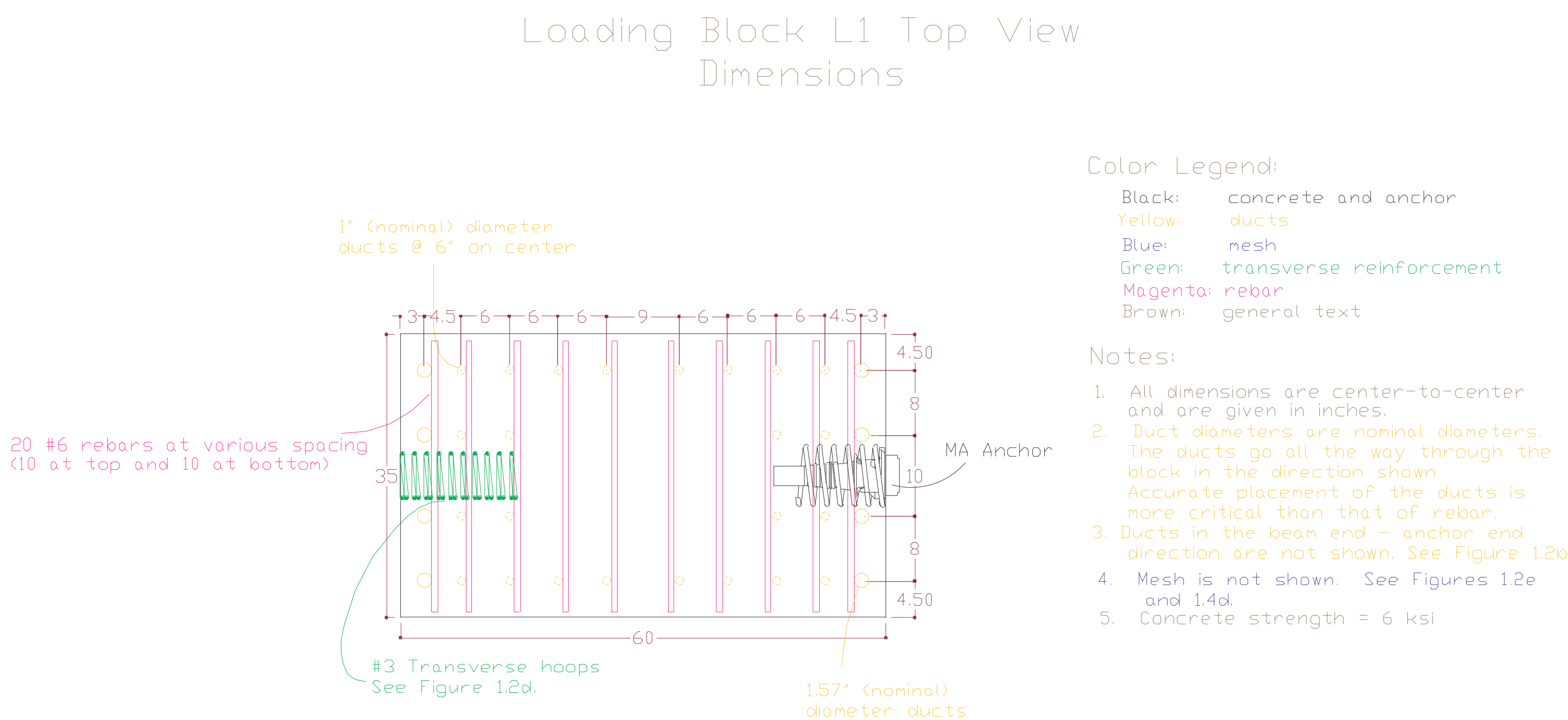

Figure E-3: Load block top view – general dimensions.

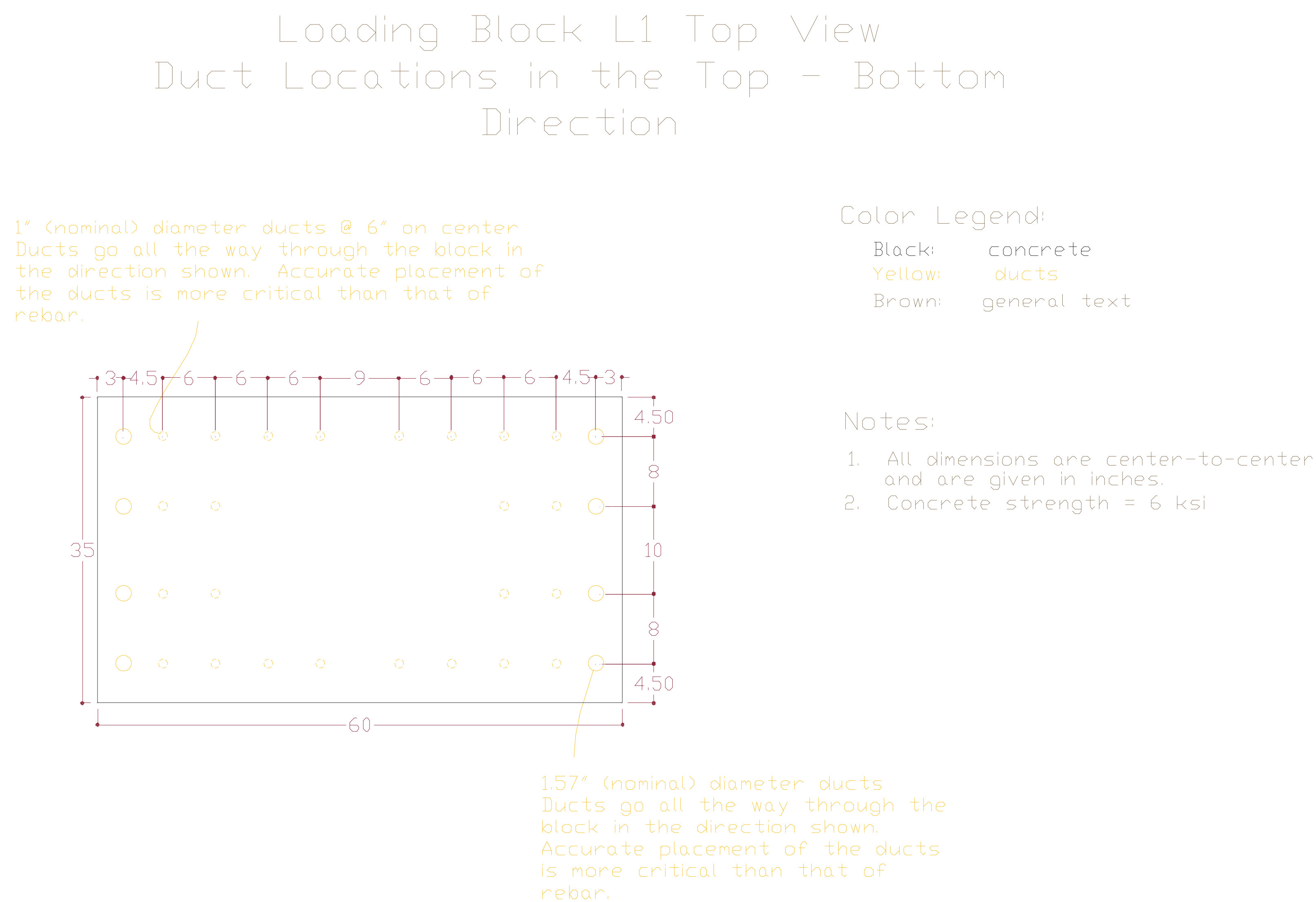

Figure E-4: Load block top view – duct placement.

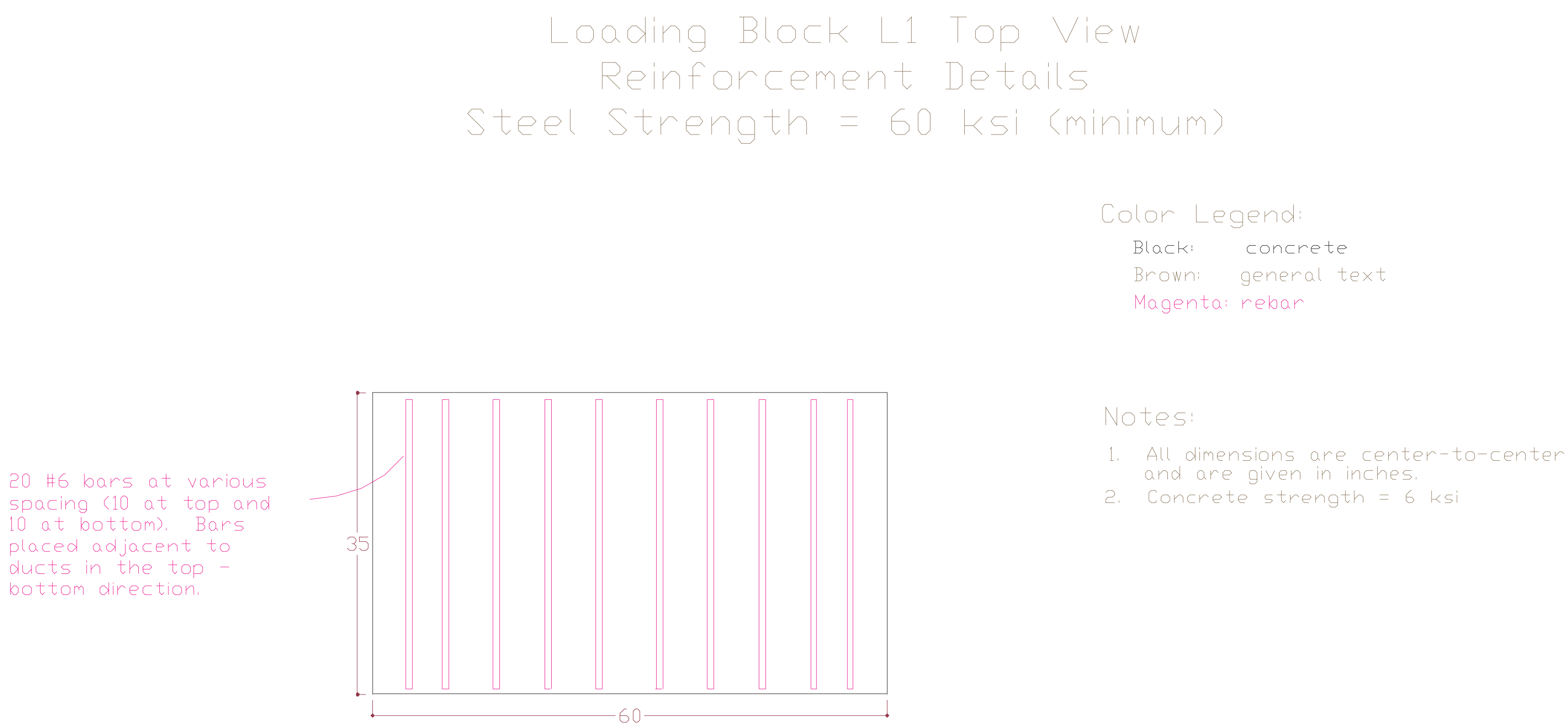

Figure E-5: Load block top view – No. 6 reinforcement details.

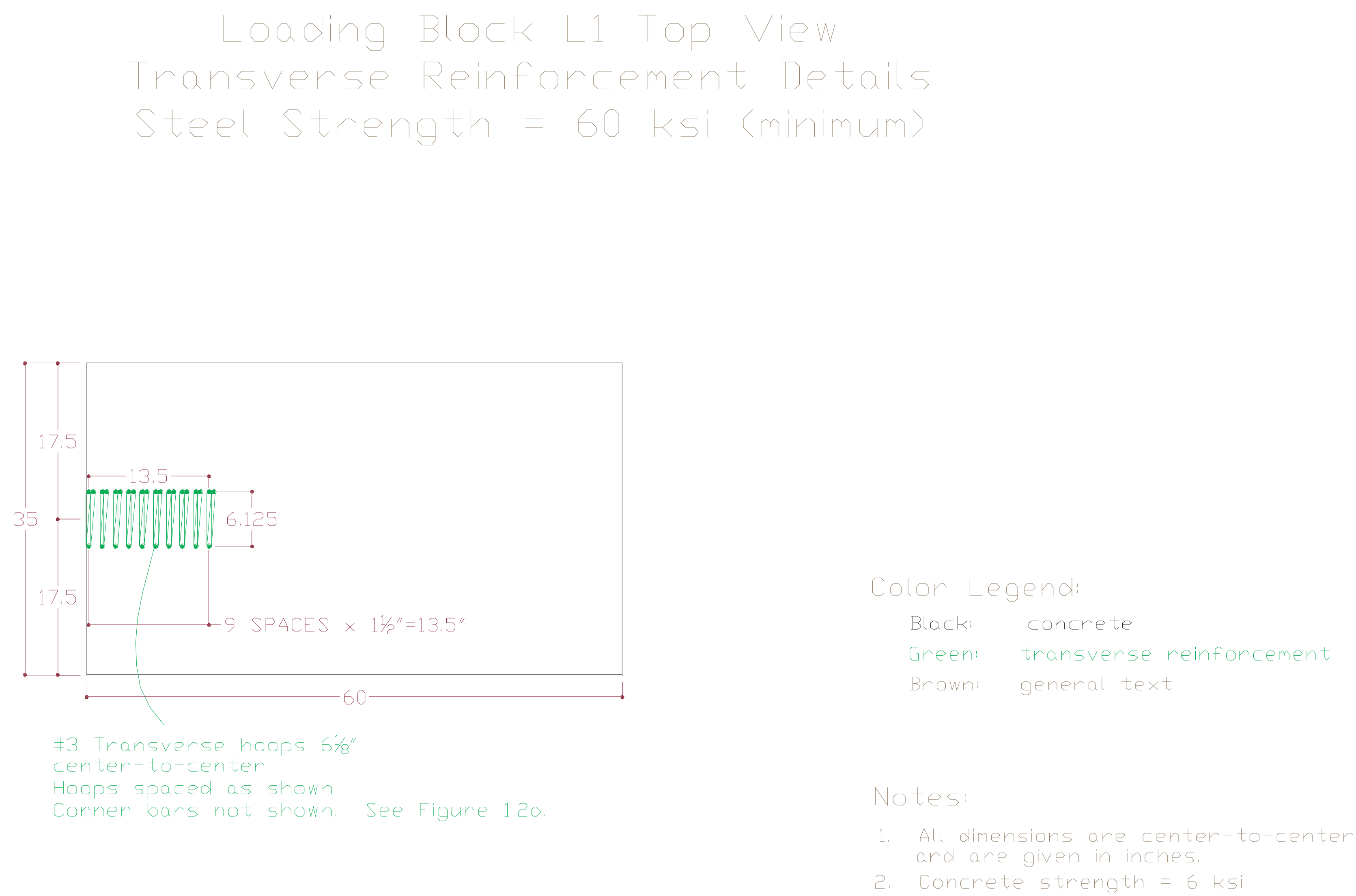

Figure E-6: Load block top view – transverse reinforcement details.

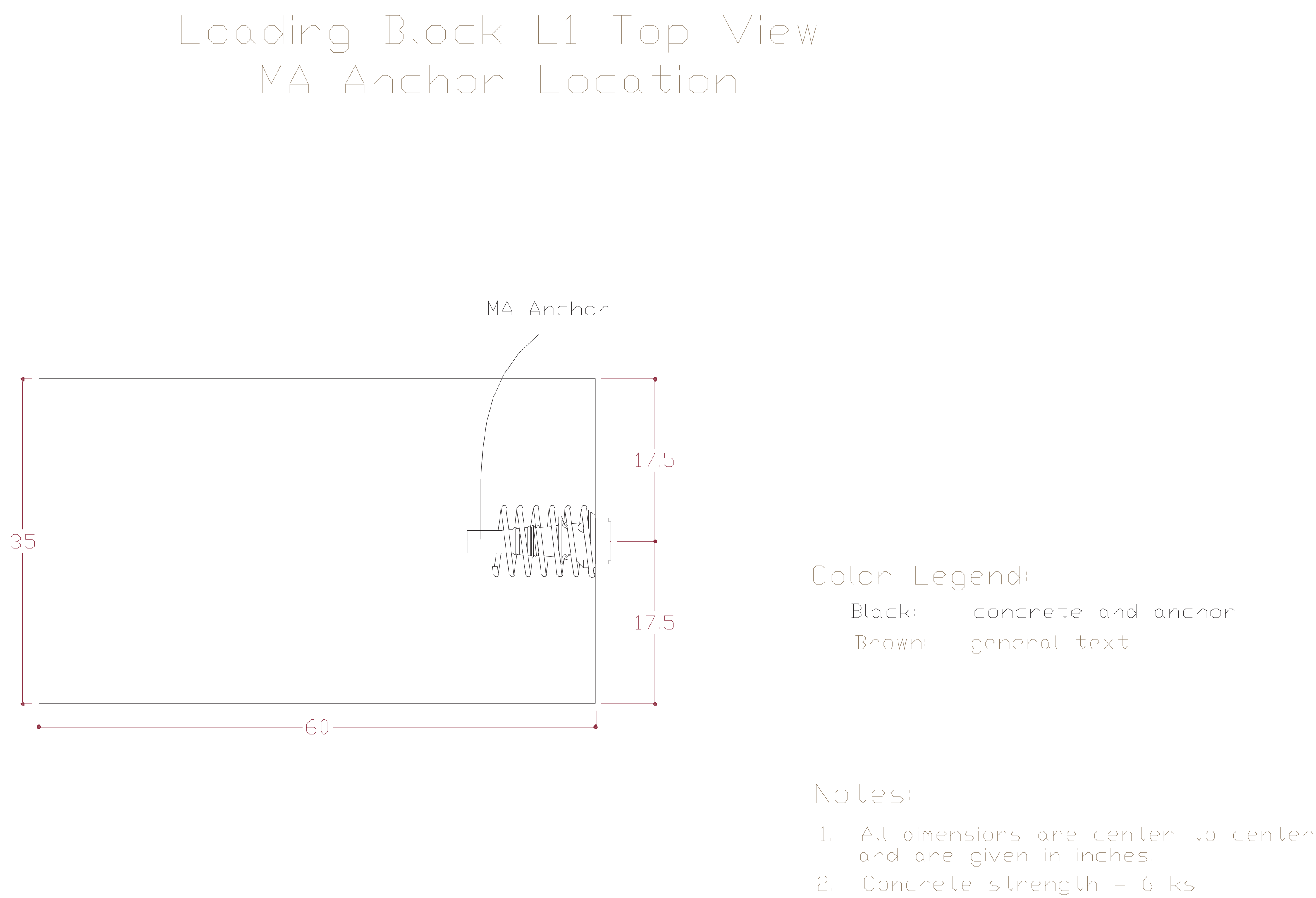

Figure E-7: Load block top view – MA anchor location.

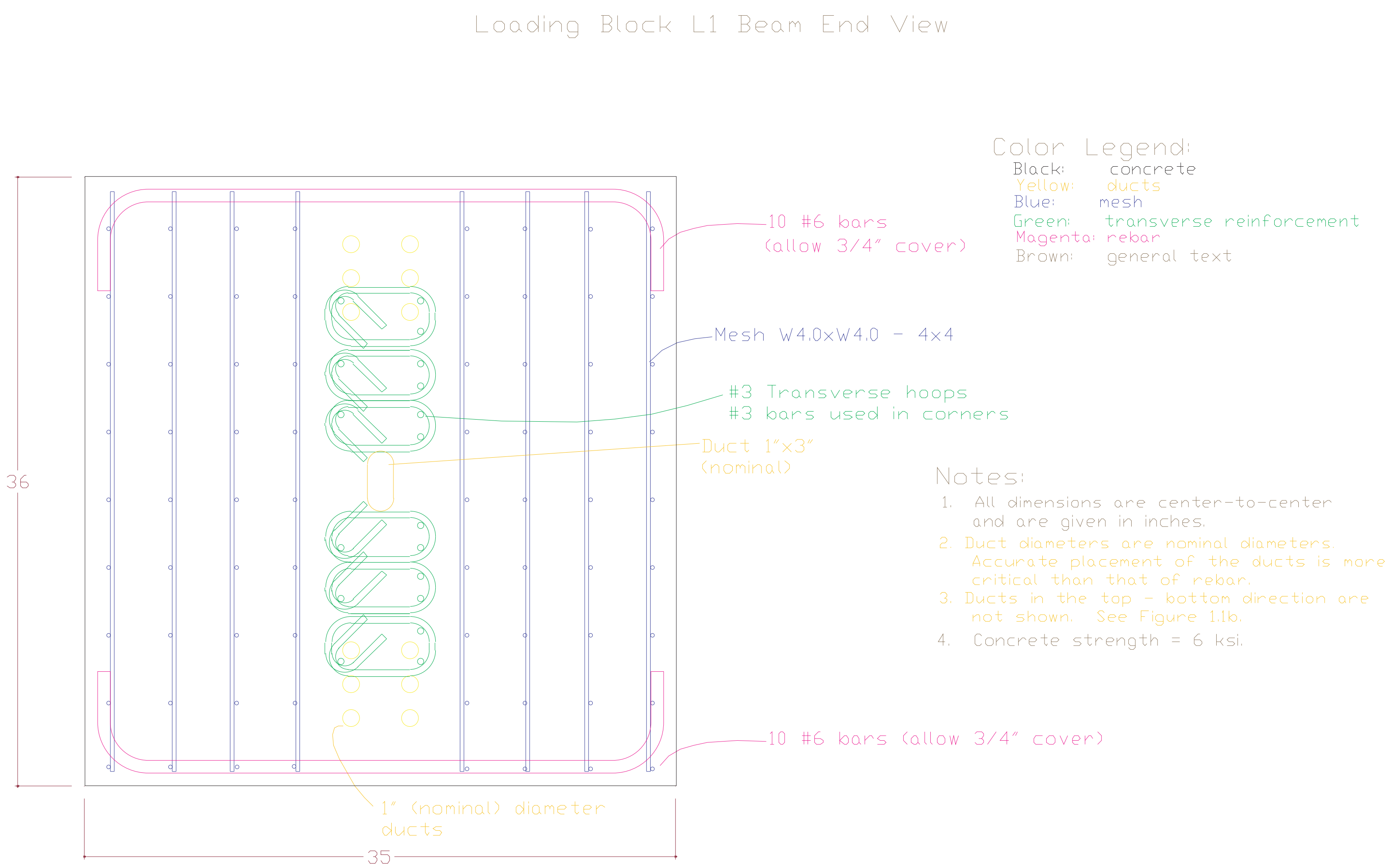

Figure E-9: Load block beam end view – general properties.

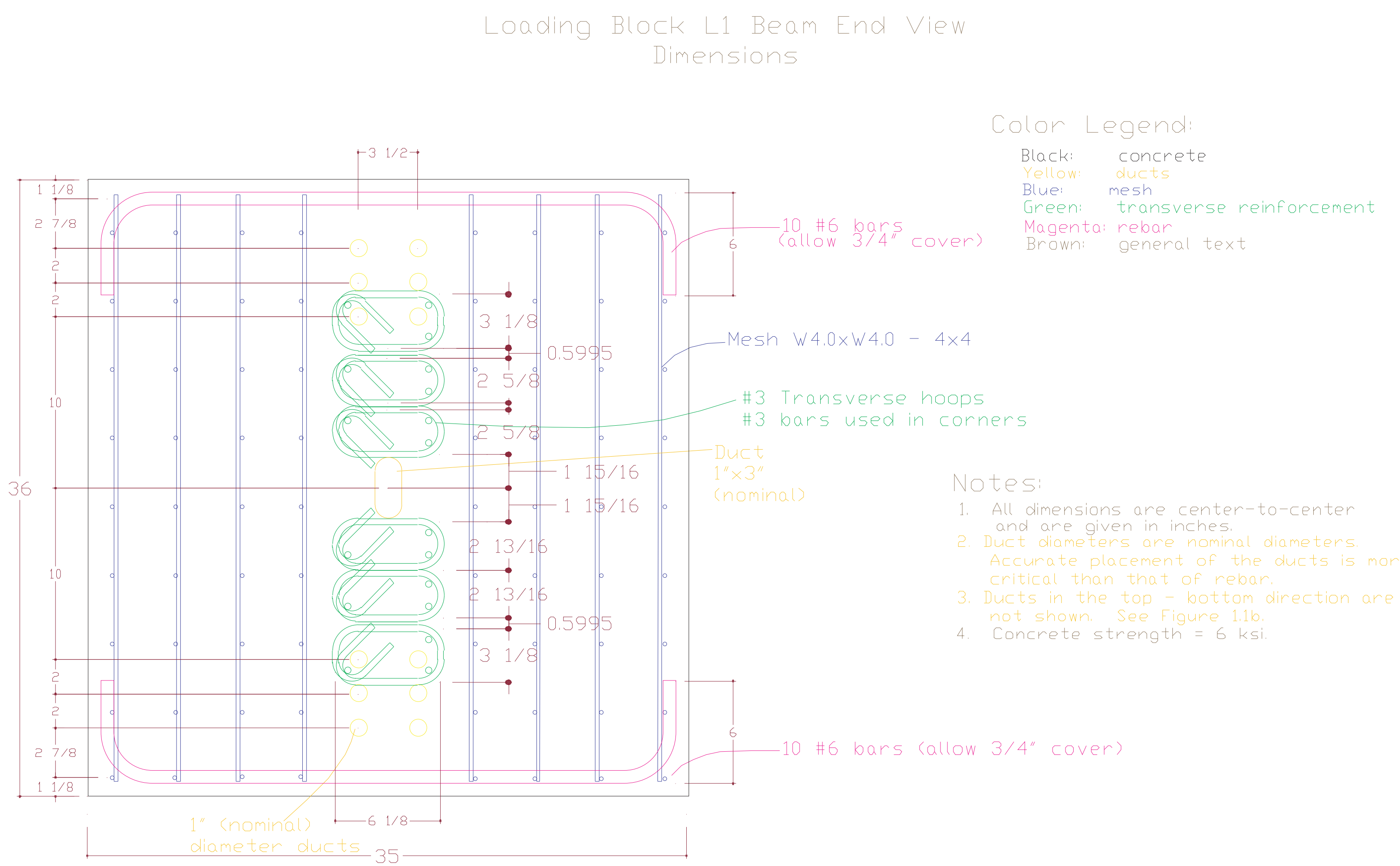

Figure E-10: Load block beam end view – general dimensions.

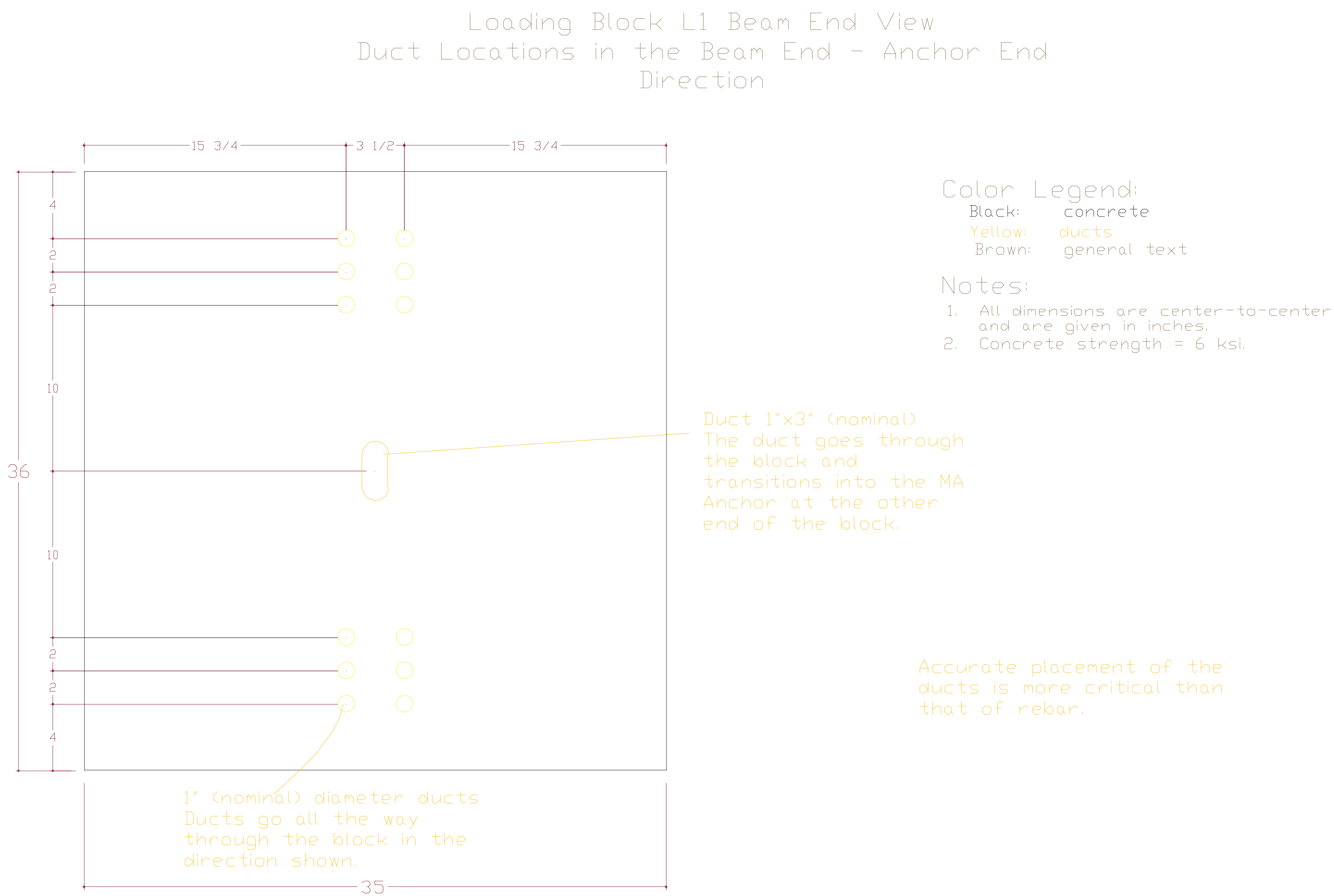

Figure E-11: Load block beam end view – duct placement.

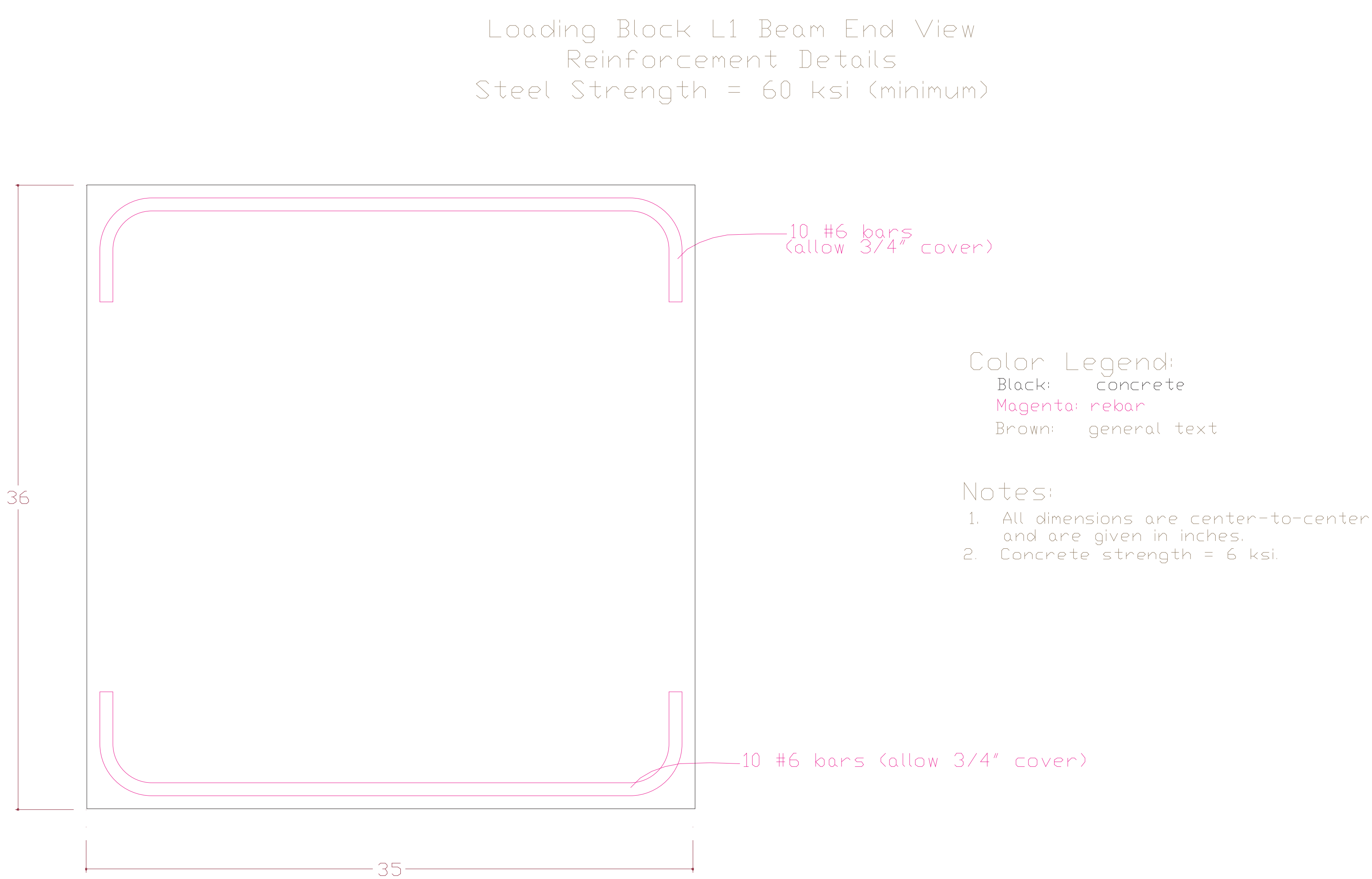

Figure E-12: Load block beam end view – No. 6 reinforcement details.

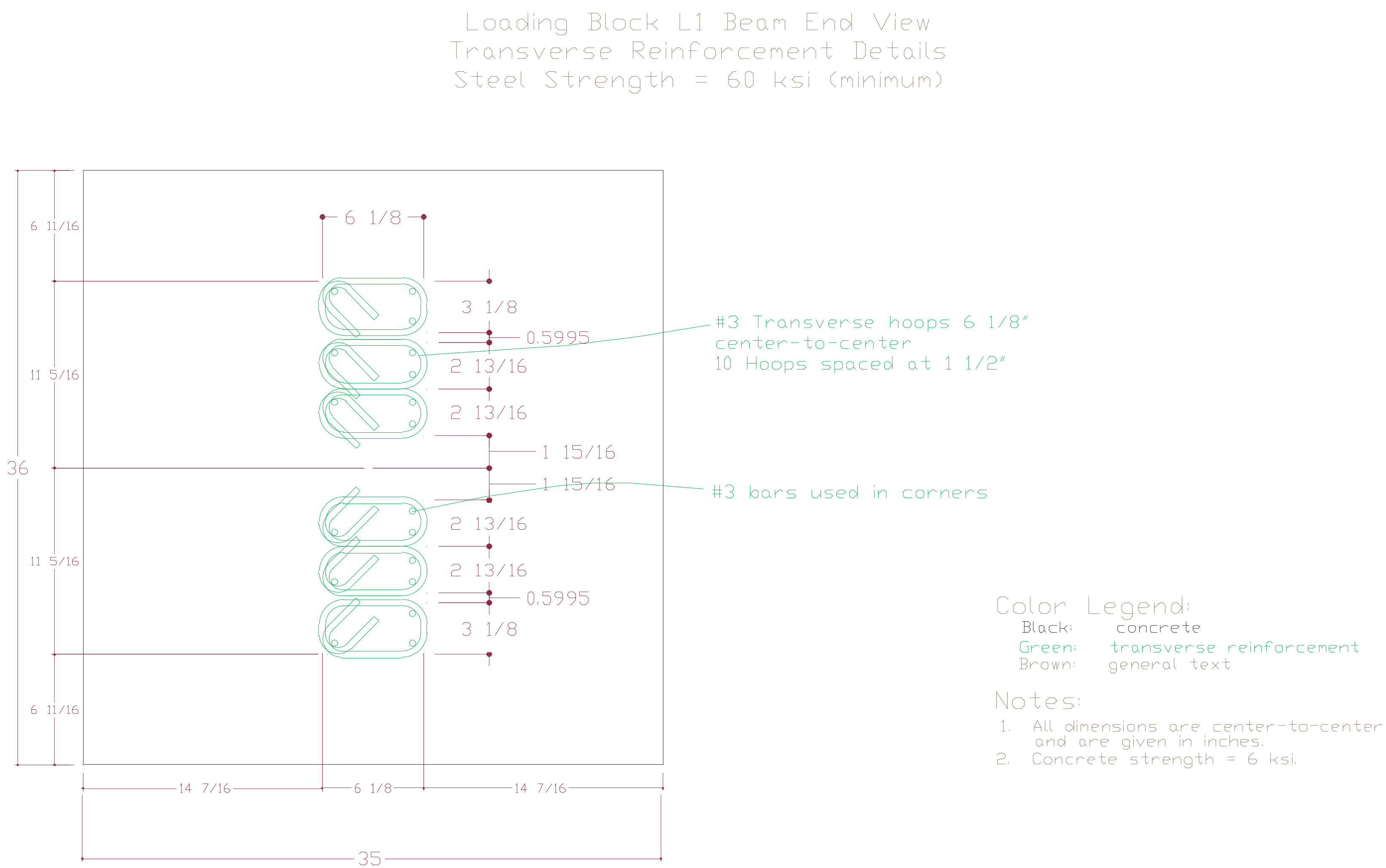

Figure E-13: Load block beam end view – transverse reinforcement details.

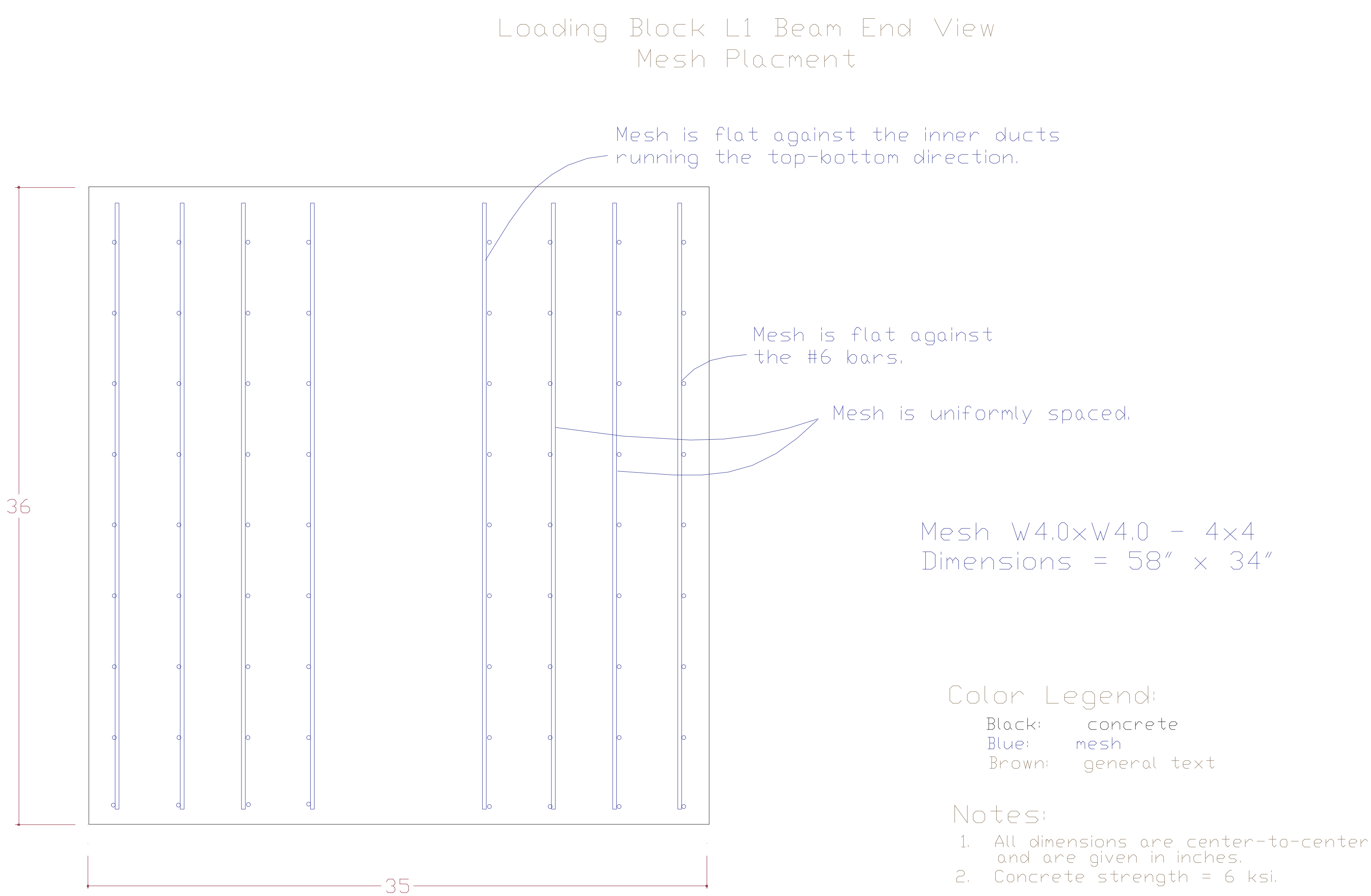

Figure E-14: Load block beam end view – mesh placement.

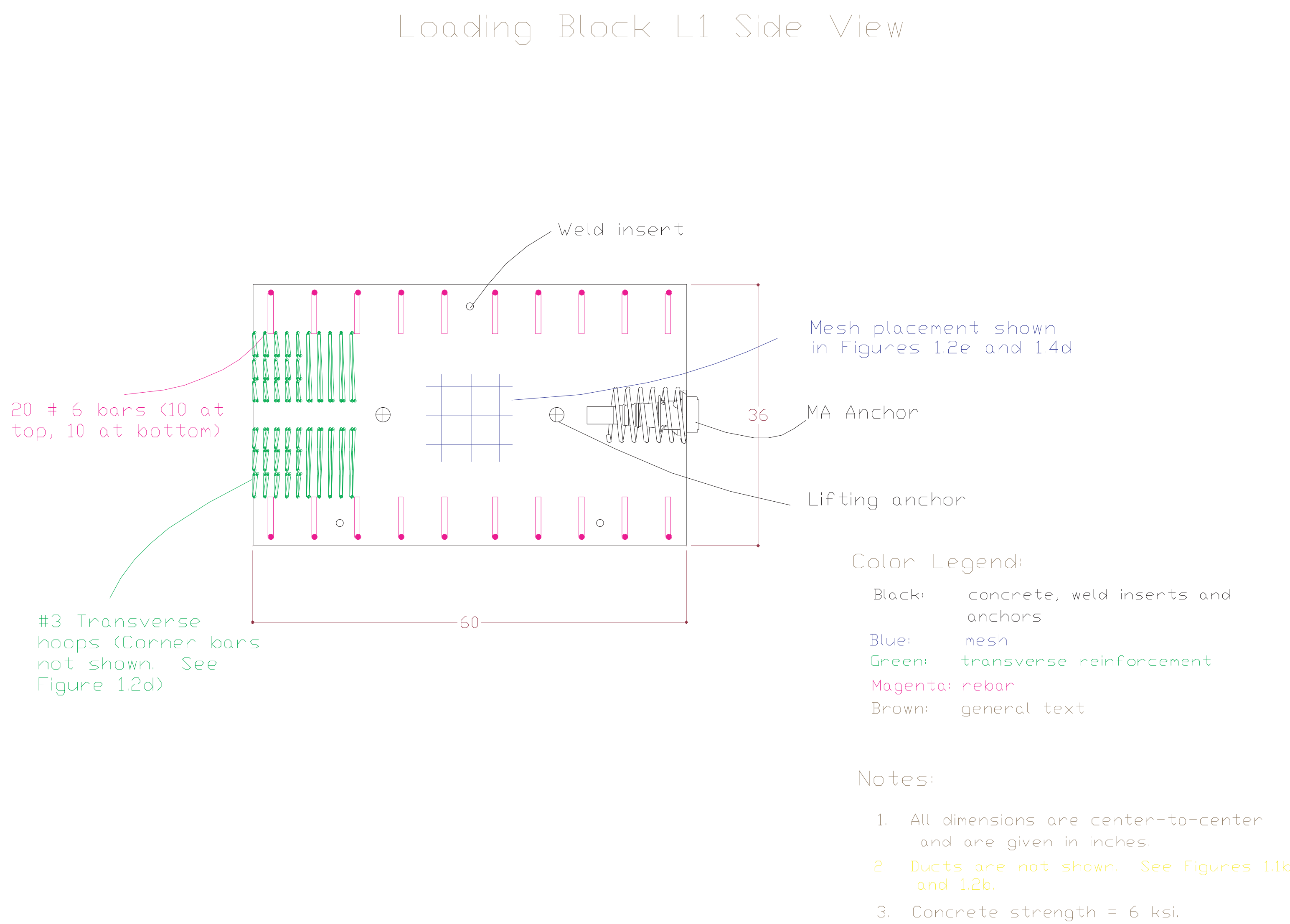

Figure E-15: Load block side view – general properties.

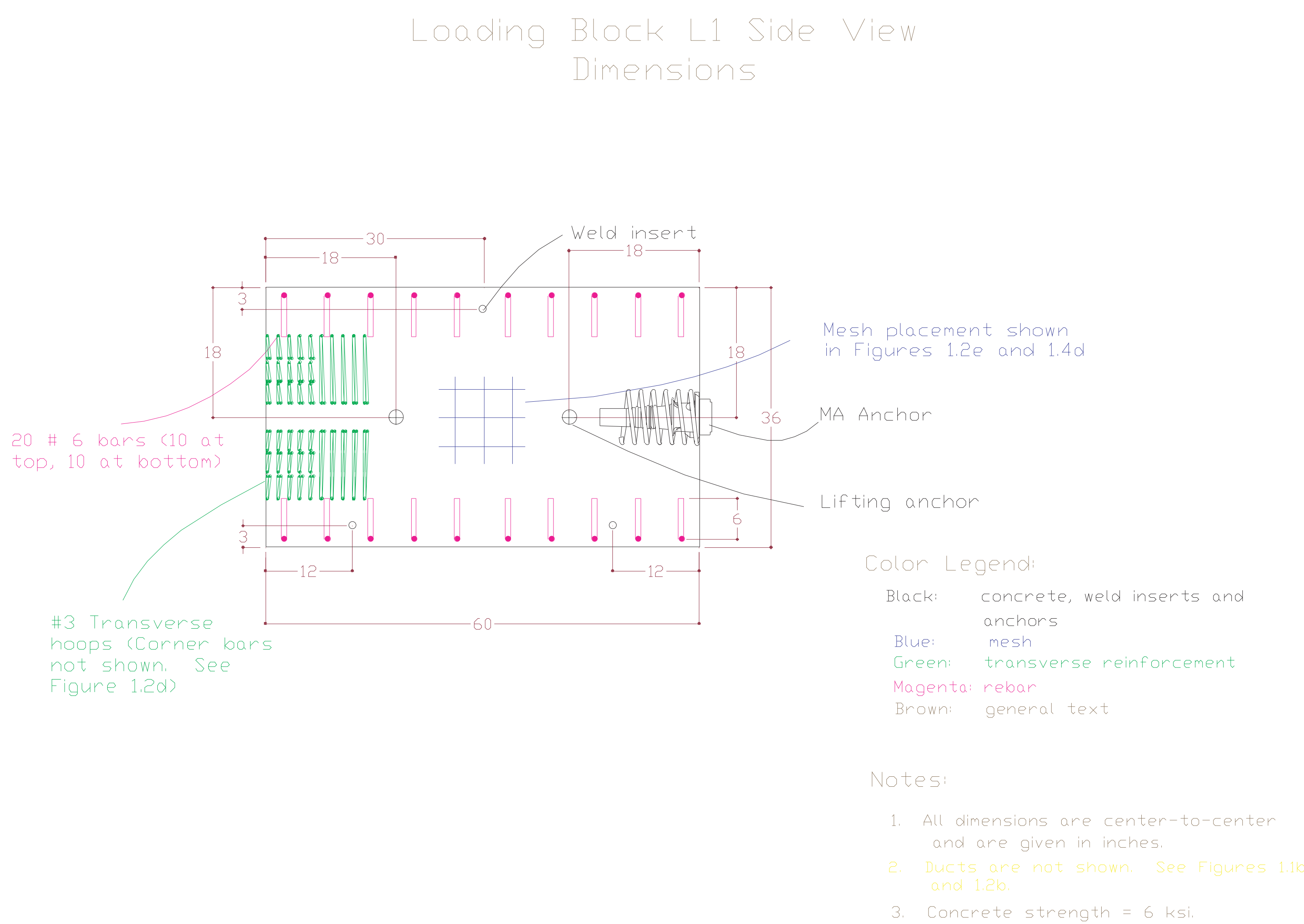

Figure E-16: Load block side view – general dimensions.

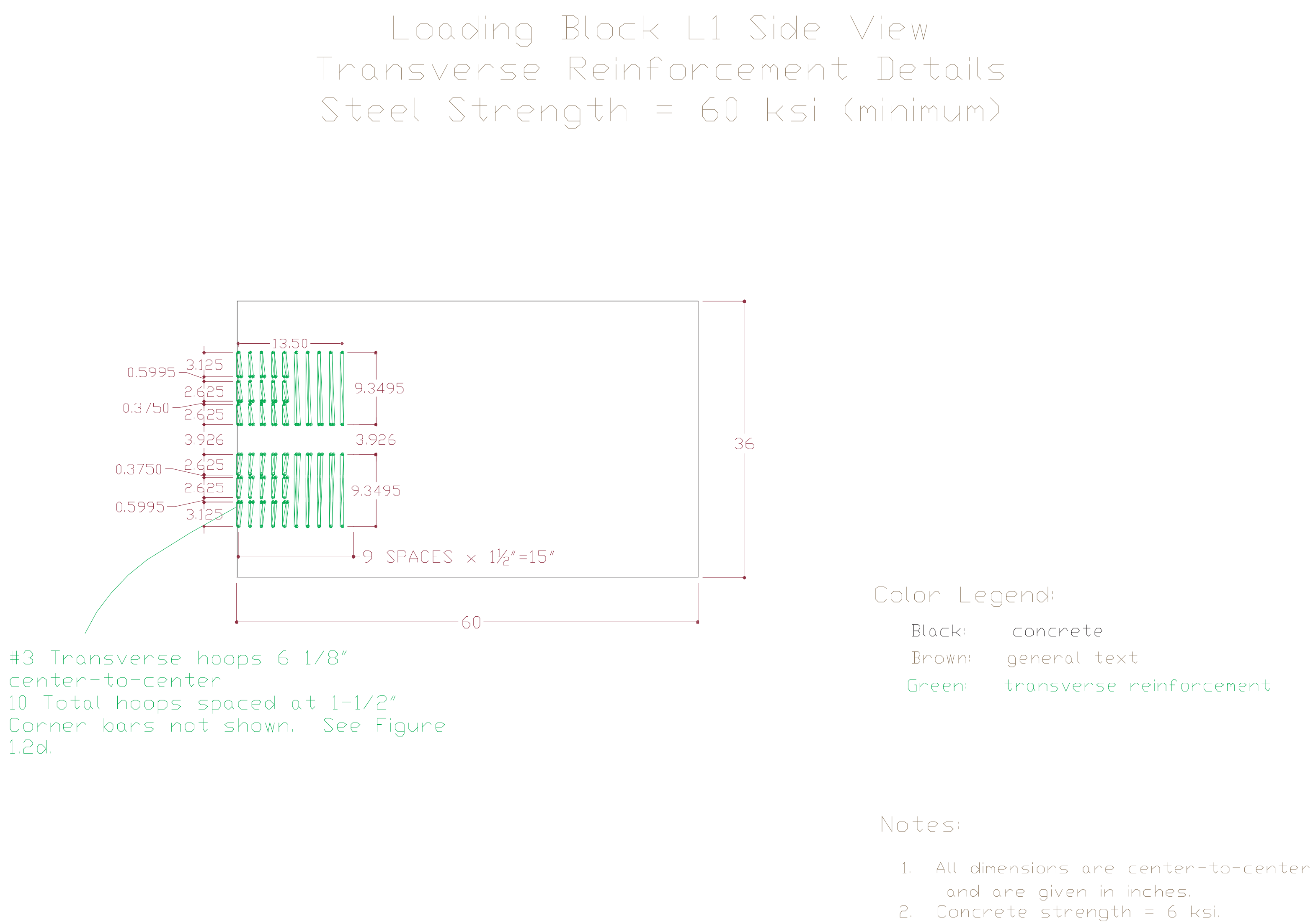

Figure E-17: Load block side view – transverse reinforcement details.

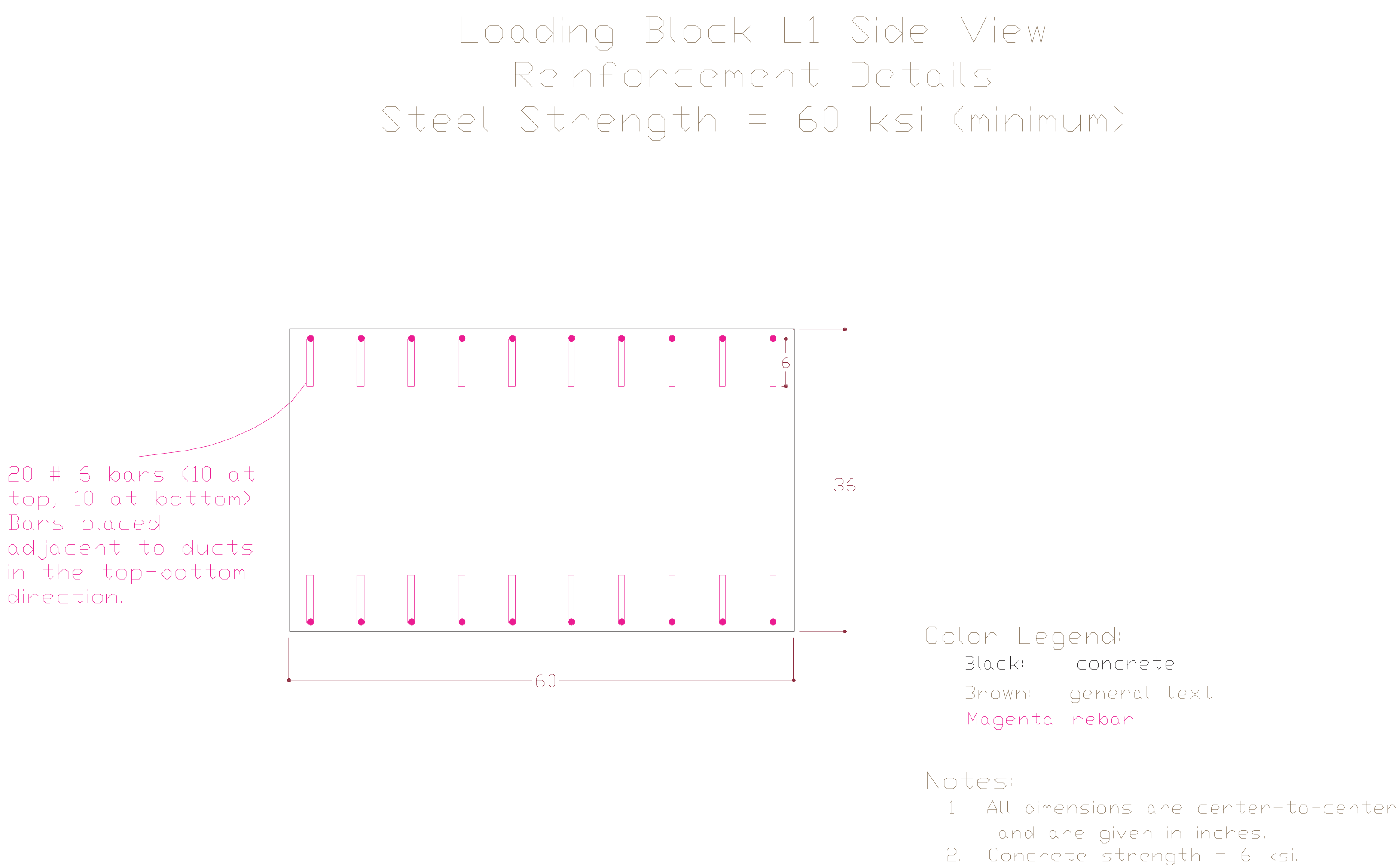

Figure E-18: Load block side view – No. 6 reinforcement details.

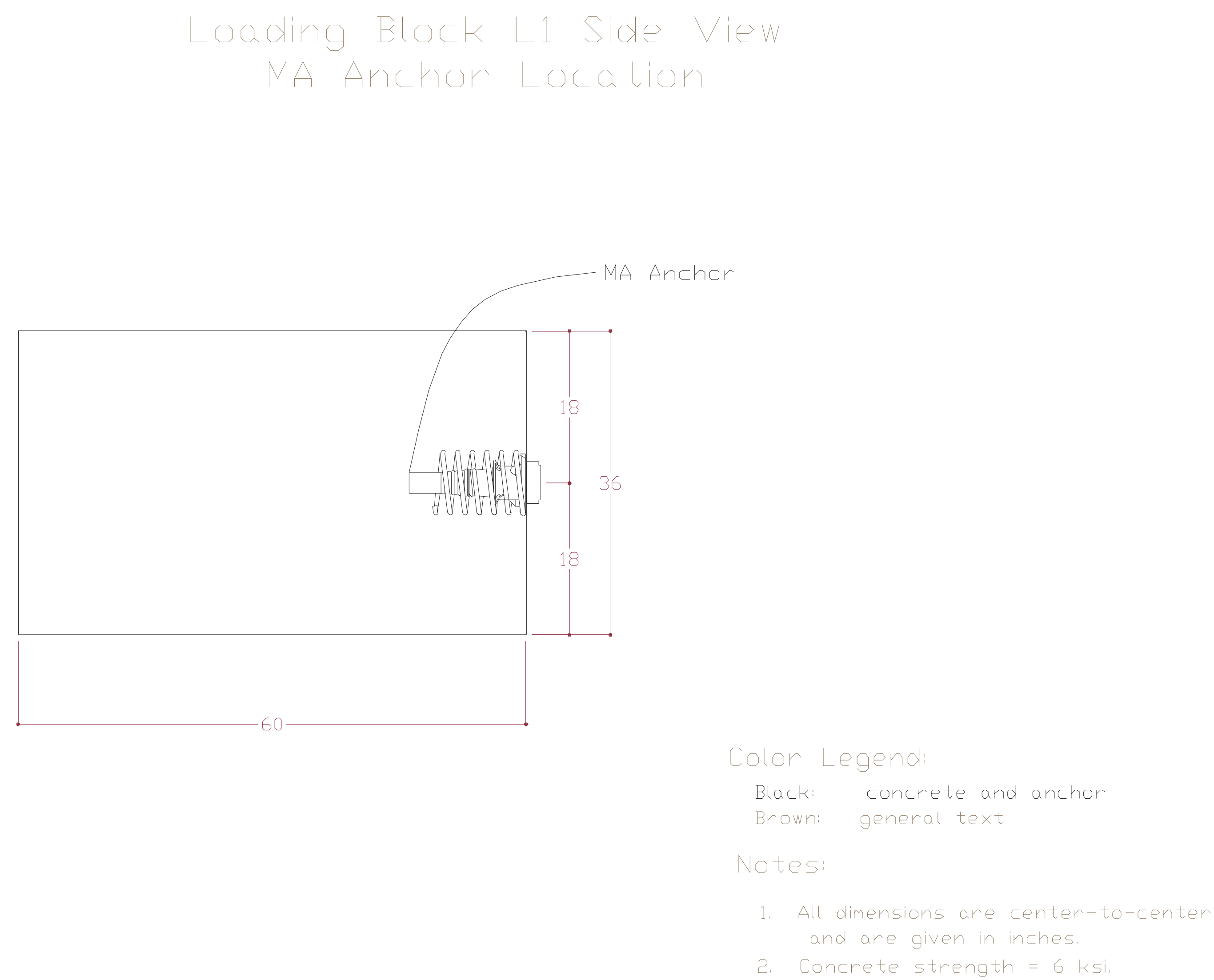

Figure E-19: Load block side view – anchor location.

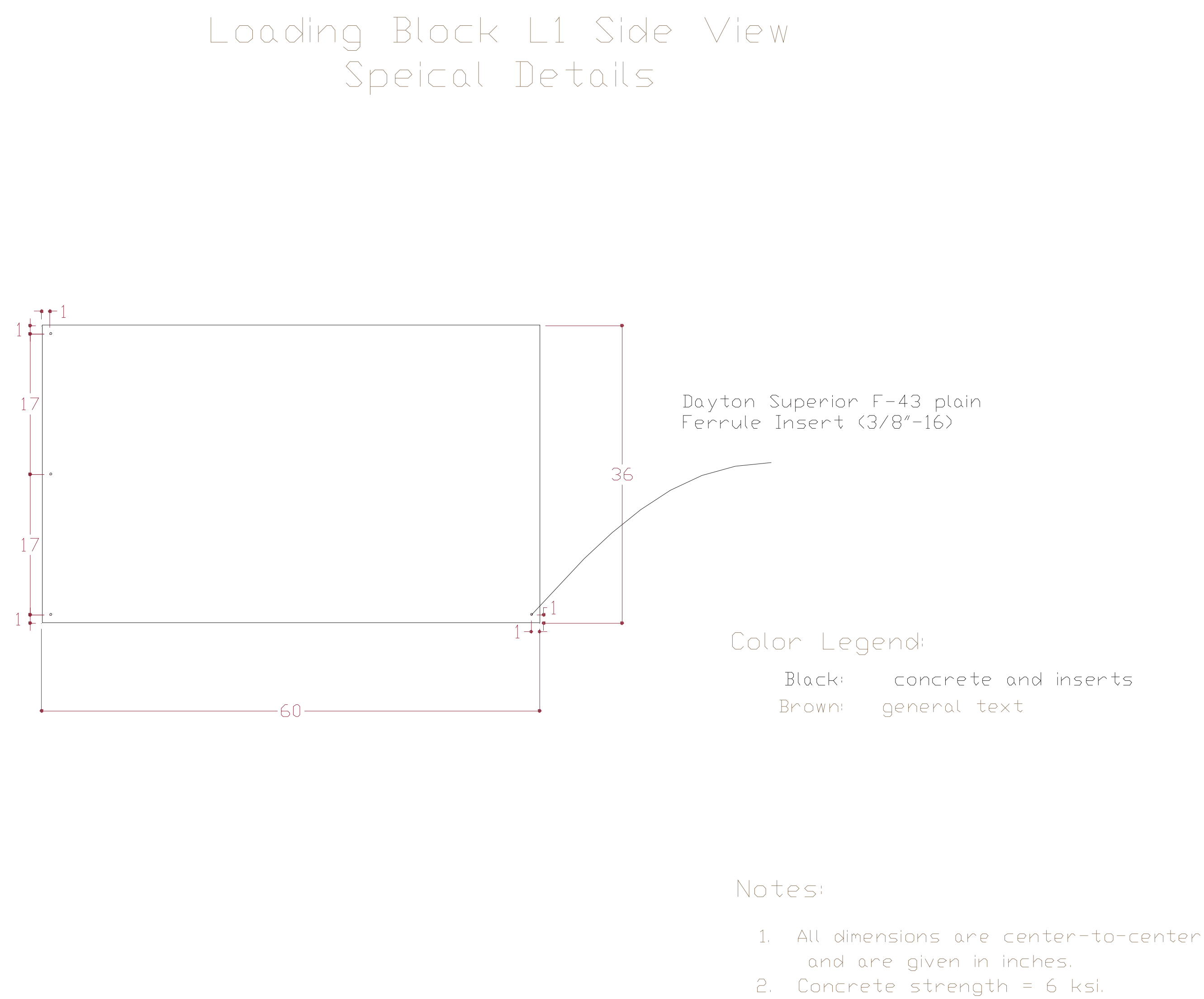

Figure E-20: Load block side view – special details.

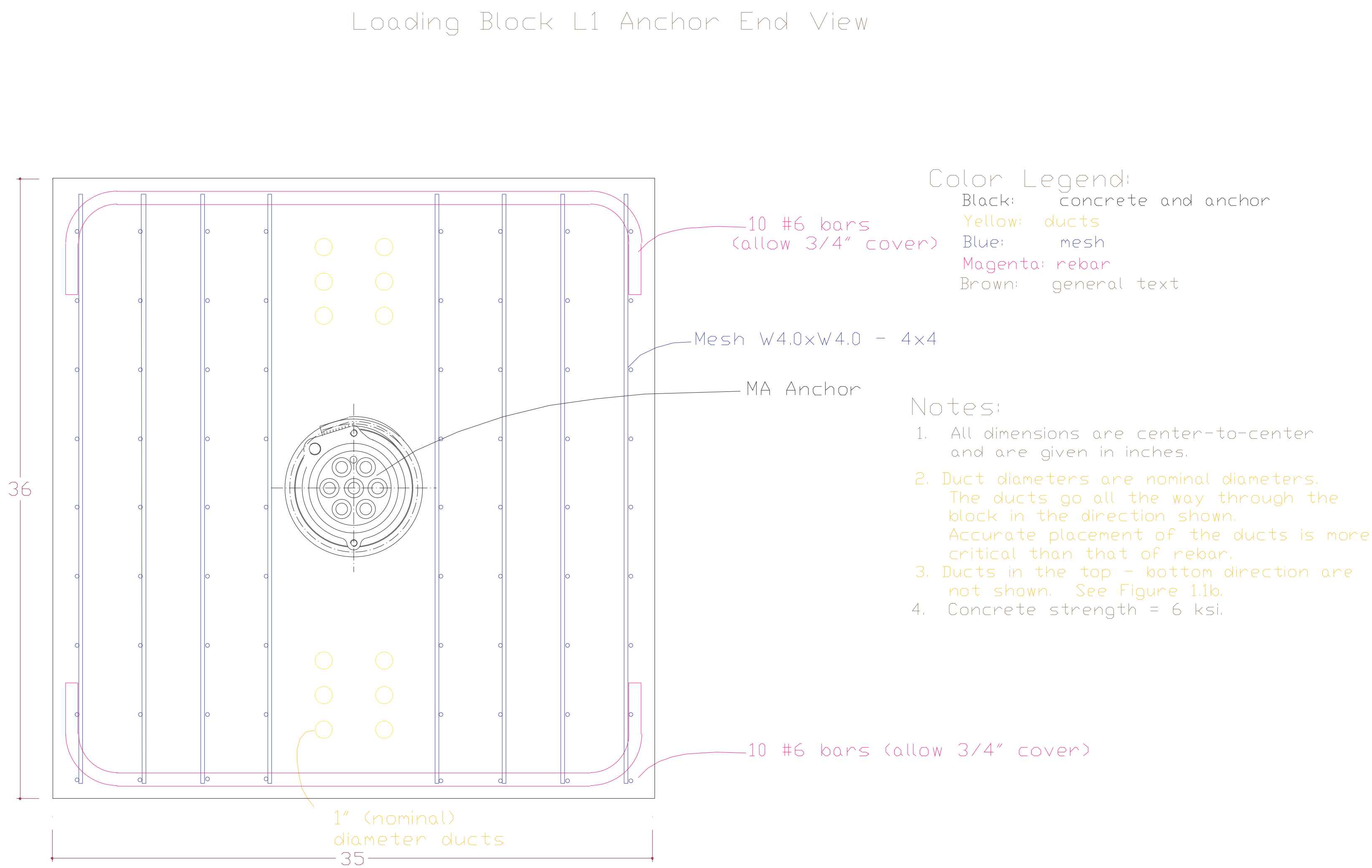

Figure E-22: Load block anchor end view – general properties.

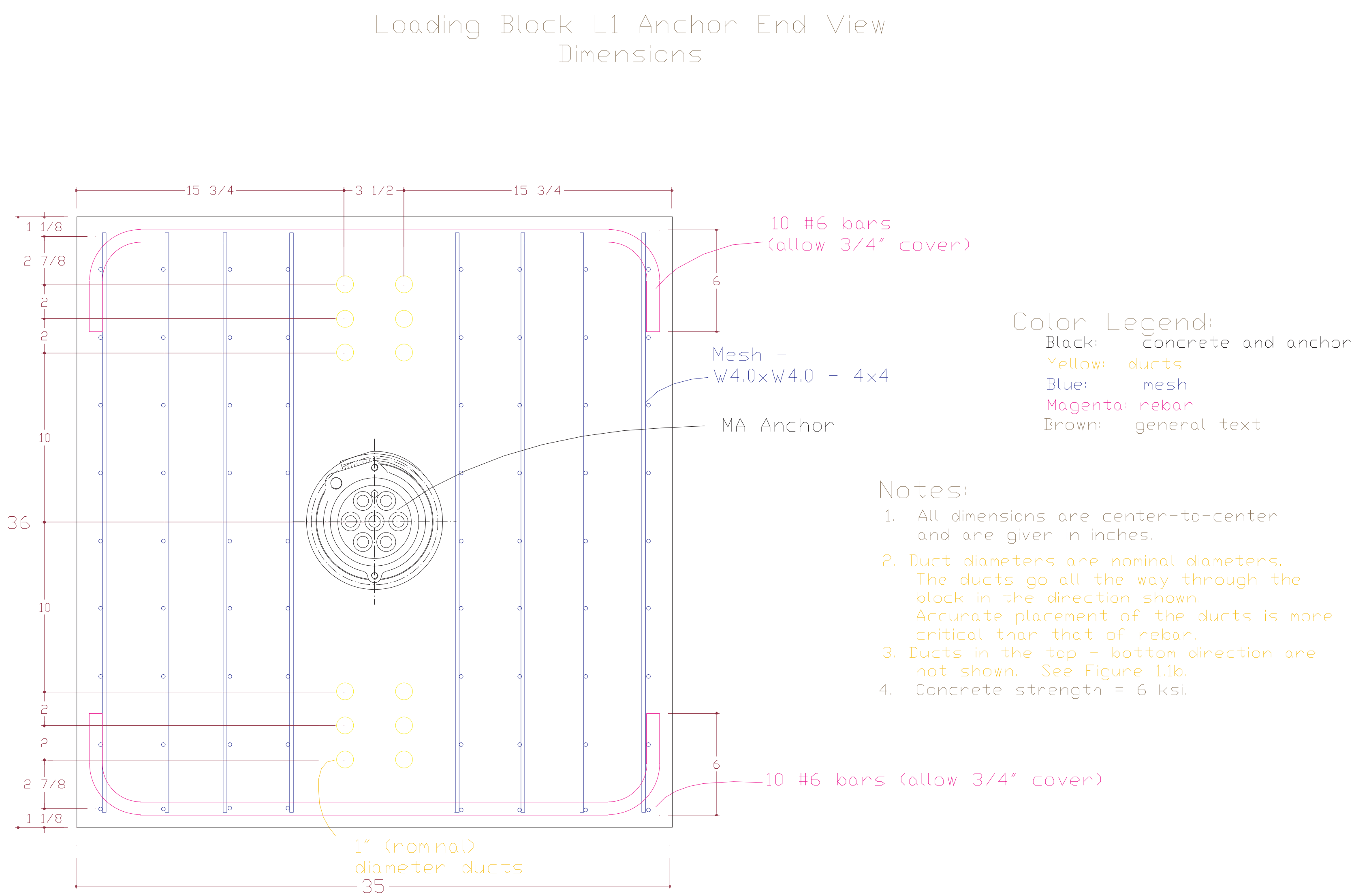

Figure E-23: Load block anchor end view – general dimensions.

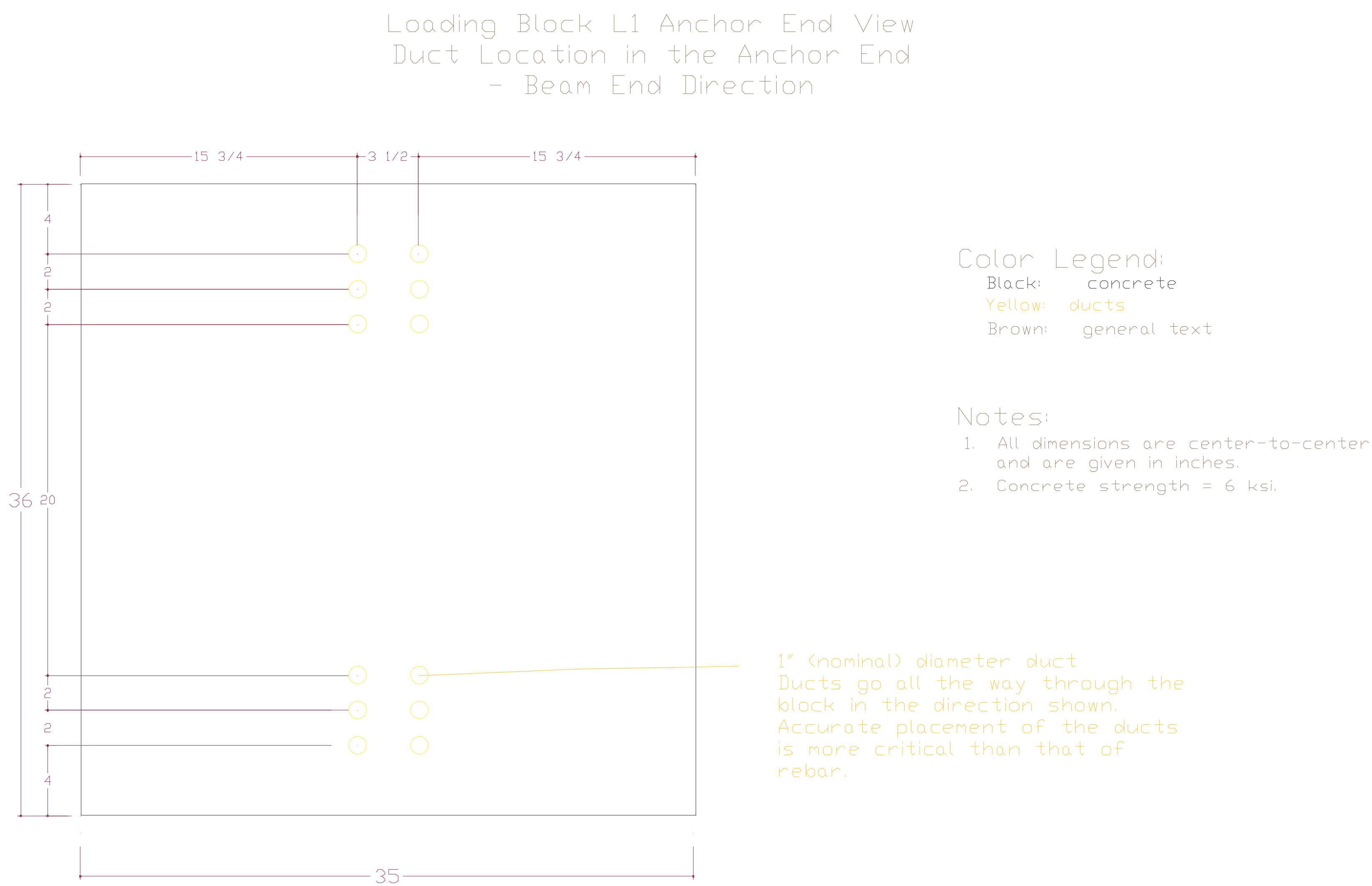

Figure E-24: Load block anchor end view – duct placement.

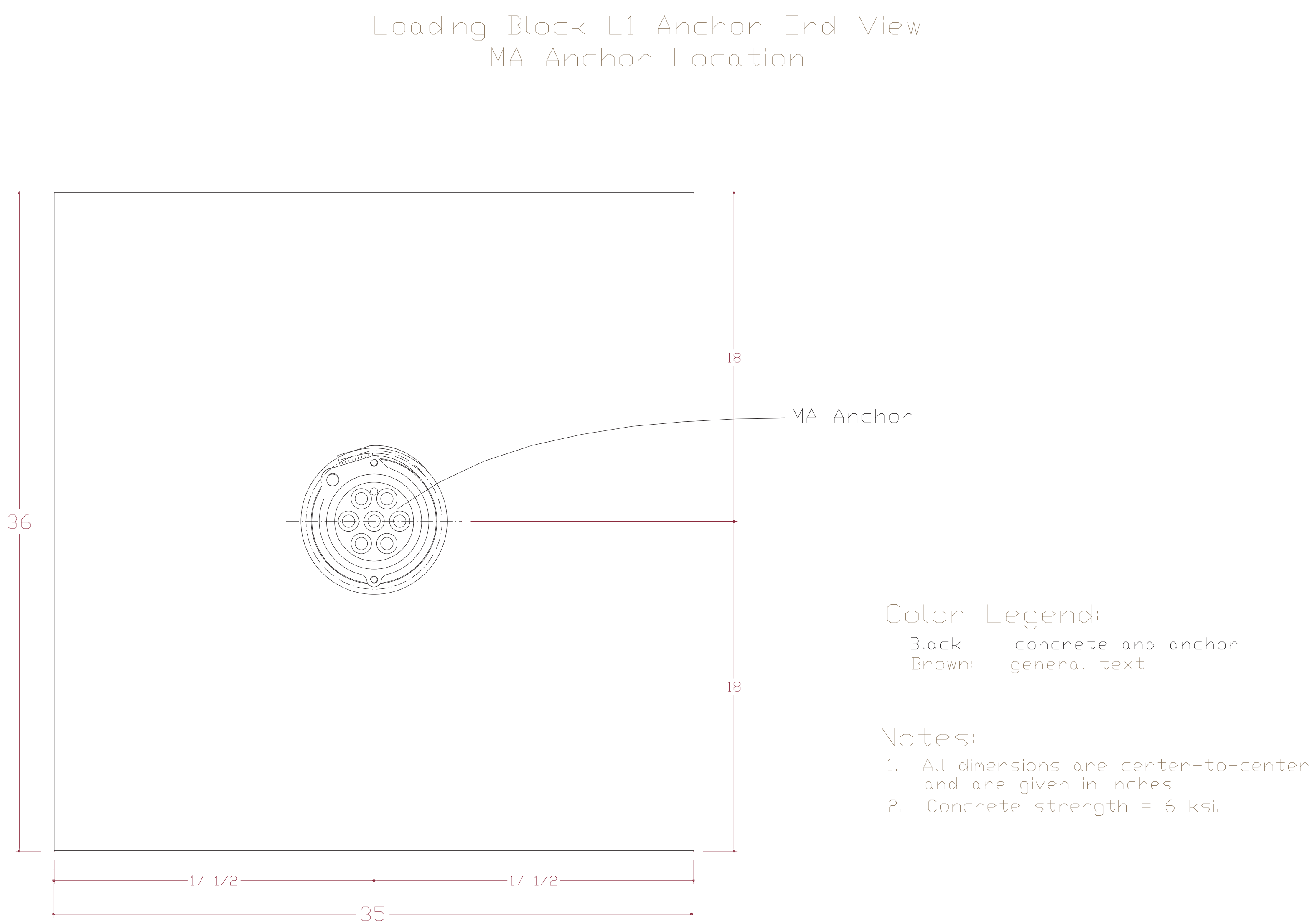

Figure E-25: Load block anchor end view – MA anchor location.

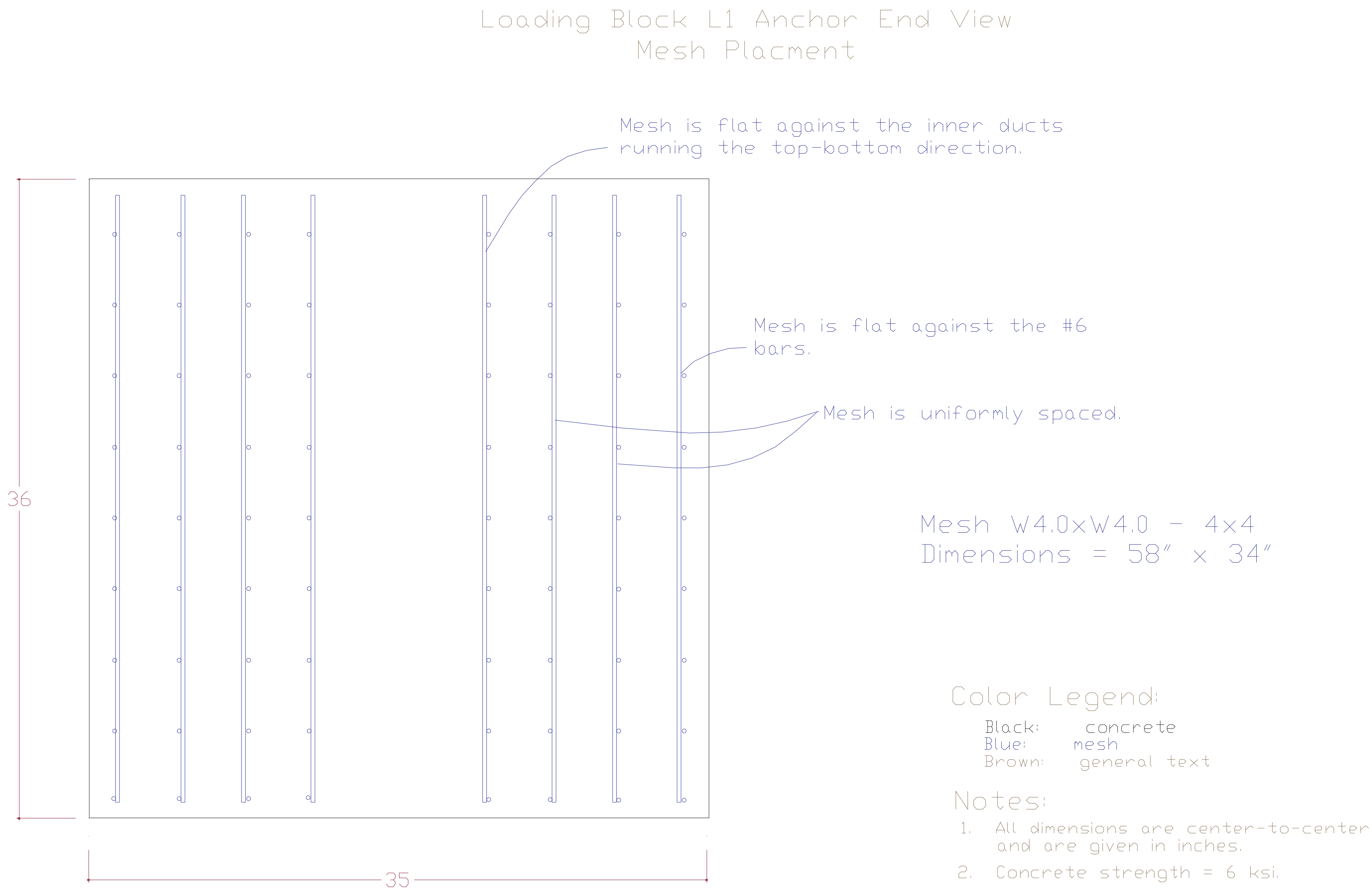

Figure E-26: Load block beam end view – mesh placement.

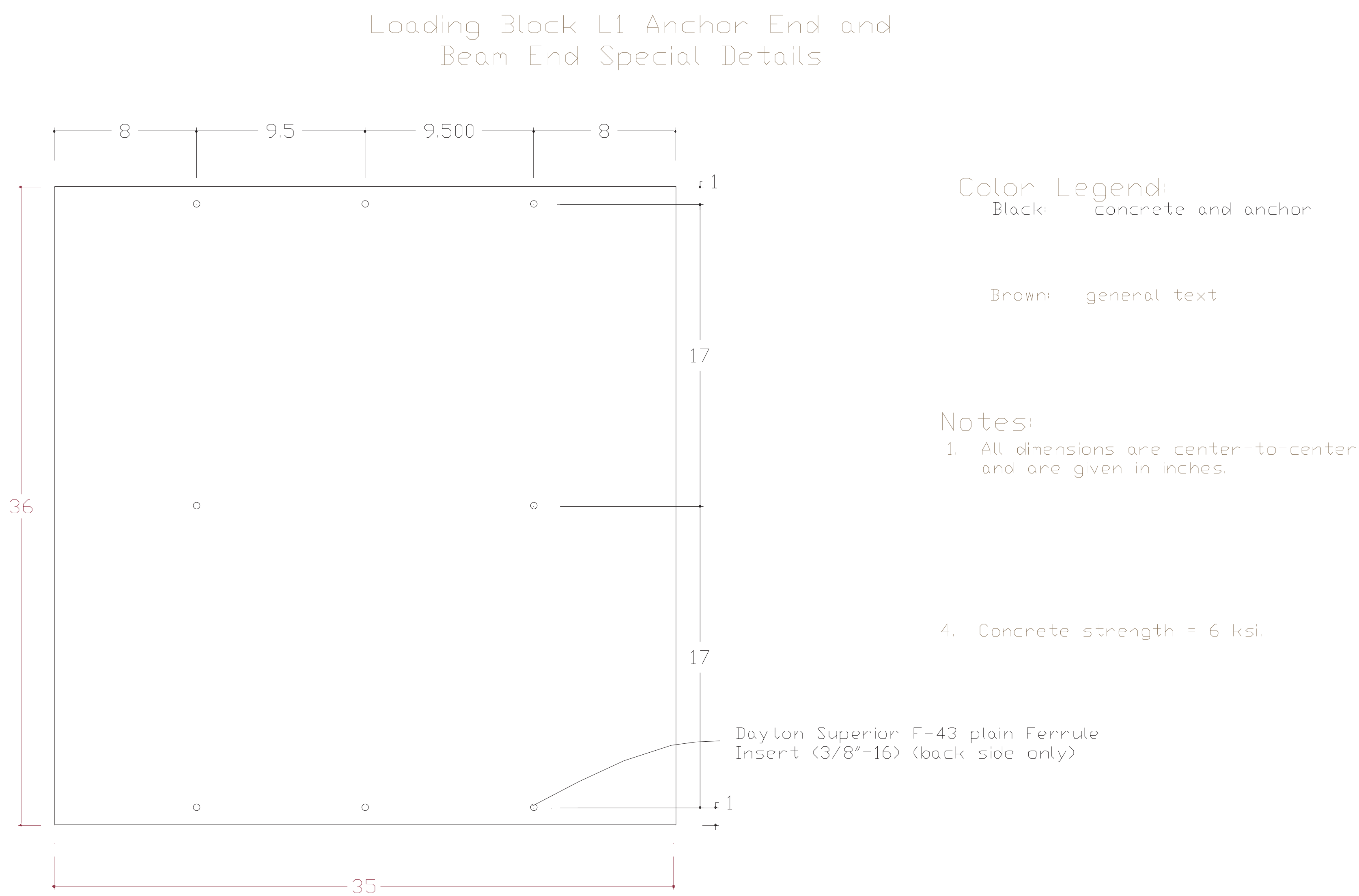

Figure E-27: Load block beam end view – special details.

APPENDIX F

CRACK PATTERNS FOR

TESTS 1, 2, 3, 4, 4B

TEST 1

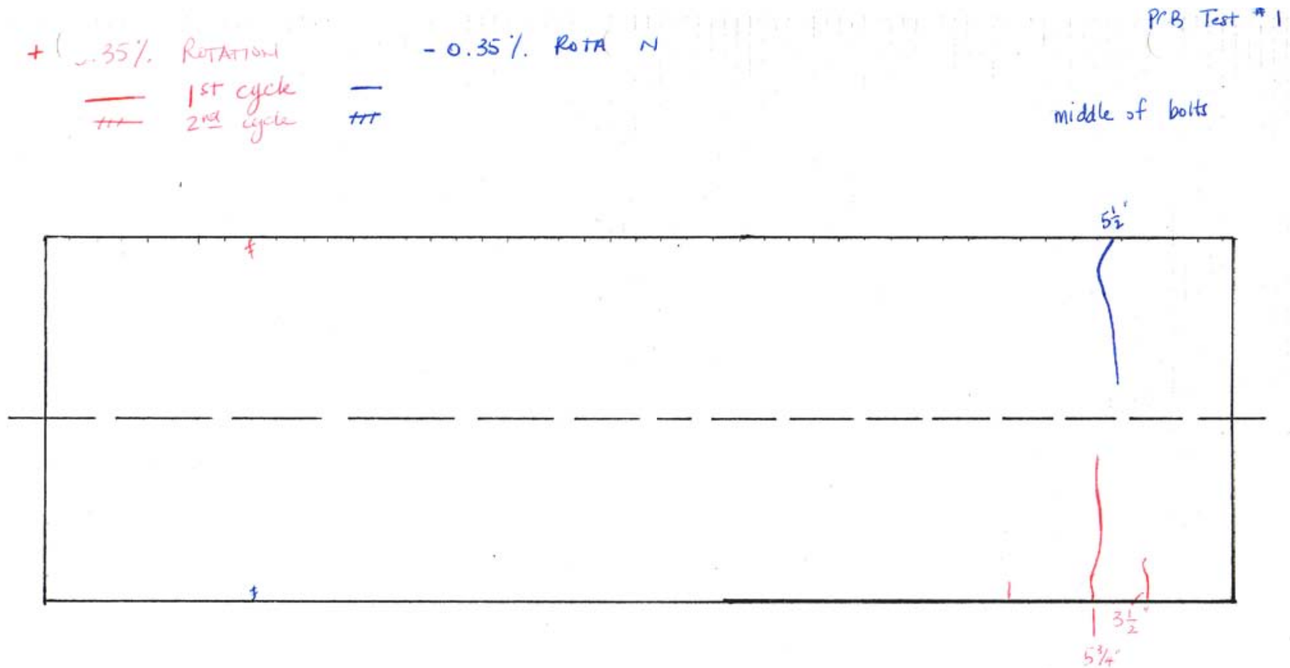

Figure F-1: Test 1 – θ_b = 0.35%.

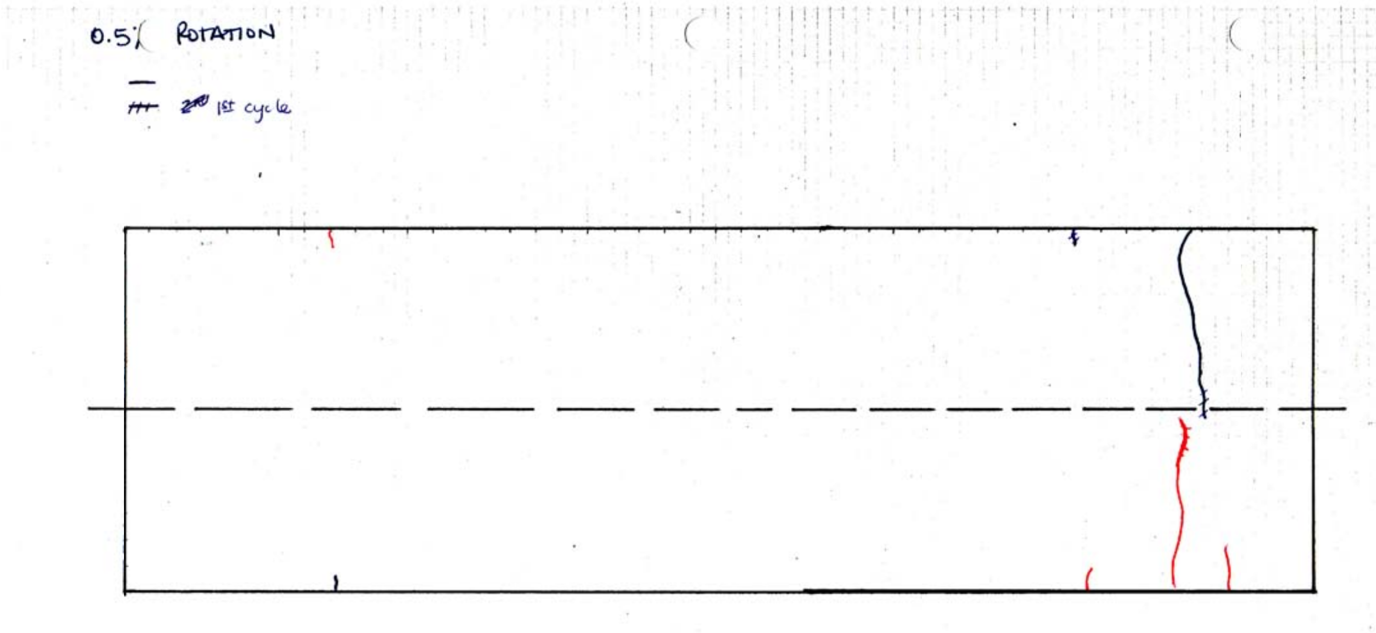

Figure F-2: Test 1 – θ_b = 0.50%.

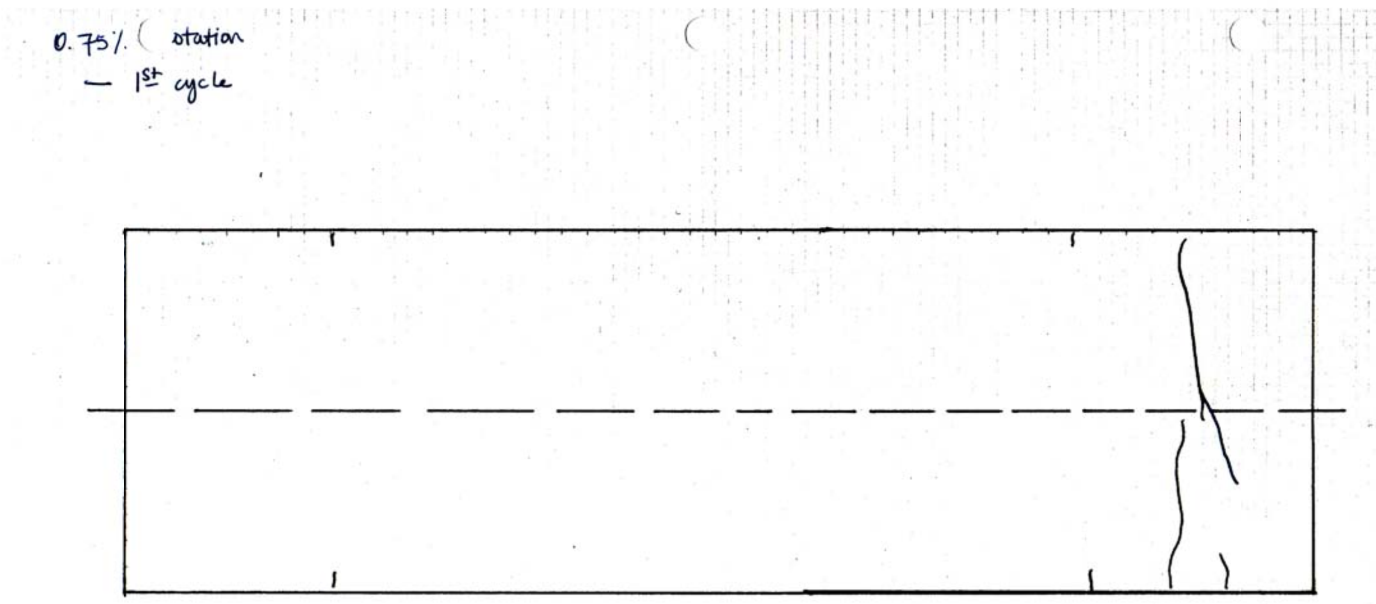

Figure F-3: Test 1 – θ_b = 0.75%.

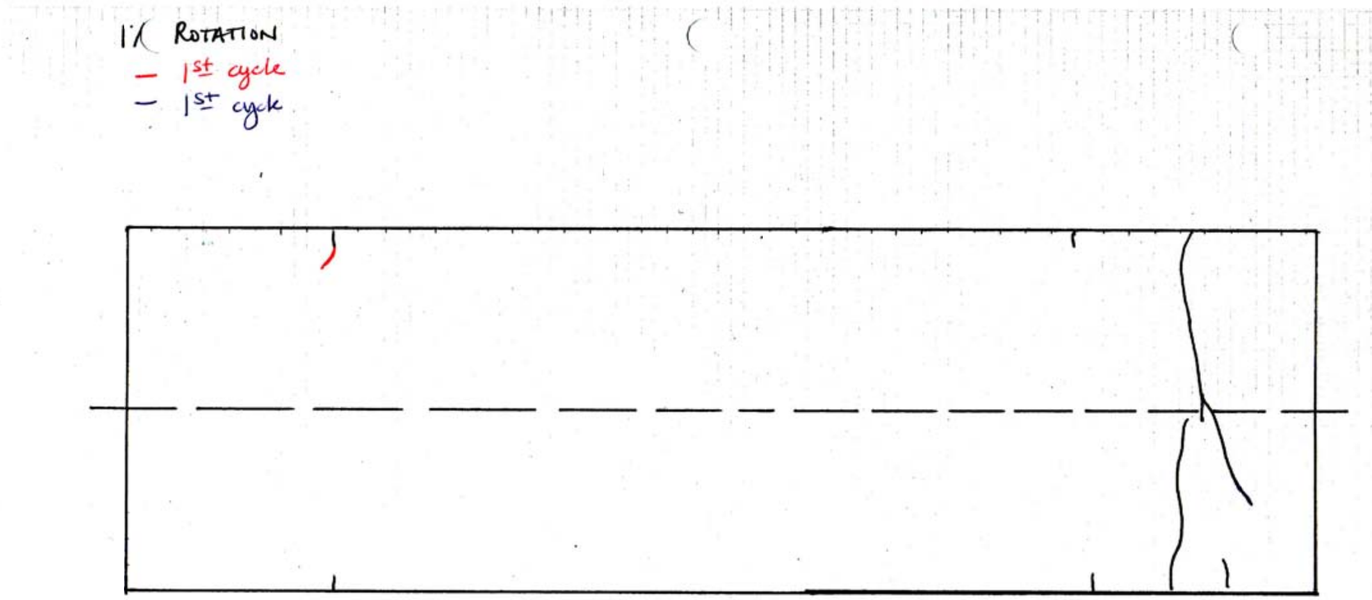

Figure F-4: Test 1 – θ_b = 1.0%.

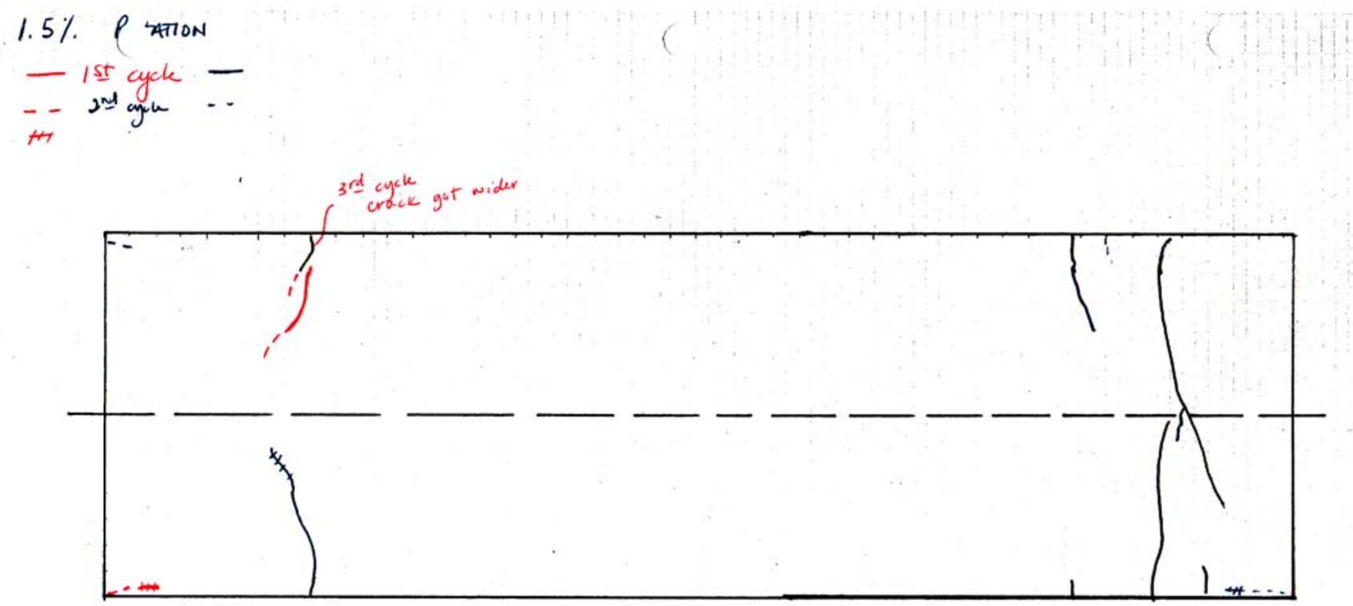

Figure F-5: Test 1 – θ_b = 1.50%.

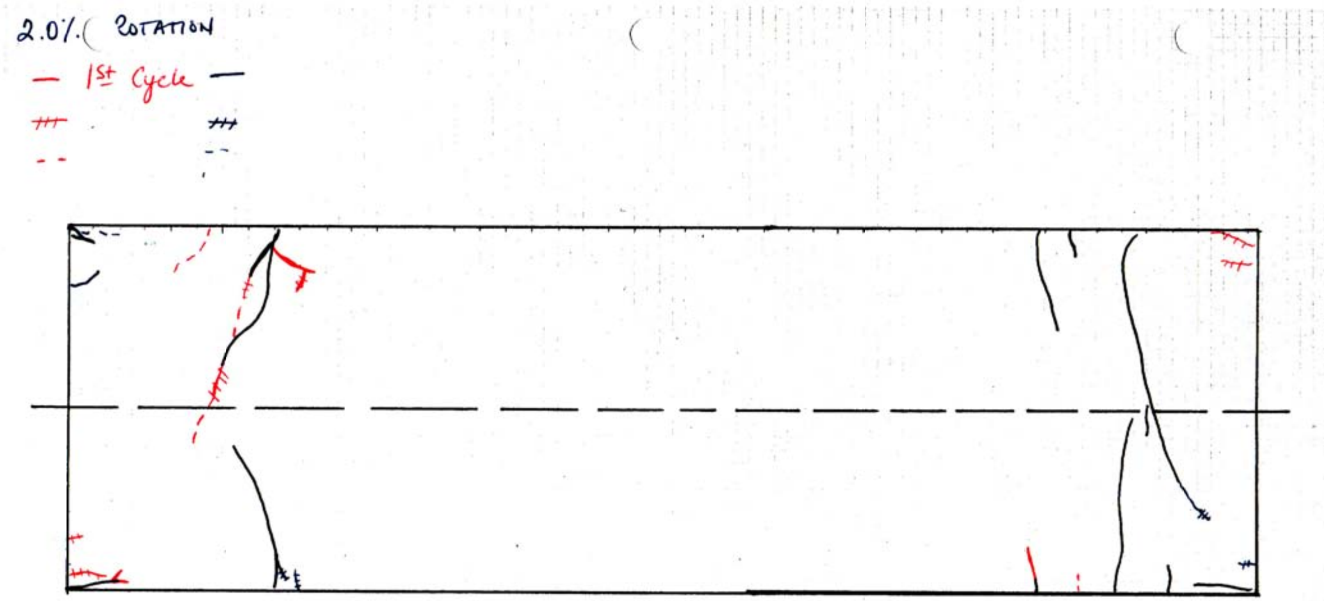

Figure F-6: Test 1 – θ_b = 2.0%.

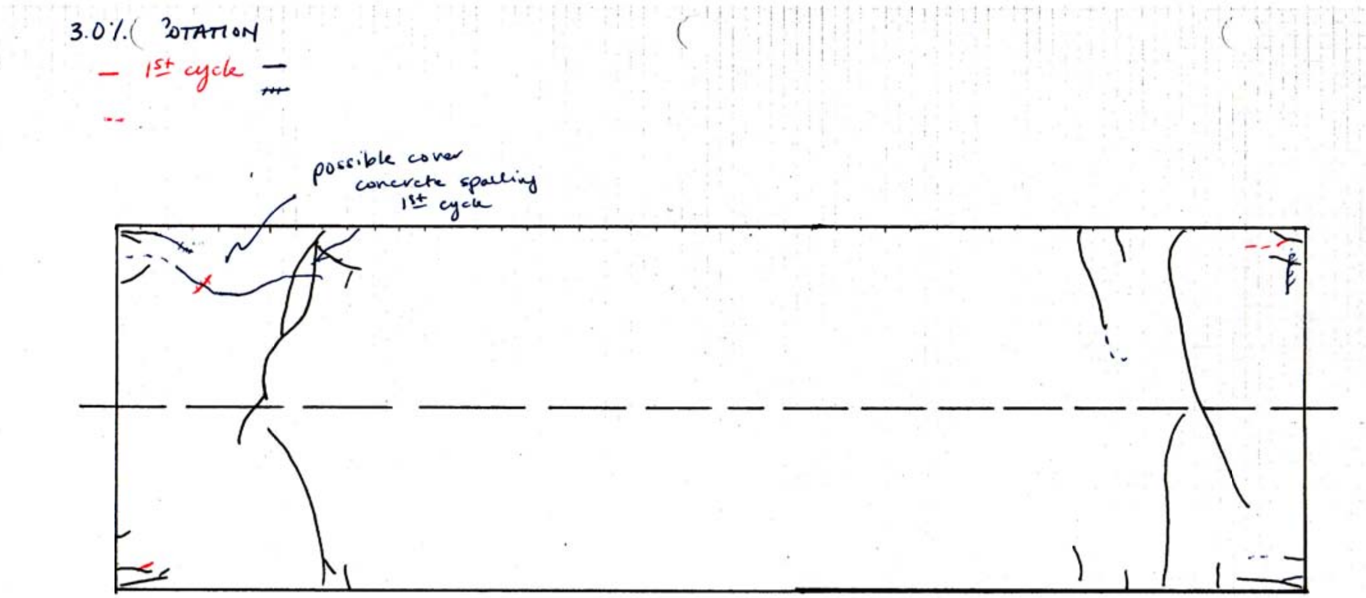

Figure F-7: Test 1 – θ_b = 3.0%.

TEST 2

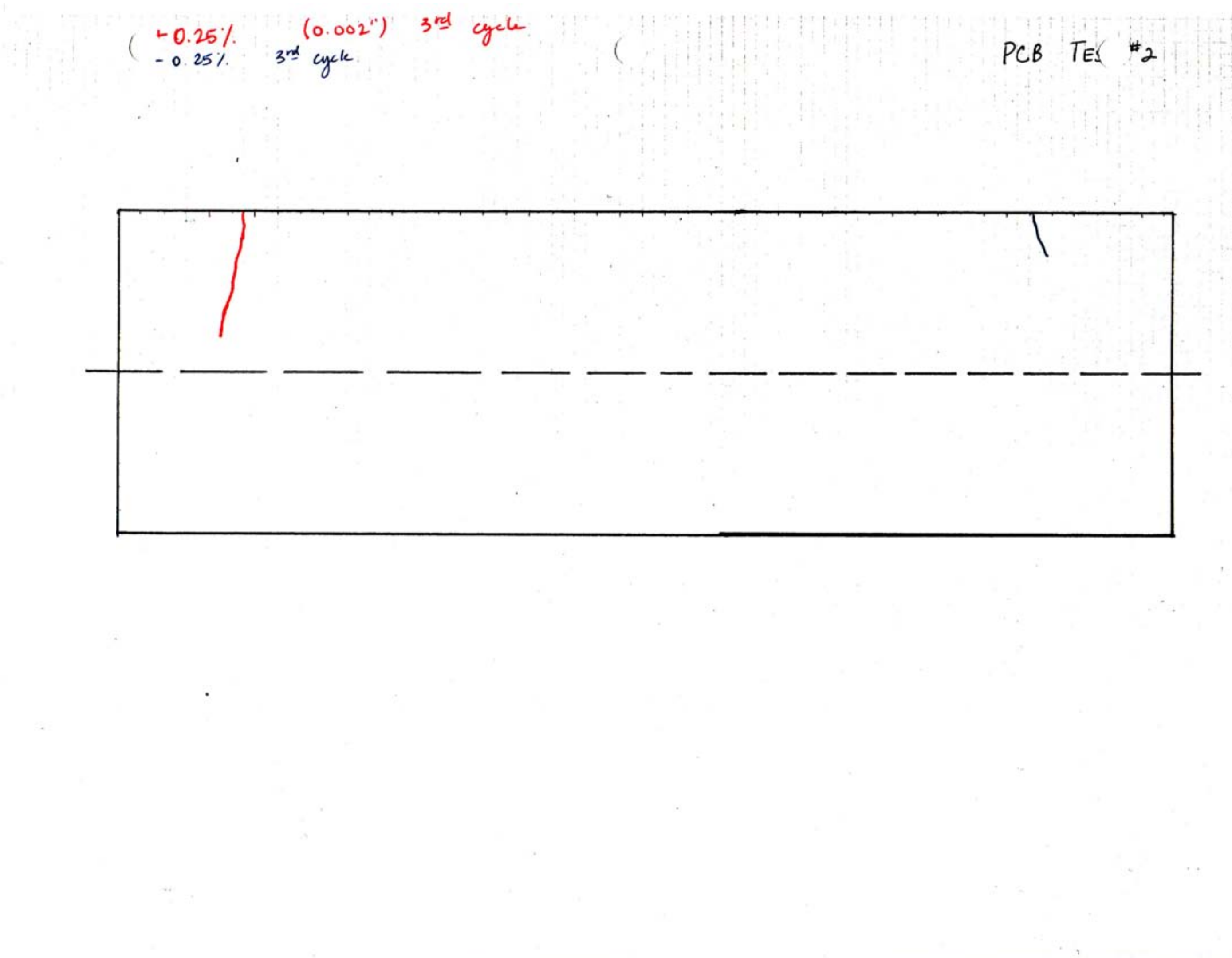

Figure F-8: Test 2 – θ_b = 0.25%.

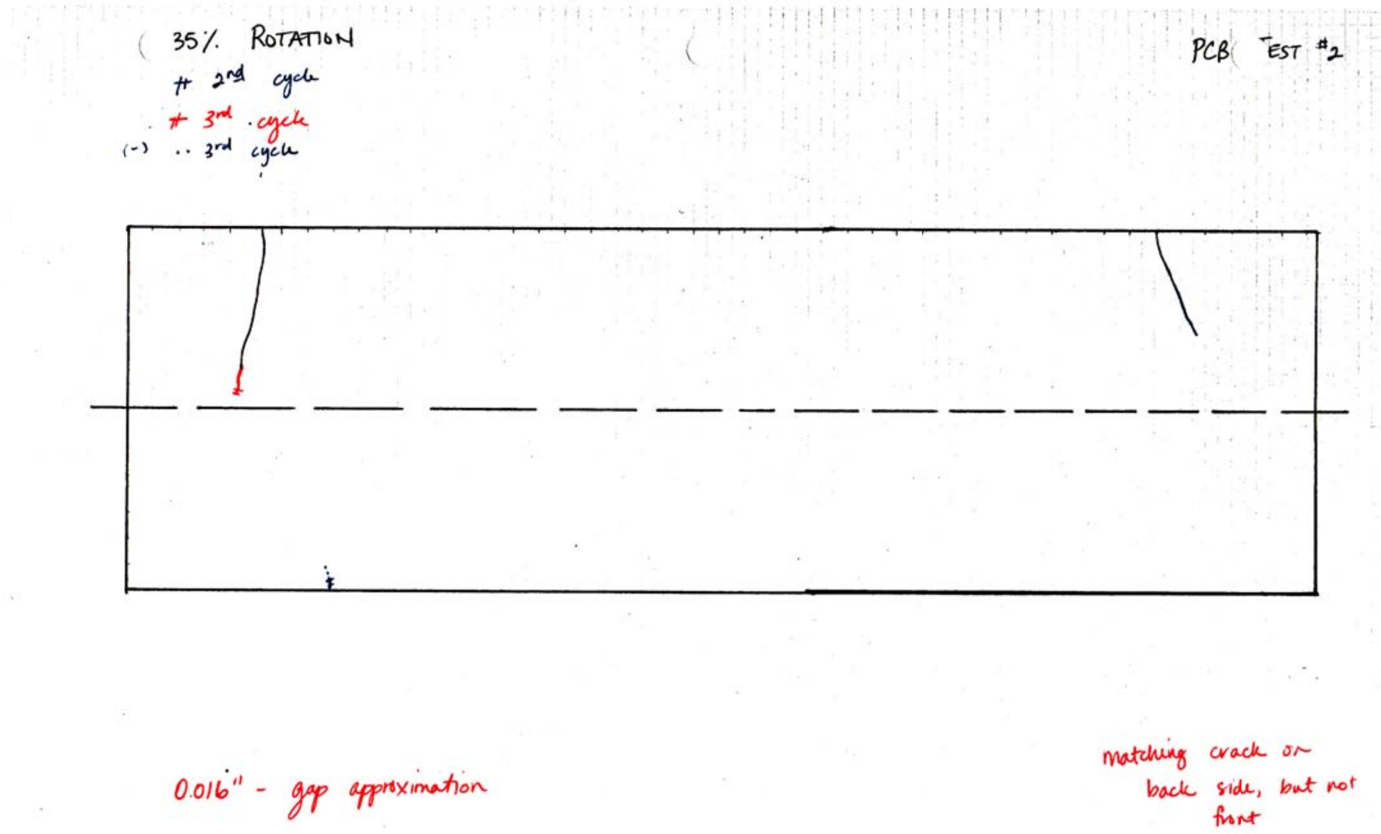

Figure F-9: Test 2 – θ_b = 0.35%.

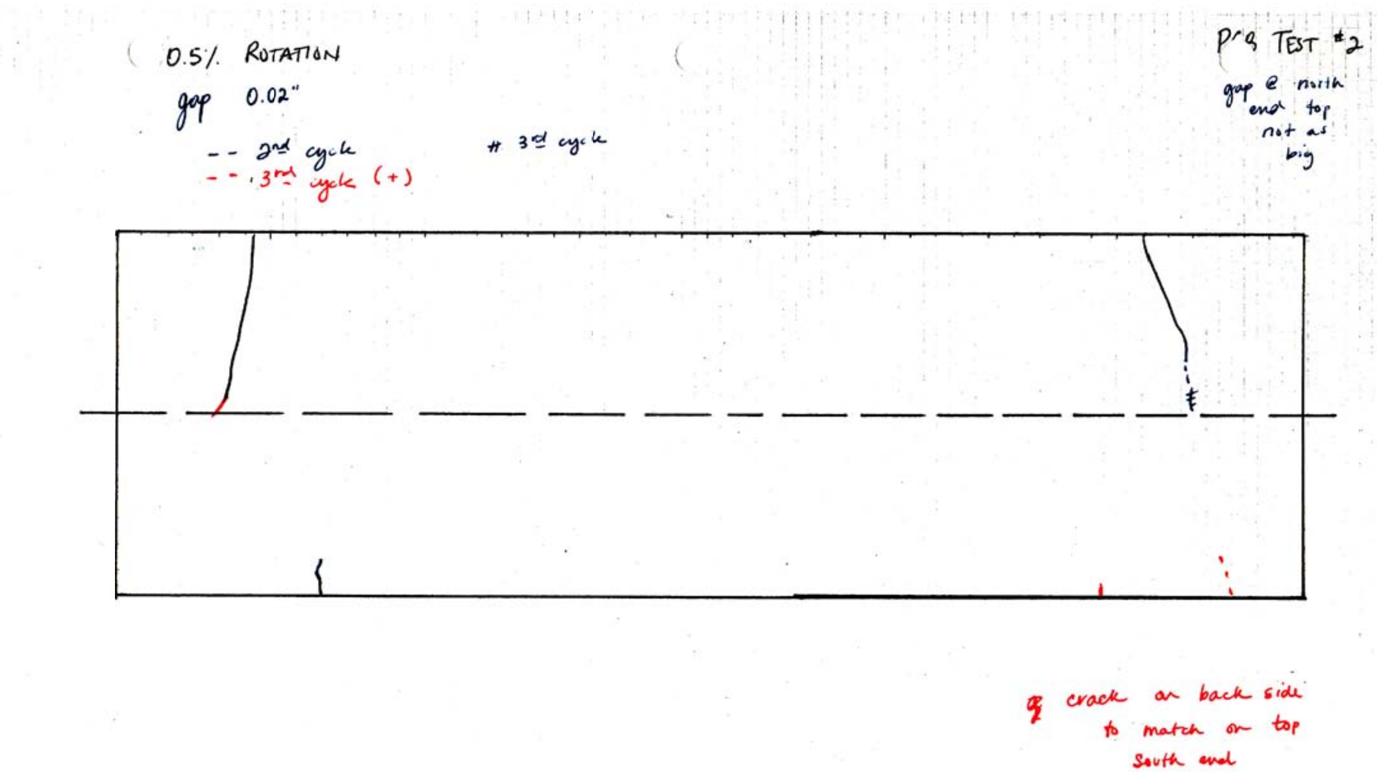

Figure F-10: Test 2 – θ_b = 0.50%.

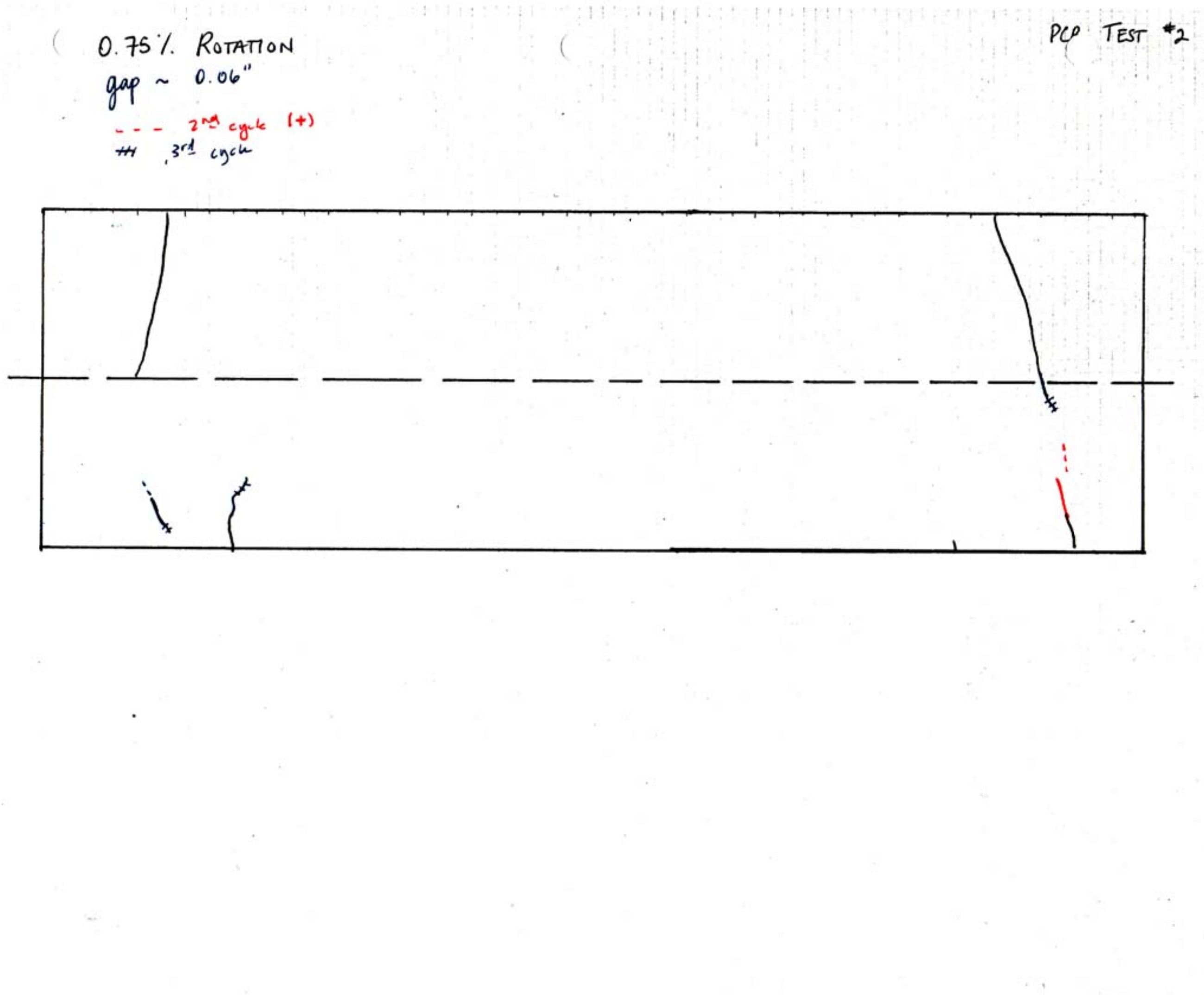

Figure F-11: Test 2 – θ_b = 0.75%.

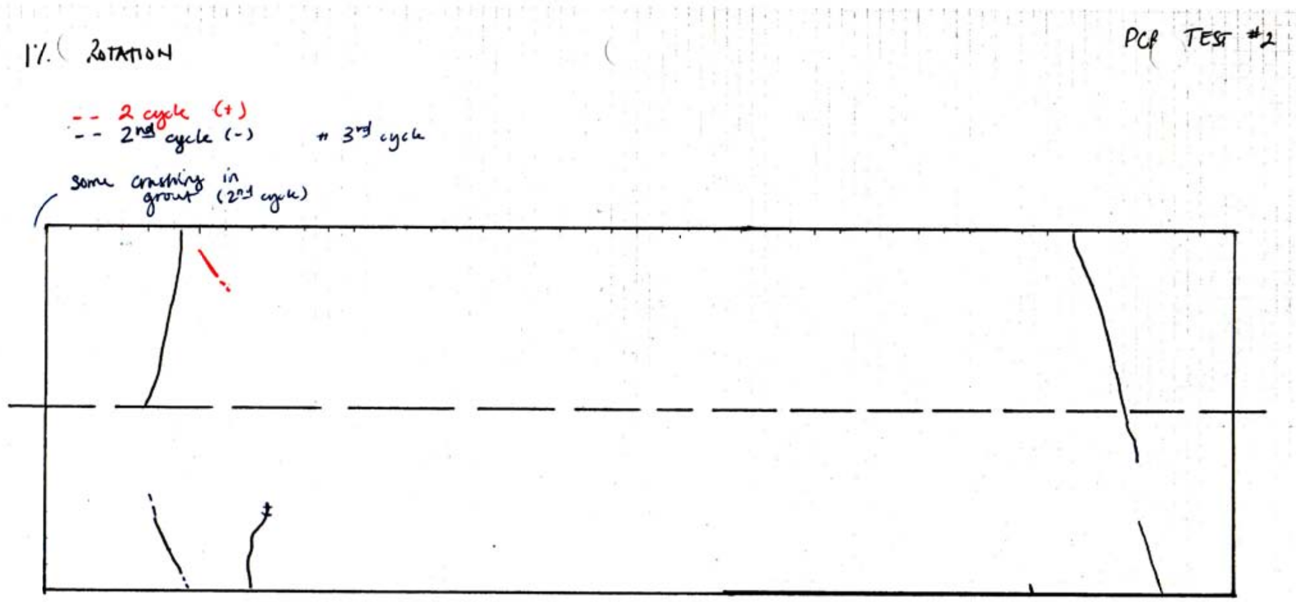

Figure F-12: Test 2 – θ_b = 1.0%.

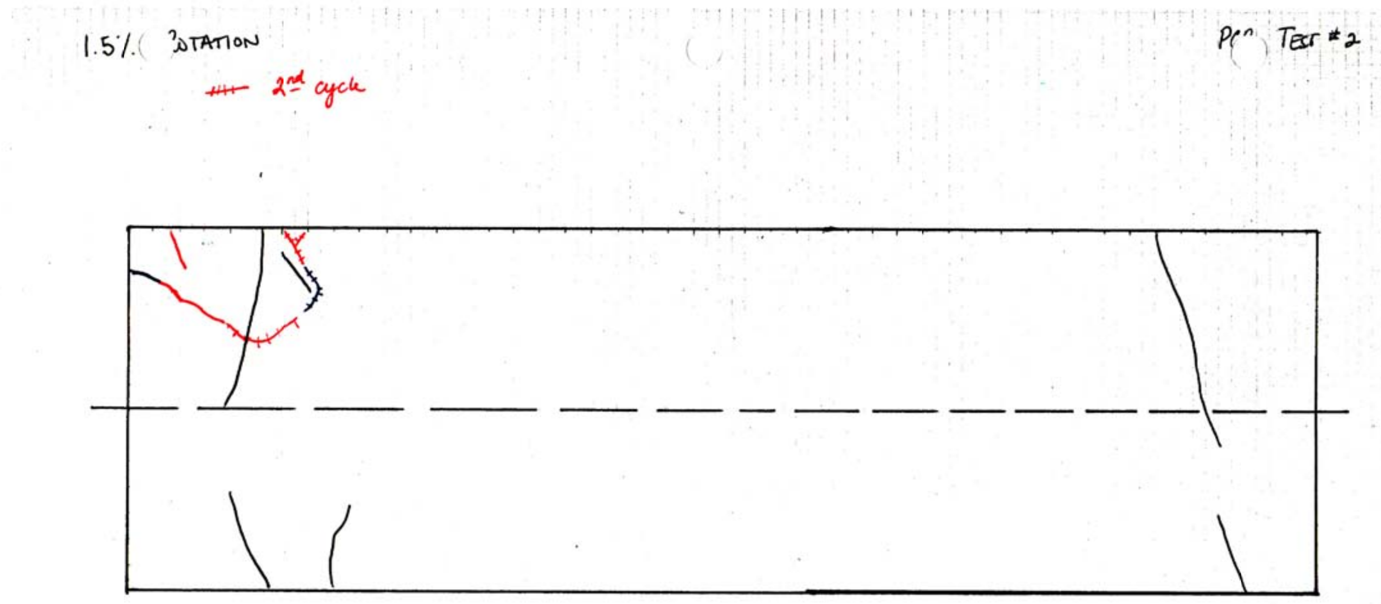

Figure F-13: Test 2 – θ_b = 1.5%.

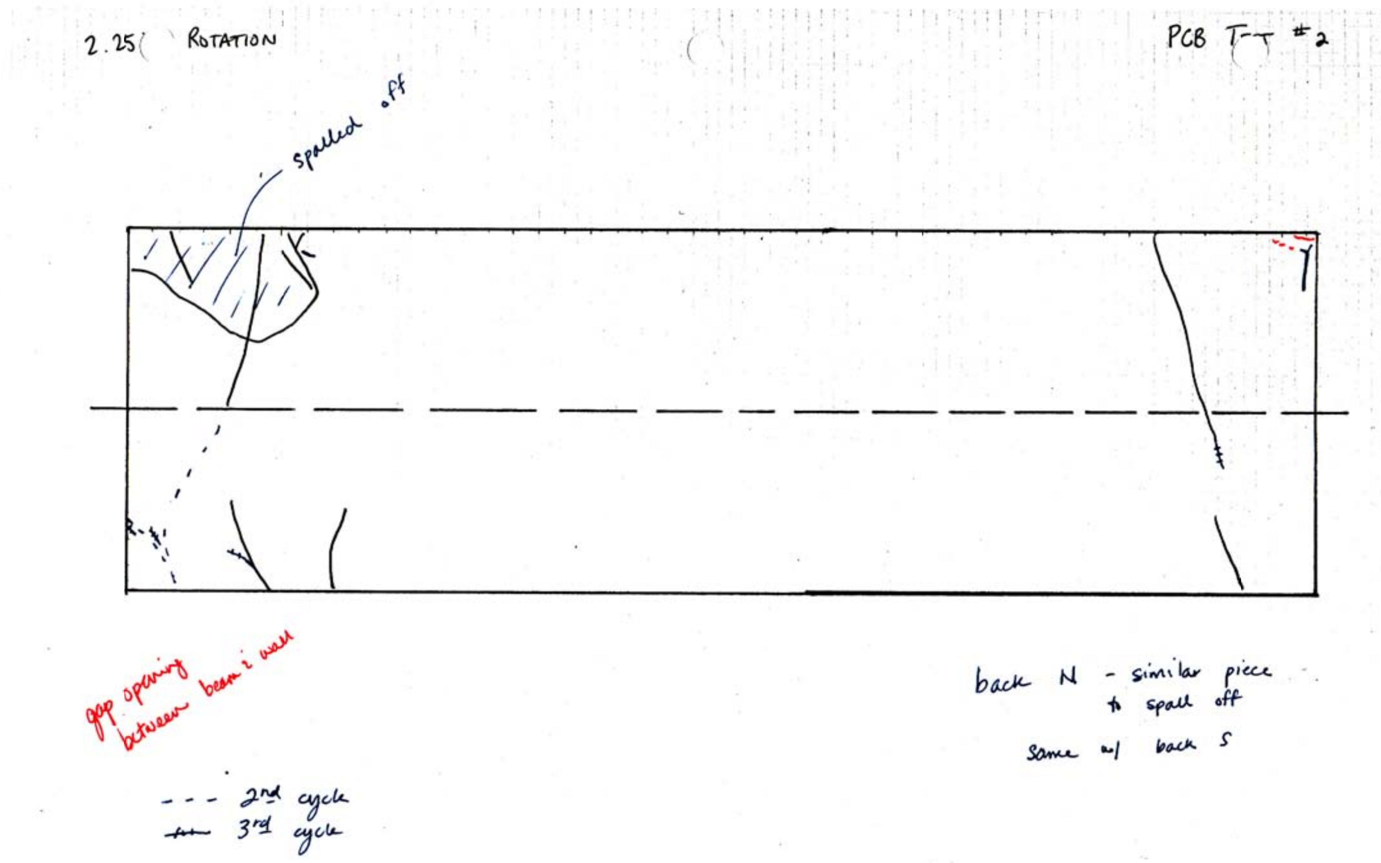

Figure F-14: Test 2 – θ_b = 2.25%.

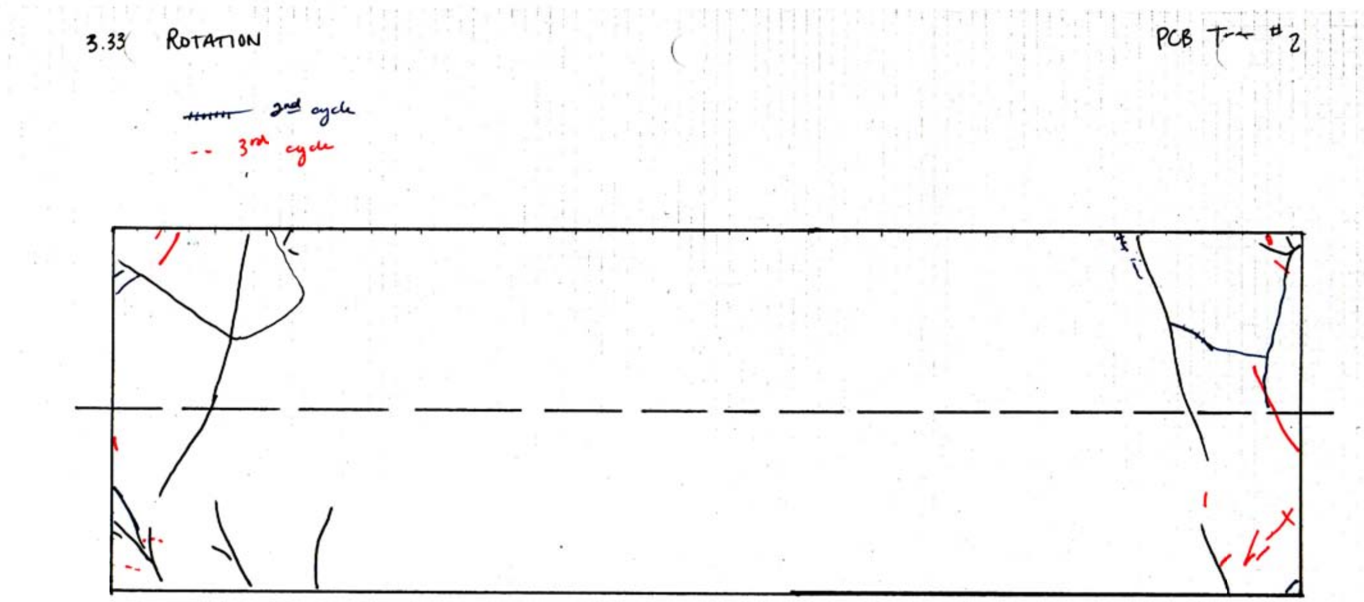

Figure F-15: Test 2 – θ_b = 3.33%.

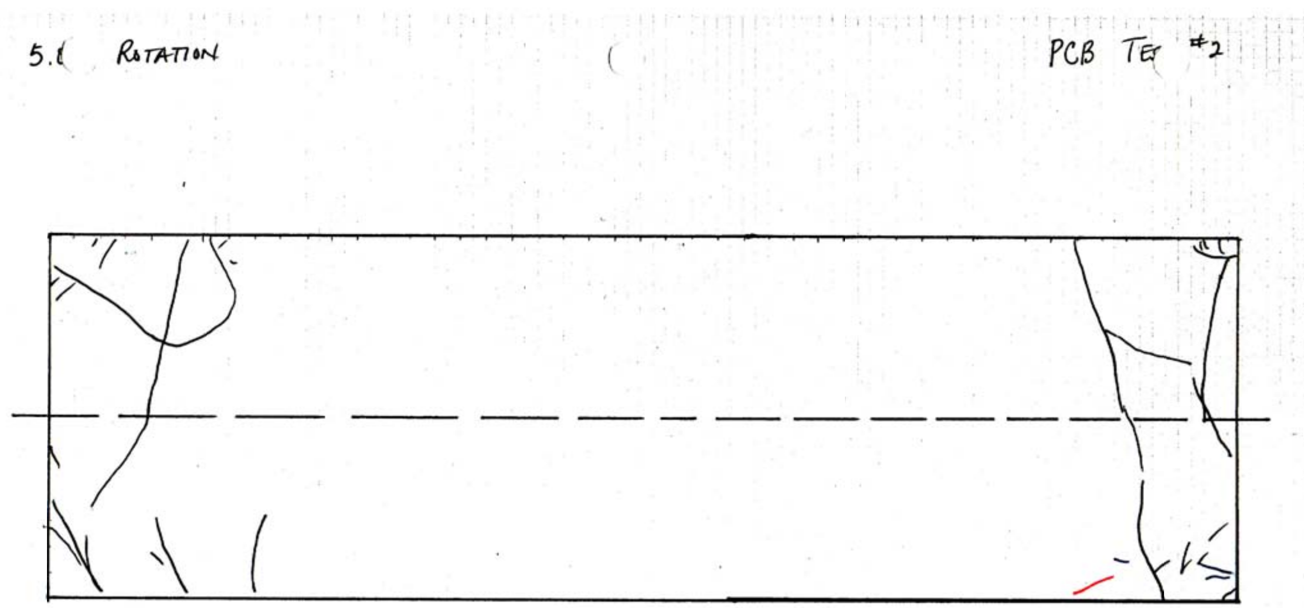

Figure F-16: Test 2 – θ_b = 5.0%.

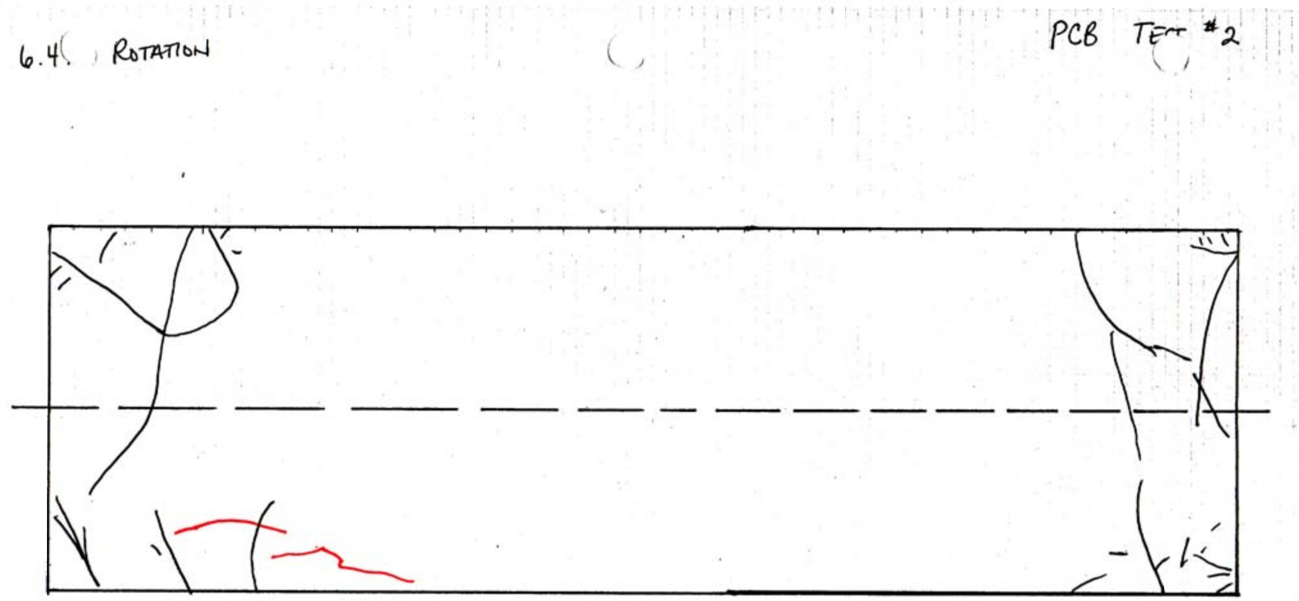

Figure F-17: Test 2 – θ_b = 6.4%.

TEST 3

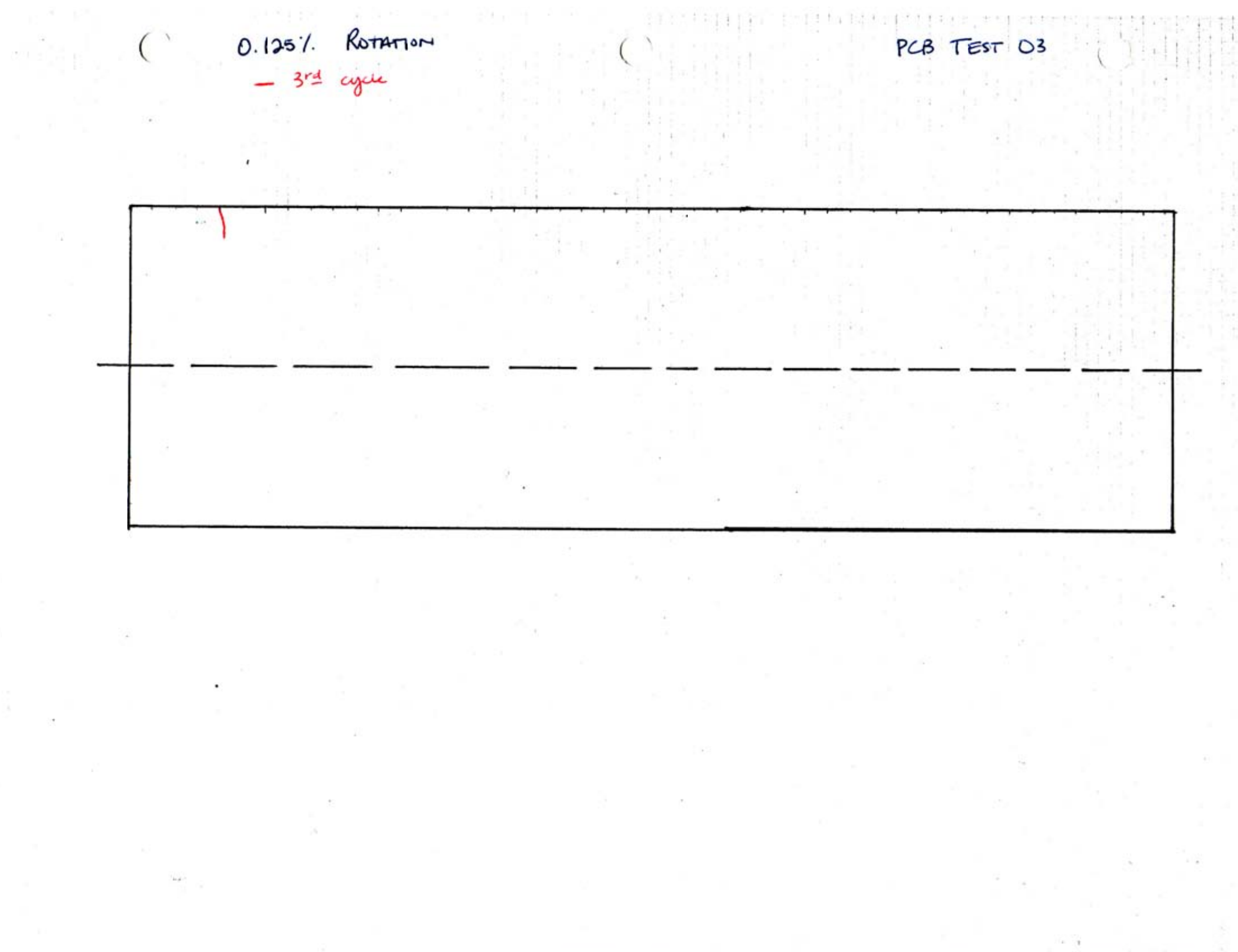

Figure F-18: Test 3 – θ_b = 0.125%.

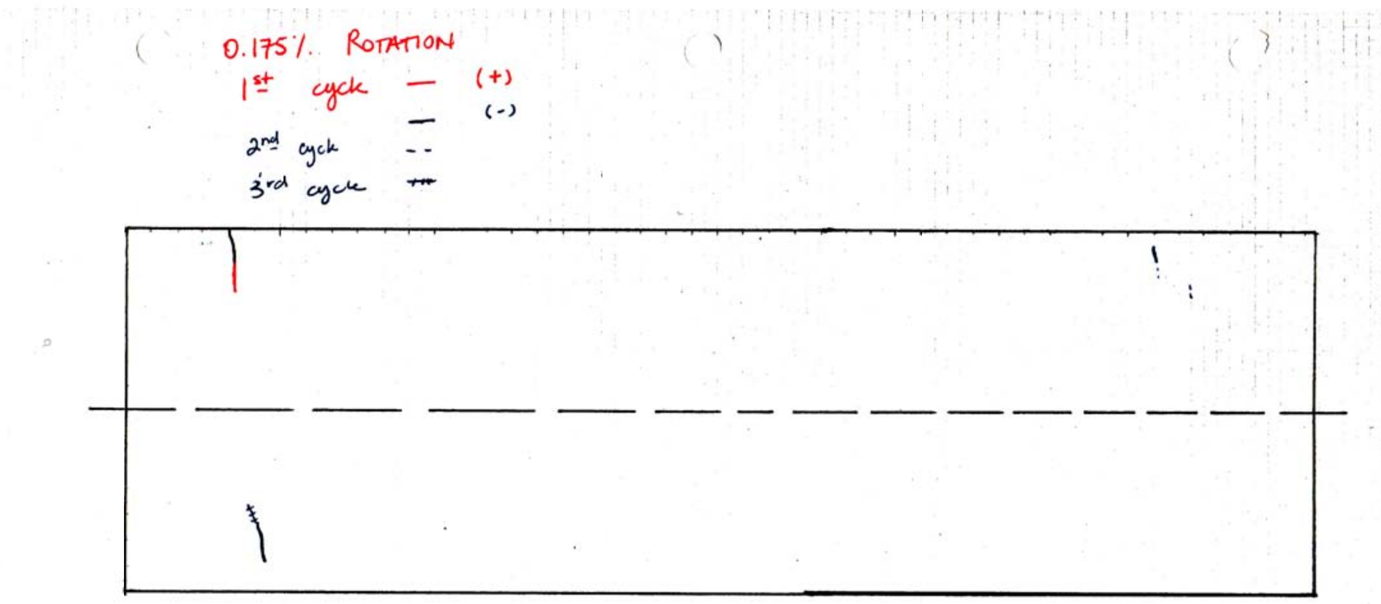

Figure F-19: Test 3 – θ_b = 0.175%.

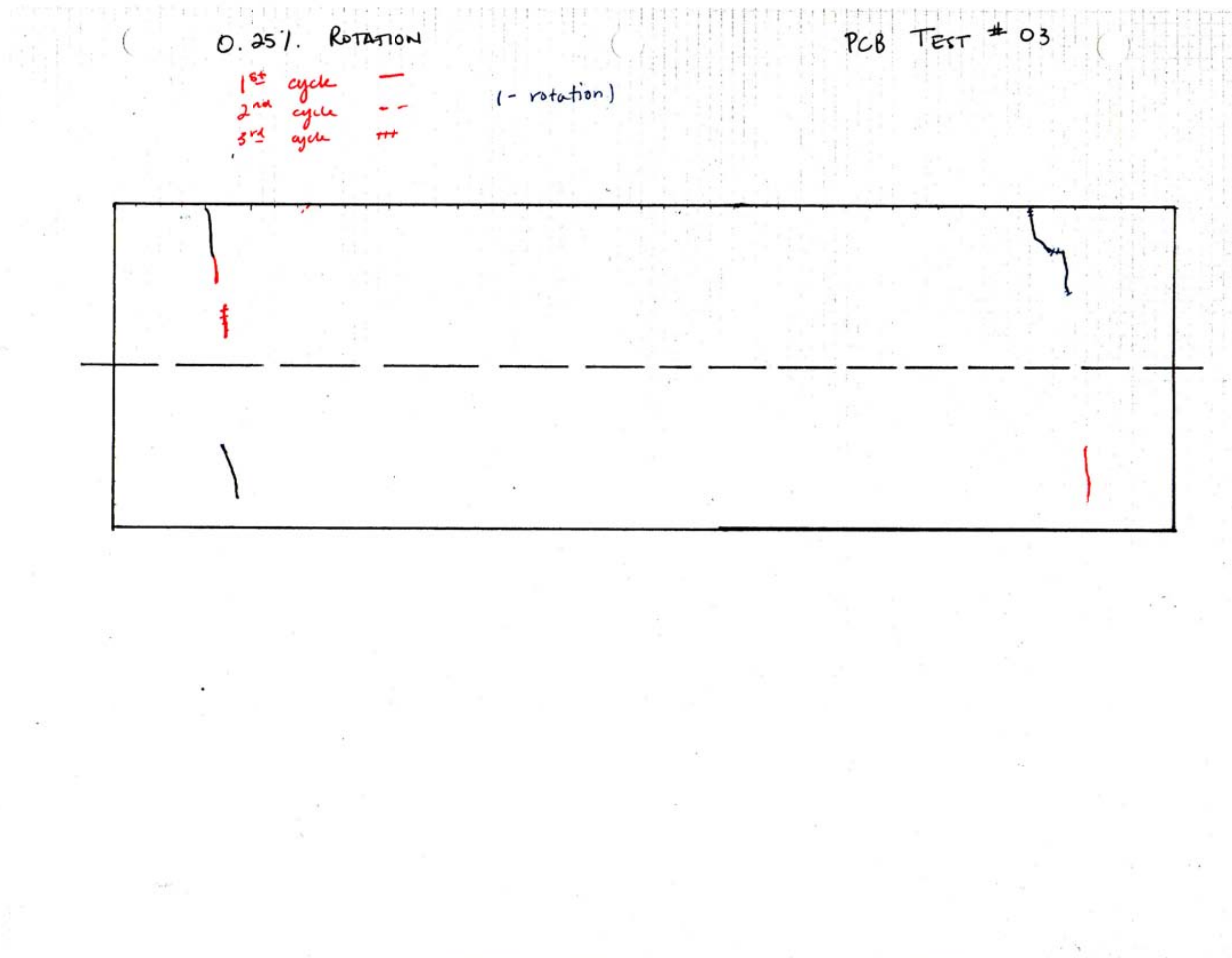

Figure F-20: Test 3 – θ_b = 0.25%.

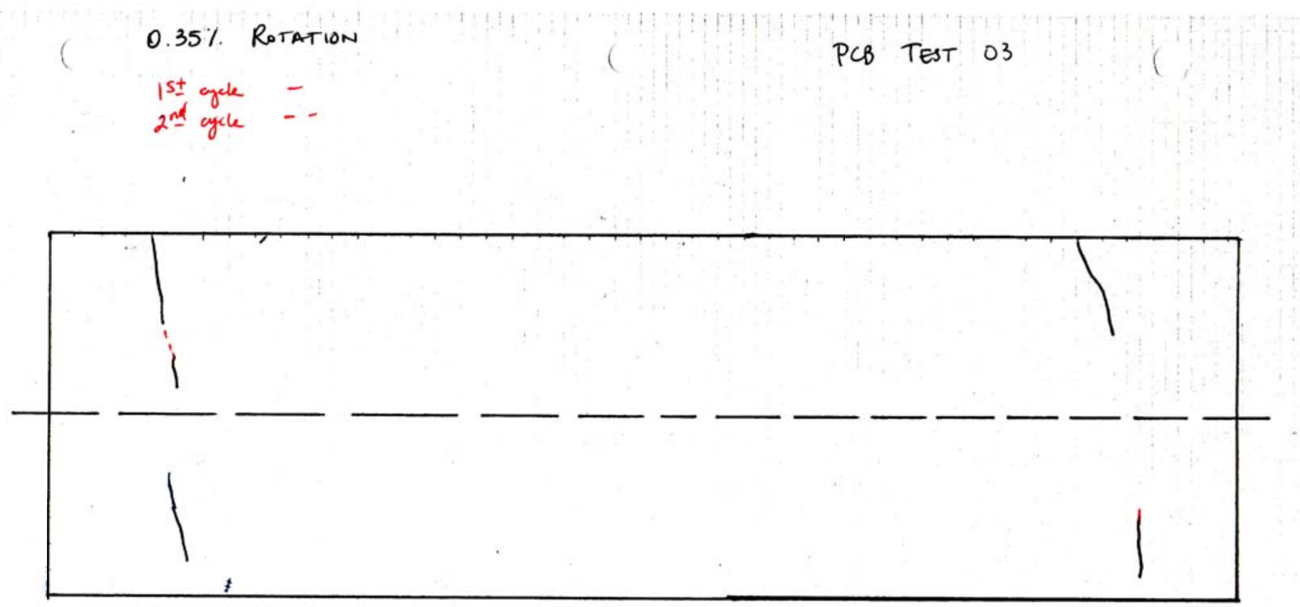

Figure F-21: Test 3 – θ_b = 0.35%.

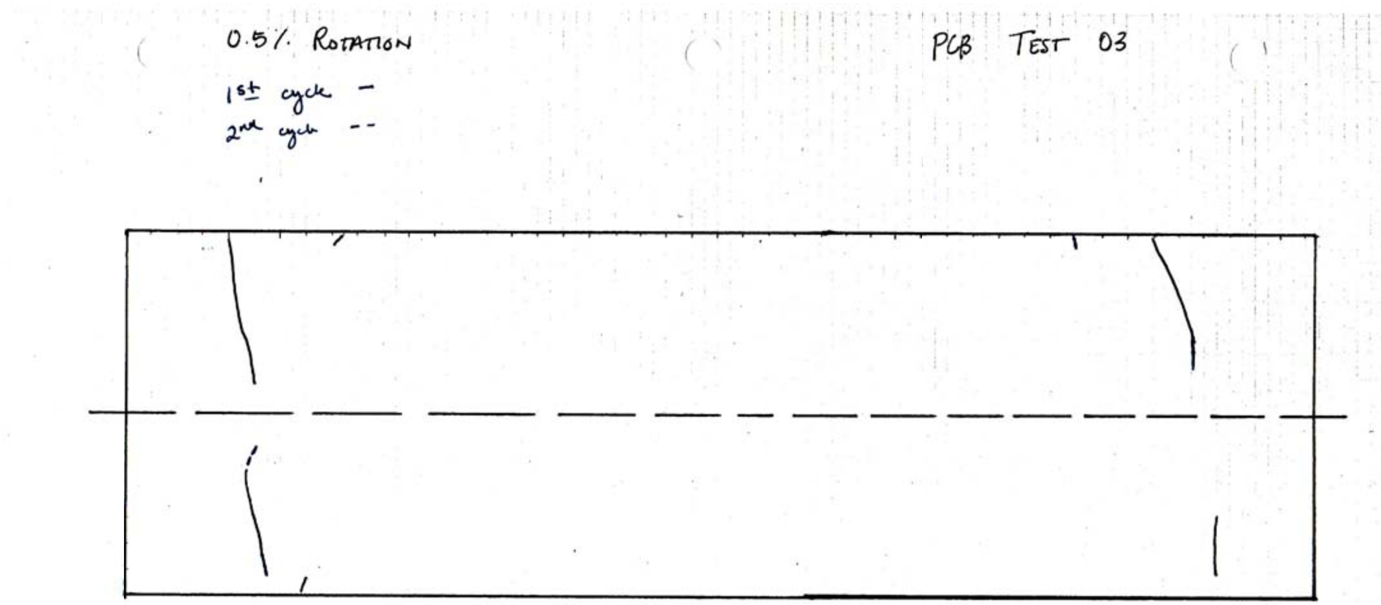

Figure F-22: Test 3 – $\theta_b = 0.5\%$.

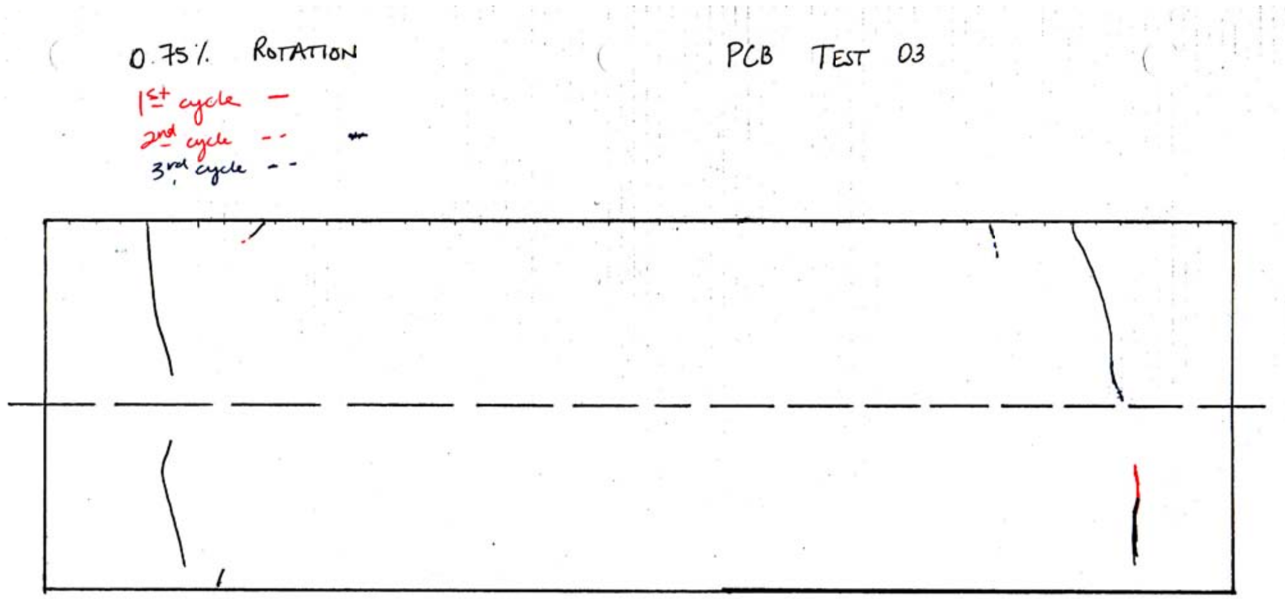

Figure F-23: Test 3 – $\theta_b = 0.75\%$.

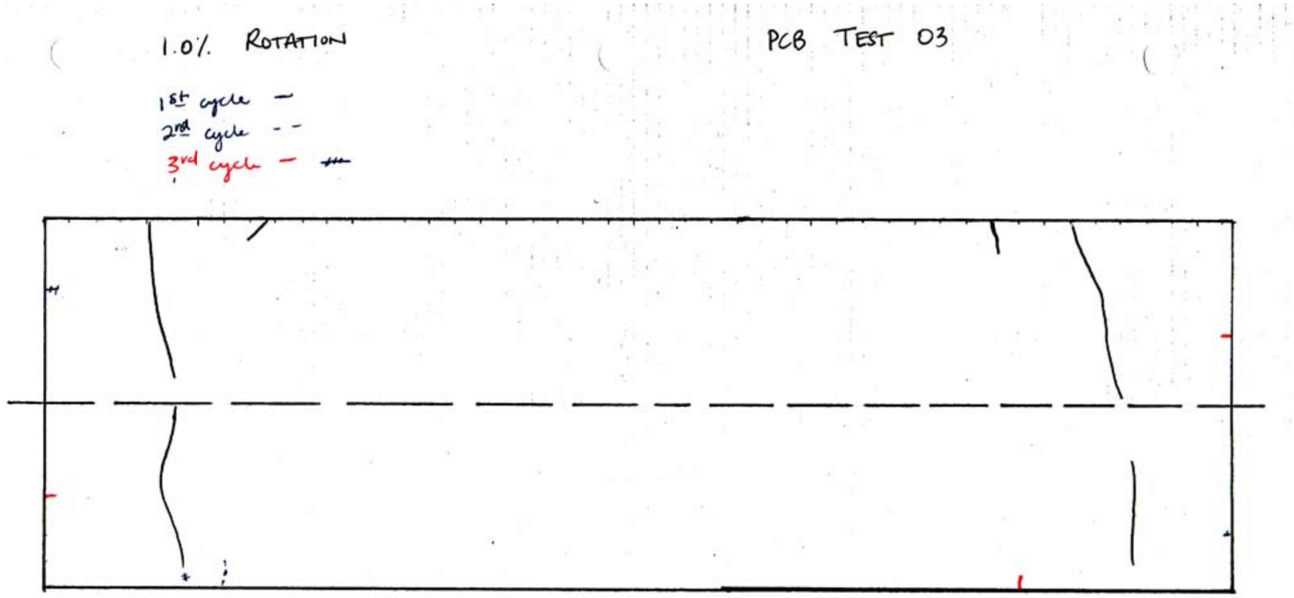

Figure F-24: Test 3 – $\theta_b = 1.0\%$.

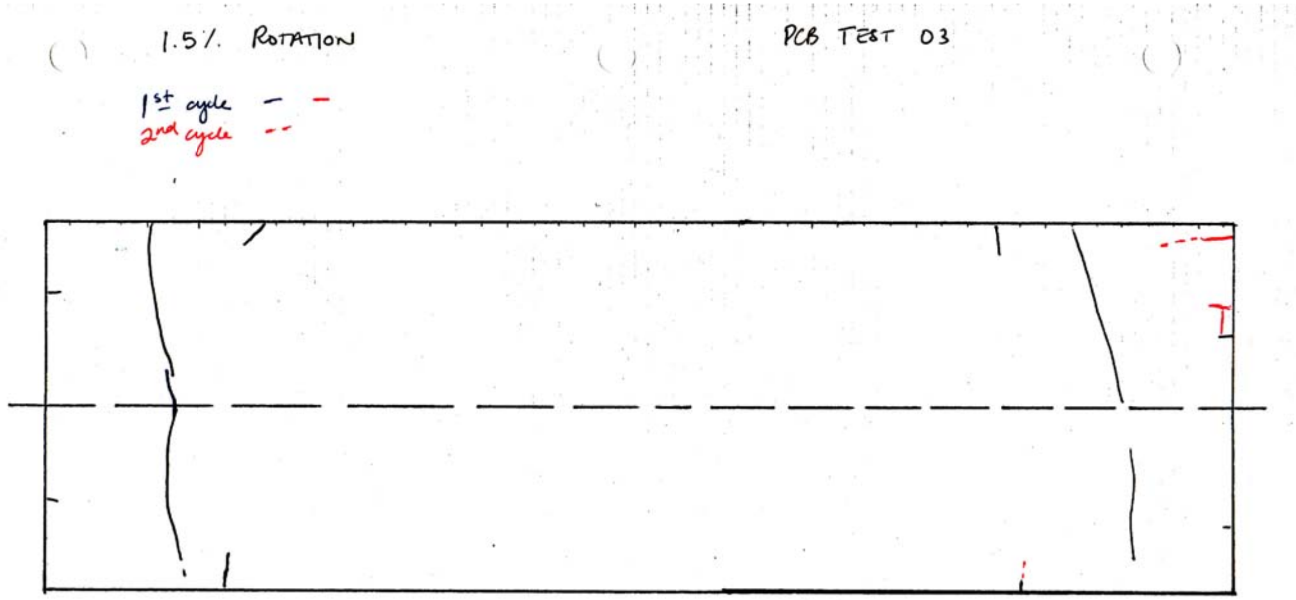

Figure F-25: Test 3 – θ_b = 1.5%.

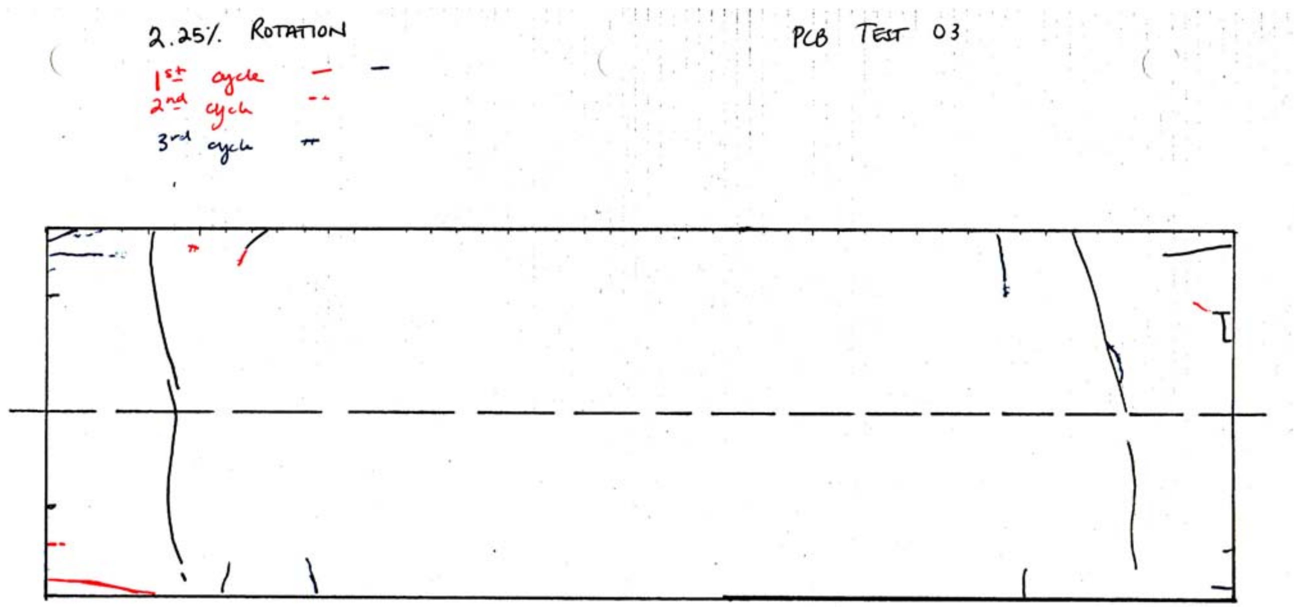

Figure F-26: Test 3 – θ_b = 2.25%.

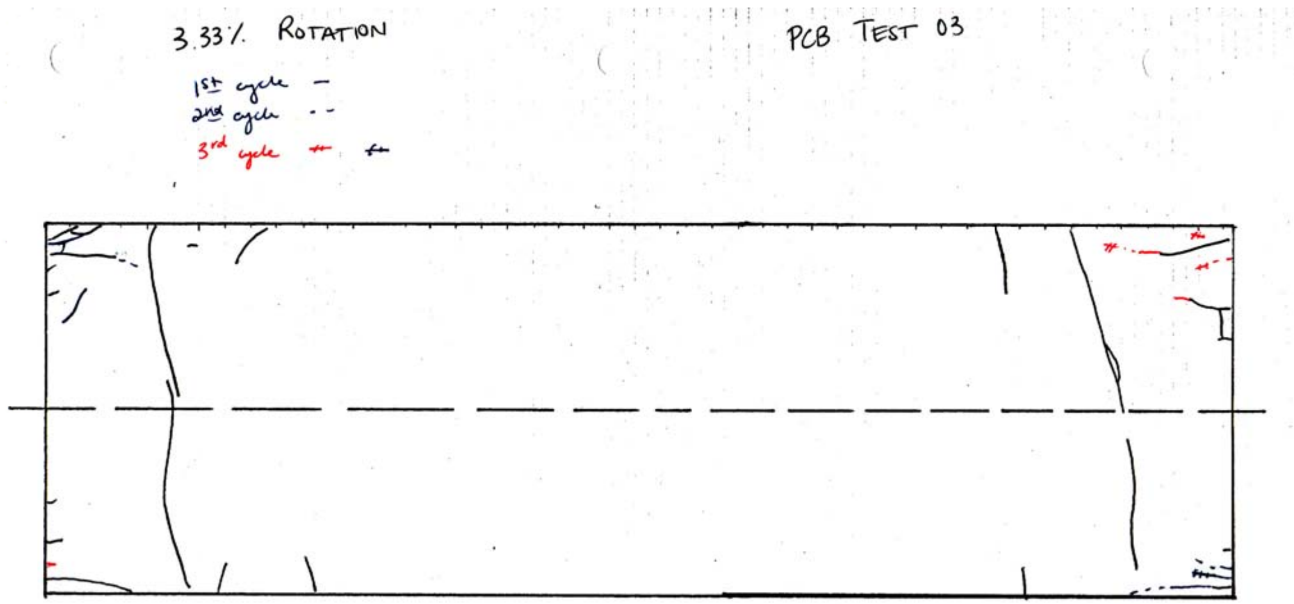

Figure F-27: Test 3 – θ_b = 3.33%.

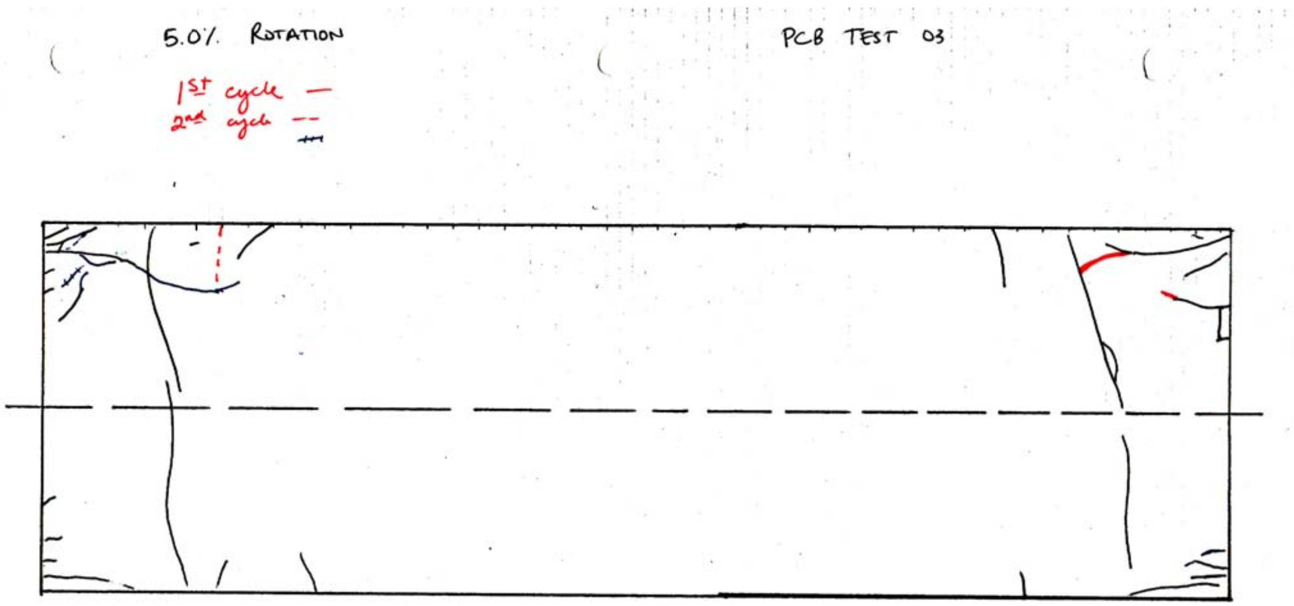

Figure F-28: Test 3 – θ_b = 5.0%.

TEST 4

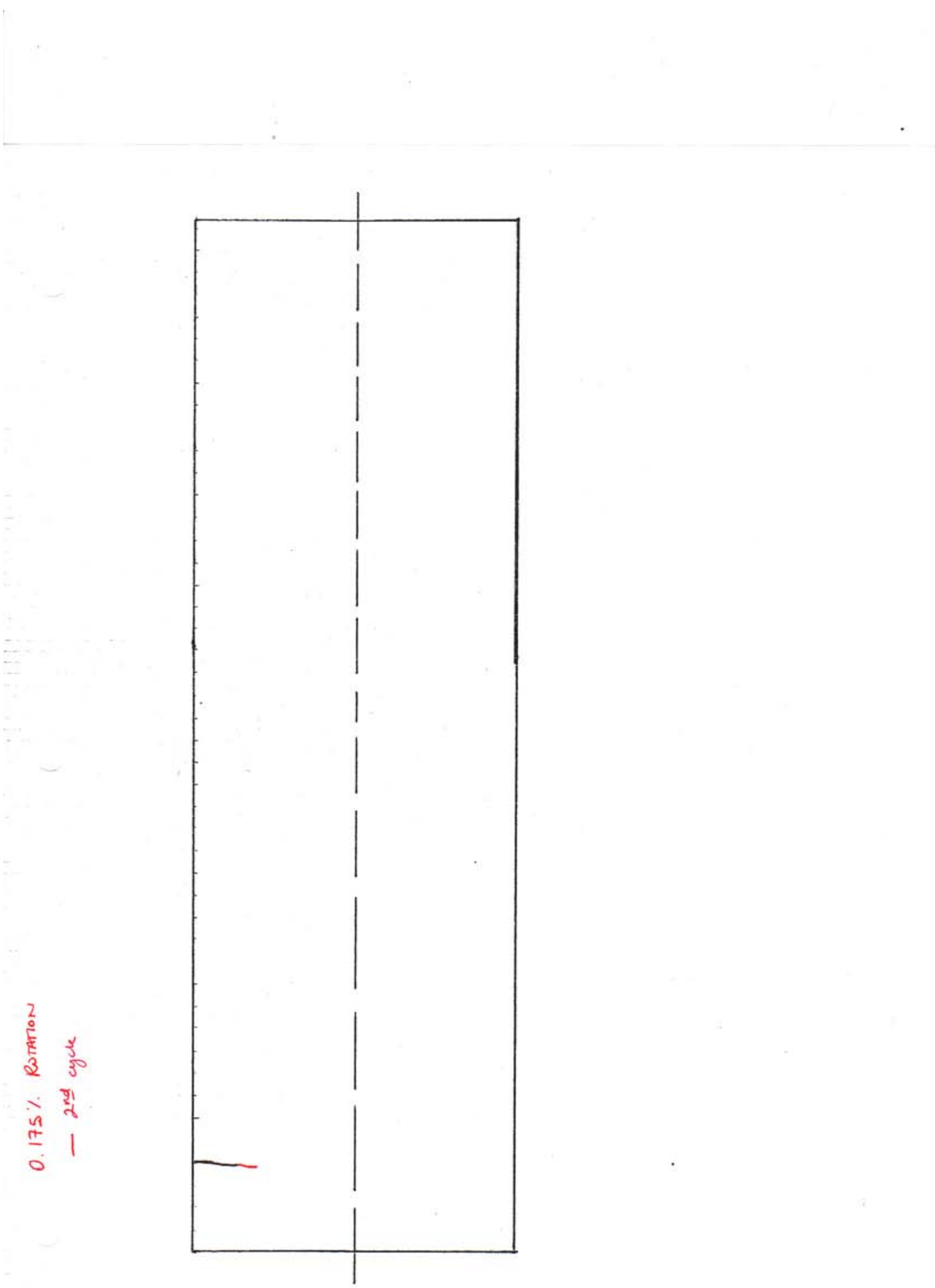

Figure F-29: Test 4 – θ_b = 0.175%.

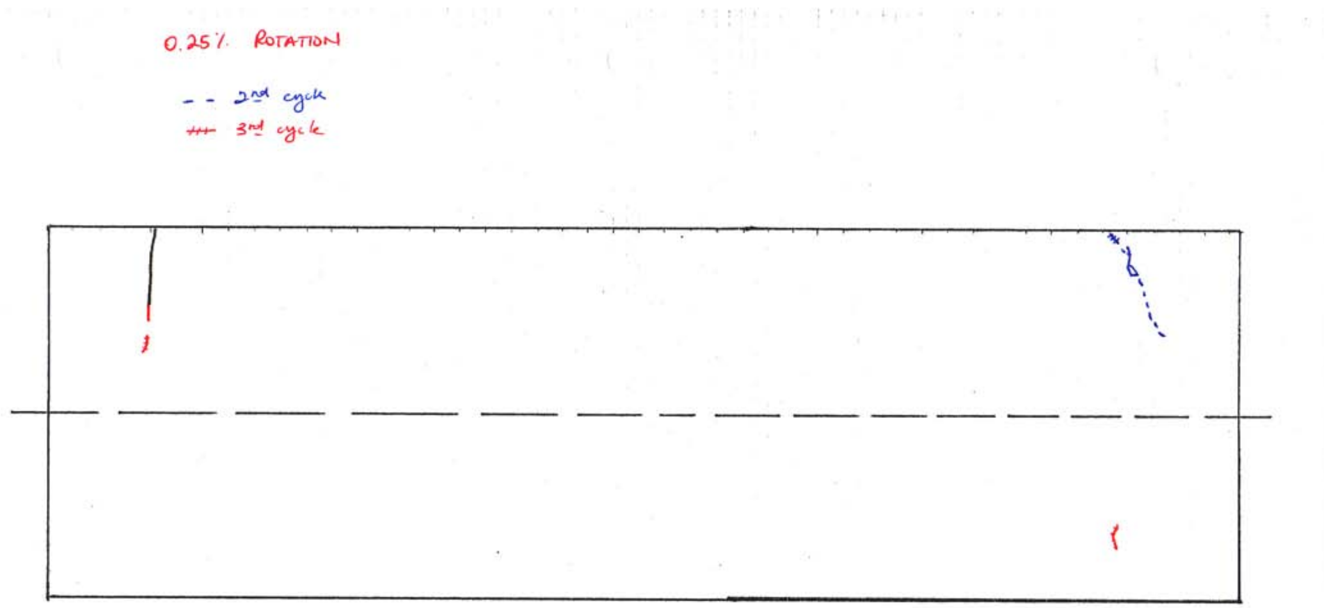

Figure F-30: Test 4 – θ_b = 0.25%.

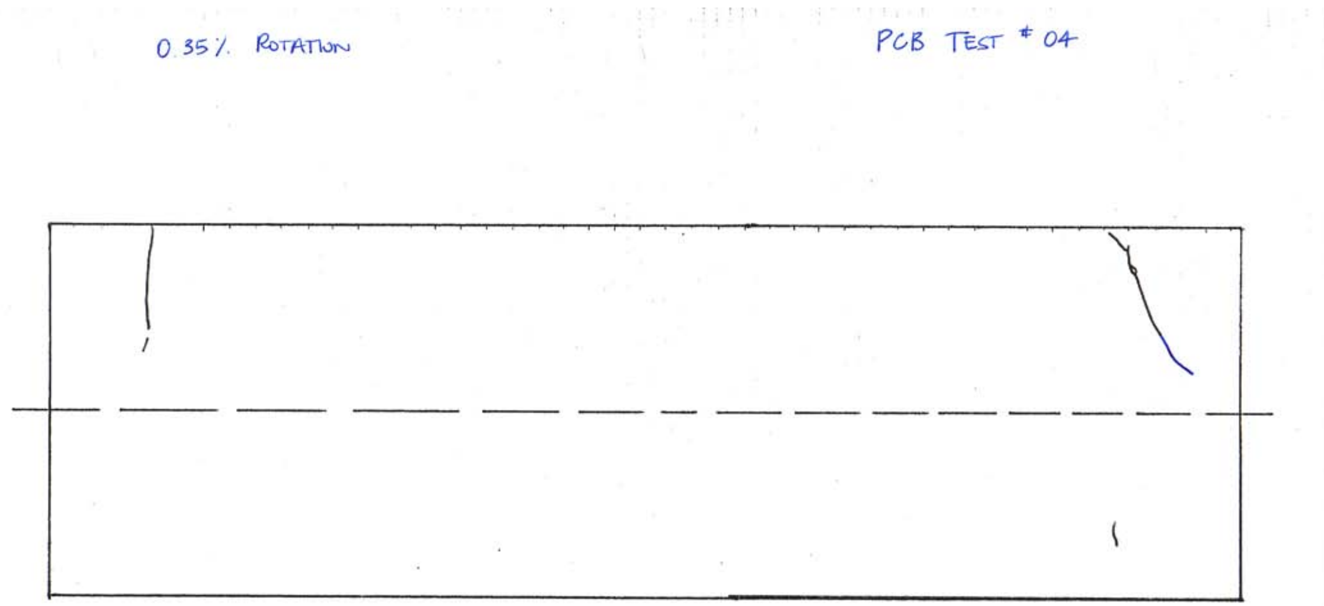

Figure F-31: Test 4 – θ_b = 0.35%.

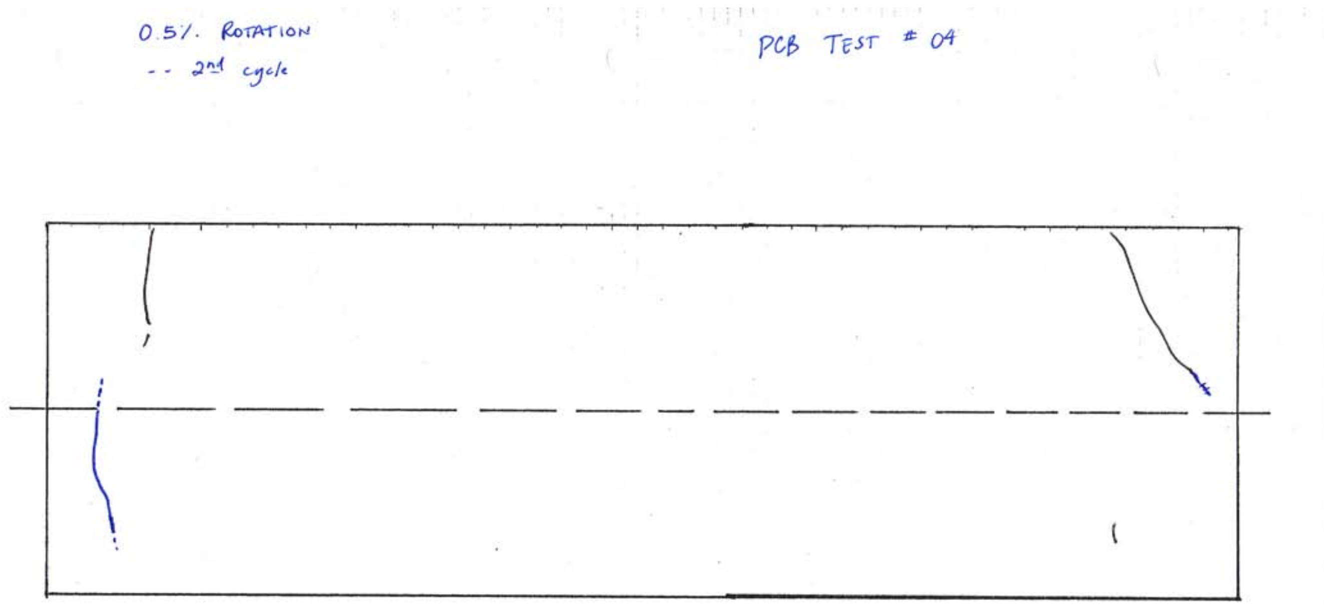

Figure F-32: Test 4 – θ_b = 0.50%.

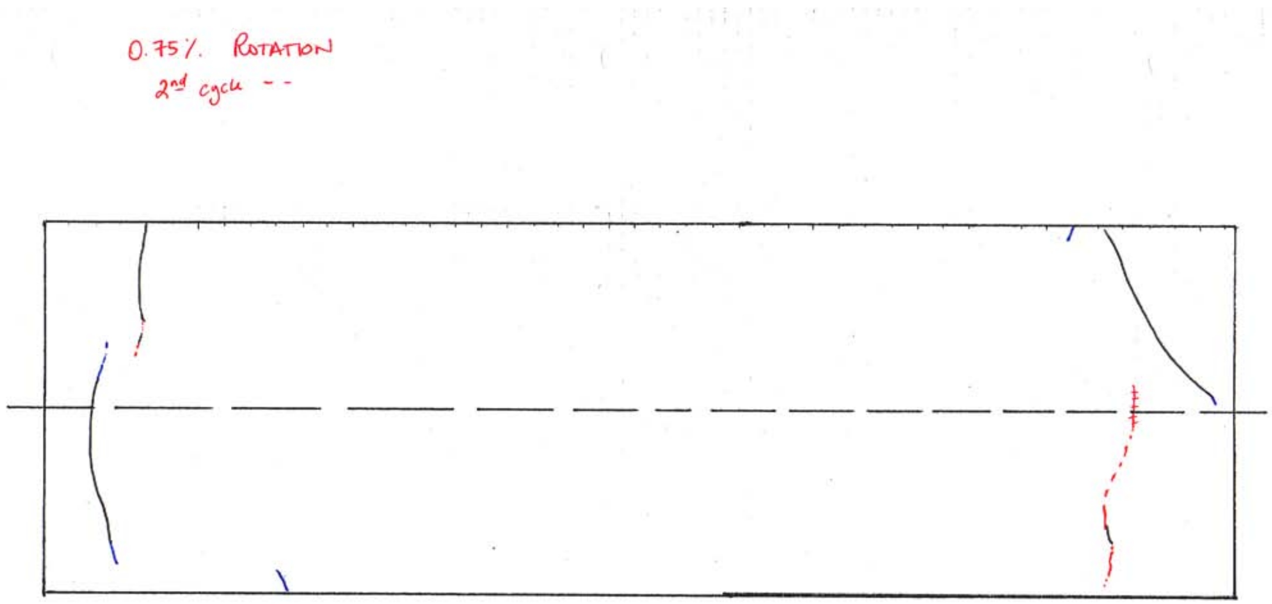

Figure F-33: Test 4 – θ_b = 0.75%.

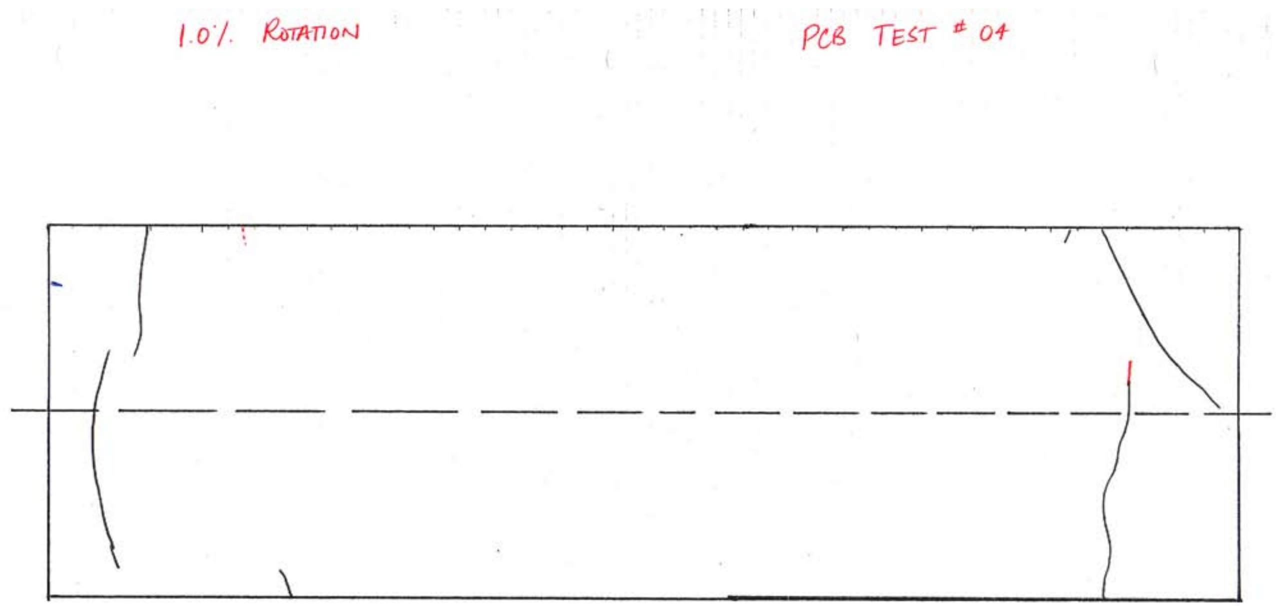

Figure F-34: Test 4 – θ_b = 1.0%.

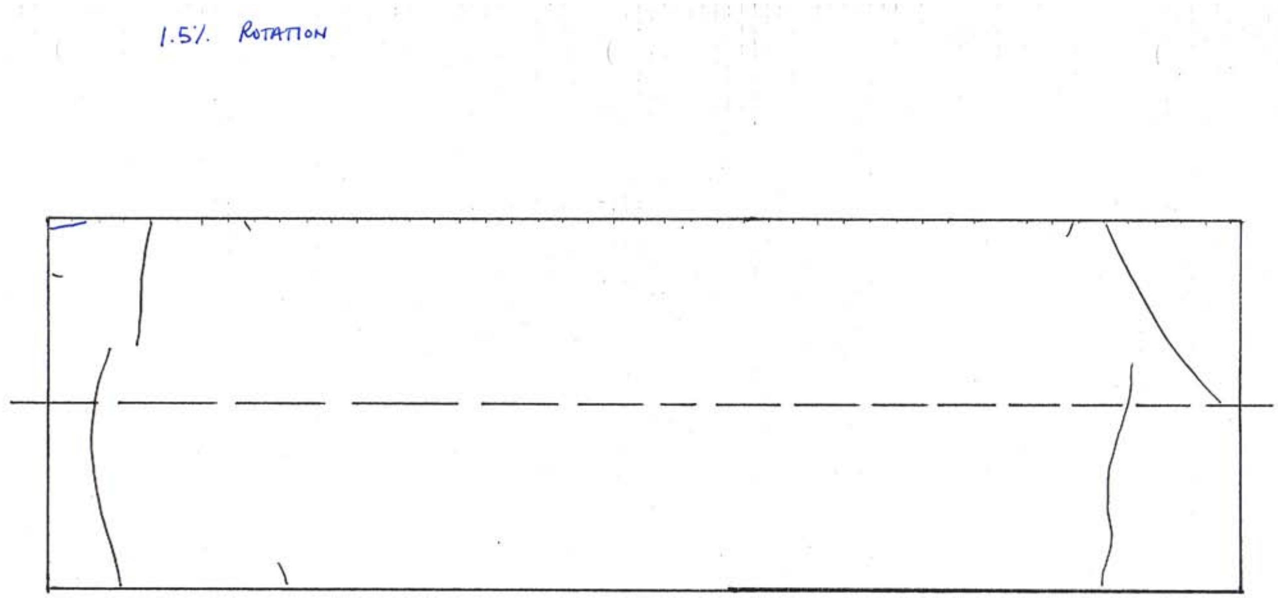

Figure F-35: Test 4 – θ_b = 1.50%.

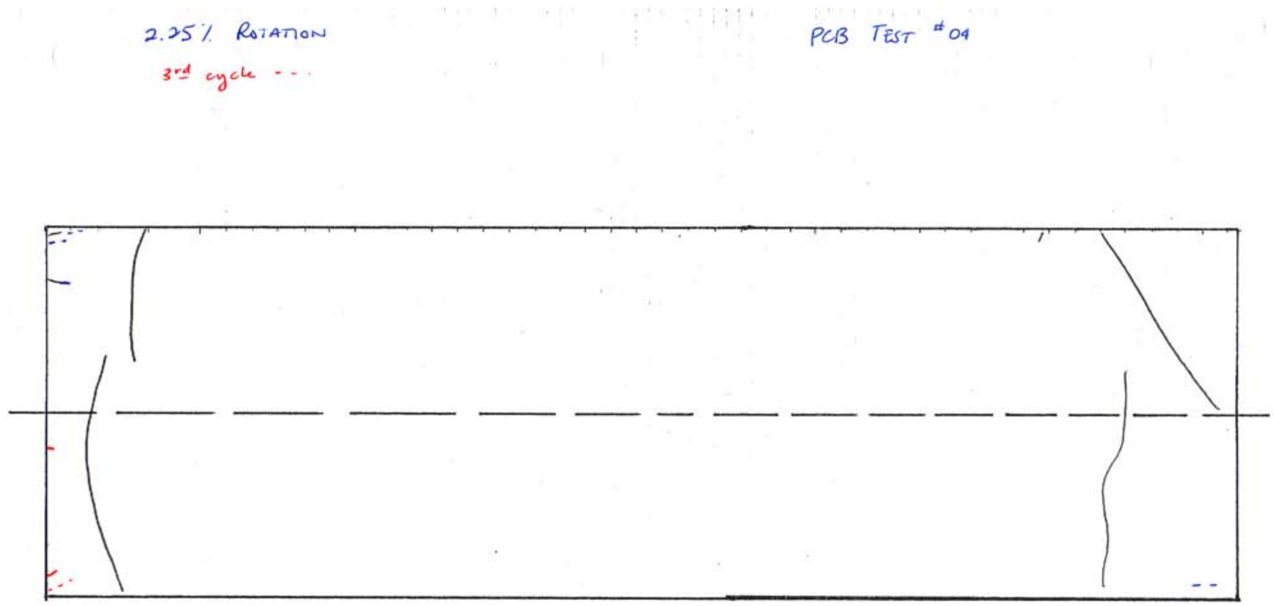

Figure F-36: Test 4 – θ_b = 2.25%.

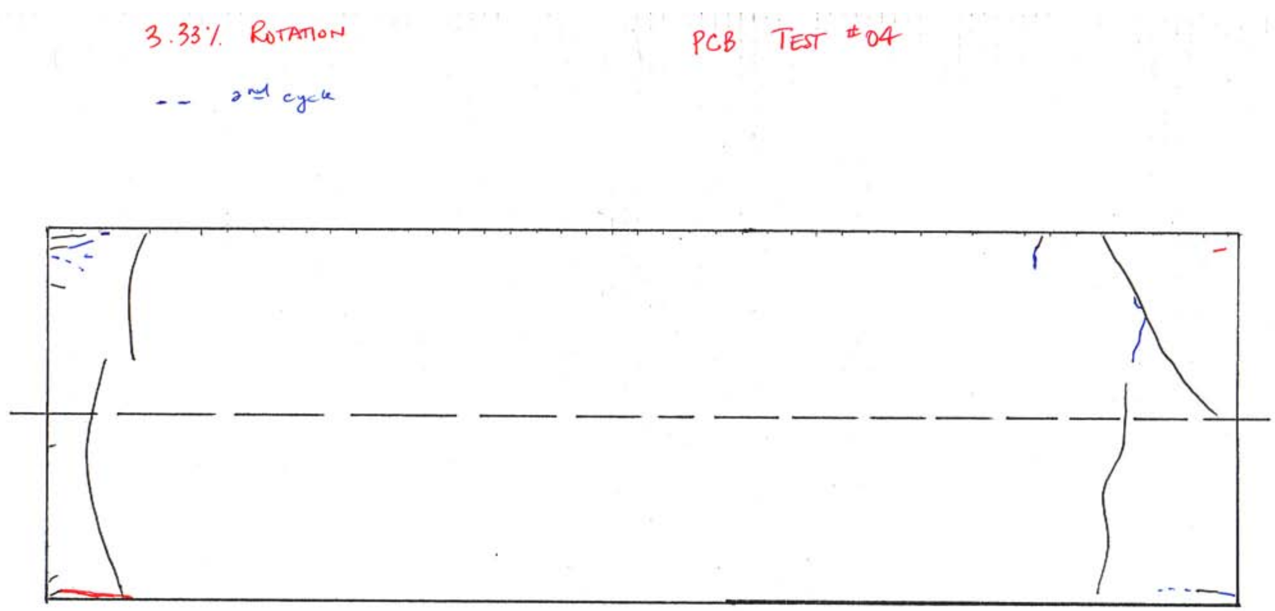

Figure F-37: Test 4 – θ_b = 3.33%.

TEST 4B

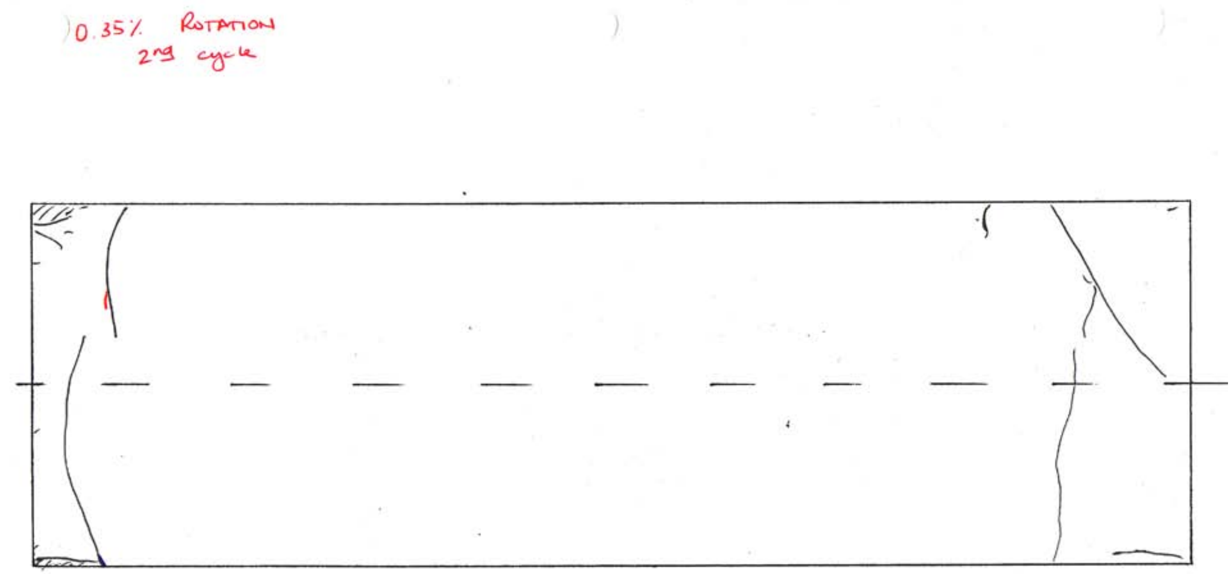

Figure F-38: Test 4B – θ_b = 0.35%.

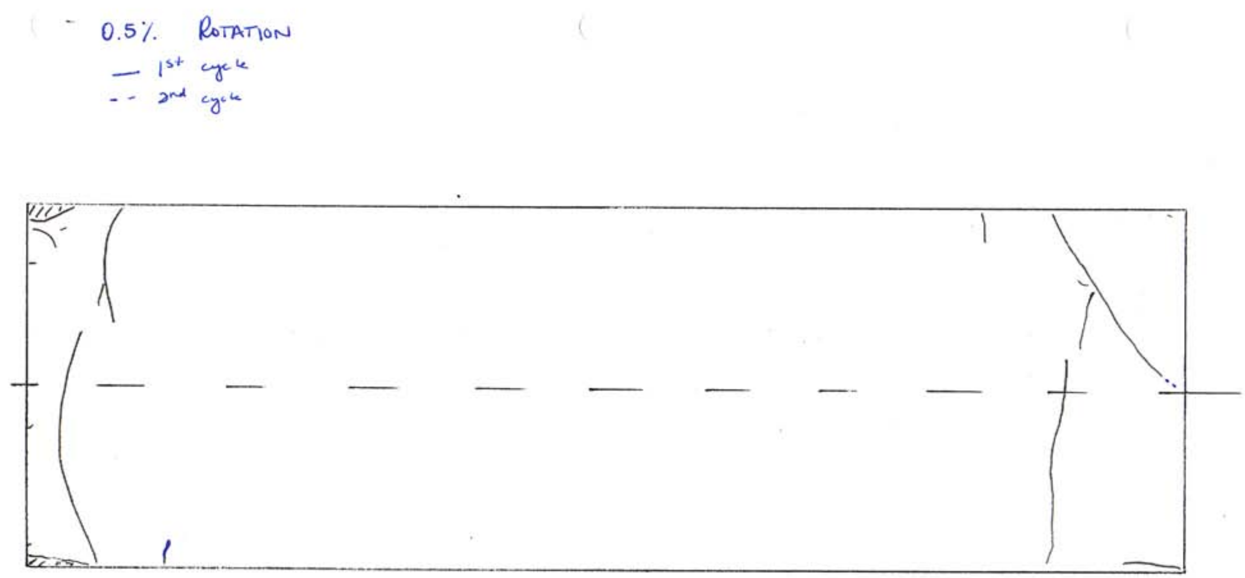

Figure F-39: Test 4B – $\theta_b = 0.50\%$.

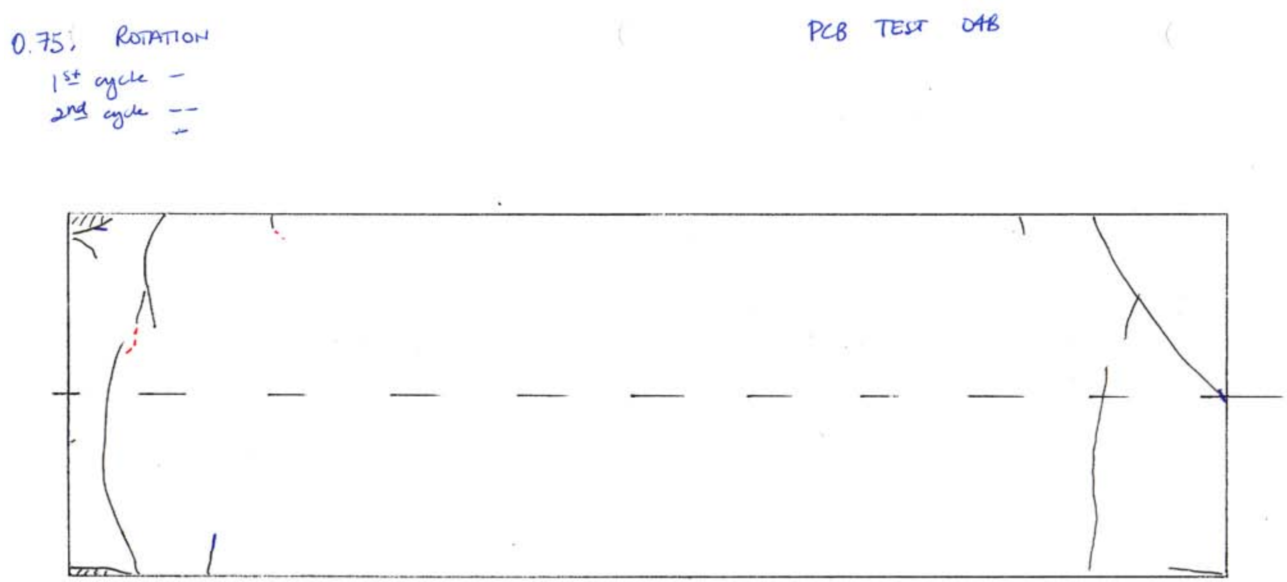

Figure F-40: Test 4B – θ_b = 0.75%.

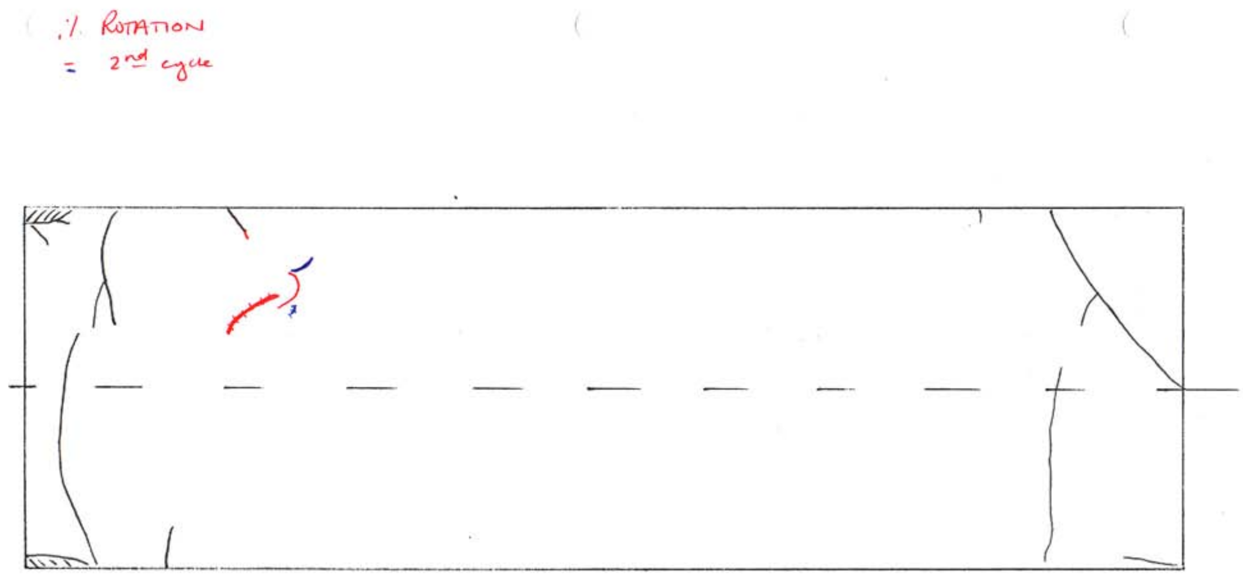

Figure F-41: Test 4B – θ_b = 1.0%.

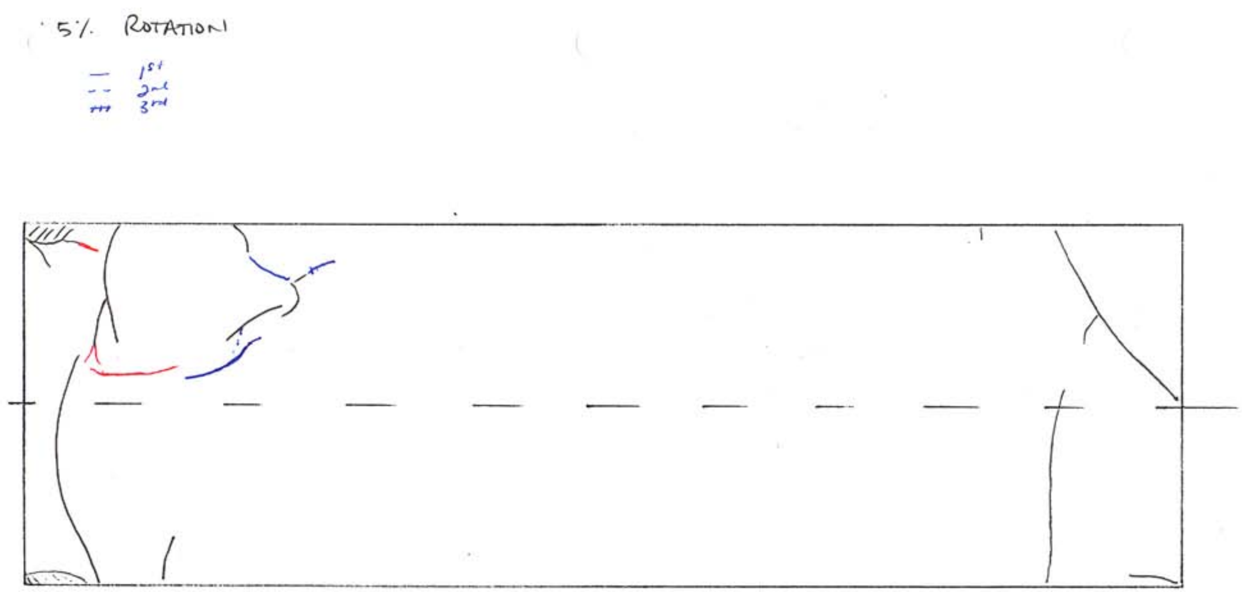

Figure F-42: Test 4B – θ_b = 1.50%.

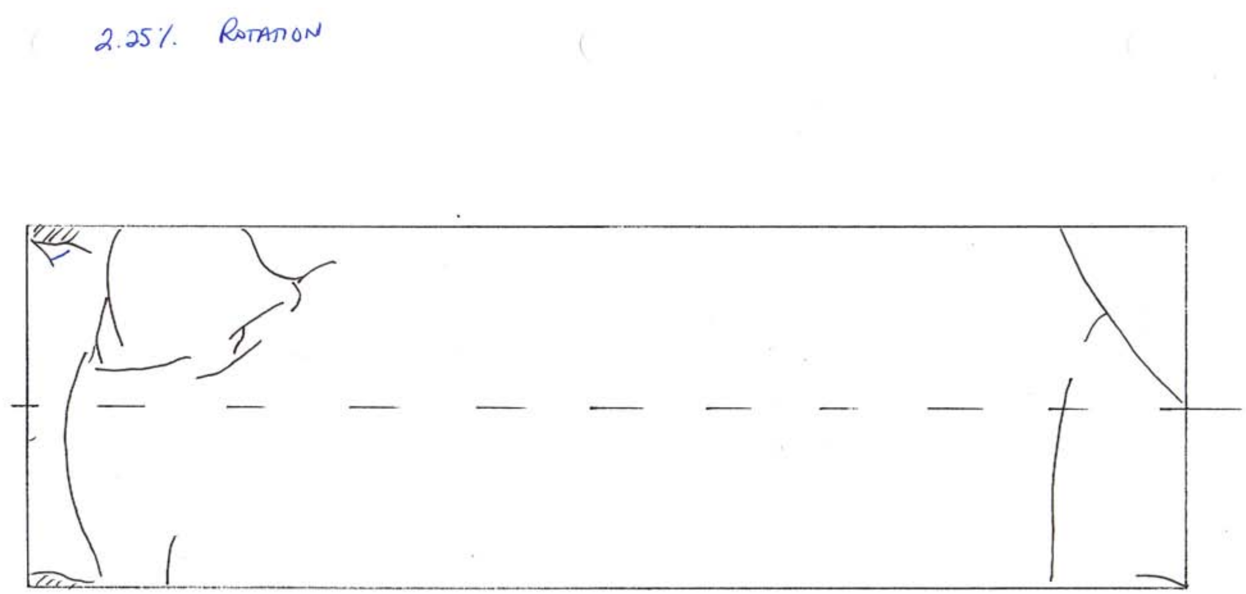

Figure F-43: Test 4B – θ_b = 2.25%.

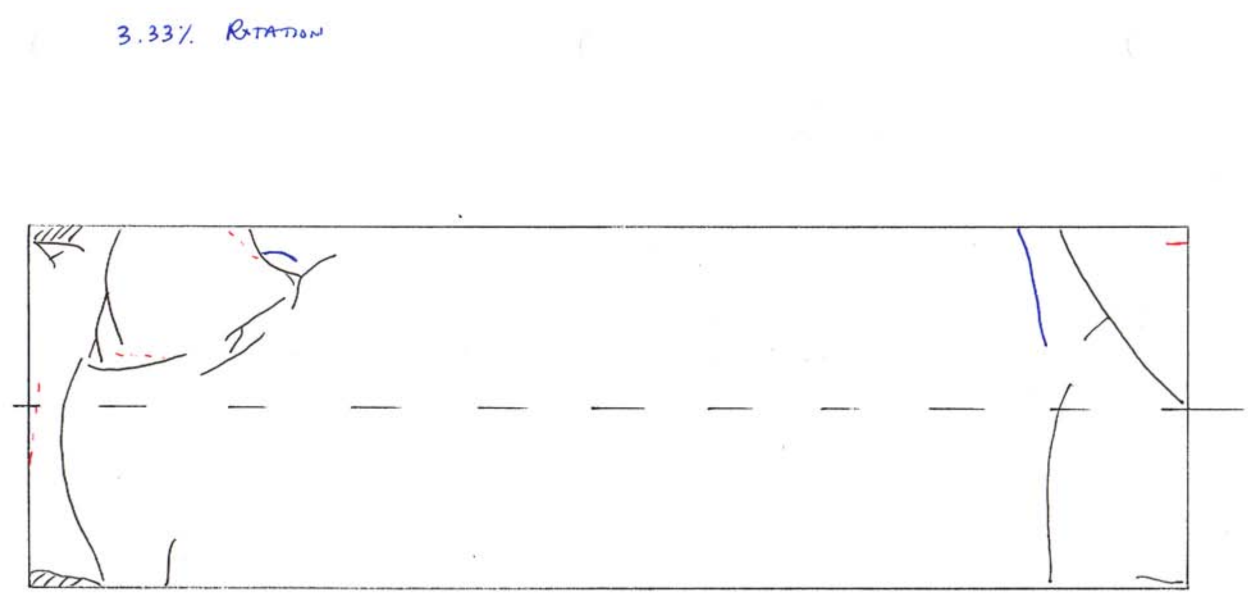

Figure F-45: Test 4B – θ_b = 3.33%.